UAB

Universitat Autònoma de Barcelona

Novel electrochemical approaches to micro- and nanoscale metallic materials for advanced magnetic and energy applications: Co-In, Fe-Rh and Fe-P systems

Irati Golvano-Escobal

Tesi Doctoral
Programa de Doctorat en Ciència de Materials

Eva Pellicer Vilà (directora i tutora)
Jordi Sort Viñas (Director)

Departament de Física
Facultat de Ciències
2017

UAB
Universitat Autònoma de Barcelona

Memòria presentada per aspirar al Grau de Doctor per

Irati Golvano-Escobal

Vist i plau

Eva Pellicer Vilà   Jordi Sort Viñas

(directora i tutora)   (director)

Bellaterra, 20/02/2017

La **Dra. Eva Pellicer Vilà**, investigadora Ramón y Cajal del Departament de Física de la Universitat Autònoma de Barcelona,

i el **Dr. Jordi Sort Viñas**, professor ICREA del Departament de Física de la Universitat Autònoma de Barcelona,

CERTIFIQUEN:

Que **Irati Golvano-Escobal** ha realitzat sota la seva direcció el treball d'investigació que s'exposa a la memòria titulada "Novel electrochemical approaches to micro- and nanoscale metallic materials for advanced magnetic and energy applications: Co-In, Fe-Rh and Fe-P systems" per optar al grau de **Doctor per la Universitat Autònoma de Barcelona.**

Que el disseny dels experiments, síntesi de mostres, llur caracteritzatió, l'anàlisi dels resultats, la redacció dels articles i d'aquesta memòria són fruit del treball d'investigació realitzat per Irati Golvano-Escobal.

I perquè així consti, signen el present certificat,

Eva Pellicer Vilà   Jordi Sort Viñas

Bellaterra, 20/02/2017

Abstract

This thesis dissertation covers the electrochemical synthesis and the characterization of the physical and physico-chemical properties of three different binary systems, namely cobalt-indium (Co-In), iron-rhodium (Fe-Rh) and iron-phosphorous (Fe-P). Several strategies toward systems miniaturization at micron- and nanoscales were pursued.

Continuous thick Co-In films (25 at.% ≤ Co ≤ 90 at.%) featuring spatio-temporal patterns (targets, concentric rings and spirals of variable sizes) were prepared on flat, conductive Si/Ti/Au substrates. X-ray diffraction analyses evidenced the formation of highly heterogeneous coatings. The spontaneous formation of these micron-sized patterns during electrodeposition gave rise to topographical, compositional and, in turn, magnetic patterning. The confined growth of Co-In in lithographically patterned arrays of cylindrical holes of 50 μm in diameter imposed restrictions to the type of spatio-temporal motifs that could be formed. Specifically, only spiral-like patterns of purely compositional nature (with virtually no topographic features) were self-generated in the microdisks. As a result, not only a periodic modulation of the magnetic but also electric and mechanical properties was uncovered using advanced surface sensitive characterization techniques. A detailed assessment of the cross-sections of the continuous Co-In electrodeposits using electron microscopy techniques revealed a layer-by-layer growth mode spanning the whole deposit thickness (10 μm). The occurrence of local changes in composition within each layer (ca. 175 nm thick) also led to stripe-like magnetic patterning.

Meanwhile, bimetallic Fe-Rh nanoparticles with different sizes, Fe/Rh ratios, and coverage degree were prepared by direct current electrodeposition from Fe(III) containing electrolyte solutions to prevent the formation of dense, continuous films. The nanoparticles were well-adhered to the substrate and could be directly tested as an electrocatalyst without the need for post-processing immobilization steps. The nanoparticles were mostly metallic as demonstrated by X-ray photoelectron spectroscopy analyses. Depending on the Fe content (15 at.% ≤ Fe ≤ 36 at.%), diameter (20-80 nm) and coverage, they showed dissimilar electrocatalytic activity towards hydrogen evolution reaction (HER) in alkaline media. Under specific synthetic conditions, the resulting nanoparticles outperformed pure Rh nanoparticles obtained from an analogous electrolytic solution.

Finally, highly-ordered, macroporous Fe-P films were prepared by electrodeposition onto Si/Ti/Au substrates pre-patterned by colloidal templating. Prior to electrodeposition, polystyrene spheres of 350 nm in diameter were self-assembled on the substrate by electrophoresis. Fully dense Fe-P films were also electrodeposited for comparison purposes. Both dense and porous films showed tunable Fe/P ratios and magnetic behavior. The electrocatalytic activity towards HER and oxygen evolution reaction (OER) was investigated in alkaline media.

Resumen

La presente tesis doctoral abarca la síntesis electroquímica y caracterización de las propiedades tanto físicas como fisicoquímicas de tres sistemas binarios diferentes, el cobalto-indio (Co-In), hierro-rodio (Fe-Rh) y hierro-fósforo (Fe-P). Se han llevado a cabo varias estrategias para miniaturizar estos sistemas tanto hacia la micro- como hacia la nanoescala.

Se han sintetizado capas continuas de Co-In, sobre sustratos conductores de silicio recubiertos con capas semilla de titanio y oro, que muestran estructuras espacio-temporales (*targets*, anillos concéntricos y espirales de distinto tamaño). Los análisis de rayos X evidencian la formación de capas heterogéneas. La formación espontánea de este tipo de estructuras micrométricas durante la electrodeposición genera a su vez un patrón tanto topográfico como composicional que a su vez deriva en un patrón magnético. En cambio, al crecer el Co-In de forma confinada, en cavidades cilíndricas litografiadas de $50\,\mu$m de diámetro, se restringe el tipo de estructuras que conforman las espacio-temporales. Concretamente, en los microdiscos, sólo se generan de manera espontánea y únicamente a nivel composicional (es decir, prácticamente sin relieve topográfico) las estructuras que tienen forma de espiral. Como consecuencia, se ha revelado a través de técnicas avanzadas de caracterización de superficies, no sólo una modulación periódica del magnetismo, sino también de las propiedades eléctricas y mecánicas. También se ha llevado a cabo un estudio detallado de la sección de las capas de Co-In. El uso de técnicas de microscopia avanzadas ha revelado un crecimiento laminar que se expande a lo largo de todo el grosor de la capa (10 μm). Además, las variaciones composicionales locales de cada capa (175 nm de grosor aproximadamente) deja un patrón de franjas magnéticas.

Por otro lado, se han depositado utilizando corriente continua nanopartículas bimetálicas de Fe-Rh con diferentes tamaños, relación Fe/Rh y grado de recubrimiento. El electrolito contenía Fe(III) para prevenir la formación de capas continuas. Las nanopartículas han quedado perfectamente adheridas al sustrato por lo que se pudieron emplear directamente como electrocatalizadores sin ningún proceso intermedio de inmovilización. Los análisis de espectroscopia de fotoelectrones emitidos por rayos X muestran que las nanopartículas son mayoritariamente metálicas. Dependiendo del contenido de hierro (15 at.% $\leq$ Fe $\leq$ 36 at.%), diámetro (20-80 nm) y grado de recubrimiento, las nanopartículas presentan una actividad catalítica diferente para la producción de hidrógeno en medio alcalino. Se han conseguido nanopartículas, fabricadas bajo condiciones de síntesis específicas, cuya actividad catalítica supera la de nanopartículas de Rh puro obtenidas a partir de un baño análogo.

Finalmente, se han crecido por electrodeposición capas macroporosas altamente ordenadas de Fe-P en sustratos con litografía coloidal. Antes de la electrodeposición, se han depositado electroforéticamente esferas de poliestireno de 350 nm de diámetro que se ordenan sobre el sustrato. Para poder comparar resultados, también se han fabricado capas continuas de Fe-P. Tanto las capas continuas como las porosas presentan una relación Fe/P y un comportamiento magnético variable. Su actividad catalítica para las reacciones de evolución de hidrógeno y de oxígeno se ha investigado en medio alcalino.

Glossary

- AAO: anodic aluminum oxide

- AFM: atomic force microscopy

- AM: amplitude modulation

- C-AFM: conductive atomic force microscopy

- CE: counter electrode

- CV: cyclic voltammetry

- DC: direct current

- ECSA: electrochemical surface area

- EDX: energy dispersive X-ray

- fcc: face-centered cubic

- FE-SEM: field emission scanning electron microscopy

- FM: frequency modulation

- H_C: coercivity

- hcp: hexagonal close-packed

- HER: hydrogen evolution reaction

- ICP-MS: inductively coupled plasma mass spectrometry

- ITO: indium tin oxide

- KPFM: Kelvin probe force microscopy

- LECD: localized electrochemical deposition

- LIGA: Lithographie, Galvanoformung and Abformung

- LSV: linear sweep voltammetry

- M_R: remanent magnetization

- M_S: saturation magnetization

- M: magnetization

- MEMS: microelectromechanical system

- MFM: magnetic force microscopy

- MOKE: magneto-optic Kerr effect

- MQ-water: Milli-Q water

- NP: nanoparticle

- NT: nanotube

- NW: nanowire

- OER: oxygen evolution reaction

- PC: polycarbonate

- PP: pulse plating

- PPy: polypyrrole

- PS: polystyrene

- RE: reference electrode

- RHE: reversible hydrogen electrode

- RPP: reverse pulse plating

- S/V: surface-to-volume

- SE: secondary electrons

- SHE: standard hydrogen electrode

- SQUID: superconducting quantum interference device

- STEM: scanning transmission electron microscopy

- TEM: transmission electron microscopy

- VSM: vibrating sample magnetometry

- WE: working electrode

- XAS: X-ray absorption spectroscopy

- XMCD-PEEM: X-ray magnetic circular dichroism and photoemission electron microscopy

- XPS: X-ray photoelectron spectroscopy

- XRD: X-ray diffraction

PREFACE

The contents of this thesis have been organized in different chapters as follows:

- Chapter 1: the introduction deals with the theoretical concepts related to the basics of metal electrodeposition and to the ferromagnetic and electrocatalytic properties of metallic materials. Special emphasis is laid on the description of the hydrogen evolution reaction (HER) and the oxygen evolution reaction (OER) processes. Besides, the state-of-the-art of Co-In and Fe-based systems prepared by electrochemical means is given, followed by the main goals of this thesis and a schedule of the whole work.

- Chapter 2: focuses on the electrodeposition setup and the experimental conditions used to fabricate the Co-In, Fe-Rh and Fe-P samples. The most relevant experimental parameters regarding the techniques used for the morphological, structural, physico-chemical, mechanical and magnetic characterization of the samples are pointed out.

- Chapter 3: presents the obtained results for Co-In and Fe-Rh systems as a compilation of articles. A brief introductory abstract is included before each set of articles.

- Chapter 4: describes the fabrication of porous Fe-P samples using hole-mask colloidal lithography and electrodeposition and the characterization of their magnetic and electrocatalytic properties. The results shown herein are not formally included as a compilation of articles but complement chapter 3 and are thus equally important.

- Chapter 5: presents a general discussion about the three different systems studied throughout this thesis, namely Co-In, Fe-Rh and Fe-P.

- Chapter 6: points out the main conclusion of the thesis.

- Chapter 7: future perspectives are briefly outlined.

CONTENTS

1

INTRODUCTION

There is an increasing demand for synthesis of novel (nano)materials and their smart integration in miniaturized devices in order to achieve enhanced performance or even provide new functionalities. Materials with sophisticated and complex architectures are being created by researchers worldwide. Through the combination of various synthesis techniques and the accurate control over the synthesis variables, scientists have broadened the spectrum of available materials and configurations at the sub-micron and nanoscales. Electrodeposition has been suggested as one of the most attractive synthetic methods to face current challenges in materials science and engineering. Metallic materials (metals, alloys, intermetallic compounds), polymers, semiconductors, graphitic layers, metal oxides (and combinations thereof) can be produced by electrochemical means onto a conductive substrate. Nevertheless, the electrosynthesis of metallic materials is by far the most exploited.

Gold (Au) and silver (Ag) were the first electrodeposited materials in 1803. In those times, electrodeposition was mainly limited to decorative purposes [1]. Only later, in the mid-1800, it started being widely used to coat steel parts and machining tools in order to increase hardness and enhance corrosion resistance [1]. Much later, in the 1970s, electrodeposition of magnetic recording systems [2] was developed at IBM, thereby extending the capabilities of the technique to microfabrication methods [3]. Nowadays, electrodeposition faces a third revolution, pushed by the need to continuously improve the performance of micro- and nanosystems and energy conversion devices [4, 5]. Electrodeposition offers unique advantages over other deposition techniques. Namely, it does not require vacuum conditions; it can be carried out at room temperature (when plating from aqueous electrolytes), and the growth parameters (overpotential, current density, and time) can be controlled very precisely. As a result, electrodeposition offers unique control over the growth process in contrast to physical deposition methods. Thin film magnetic sensors [6] and magnetic field generators [7], thermoelectric materials and nanostructures [8], and photovoltaics and energy conversion [2, 9, 10, 11, 12] are just some of the fields in which electrodeposition is widely applied.

Both mask-less and mask-assisted electrodeposition approaches have enabled the production of micro- and nanomaterials with unimaginable shapes and degrees of complexity. For example, the maskless meniscus confined electrodeposition approach has been recently utilized to grow Cu microwires [13]. Likewise, microcolumns of several metals and a few alloys have been obtained by localized electrochemical

deposition (LECD) technique [14]. Regarding mask-assisted approaches, Yang et al. synthesized Pd and Cu nanowires (NWs) with large surface-to-volume (S/V) ratio using pre-contoured shapes inside the nanochannels of anodic aluminum oxide (AAO) templates [15]. Hybrid helical magnetic microrobots that imitate bacteria flagella motion have been recently fabricated by sequential electrodeposition of CoNi alloy and polypyrrole (PPy) on 3D patterned substrates [16].

1.1. Electrodeposition

Electrodeposition is an electrochemical process by which a coating of a given material (typically a metal) is produced onto a conductive substrate (termed working electrode, WE) by the action of an external electric current. Hence, the reaction of interest (i.e., deposition) occurs on the WE. The WE is in conjunction with either an anode (two-electrode configuration) or a reference electrode (RE) and an auxiliary or counter electrode (CE) (three-electrode configuration). Typically, the reaction of interest is a reduction and hence, the WE is negatively charged (it acts as the cathode) (Figure 1.1). In such a case, when the WE is immersed in an electrolyte solution that contains the parent ions (typically cations) of the target metallic coating, these get reduced on the WE. The WE provides the electrons required to discharge the ions into their metallic form:

$$M^{2+} + 2e^- \rightarrow M^0 \tag{1.1}$$
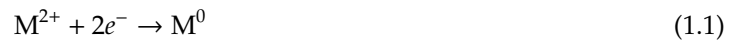
In short, electrodeposition involves the reduction of a metallic compound dissolved in the electrolyte and the deposition of the resulting metal onto the WE.

Electrodeposition is based on the Faraday's laws of electrolysis which describe the quantitative relationship between electricity and ions discharged at electrodes (Eq. 1.2 and 1.3).

$$\text{Faraday's first law: } W \propto Q \tag{1.2}$$

where W is the mass of ions liberated in grams and Q the quantity of electricity passed in Coulombs.

$$\text{Faraday's second law: } E \propto Z \tag{1.3}$$

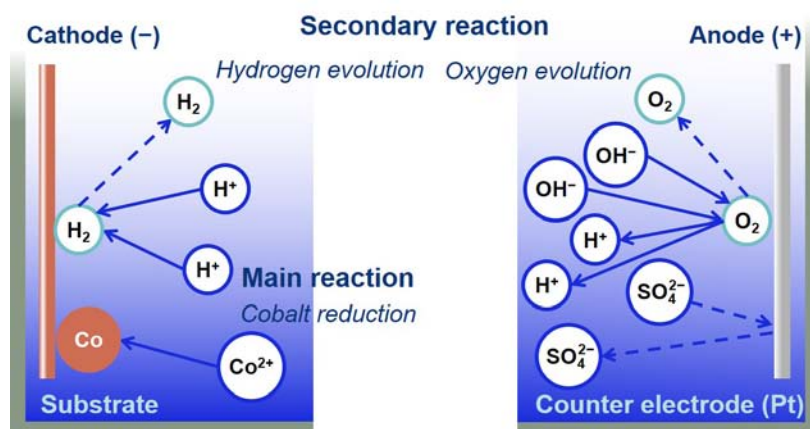where E is the weight and Z the electrochemical equivalent.

Figure 1.1: Schematic drawing of the reactions taking place at the cathode and the anode in cathodic electrodeposition.
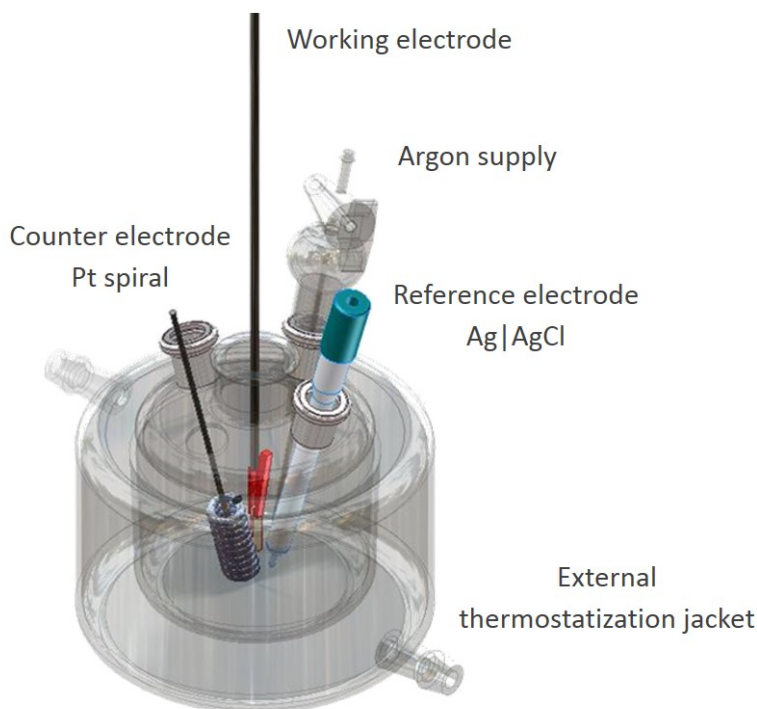
Figure 1.2: Schematic drawing of a three-electrode cell. Courtesy of S. Pané.

Through these laws it can be predicted that:

- the quantity of electricity passed by is a measurement of the amount of chemical change that will be produced;

- the amount of substance that will be liberated by a given quantity of electricity can be predicted if the chemical equivalent weight of a substance is known.

There are no exceptions to these laws. Apparent exceptions are due to the fact that Faraday's laws assume 100% current efficiency. In broad strokes, they assume that only the material of interest is being deposited onto the WE. However, hydrogen evolution reaction and/or other secondary reactions can occur, which make the actual current efficiency lower. Even non-electrolytic reactions can occasionally take place. Therefore, current efficiency is an important parameter in the galvanic industry. High current efficiency baths are required for obvious economic reasons. However, in some cases, low efficiency electrolytic solutions might be designed on purpose when the growth of a fully dense coating is to be precluded (e.g. in order to favor the formation nanoparticles (NPs) onto a substrate).

As aforementioned, an electrolytic cell (Figure 1.2) consists of a WE, a CE, usually made of platinum, and a RE, which can be removed when a precise control of the potential across the electrochemical interface is not needed. The plating solution and the external circuit connect the electrodes to fulfill the physical embodiment needed for the electrodeposition process.

The composition, morphology, physical and physico-chemical properties of the deposits can be fine-tuned by adjusting the electrolyte composition as well as its temperature and pH. These factors, together with the applied electrodeposition parameters (deposition mode, potential or current density, stirring regime, etc.), determine the properties of deposits. Since electrochemical deposition techniques are in-

creasingly being used in advanced technology applications, a greater control over growth processes is needed, which in turns requires a better understanding of the fundamental phenomena involved.

1.1.1. Mask-less and mask-assisted electrodeposition

Electrodeposition has conquered diverse areas since its first use two centuries ago, ranging from applications as protective coatings to advanced micro- and nanorobotic platforms in order to meet society's rising expectations. The production of NPs (0), NWs and nanotubes (NTs) (1D), thin films (2D), bulk nanocrystalline metals (3D) [17], multilayered coatings, and nanoparticle-reinforced composite coatings [18] has been demonstrated by electrochemical deposition.

The development of mask-less and template-assisted electrodeposition methods has enabled the production of myriad patterned micro- and nanostructures (Table 1.1). Figure 1.3 depicts the two modes of electrodeposition leading to patterned structures. Metallic microstructures have been the object of intensive research due to their applications in electronics and optics. High aspect-ratio microstructures typically made of Cu and Ni have been extensively fabricated by LIGA, the German acronym for Lithographie, Galvanoformung and Abformung [19, 20]. LIGA is a hybrid fabrication technique that involves the following steps: lithography, electrodeposition and molding. While X-ray LIGA is used to fabricate with great precision high aspect ratio microstructures, extreme ultraviolet (EUV) LIGA is used to fabricate lower quality microstructures. Template-assisted methods have also become very popular when it comes to the synthesis of arrays of metallic NWs, NTs and nanorods. AAO and track-etched polycarbonate (PC) membranes are typically used as templates. The number of publications showing the synthesis of NW arrays via template-assisted electrodeposition has increased exponentially during the last two decades. NWs with controlled diameter, which is related to the template pore size, and controlled length, which can be tuned by adjusting the electrodeposition time, can be straightforwardly obtained (Figure 1.3b).

Colloidal lithography, Figure 1.3c, is also a widely used technique, often combined with electrodeposition to fabricate pseudo-ordered porous films. There exist several methods to create a pattern of colloidal crystals e.g., dip-coating, ultrasonically-assisted self-assembly, solvent evaporation methods, and electrophoretic deposition. When combined with electrodeposition, colloidal lithography is based on the use of a template of spherical particles (usually made of polystyrene (PS) or an easily removable polymer with mild solvents) with diameters ranging from nanometers to micrometers arranged over a conductive substrate. The subsequent electrodeposition of the metal or metallic alloy takes place at the interstitial voids existing between the particles. Afterwards, the selective removal of the beads results in the formation of pseudo-ordered 3D porous structures. The dimension of the colloids determines the pitch and the

Table 1.1: Template-free and template-assisted electrodeposition approaches toward metallic micro- and nanostructures. Some examples are given on the right columns.

| Template-free electrodeposition		Template-assisted electrodeposition	
Localized electrochemical deposition (LECD): **high aspect-ratio of microstructures**	Co, Ni, Cu and Cu-Ni microcolumns [21]	**Lithographed substrates** **Photo: microstructures** **e-beam: nanostructures**	Micro- and nanostructures of magnetic alloys [22], [23]
Diluted solutions/ **Low conductive substrates/** **Short deposition times:** **nanoparticles and nanowires**	Zero- and 1-dimensional nanostructures of metals, alloys, core-shell architectures [24]	**Alumina and polycarbonate templates:** **nanotubes and nanowires**	Arrays of single-phase, multi-segmanted, core-shell structures [25, 26]
Ionic liquids: **nanowires**	Alloy filament arrays (e.g. Ni-Zn) [27]		
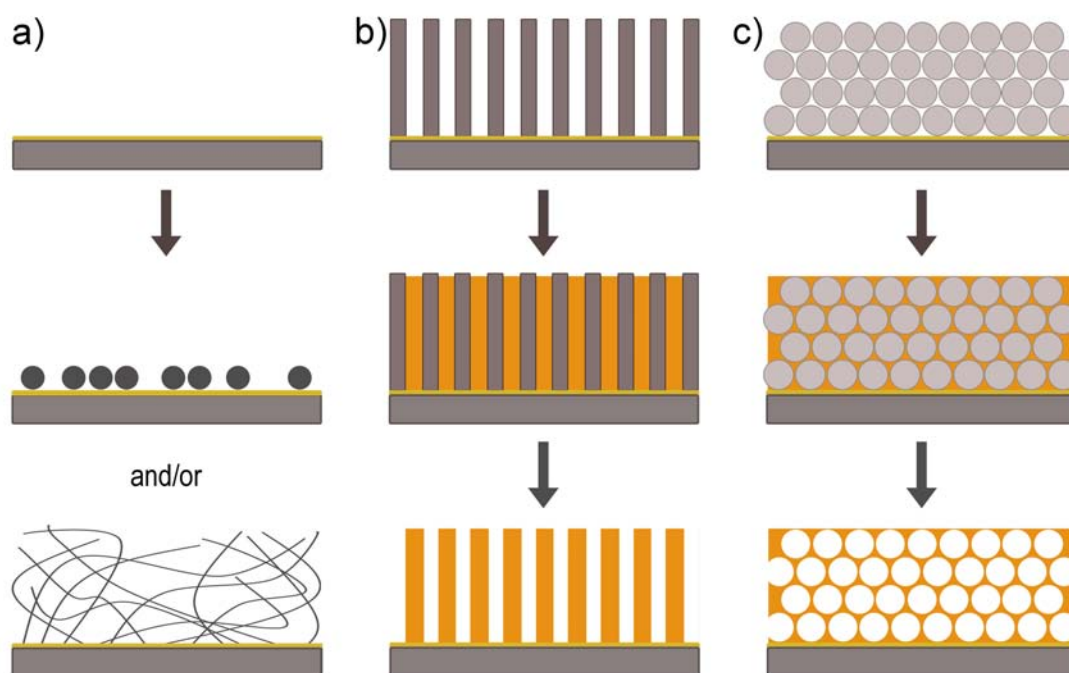
FIGURE 1.3: a) Mask-less and b-c) mask-assisted electrodeposition approaches are schematically shown. The first row represents the substrate onto which electrodeposition takes place. Case a) represents the growth of NPs and a forest of NWs directly onto the substrate, without the assistance of any solid mask, by electrodeposition under suitable conditions. Conversely, a nanoporous template and a colloidal crystal previously assembled on the substrate serve as templates in b) and c), respectively. In both cases this is followed by electrodeposition inside b) the pores and c) the interstitial voids between the spheres. The third row represents the chemical etching of the rigid template to obtain b) free standing NWs and c) a 3D porous material.

pore size of the final material. The combination of both, colloidal lithography and electrodeposition, can render metallic macro- or mesoporous films characterized by a large surface area and light weight, which can exhibit enhanced (electro)catalytic activity and superhydrophobic behavior, among other properties [28, 29].

Meanwhile, the growth of patterned structures that do not involve a rigid template (mask-less electrodeposition) has been much less exploited [30]. The electrodeposition of NPs with controlled characteristics, namely, size, morphology and composition has been successfully explored. Although NPs typically deposit onto the substrate without any long-range order, they are immobilized on it, which can be advantageous for several applications. The main disadvantage of this approach is the difficulty to achieve narrow particle size distributions [31, 32, 33]. Both potentiostatic and galvanostatic methods have been employed to grow NPs on various substrates, most typically low conductive substrates in order to avoid particles coalescence. Ma et al. electrodeposited quasi-spherical Au NPs on indium tin oxide (ITO) coated glass showing high electrocatalytic reactivity towards glucose oxidation [34]. Likewise, Zhu et al. synthesized Ni NP chains embedded in TiO_2 [35]. Very recently, a novel 3D printing method able to locally electroplate structures ranging from simple walls to triple helices using scanning probes has been demonstrated [36]. These examples illustrate the burgeoning interest of researchers to seek new solutions in the electrodeposition field.

Among all physical and physico-chemical properties of electrodeposited metallic materials, magnetic and electrocatalytic properties currently attract a great deal of interest. Therefore, next sections 1.2 and 1.3 are focused on the fundamentals of ferromagnetism and ferromagnetic materials, and electrocatalytic properties of metals, with particular emphasis on the hydrogen evolution reaction (HER) and the oxygen evolution reaction (OER).

1.2. FERROMAGNETIC MATERIALS

Materials can be classified into different categories depending on the response to an applied external field, H. Namely, diamagnetism, paramagnetism, ferromagnetism, antiferromagnetism and ferrimagnetism are the different magnetic behaviors in nature. The magnetization curves depicted in Figure 1.4a show the magnetic response of the various types of materials to an applied field. Such response is associated with how the magnetic moments are arranged in the atoms (Figure 1.4b). In particular, the magnetization curves of ferromagnetic and ferrimagnetic materials show a cycle termed "hysteresis loop", from which saturation magnetization (M_S), remanent magnetization (M_R), and coercivity (H_C) values can be obtained. Depending on their magnitude, ferromagnetic materials can be classified into soft (low H_C and typically high M_S) and hard (large H_C and M_R) materials (Table 1.2).
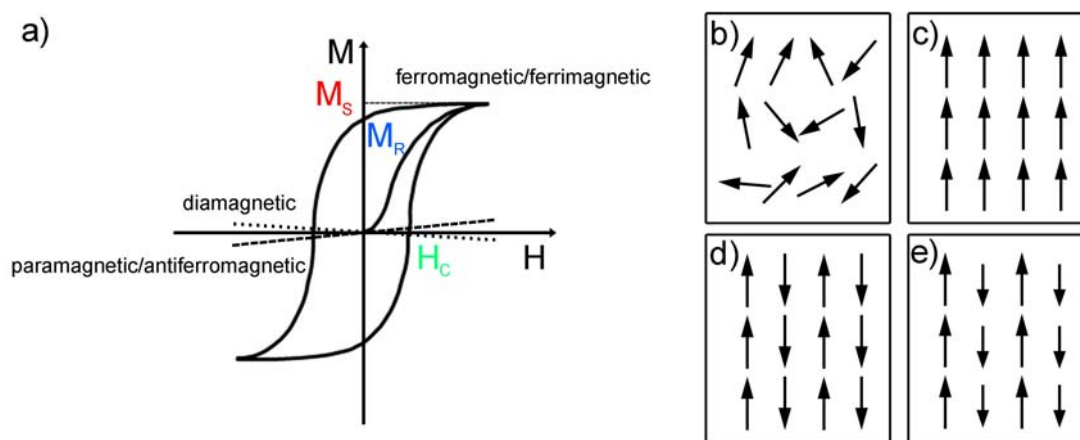
FIGURE 1.4: a) Magnetic response (M) of materials as a function of an external magnetic field (H), and schematic representation of the magnetic moments configuration for: b) paramagnetic, c) ferromagnetic, d) antiferromagnetic, and e) ferrimagnetic materials.

TABLE 1.2: Typical H_C and M_S values for soft- and hard-magnetic materials, examples and applications.

	H_C	M_S	e.g.	Applications
Soft-magnetic	<10 Oe	>100 emu/g	Fe Ni permalloy ($Fe_{20}Ni_{80}$)	electromagnets transformers cores
Hard-magnetic (permanent magnet)	>1000 Oe	<100 emu/g	$SmCo_5$ Al-Ni-Co alloys $Nd_2Fe_{14}B$	motors and generators high-density recording media synchrotrons

The exact shape of the hysteresis loop in either hard- and soft-magnetic materials depends on several factors, such as crystallite size, magnetic anisotropy, orientation, particle shape, and exchange interactions. For these reasons both routine and advanced instrumentation is used to capture and understand the magnetic behavior of ferromagnetic materials:

- Vibrating Sample Magnetometer (VSM) is the most common equipment to measure the hysteresis loop at room and higher temperatures.

- Superconducting Quantum Interference Device (SQUID) is able to detect incredibly weak magnetization signals. Compared to VSM, it is typically used to perform measurements at low temperatures.

- Magnetic Force Microscope (MFM) is an special mode of operation in the Atomic Force Microscope (AFM). MFM measures the near-surface stray fields produced between the tip and the sample. MFM images contain information of magnetic domain distributions on the sample surface.

- Magneto-optic Kerr Effect Magnetometer (MOKE) has been extensively used in the field of surface magnetism since it is highly sensitive to the magnetization within the skin depth region, typically 10-20 nm in most metals [37].

- X-ray magnetic circular dichroism and photoemission electron microscopy (XMCD-PEEM) provide simultaneously the relationship between the microstructure of a material and the characteristics of the magnetic reversal. XMCD-PEEM constitutes an extremely flexible and widely used analytic tool that combines surface analysis technique and spectroscopic chemical information with high spatial resolution. It is a promising method for the analysis of complicated domain structures and heterogeneous morphologies. However, it is not a routinely-based technique as it normally uses synchrotron radiation.

Electrodeposited materials with unique magnetic properties have been extensively investigated by the scientific community. For example, although the production of ultra-thin films by electrochemical means is very challenging [38], several authors have reported on the growth of iron-group metal films with enhanced H_C. Bartlett et al. electrochemically synthesized nanostructured Co films consisting of a hexagonal array of cylindrical pores with three to five times greater H_C than polycrystalline cobalt [39]. Mangen et al. also obtained smooth Co films, thinner than 7 nm, and observed that a hysteresis loop showed up for the first time at a thickness of 0.33 nm by using MOKE in longitudinal configuration. The authors also observed that the Kerr intensity linearly increased with film thickness up to 7 nm [40]. The production of relatively thick magnetic coatings by electrodeposition has been even more thoroughly investigated. Kulkarni and Roy reported on the electrodeposition of Co-rich CoPtP films with thicknesses up to 82 μm for use in magnetic microelectromechanical systems (MEMS) applications [41]. Pané et al. electrodeposited ferromagnetic CoNiReP films by direct current (DC) and reverse pulse plating (RPP). The composition, microstructure and, in turn, magnetic properties of these films were shown to strongly depend on the applied current density. Depending on the Co content, either soft-magnetic (for <35 at.% Co) or hard-magnetic behavior (Co-rich compositions) with perpendicular anisotropy, were obtained [42]. Nasirpouri et al. studied the effect of different current modulation techniques on the texture, surface morphology, and magnetic properties of Ni films. They concluded that pulse plating (PP) and RPP deposition methods lead to better quality nanocrystalline Ni films than the DC. In addition, H_C for films

prepared by PP and RPP methods was higher than that of DC-plated films [43]. These are just some examples to grasp the opportunities offered by electrodeposition to the magnetic field.
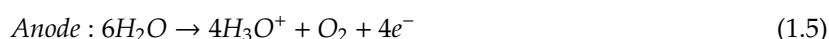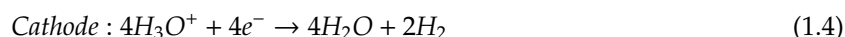
1.3. Electrocatalytic properties of metallic materials: HER and OER

Materials can exhibit electrocatalytic properties, meaning that they are able to transfer electrons between an electrode and target reactants, and/or facilitate and intermediate chemical transformation by either oxidation or reduction. Among the different investigated reactions in the field of electrochemistry, water electrolysis using nanostructured metals, metallic alloys, and bimetallic structures as catalysts in acidic or alkaline media is currently being deeply studied in order to produce hydrogen gas. Water electrolysis has unique advantages over other approaches to produce hydrogen including reactant availability, safety, stable output and product purity.

There are several reasons why hydrogen is getting more and more attention:

- it is a key energy carrier for future fuel cell applications.

- it is easy to produce.

- it is the most friendly fuel to the environment, enabling zero emission of greenhouse gases, and has the largest energy density.

The electrolysis of water consists of two half reactions; the HER and the OER (Figure 1.5). The OER is thus an important anodic process in water splitting and also in CO_2 reduction applications. Depending on the media, the processes taking place at the electrode surface can be described differently. In the case of HER in acidic or neutral electrolytes:

$$Cathode: 4H_3O^+ + 4e^- \rightarrow 4H_2O + 2H_2 \tag{1.4}$$

$$Anode: 6H_2O \rightarrow 4H_3O^+ + O_2 + 4e^- \tag{1.5}$$

$$Net: 2H_2O \rightarrow 2H_2 + O_2 + Heat \tag{1.6}$$

Instead, when the process takes place in an alkaline electrolyte, electrochemical reactions occurring at the cathode and anode are:

$$Cathode: 2H_2O + 2e^- \rightarrow 2OH^- + H_2 \tag{1.7}$$

$$Anode: 2OH^- \rightarrow 1/2O_2 + H_2O + 2e^- \tag{1.8}$$
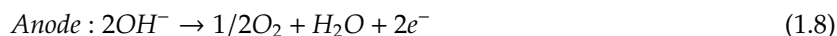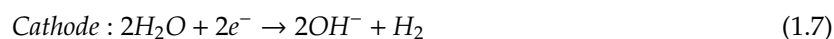
The net reaction in alkaline media will be the same as the one in acidic conditions. Because hydrogen can be extracted from H_3O^+ (acid solution) easier than from H_2O (alkaline solution), the reaction rate on acidic electrolytes has proven to be faster. Although acidic electrolytes are used from the beginning of electrolysis, there is a current trend towards alkaline electrolytes, e.g. potassium hydroxide (KOH), for HER. The latter offer additional advantages including the possibility of using stainless steel flow fields and endplates (with the subsequent reduction in costs) and the possibility of using cheaper non-platinum-group-metal electrocatalysts for the OER. However, the slow kinetics for the HER in alkaline media is currently a key drawback [44].

Electrodes used for HER should preferably be made from a material exhibiting high conductivity, resistance to corrosion and erosion during the electrolysis and should be able to catalyze the electrode
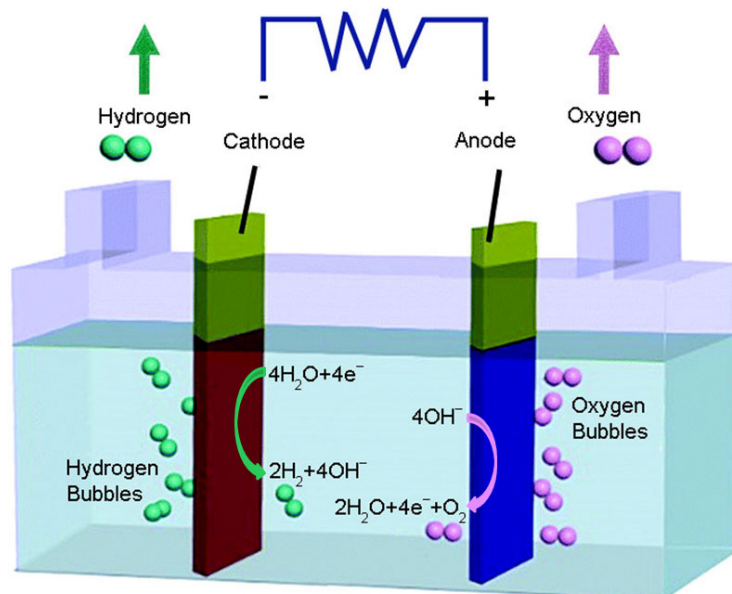
Figure 1.5: Schematic drawing of the two half reactions that take place during the electrolysis of water; the hydrogen evolution reaction (HER) and the oxygen evolution reaction (OER).

reactions. If they are designed for industrial uses, they should be relatively inexpensive. Noble metals are excellent candidates for HER but constitute an expensive electrode material. While more complex surface structures involving Pt have exhibited experimental improvements [45], efficient electrocatalysts consisting of non-precious elements have recently been more actively studied. There is a tendency to alloy Pt, typically with Ni, or even completely replace it, with more abundant and less expensive elements and/or compounds. Current research in HER electrodes focuses on exploring: i) the intrinsic nature of the reaction; ii) the influence of composition and surface morphology of the electrocatalyst on HER performance; iii) its structure, chemical and electronic properties, and v) the effect of physical, chemical and electrochemical activation treatments applied.

Several strategies can be fulfilled in order to obtain good electrodes for HER: i) an increase of the S/V ratio to improve the catalytic performance, ii) the synthesis of substrate-supported catalysts in order to avoid post-synthesis immobilization steps which typically involve polymeric binders that can worsen the electrocatalytic properties [46], iii) minimization of noble elements usage by partly replacing Pt-group elements by more abundant and less expensive elements and, iv) use of bimetallic electrodes in order to enhance the HER performance thanks to synergistic metal-metal interactions [47, 48].

As outlined above, water splitting consists in two half reactions, HER and OER. Of these, the OER has more sluggish kinetics [49, 50] because it is thermodynamically and kinetically unfavorable to remove four electrons to form oxygen–oxygen double bonds [51]. So far IrO_2 and RuO_2 are the benchmark OER catalysts in acidic media, owing to their high catalytic activity [52]. However, Ru and Ir resources are scarce and very expensive, and therefore, not suitable for large scale applications [53, 54]. Electrocatalysts based on transition metal oxides/hydroxides such as Co, Ni, and Fe have demonstrated to be the most active and low cost OER catalysts in alkaline conditions [55, 56, 57, 58, 59].

The use of porous electrocatalysts is currently attracting a great deal of attention for both HER and OER applications. Very recently, Lu et al. obtained mesoporous amorphous NiFe hydroxide nanosheets onto macroporous nickel foam substrates by electrodeposition. The authors demonstrated that these hybrid

structures show a highly efficient response as electrocatalyst for OER, owing to the large active surface area provided by a hierarchical micro- to nanoscale porosity. It was proven that the catalyst enabled OER at very low overpotentials ($\sim 200\,\mathrm{mV}$) and that it showed high durability under high current densities [60]. Aslan et al. recently reported on the excellent catalytic activity towards HER of Cu NPs electrodeposited at liquid-liquid interfaces [61]. Zhang et al. produced two-phase Cu-Ni porous films using bubble-assisted template electrodeposition approach with tunable HER activity depending on the Cu/Ni ratio [62]. Ahn et al. synthesized Ni-based dendrites, particles and films by electrodeposition and correlated the type of structure with the HER activity. They concluded that the Ni dendrites showed the highest catalytic activity and stability for HER among the studied structures [63].

1.4. State-of-the-art of electrodeposited cobalt-indium and iron-based systems

1.4.1. Cobalt-indium system: spatio-temporal patterns

Combining cobalt and indium in a single material has been rather uncommon in the electroplating field. Indeed, whilst the electrodeposition of cobalt alone has been widely explored, mostly because it is a ferromagnetic element, In electroplating has been much less reported. The deposition of either hexagonal close-packed (hcp) of face-centered cubic (fcc) Co coatings has been demonstrated from a variety of baths [64]. Compared to Co, In is mechanically softer and possesses lower electrical resistivity. Therefore, the main aim when alloying Co with In or viceversa is to produce deposits with minimal or no stress, and improve the electrical properties. However, the mutual solubility of Co and In is low (Figure 1.6), which means that when the amount of the 'alloying element' added to the base metal surpasses the solubility limit, the excess will form one or more phases rich in that 'alloying element'. Although electrodeposition allows obtaining phases not necessarily predicted by the phase diagram, the resulting coatings are multi-phase in nature and, therefore, heterogeneous. It is known that the properties of heterogeneous alloy coatings are a mixture of the properties of the different phases presented therein. Usually, these phases are randomly distributed over the coating due to the complexity of the electrodeposition processes and because the co-deposition of both metals happens simultaneously on substrate elements that might not be the same [65, 66]. Nevertheless, in some particular cases, oscillatory processes naturally occur during deposition, which result in the formation of a periodic coating structure, such as the well known spontaneous growth of layered films [67, 68]. In addition, an ordered distribution of the different phases composing the heterogeneous alloy might be observed on top. The formation of such type of coatings can be somehow anticipated having in mind that the electrochemical cell is an open non-linear system, electrochemically driven far from equilibrium, where co-operative phenomena, synergistic effects, and ordered structures formation are possible. The co-deposition of Co and In is an example of a binary system where an spontaneous self-organization might occur if favorable electrodeposition conditions are settled.

Back in 1975, Sadana et al., in an effort to continue with the studies on the electrodeposition of alloys and the characterization of their structures, were the first establishing that Co-In alloys ranging from 2.0 wt.% to 90.6 wt.% cobalt could be electrodeposited from aqueous solutions. The influence of current density and bath formulation on the composition of the electrodeposits as well as the current efficiency and the crystallographic structure of the coatings were reported. They concluded that an increase in the current
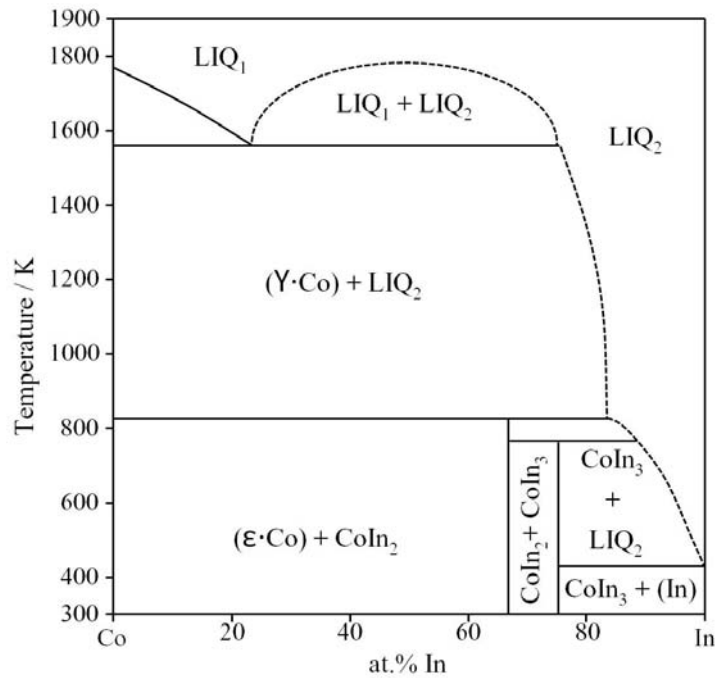
Figure 1.6: Equilibrium phase diagram of the [Co+In] system [69].

density increased the cobalt content in the deposits and that the addition of ammonium citrate to the electrolyte improved the current efficiency. Besides, X-ray studies of the deposits indicated the presence of two intermediate phases, $CoIn_3$ and Co_3In_2 [70]. However, they did not report on the formation of spatio-temporal structures on the electrode.

It was not until 2010 when Krastev's group, after having worked with the electrodeposition of some silver alloy coatings such as Ag-Sb [71], Ag-Bi [72], Ag-In [73], Ag-Sn [74] and Ag-Cd [75] showing spatio-temporal patterns (Figure 1.7), anticipated the possible existence of similar structures for the Co-In system. Usually the electrodeposition of silver-based alloys involve the use of cyanide electrolytes in order to bring the potentials of both metals closer, which turns out in hazardous electrolyte formulations [71, 74, 76, 77, 78, 79]. Instead, the possibility of obtaining spatio-temporal patterns in Co-In coatings enabled the investigation of self–organization phenomena during alloy electrodeposition from more environmentally-friendly electrolytes. Krastev's group thus observed for first time an spontaneous pattern formation during electrodeposition of a silver free alloy. According to the authors, two conditions hold for the formation of periodic structures in an alloy: (1) the alloying element is co-deposited in amounts higher than the saturation limit of the lattice of the basic metal and, (2) heterogeneous coatings are formed. Due to the difficulties in determining the local phase composition of the periodic spatio-temporal structures, Krastev and co-workers combined anodic linear sweep voltammetry (ALSV) and X-ray diffraction techniques to determine the exact phase composition in different coating areas of Ag-In, Ag-Cd, and In-Co alloys featuring spatio-temporal patterns. They concluded that the observed periodic patterns consisted of Ag and Ag_3In (Ag-In), Cd and Cd_3Ag (Ag-Cd) and Co and $CoIn_3$ (Co-In) phases, respectively [80].

Afterwards, Krastev's group tried to find out the conditions leading to self-organized phenomena during electrodeposition of Co-In alloys. They established that it was possible to obtain spatio-temporal structures under galvanostatic conditions at high current densities. In such a case, the concentration of
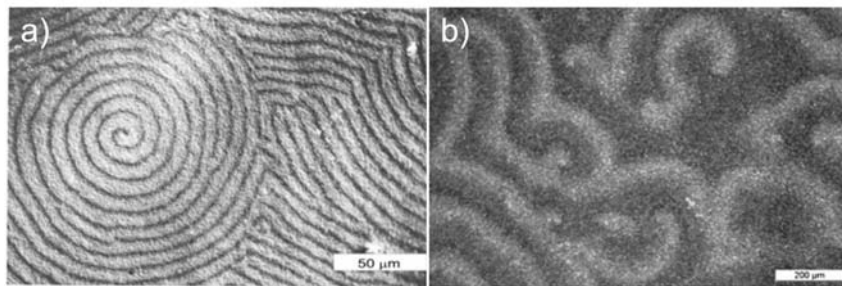
11

Figure 1.7: Optical images of a) a Ag-Sb alloy coating; 1.5 A dm^{-2}; 12 wt.% Sb and b) a Ag-Bi alloy coating; 0.6 A dm^{-2}, 40 wt.% Bi. Images taken from [65].

the metal ions in the bath strongly fluctuate and a convection flow of the electrolyte is settled [81].

Later in 2012, Krastev et al. published a deep research on the effect of the electrolysis conditions, including high speed electroplating, on the content, the structure, the morphology and some properties of electrodeposited In-Co alloys from citrate electrolytes [82]. After an analysis of the data collected, they concluded that: a) In and Co could be successfully co-deposited from acid citrate elecrolytes with In contents between 20 wt.% and 80 wt.%, b) coatings exhibiting spatio-temporal patterns can be obtained for high Co contents, c) for the first time such exotic patterns can be obtained from silver- and cyanide-free non alkaline stable electrolytes of a relatively simple composition, and d) spatio-temporal patterns could be observed under intensive hydrodynamic flow and improved mass transport conditions at high current densities.

The spatio-temporal pattern formation has attracted interest not only from an experimental viewpoint but also theoretically. Bozzini et al. recently published a robust mathematical model to describe the formation of spatio-temporal patterns in alloy electrodeposition. The authors propose an innovative electrochemical source term, much more straightforward and flexible than previous mathematical formulations, to take into account the electrokinetic control phenomena, that considers both, the change transfer and the mass transport. In addition, with this new term they are able to reproduce all the spatio-temporal organization types found in the literature by suitable numerical solutions of their model [83].

Interestingly, the occurrence of spatio-temporal patterning is a phenomenon related to chaos that has been observed in many fields of physics, chemistry, material science, as well as in biology. A wide range of natural phenomena show spatio-temporal pattern formation such as the mixing of water in the oceans, the movement of air in the atmosphere, cardiac fibrillation and the skin of some animals like zebra or pufferfish (Figure 1.8).
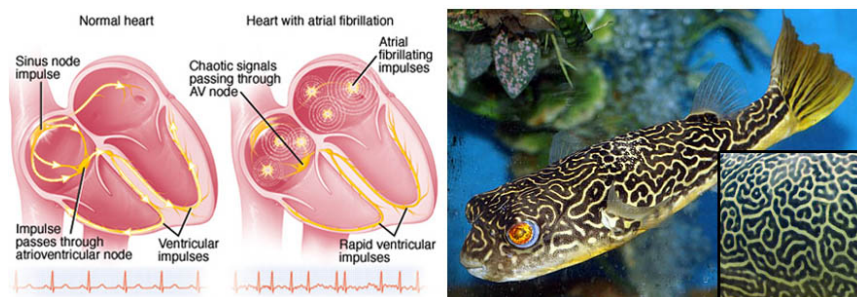

Figure 1.8: (Left) Spatio-temporal patterns develop when a normal heart rhythm undergoes atrial fibrillation. (Right) Spatio-temporal patterns on the skin of a pufferfish.

1.4.2. Iron-based systems

Electrodeposition of iron is usually carried from acidic solutions of Fe(II) (ferrous) salts. The presence of iron as Fe(III) (ferric) state in solution in an appreciable concentration has been claimed to be undesirable because it lowers the cathode efficiency and it may cause deposits to be brittle, stressed, and pitted [84]. In addition, the formation of metal hydroxides competes with metal deposition. However, there are several reasons for the persistent interest in iron plating. Iron is cheap and is one of the most abundant metals on the earth's crust. It can be deposited as a hard and brittle metal which, by heat treatment, can be rendered soft and malleable, or as a soft and ductile metal to which by surface hardening methods such as carburizing, cyaniding, or nitriding, the wear resistance can be improved.

Among platable binary iron alloys, Fe-Ni has received most of the attention in recent years, as indicated by the number of publications. Initially, the focus was on decorative and protective purposes since the addition of nickel to iron causes a dramatic improvement of its corrosion resistance. In addition, Fe-Ni alloy coating presents a bright appearance, making it appealing for both aesthetic and economic reasons compared to pure nickel plating [85, 86]. Lately, Fe-Ni alloy electrodeposition has been widely studied for magnetic purposes [87, 88, 89]. In particular, iron (20 at%)–nickel alloy (Permalloy) deposits have been the subject of considerable interest for their use in magnetic devices such as thin-film recording heads, magnetic yokes in printer heads, bubble memories, shielding, logic devices, and magnetic cores in microsolenoids because of their magnetic flux density as high as 1.6 T [90, 91].

Electrodeposition offers the possibility to produce non-equilibrium alloys in the as-prepared state, which is very interesting when amorphous materials are pursued. In addition, little changes in the growth conditions can result in a significant change in the phase structure of electrodeposits of the same chemical composition [92]. In order to obtain glass-forming compositions, 80 at.% of transition metals (e.g., Fe, Co, Ni, Pd, Au) plus 20 at.% of metalloids (B, Si, P, C, Ge) are typically combined. In the case of amorphous alloys prepared by electrodeposition, those containing B, P and/or Si are mostly studied. Interestingly, Fe–P with 20 at.% belongs to a group of amorphous alloys that can be obtained by electrochemical means under relatively simple experimental conditions [93].

Fe-P alloys are of major interest owing to its magnetic and protective properties which, in turn, depend on their composition. Iron can form different metal phosphides (Figure 1.9) like Fe_3P, Fe_2P, FeP, and FeP_2 [94, 95] depending on the phosphorus content and operating temperatures [96]. The electrodeposition of Fe-P alloy coatings suitable for various purposes has been studied by several researchers. In particular, Fe-P has been advocated as an outstanding soft magnetic material due to its low coercivity and high magnetic flux density [97, 98]. Particular emphasis has been laid in the production of amorphous films. Vitkova et al. established the optimum conditions for the electrodeposition of amorphous Fe-P films [93]. Likewise, Kamei and Maehara characterized the magnetic properties and the microstructure of electroplated amorphous Fe-P alloys. They concluded that the coatings became amorphous for phosphorus contents of about 20 at% or higher. The H_C decreased upon annealing at low temperatures, and the lowest H_C was about 0.05 Oe, probably due to a structural relaxation [99].

Although the influence of various electrodeposition parameters such as the deposition mode (DC vs PP), time, pH and bath temperature on the composition and structure of Fe-P films has been investigated to some extent, such studies deal with dense films. The electrosynthesis of Fe-P ordered porous films remains mostly unexplored. The same is true about their electrochemical performance toward HER and OER. Very recently nanostructured Fe-P materials produced by other means are gaining tremendous
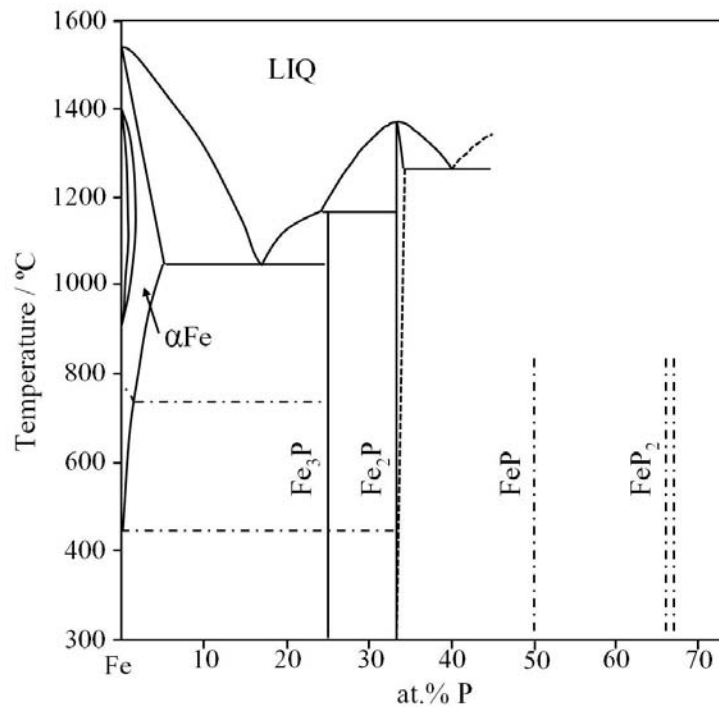
Figure 1.9: Equilibrium phase diagram of the [Fe+P] system [92].

interest in energy-related fields [100, 101, 102].

Fe-Rh has also attracted the interest of the materials science community from the magnetic point of view since Fallot reported in 1938 the antiferromagnetic-ferromagnetic transition in Fe-Rh alloys [103]. Studies dealing with the fabrication of Re-Rh films using sputtering techniques and the characterization of the metamagnetic transition can be found in the literature [104, 105, 106]. Rhodium is a noble transition metal very stable against oxidation, it is mechanically hard and offers excellent wear characteristics. In addition, it exhibits (electro)catalytic properties. However, its high cost restricts its massive use. Alloying Rh with Fe reduces the cost of the final product and the environmental footprint. Nakamula et al. reported the synthesis Rh/Fe bimetallic nanoparticles as an efficient catalyst for the hydrogenation of olefines and nitroarenes [107]. Noteworthy, very little is known about the electrodeposition of Fe-Rh. Noce et al. produced Fe-Rh deposits from a glycine-containing bath for the first time [108]. Depending on the surface onto which the deposit was grown, Ag or brass, they obtained crystalline and nanocrystalline deposits, respectively. Salen-Sugui et al. studied the magnetic properties of electrodeposited Fe-Rh [109]. The authors obtained $Fe_{1-x}Rh_x$ with x $\approx$ 0.5 on a foil of ordered Fe_3Pt.

1.5. OBJECTIVES

This thesis covers the synthesis (by electrodeposition) and the characterization (of the physical and physico-chemical properties) of multiphase metallic materials. Three different systems, namely Co-In, Fe-Rh and Fe-P, are tackled. Each study goes beyond the classical thin film technology, thus highlighting the great potential of electrodeposition to yield non-conventional material architectures. Firstly, Co-In films showing self-organized spatio-temporal patterns have been grown (without the assistance of any mask) and characterized by correlating the composition and microstructure of deposits with their magnetic and mechanical properties. Further miniaturization of this system has been performed via electrodeposition on photo-lithographed substrates and their surface properties investigated using advanced techniques. Secondly, the production and electrochemical response of compositionally tunable Rh-Fe NPs towards HER has been accomplished. Nanoparticulated denser films of analogous compositions have been prepared to disclose the effect of nanostructuration (increased S/V ratio) on HER performance. Finally, pseudo-ordered porous Fe-P films have been prepared by colloidal lithography followed by electrodeposition, and their wettability, magnetic behavior and electrocatalytic activity towards both HER and OER have been investigated.

The goals of this Thesis can be summarized as follows:

1. To grow Co-In films showing self-organized spatio-temporal patterns by electrodeposition. The main purpose is to systematically study the morphology, composition and crystallographic structure of the deposits, with special emphasis on the surface patterns, and establish a correlation with the magnetic and mechanical properties.

2. To miniaturize the Co-In system in confined areas of previously patterned micrometer cylindrical holes by photo-lithography. The main purpose is to investigate if the constrains imposed by the cylindrical cavities are able to promote a defined class of pattern instead of a mixture of 'labyrinths', 'waves', 'targets', spirals, and broken spirals, as shown in the continuous films. The second goal is to link the compositional patterning with the physical (magnetic, electrical and mechanical) properties.

3. To take a closer look at the cross-section of Co-In films deposited in (1) in order to perform an in-depth study of the first-ever evidence of its layer-by-layer growth.

4. To synthesize Fe- and Rh- containing NPs by electrodeposition and to characterize their morphology and crystallographic structure. The main objective is to control the chemical composition and size of the NPs by simply adjusting the current density and deposition time. The second goal is to investigate their electrocatalityc activity towards HER in alkaline media.

5. To prepare macroporous Fe-P films using electrodeposition through colloidal crystal templates and to characterize their physical (magnetic) and physico-chemical (wettability, HER, OER) properties. The results obtained are to be correlated with those of dense Fe-P films with similar phosphorous content.

1.6. Schedule

A schedule of the work is chronologically shown in the following table. Notice that the whole work was conducted in an equivalent full-time work of 2 years and 7 months.
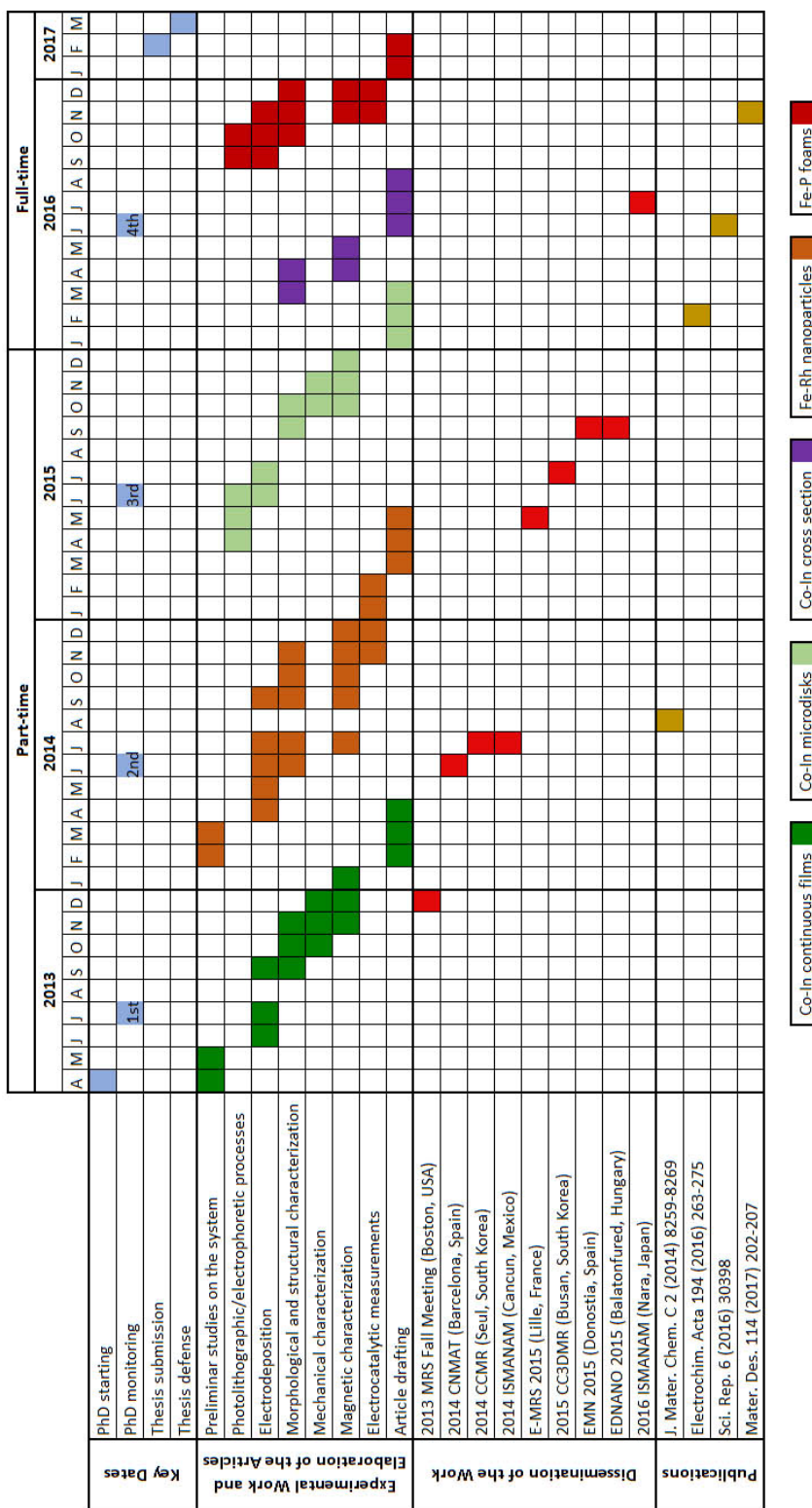
Bibliography

[1] L. B. Hunt, "The early history of gold plating," *Gold Bulletin*, vol. 6, no. 1, pp. 16 – 27, 1973.

[2] L. T. Romankiw, "A path: from electroplating through lithographic masks in electronics to LIGA in MEMS," *Electrochimica Acta*, vol. 42, no. 20 - 22, pp. 2985 – 3005, 1997.

[3] S. Krongelb, L. T. Romankiw, and J. A. Tornello, "Electrochemical process for advanced package fabrication," *IBM Journal of Research and Development*, vol. 42, no. 5, pp. 575 – 585, 1998.

[4] N. Shaigan, *Electrodeposition for Electrochemical Energy Conversion and Storage Devices*, pp. 117 – 162. Springer New York, 2010.

[5] M. Gibbs, E. Hill, and P. Wright, "Chapter 6: Magnetic microelectromechanical systems: Mag-MEMS," vol. 17 of *Handbook of Magnetic Materials*, pp. 457 – 526, Elsevier, 2007.

[6] J. Heremans, "Solid state magnetic field sensors and applications," *Journal of Physics D: Applied Physics*, vol. 26, no. 8, pp. 1149 – 1168, 1993.

[7] S. R. Brankovic, X. Yang, T. J. Klemmer, and M. Seigler, "Pulse electrodeposition of 2.4 T $Co_{37}Fe_{63}$ alloys at nanoscale for magnetic recording application," *IEEE Transactions on Magnetics*, vol. 42, no. 2, pp. 132 – 139, 2006.

[8] F. Xiao, C. Hangarter, B. Yoo, Y. Rheem, K.-H. Lee, and N. V. Myung, "Recent progress in electrodeposition of thermoelectric thin films and nanostructures," *Electrochimica Acta*, vol. 53, no. 28, pp. 8103 – 8117, 2008.

[9] R. Yan, D. Gargas, and P. Yang, "Nanowire photonics," *Nature Photonics*, vol. 3, no. 10, pp. 569 – 576, 2009.

[10] H. A. Atwater and A. Polman, "Plasmonics for improved photovoltaic devices," *Nature Materials*, vol. 9, no. 3, pp. 205 – 213, 2010.

[11] I. Lombardi, S. Marchionna, G. Zangari, and S. Pizzini, "Effect of Pt particle size and distribution on photoelectrochemical hydrogen evolution by p-Si photocathodes," *Langmuir*, vol. 23, no. 24, pp. 12413 – 12420, 2007.

[12] M. B. Vukmirovic, S. T. Bliznakov, K. Sasaki, J. X. Wang, and R. R. Adzic, "Electrodeposition of metals in catalyst synthesis: The case of platinum monolayer electrocatalysts," *Interface-Electrochemical Society Interface*, vol. 20, no. 2, pp. 33 – 40, 2011.

[13] Z. Yi, J. Guo, Y. Chen, H. Zhang, S. Zhang, G. Xu, M. Yu, and P. Cui, "Vertical, capacitive microelectromechanical switches produced via direct writing of copper wires," *Microsystems & Nanoengineering*, vol. 2, p. 16010, 2016.

[14] E. Pellicer, S. Pané, V. Panagiotopoulou, S. Fusco, K. M. Sivaraman, S. Suriñach, M. D. Baró, B. J. Nelson, and J. Sort, "Localized electrochemical deposition of porous Cu-Ni microcolumns: Insights into the growth mechanisms and the mechanical performance," *International Journal of Electrochemical Science*, vol. 7, no. 6, pp. 4014 – 4029, 2012.

[15] D. Yang, J. Carpena-Núñez, L. F. Fonseca, A. Biaggi-Labiosa, and G. W. Hunter, "Shape-controlled synthesis of palladium and copper superlattice nanowires for high-stability hydrogen sensors," *Scientific Reports*, vol. 4, p. 3773, 2014.

[16] M. A. Zeeshan, R. Grisch, E. Pellicer, K. M. Sivaraman, K. E. Peyer, J. Sort, B. Özkale, M. S. Sakar, B. J. Nelson, and S. Pané, "Hybrid helical magnetic microrobots obtained by 3D template-assisted electrodeposition," *Small*, vol. 10, no. 7, pp. 1284 – 1288, 2014.

[17] M. Etienne and A. Walcarius, "Electrochemistry within template nanosystems," in *Electrochemistry: Volume 11 - Nanosystems Electrochemistry*, vol. 11, pp. 124 – 197, The Royal Society of Chemistry, 2013.

[18] E. García-Lecina, I. García-Urrutia, J. Díez, J. Morgiel, and P. Indyka, "A comparative study of the effect of mechanical and ultrasound agitation on the properties of electrodeposited Ni/Al$_2$O$_3$ nanocomposite coatings," *Surface and Coatings Technology*, vol. 206, no. 11–12, pp. 2998 – 3005, 2012.

[19] H. Kido, T. Kuroki, M. Okubo, and Y. Utsumi, "Application of photo-etching of polytetrafluoroethylene induced by high energy synchrotron radiation to LIGA," *Microsystem Technologies*, vol. 19, no. 3, pp. 301 – 307, 2013.

[20] C. Marques, Y. M. Desta, J. Rogers, M. C. Murphy, and K. Kelly, "Fabrication of high-aspect-ratio microstructures on planar and nonplanar surfaces using a modified LIGA process," *Journal of Microelectromechanical Systems*, vol. 6, no. 4, pp. 329 – 336, 1997.

[21] J. Lin, T. Chang, J. Yang, Y. Chen, and C. Chuang, "Localized electrochemical deposition of micrometer copper columns by pulse plating," *Electrochimica Acta*, vol. 55, no. 6, pp. 1888 – 1894, 2010.

[22] E. Gómez, E. Pellicer, and E. Vallés, "Microstructures of soft-magnetic cobalt–molybdenum alloy obtained by electrodeposition on seed layer/silicon substrates," *Electrochemistry Communications*, vol. 6, no. 8, pp. 853 – 859, 2004.

[23] M. Zenger, W. Breuer, M. Zolfl, R. Pulwey, J. Raabe, and D. Weiss, "Electrodeposition of NiFe and Fe nanopillars," *IEEE Transactions on Magnetics*, vol. 37, no. 4, pp. 2094 – 2097, 2001.

[24] G. She, W. Shi, X. Zhang, T. Wong, Y. Cai, and N. Wang, "Template-free electrodeposition of one-dimensional nanostructures of tellurium," *Crystal Growth & Design*, vol. 9, no. 2, pp. 663 – 666, 2009.

[25] M. A. Zeeshan, K. Shou, S. Pané, E. Pellicer, J. Sort, K. M. Sivaraman, M. D. Baró, and B. J. Nelson, "Structural and magnetic characterization of batch-fabricated nickel encapsulated multi-walled carbon nanotubes," *Nanotechnology*, vol. 22, no. 27, p. 275713, 2011.

[26] I. Schubert, L. Burr, C. Trautmann, and M. E. Toimil-Molares, "Growth and morphological analysis of segmented AuAg alloy nanowires created by pulsed electrodeposition in ion-track etched membranes," *Beilstein Journal of Nanotechnology*, vol. 6, pp. 1272 – 1280, 2015.

[27] J.-M. Yang, S.-P. Gou, and I.-W. Sun, "Single-step large-scale and template-free electrochemical growth of Ni-Zn alloy filament arrays from a zinc chloride based ionic liquid," *Chemical Communications*, vol. 46, pp. 2686 – 2688, 2010.

[28] P. N. Bartlett, M. A. Ghanem, I. S. El Hallag, P. de Groot, and A. Zhukov, "Electrochemical deposition of macroporous magnetic networks using colloidal templates," *Journal of Materials Chemistry*, vol. 13, pp. 2596 – 2602, 2003.

[29] L. Xu, W. L. Zhou, C. Frommen, R. H. Baughman, A. A. Zakhidov, L. Malkinski, J.-Q. Wang, and J. B. Wiley, "Electrodeposited nickel and gold nanoscale metal meshes with potentially interesting photonic properties," *Chem. Commun.*, pp. 997 – 998, 2000.

[30] P. Wang, R. C. Roberts, and A. H. W. Ngan, "Direct microfabrication of oxide patterns by local electrodeposition of precisely positioned electrolyte: the case of Cu_2O," *Scientific Reports*, vol. 6, p. 27423, 2016.

[31] M. O. Finot, G. D. Braybrook, and M. T. McDermott, "Characterization of electrochemically deposited gold nanocrystals on glassy carbon electrodes," *Journal of Electroanalytical Chemistry*, vol. 466, no. 2, pp. 234 – 241, 1999.

[32] F. Pagnanelli, P. Altimari, M. Bellagamba, G. Granata, E. Moscardini, P. G. Schiavi, and L. Toro, "Pulsed electrodeposition of cobalt nanoparticles on copper: influence of the operating parameters on size distribution and morphology," *Electrochimica Acta*, vol. 155, pp. 228 – 235, 2015.

[33] U. S. Mohanty, "Electrodeposition: a versatile and inexpensive tool for the synthesis of nanoparticles, nanorods, nanowires, and nanoclusters of metals," *Journal of Applied Electrochemistry*, vol. 41, no. 3, pp. 257 – 270, 2011.

[34] Y. Ma, J. Di, X. Yan, M. Zhao, Z. Lu, and Y. Tu, "Direct electrodeposition of gold nanoparticles on indium tin oxide surface and its application," *Biosensors and Bioelectronics*, vol. 24, no. 5, pp. 1480 – 1483, 2009.

[35] W. Zhu, G. Wang, X. Hong, X. Shen, D. Li, and X. Xie, "Metal nanoparticle chains embedded in TiO_2 nanotubes prepared by one-step electrodeposition," *Electrochimica Acta*, vol. 55, no. 2, pp. 480 – 484, 2009.

[36] L. Hirt, S. Ihle, Z. Pan, L. Dorwling-Carter, A. Reiser, J. M. Wheeler, R. Spolenak, J. Vörös, and T. Zambelli, "Template-free 3D microprinting of metals using a force-controlled nanopipette for layer-by-layer electrodeposition," *Advanced Materials*, vol. 28, no. 12, pp. 2311 – 2315, 2016.

[37] J. A. C. Bland, M. J. Padgett, K. D. Mackay, and A. D. Johnson, "Investigation of the magnetic properties of sandwiched epitaxial Fe and Co films using the magneto-optic Kerr effect," *Journal of Physics: Condensed Matter*, vol. 1, no. 27, p. 4407, 1989.

[38] A. Franczak, A. Levesque, M. Coïsson, D. Li, G. Barrera, F. Celegato, Q. Wang, P. Tiberto, and J.-P. Chopart, "Magnetic properties dependence on the coupled effects of magnetic fields on the microstructure of as-deposited and post-annealed Co/Ni bilayer thin films," *Journal of Magnetism and Magnetic Materials*, vol. 372, pp. 159 – 166, 2014.

[39] P. N. Bartlett, P. N. Birkin, M. A. Ghanem, P. de Groot, and M. Sawicki, "The electrochemical deposition of nanostructured cobalt films from lyotropic liquid crystalline media," *Journal of The Electrochemical Society*, vol. 148, no. 2, pp. C119 – C123, 2001.

[40] T. Mangen, H. Bai, and J. Tsay, "Structures and magnetic properties for electrodeposited Co ultrathin films on copper," *Journal of Magnetism and Magnetic Materials*, vol. 322, no. 13, pp. 1863 – 1867, 2010.

[41] S. Kulkarni and S. Roy, "Deposition of thick Co-rich CoPtP films with high energy product for magnetic microelectromechanical applications," *Journal of Magnetism and Magnetic Materials*, vol. 322, no. 9–12, pp. 1592 – 1596, 2010.

[42] S. Pané, E. Pellicer, K. Sivaraman, S. Suriñach, M. Baró, B. Nelson, and J. Sort, "High-performance electrodeposited Co-rich CoNiReP permanent magnets," *Electrochimica Acta*, vol. 56, no. 24, pp. 8979 – 8988, 2011.

[43] F. Nasirpouri, M. Sanaeian, A. Samardak, E. Sukovatitsina, A. Ognev, L. Chebotkevich, M.-G. Hosseini, and M. Abdolmaleki, "An investigation on the effect of surface morphology and crystalline texture on corrosion behavior, structural and magnetic properties of electrodeposited nanocrystalline nickel films," *Applied Surface Science*, vol. 292, pp. 795 – 805, 2014.

[44] S. Romain, L. Vigara, and A. Llobet, "Oxygen–oxygen bond formation pathways promoted by ruthenium complexes," *Accounts of Chemical Research*, vol. 42, no. 12, pp. 1944 – 1953, 2009.

[45] H. Yin, S. Zhao, K. Zhao, A. Muqsit, H. Tang, L. Chang, H. Zhao, Y. Gao, and Z. Tang, "Ultra-thin platinum nanowires grown on single-layered nickel hydroxide with high hydrogen evolution activity," *Nature Communications*, vol. 6, p. 6430, 2015.

[46] J. Ji, L. L. Zhang, H. Ji, Y. Li, X. Zhao, X. Bai, X. Fan, F. Zhang, and R. S. Ruoff, "Nanoporous $Ni(OH)_2$ thin film on 3D ultrathin-graphite foam for asymmetric supercapacitor," *ACS Nano*, vol. 7, no. 7, pp. 6237 – 6243, 2013.

[47] K. Zhang, J. Liu, W. Xiao, and C. Yan, "Electrodeposition of graded Ni-S film for hydrogen evolution reaction," *Materials Letters*, vol. 193, pp. 77 – 80, 2017.

[48] Y. Sun, C. Liu, D. C. Grauer, J. Yano, J. R. Long, P. Yang, and C. J. Chang, "Electrodeposited cobalt-sulfide catalyst for electrochemical and photoelectrochemical hydrogen generation from water," *Journal of the American Chemical Society*, vol. 135, no. 47, pp. 17699 – 17702, 2013.

[49] R. D. L. Smith, M. S. Prévot, R. D. Fagan, Z. Zhang, P. A. Sedach, M. K. J. Siu, S. Trudel, and C. P. Berlinguette, "Photochemical route for accessing amorphous metal oxide materials for water oxidation catalysis," *Science*, vol. 340, no. 6128, pp. 60 – 63, 2013.

[50] T. R. Cook, D. K. Dogutan, S. Y. Reece, Y. Surendranath, T. S. Teets, and D. G. Nocera, "Solar energy supply and storage for the legacy and nonlegacy worlds," *Chemical Reviews*, vol. 110, no. 11, pp. 6474 – 6502, 2010.

[51] T. J. Meyer, "Catalysis: The art of splitting water," *Nature*, vol. 451, no. 7180, pp. 778 – 779, 2008.

[52] M. Carmo, D. L. Fritz, J. Mergel, and D. Stolten, "A comprehensive review on PEM water electrolysis," *International Journal of Hydrogen Energy*, vol. 38, no. 12, pp. 4901 – 4934, 2013.

[53] T. Reier, M. Oezaslan, and P. Strasser, "Electrocatalytic oxygen evolution reaction (OER) on Ru, Ir, and Pt catalysts: A comparative study of nanoparticles and bulk materials," *ACS Catalysis*, vol. 2, no. 8, pp. 1765 – 1772, 2012.

[54] M. G. Walter, E. L. Warren, J. R. McKone, S. W. Boettcher, Q. Mi, E. A. Santori, and N. S. Lewis, "Solar water splitting cells," *Chemical Reviews*, vol. 110, no. 11, pp. 6446 – 6473, 2010.

[55] X. Lu, Y. H. Ng, and C. Zhao, "Gold nanoparticles embedded within mesoporous cobalt oxide enhance electrochemical oxygen evolution," *ChemSusChem*, vol. 7, no. 1, pp. 82 – 86, 2014.

[56] C. Bocca, A. Barbucci, M. Delucchi, and G. Cerisola, "Nickel–Cobalt oxide-coated electrodes: influence of the preparation technique on oxygen evolution reaction (OER) in an alkaline solution," *International Journal of Hydrogen Energy*, vol. 24, no. 1, pp. 21 – 26, 1999.

[57] L. Trotochaud, J. K. Ranney, K. N. Williams, and S. W. Boettcher, "Solution-cast metal oxide thin film electrocatalysts for oxygen evolution," *Journal of the American Chemical Society*, vol. 134, no. 41, pp. 17253 – 17261, 2012.

[58] R. L. Doyle and M. E. G. Lyons, "An electrochemical impedance study of the oxygen evolution reaction at hydrous iron oxide in base," *Physical Chemistry Chemical Physics*, vol. 15, pp. 5224 – 5237, 2013.

[59] D. Cibrev, M. Jankulovska, T. Lana-Villarreal, and R. Gómez, "Oxygen evolution at ultrathin nanostructured Ni(OH)$_2$ layers deposited on conducting glass," *International Journal of Hydrogen Energy*, vol. 38, no. 6, pp. 2746 – 2753, 2013.

[60] X. Lu and C. Zhao, "Electrodeposition of hierarchically structured three dimensional nickel iron electrodes for efficient oxygen evolution at high current densities," *Nature Communications*, vol. 6, p. 6616, 2015.

[61] E. Aslan, I. H. Patir, and M. Ersoz, "Cu nanoparticles electrodeposited at liquid–liquid interfaces: A highly efficient catalyst for the hydrogen evolution reaction," *Chemistry – A European Journal*, vol. 21, no. 12, pp. 4585 – 4589, 2015.

[62] J. Zhang, M. D. Baro, E. Pellicer, and J. Sort, "Electrodeposition of magnetic, superhydrophobic, non-stick, two-phase Cu-Ni foam films and their enhanced performance for hydrogen evolution reaction in alkaline water media," *Nanoscale*, vol. 6, pp. 12490 – 12499, 2014.

[63] S. H. Ahn, S. J. Hwang, S. J. Yoo, I. Choi, H.-J. Kim, J. H. Jang, S. W. Nam, T.-H. Lim, T. Lim, S.-K. Kim, and J. J. Kim, "Electrodeposited Ni dendrites with high activity and durability for hydrogen evolution reaction in alkaline water electrolysis," *Journal of Materials Chemistry*, vol. 22, pp. 15153 – 15159, 2012.

[64] E. Gómez and E. Vallés, "Thick cobalt coatings obtained by electrodeposition," *Journal of Applied Electrochemistry*, vol. 32, no. 6, pp. 693 – 700, 2002.

[65] I. Krastev and T. Dobrovolska, "Pattern formation during electrodeposition of alloys," *Journal of Solid State Electrochemistry*, vol. 17, no. 2, pp. 481 – 488, 2013.

[66] M. Srivastava, V. E. Selvi, V. W. Grips, and K. Rajam, "Corrosion resistance and microstructure of electrodeposited nickel–cobalt alloy coatings," *Surface and Coatings Technology*, vol. 201, no. 6, pp. 3051 – 3060, 2006.

[67] A. Hrussanova, I. Krastev, G. Beck, and A. Zielonka, "Properties of silver-tin alloys obtained from pyrophosphate-cyanide electrolytes containing EDTA salts," *Journal of Applied Electrochemistry*, vol. 40, no. 12, pp. 2145 – 2151, 2010.

[68] A. Brenner, *Electrodeposition of Alloys, Principles and Practice.*, vol. 1, pp. 171 – 179. Academic Press, New York, 1963.

[69] J. Bros, M. Gaune-Escard, D. E. Allam, R. Haddad, and E. Hayer, "The cobalt-indium system: enthalpy of formation and phase diagram," *Journal of Alloys and Compounds*, vol. 233, no. 1–2, pp. 264 – 271, 1996.

[70] Y. Sadana, A. Keskinen, and M. Guindon, "Electrodeposition of alloys III. Electrodeposition and X-ray structure of cobalt-indium alloys (initial studies)," *Electrodeposition and Surface Treatment*, vol. 3, no. 3, pp. 149 – 157, 1975.

[71] I. Kristev and M. Nikolova, "Structural effects during the electrodeposition of silver-antimony alloys from ferrocyanide-thiocyanate electrolytes," *Journal of Applied Electrochemistry*, vol. 16, no. 6, pp. 875 – 878, 1986.

[72] I. Krastev, T. Valkova, and A. Zielonka, "Effect of electrolysis conditions on the deposition of silver–bismuth alloys," *Journal of Applied Electrochemistry*, vol. 33, no. 12, pp. 1199 – 1204, 2003.

[73] T. Dobrovolska, L. Veleva, I. Krastev, and A. Zielonka, "Composition and structure of silver-indium alloy coatings electrodeposited from cyanide electrolytes," *Journal of The Electrochemical Society*, vol. 152, no. 3, pp. C137 – C142, 2005.

[74] A. Hrussanova and I. Krastev, "Electrodeposition of silver–tin alloys from pyrophosphate-cyanide electrolytes," *Journal of Applied Electrochemistry*, vol. 39, no. 7, pp. 989 – 994, 2009.

[75] T. Dobrovolska, I. Krastev, and A. Zielonka, "Pattern formation in electrodeposited silver-cadmium alloys," *ECS Transactions*, vol. 25, no. 20, pp. 1 – 9, 2010.

[76] T. Dobrovolska, I. Krastev, B. Jović, V. Jović, G. Beck, U. Lačnjevac, and A. Zielonka, "Phase identification in electrodeposited Ag–Cd alloys by anodic linear sweep voltammetry and X-ray diffraction techniques," *Electrochimica Acta*, vol. 56, no. 11, pp. 4344 – 4350, 2011.

[77] I. Krastev, T. Valkova, and A. Zielonka, "Structure and properties of electrodeposited silver–bismuth alloys," *Journal of Applied Electrochemistry*, vol. 34, no. 1, pp. 79 – 85, 2004.

[78] T. Valkova, I. Krastev, and A. Zielonka, "Influence of the D(+)-glucose on the electrochemical deposition of Ag-Bi alloy from a cyanide electrolyte," *Bulgarian Chemical Communications*, vol. 42, pp. 317 – 322, 2010.

[79] T. Dobrovolska, I. Krastev, and A. Zielonka, "Effect of the electrolyte composition on In and Ag–In alloy electrodeposition from cyanide electrolytes," *Journal of Applied Electrochemistry*, vol. 35, no. 12, pp. 1245 – 1251, 2005.

[80] I. Krastev and T. Dobrovolska, "Self-organized structure formation and phase identification in electrodeposited silver–cadmium, silver-indium and cobalt–indium alloys," *Journal of Engineering & Processing Management*, vol. 2, no. 2, pp. 99 – 105, 2010.

[81] M. A. Estrella Gutiérrez, T. Dobrovolska, D. A. López Sauri, L. Veleva, and I. Krastev, "Self–organization phenomena during electrodeposition of Co–In alloys," *ECS Transactions*, vol. 36, no. 1, pp. 275 – 281, 2011.

[82] I. Krastev, T. Dobrovolska, U. Lačnjevac, and S. Nineva, "Pattern formation during electrodeposition of indium–cobalt alloys," *Journal of Solid State Electrochemistry*, vol. 16, no. 11, pp. 3449 – 3456, 2012.

[83] B. Bozzini, D. Lacitignola, and I. Sgura, "Spatio-temporal organization in alloy electrodeposition: a morphochemical mathematical model and its experimental validation," *Journal of Solid State Electrochemistry*, vol. 17, no. 2, pp. 467 – 479, 2013.

[84] M. Izaki, *Electrodeposition of Iron and Iron Alloys*, pp. 309 – 326. John Wiley & Sons, Inc., 2010.

[85] R. J. Clauss, R. A. Tremmel, and R. W. Klein, "Decorative nickel-iron alloy electrodeposits: Present status and future possibilities.," *Transactions of the Institute of Metal Finishing*, vol. 53, no. 1, pp. 22 – 27, 1975.

[86] R. Tremmel, "Decorative nickel-iron coatings - An acceptable and economic-alternative to bright nickel.," *Plating and Surface Finishing*, vol. 68, no. 1, pp. 22 – 26, 1981.

[87] R. S. Smith, L. E. Godycki, and J. C. Lloyd, "Effects of saccharin on the structural and magnetic properties of iron-nickel films," *Journal of The Electrochemical Society*, vol. 108, no. 10, pp. 996 – 998, 1961.

[88] H. V. Venkatasetty, "Electrodeposition of thin magnetic permalloy films," *Journal of The Electrochemical Society*, vol. 117, no. 3, pp. 403 – 407, 1970.

[89] S. H. Liao and S. E. Anderson, "Domain characteristics and conformal deposition of NiFe thin films," *Journal of The Electrochemical Society*, vol. 140, no. 1, pp. 208 – 211, 1993.

[90] R. L. White, "Throwing power effects in permalloy electroplating," *Plating and Surface Finishing*, vol. 75, no. 4, pp. 70 – 76, 1988.

[91] K. Komaki, "Analysis of domain structure and permeability of electrodeposited NiFe strip films," *Journal of The Electrochemical Society*, vol. 140, no. 2, pp. 529 – 533, 1993.

[92] S. Zečević, J. Zotović, S. Gojković, and V. Radmilović, "Electrochemically deposited thin films of amorphous Fe–P alloy: Part I. chemical composition and phase structure characterization," *Journal of Electroanalytical Chemistry*, vol. 448, no. 2, pp. 245 – 252, 1998.

[93] S. Vitkova, M. Kjuchukova, and G. Raichevski, "Electrochemical preparation of amorphous Fe-P alloys," *Journal of Applied Electrochemistry*, vol. 18, no. 5, pp. 673 – 678, 1988.

[94] J. W. Hall, N. Membreno, J. Wu, H. Celio, R. A. Jones, and K. J. Stevenson, "Low-temperature synthesis of amorphous FeP_2 and its use as anodes for Li Ion batteries," *Journal of the American Chemical Society*, vol. 134, no. 12, pp. 5532 – 5535, 2012.

[95] S. Boyanov, J. Bernardi, F. Gillot, L. Dupont, M. Womes, J.-M. Tarascon, L. Monconduit, and M.-L. Doublet, "FeP: another attractive anode for the Li-Ion battery enlisting a reversible two-step insertion/conversion process," *Chemistry of Materials*, vol. 18, no. 15, pp. 3531 – 3538, 2006.

[96] M. E. Schlesinger, "The thermodynamic properties of phosphorus and solid binary phosphides," *Chemical Reviews*, vol. 102, no. 11, pp. 4267 – 4302, 2002.

[97] C. M.S. and S. Mitra, "Electrodeposition of iron phosphide on copper substrate as conversion negative electrode for lithium-ion battery application," *Ionics*, vol. 20, no. 1, pp. 137 – 140, 2014.

[98] A. Mikó, R. Hempelmann, M. Lakatos-Varsányi, and E. Kálmán, "Iron-phosphorous layers deposited by pulse electrochemical technique," *Electrochemical and Solid-State Letters*, vol. 9, no. 8, pp. C126 – C130, 2006.

[99] K. Kamei and Y. Maehara, "Magnetic properties and microstructure of electrodeposited Fe−P amorphous alloy," *Journal of Applied Electrochemistry*, vol. 26, no. 5, pp. 529 – 535, 1996.

[100] R. Liu, S. Gu, H. Du, and C. M. Li, "Controlled synthesis of FeP nanorod arrays as highly efficient hydrogen evolution cathode," *Journal of Materials Chemistry A*, vol. 2, pp. 17263 – 17267, 2014.

[101] L. Tian, X. Yan, and X. Chen, "Electrochemical activity of iron phosphide nanoparticles in hydrogen evolution reaction," *ACS Catalysis*, vol. 6, no. 8, pp. 5441 – 5448, 2016.

[102] P. Jiang, Q. Liu, Y. Liang, J. Tian, A. M. Asiri, and X. Sun, "A cost-effective 3D hydrogen evolution cathode with high catalytic activity: FeP nanowire array as the active phase," *Angewandte Chemie International Edition*, vol. 53, no. 47, pp. 12855 – 12859, 2014.

[103] M. Fallot and R. Hocart, "On the appearance of ferromagnetism upon elevation of the temperature of iron and rhodium," *Rev. Sci*, vol. 8, pp. 498 – 500, 1939.

[104] S. Hashi, S. Yanase, Y. Okazaki, and M. Inoue, "A large thermal elasticity of the ordered FeRh alloy film with sharp magnetic transition," *IEEE Transactions on Magnetics*, vol. 40, no. 4, pp. 2784 – 2786, 2004.

[105] M. A. Tomaz, G. R. Harp, E. Mayo, D. Lederman, R. Wu, and W. L. O'Brien, "Structural and magnetic properties of Fe/Rh(001) sputter deposited multilayers," *Journal of Vacuum Science & Technology A: Vacuum, Surfaces, and Films*, vol. 16, no. 3, pp. 1336 – 1341, 1998.

[106] C. Le Graët, M. A. de Vries, M. McLaren, R. M. Brydson, M. Loving, D. Heiman, L. H. Lewis, and C. H. Marrows, "Sputter growth and characterization of metamagnetic B2-ordered FeRh epilayers," *Journal of Visualized Experiments: JoVE*, no. 80, p. 50603, 2013.

[107] I. Nakamula, Y. Yamanoi, T. Imaoka, K. Yamamoto, and H. Nishihara, "A uniform bimetallic rhodium/iron nanoparticle catalyst for the hydrogenation of olefins and nitroarenes," *Angewandte Chemie International Edition*, vol. 50, no. 26, pp. 5830 – 5833, 2011.

[108] R. Noce, A. Benedetti, E. Passamani, H. Kumar, D. Cornejo, and M. Magnani, "Use of conventional electrochemical techniques to produce crystalline FeRh alloys induced by Ag seed layer," *Journal of Alloys and Compounds*, vol. 573, pp. 37 – 42, 2013.

[109] S. Salem-Sugui Jr., A. D. Alvarenga, R. D. Noce, R. B. Guimarães, C. S. Mejia, H. Salim, and F. G. Gandra, "Anomalous metamagnetic-like transition in a FeRh/Fe$_3$Pt interface occurring at T ≈ 120 K in the field-cooled-cooling curves for low magnetic fields," *AIP Advances*, vol. 2, no. 3, p. 032168, 2012.

<div align="right">

2

</div>

EXPERIMENTAL

In the following, the experimental details of the main experimental techniques used throughout the thesis are briefly mentioned. The fundamentals of each technique are not given as we consider they can be found in advanced textbooks.

2.1. ELECTROCHEMICAL PROCEDURES

2.1.1. DEPOSITS PREPARATION

Electrochemical experiments were conducted in a three-electrode cell configuration connected to a PGSTAT302N Autolab potentiostat/galvanostat (Ecochemie) (Figure 2.1). A double junction Ag|AgCl (E=+0.210 V/SHE) reference electrode (Metrohm AG) was used with 3 M KCl as the inner solution and 1 M NaCl or 1M Na_2SO_4 as the outer solution. A platinum spiral served as CE.
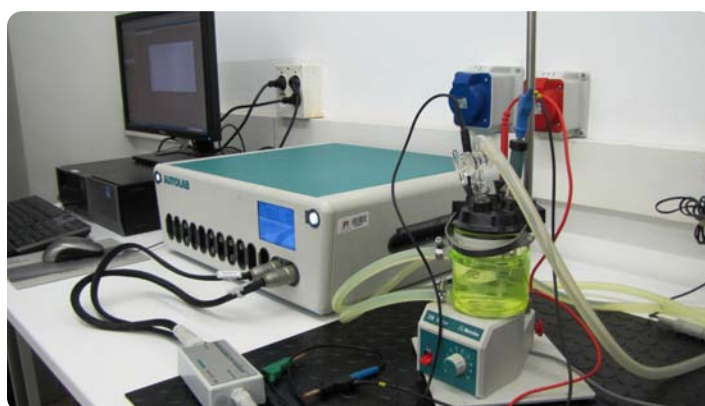

FIGURE 2.1: Picture of three-electrode glass cell connected to the Autolab Potentiostat model PGSTAT302N controlled by a PC.

Silicon (111) substrates with e-beam evaporated Ti (100 nm)/Au (125 nm) adhesion/seed layers were used as WE for deposit growth. Also pre-lithographed Si/Ti/Au substrates were used for the growth

of metallic microstructures. In this case arrays of cylindrical holes of 50 μm in diameter and 1 μm in height were patterned by photolithography using AZ-9260 photoresist and AZ-400K developer. For the production of pseudo-ordered metallic porous films, PS spheres of 350 nm in diameter were assembled on the Si/Ti/Au substrates (Figure 2.2). The PS spheres were electrophoretically deposited by applying 60 V during 5 min using a home-made setup consisting of a chamber (1 cm x 1 cm x 0.6 cm) of poly(methyl methacrylate) (PMMA) glued to a counter electrode of platinized titanium (Figure 2.3).
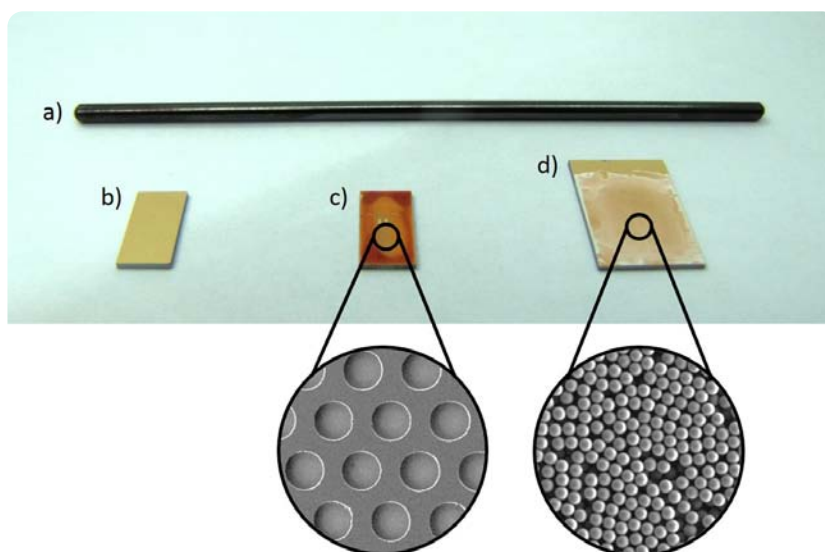

Figure 2.2: Different types of substrates used throughout the work: a) vitreous carbon cylindrical rod, b) Si substrate with e-beam evaporated Ti/Au adhesion/seed layers (denoted as Si/Ti/Au), c) lithographed Si/Ti/Au substrate, and d) PS spheres electrophoretically deposited on Si/Ti/Au.

Analytical grade reagents and Millipore MilliQ water (MQ-water) were used to prepare the electrolytes. The pH was left as-prepared or either adjusted with NaOH or HCl. The electrolyte volume was typically between 75 and 100 mL. Before each deposition, the electrolyte was de-aerated with nitrogen gas for 5-10 min. Prior to deposition, the Au seed layer (substrate b in Figure 2.2) was first degreased with acetone followed by isopropyl alcohol and MQ-water. Deposition was conducted either galvanostatically or potentiostatically at controlled temperature and stirring regime.

2.1.2. Cyclic voltammetry studies

A vitreous carbon cylindrical rod (Figure 2.2a) with π x 10^{-2} cm^2 surface area was used as WE for cyclic voltammetry (CV) studies whenever needed. The potential was initially scanned from a value close to 0 V towards different cathodic limits, at a scan rate of 50 mV s^{-1}.

2.1.3. Electrocatalytic activity towards HER and OER

The electrocatalytic activity of Fe-Rh and Fe-P samples towards HER and/or OER was assessed in alkaline medium using the same three-electrode cell described in section 2.1.1, with Ag|AgCl (3 M KCl) and a Pt spiral as RE and CE, respectively. Linear sweep voltammetry (LSV) and CV measurements were conducted under stagnant conditions in de-aerated 0.1 M NaOH or 1M KOH solution at 25 $^{\circ}$C.

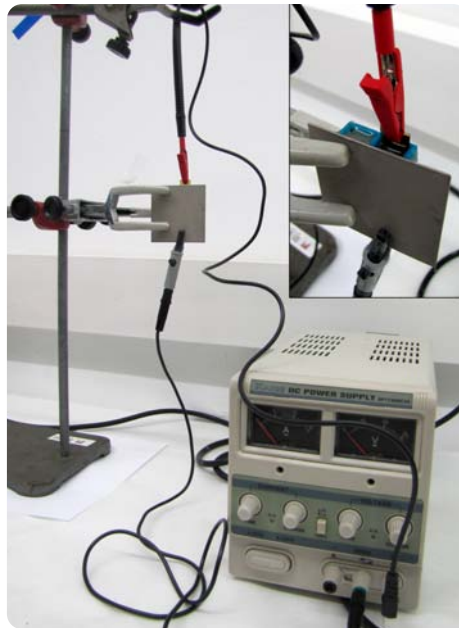Figure 2.3: Picture of the homebuilt electrophoresis setup donated by Dr. S. Pané from ETH-Zürich.

2.2. Characterization techniques

2.2.1. Electron microscopy

The morphology and the composition of the deposits were characterized on a Zeiss Merlin field emission scanning electron microscope (FE-SEM), operated between 0.8 and 3 kV for imaging purposes. The FE-SEM was equipped with an energy dispersive X-ray (EDX) detector, which was typically operated at 20 kV.

Scanning transmission electron microscopy (STEM)-EDX line profile analyses were performed on a Tecnai F20 microscope.

Besides standard X-ray diffraction (XRD) analyses, the crystallographic features of the samples were studied by transmission electron microscopy (TEM) on a JEOL JEM-2011 microscope operated at 200 kV.

2.2.2. Surface microscopy

Conductive atomic force microscope (C-AFM) measurements were performed with a commercial AFM (Agilent 5500LS) operating in contact mode with a commercial tip from AppNano (DD-SICONA) with k = 0.2 N m^{-1}. A bias voltage of V_{bias} = 500 mV was applied to the sample while the tip was grounded.

An Asylum AFM (MFP3D) operated in two different modes was used for the nanomechanical and magnetic characterization and surface potential function mapping. Amplitude modulation-frequency modulation (AM-FM) viscoelastic mapping was used for the nanomechanical characterization. In this mode the cantilever is driven simultaneously at two excitation signals that are combined to excite the fundamental and second cantilever resonances. While the topography is recorded in normal AM mode at the fundamental resonance, the second resonance frequency is driven in FM, and the measured changes in

frequency and dissipation of this resonance are correlated to loss tangent, sample stiffness and elasticity, and viscous behavior or dissipation. To visualize the magnetic domains a MFM study was performed in a dual-scan mode using a magnetized tip (Nanosensors MFMR tip with k = 2 N m^{-1} and a CoCr coating of 35 nm). To map the different surface potential function, Kelvin probe force microscope (KPFM) mode was used.

Some of the deposits were analyzed by AFM/MFM using a Dual Scope C-26 system from Danish Micro Engineering. The MFM maps were taken at a tip lift height of 100 nm.

2.2.3. X-ray diffraction

The crystallographic structure of the samples was studied using a Philips X'Pert diffractometer in Bragg-Brentano geometry (Figure 2.4), with Cu K$_\alpha$ radiation (note that both wavelengths $\lambda(K_{\alpha 1})$=1.5406 Å and $\lambda(K_{\alpha 2})$=1.5443 Å were used in the intensity proportion of I(K$_{\alpha 2}$)=I(K$_{\alpha 1}$) = 0.5). A 0.03º step size and 10 s holding time were applied within an specific 2Θ range, depending on the samples' needs.
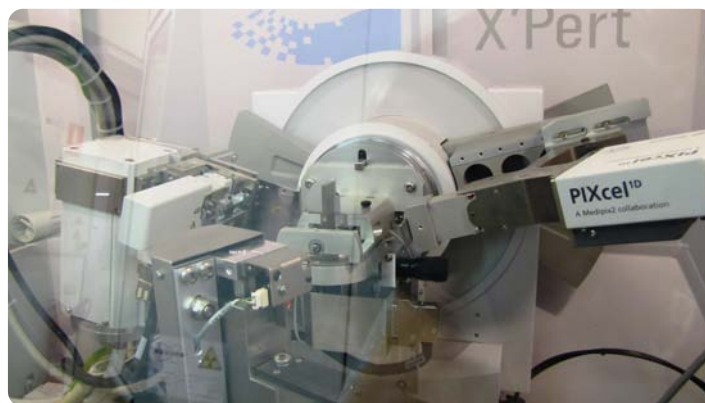

Figure 2.4: Picture of the Philips X'Pert diffractometer available at the X-ray diffraction service of UAB.

2.2.4. Magnetic measurements

The room temperature magnetic properties of the deposits were measured using a VSM from Oxford Instruments or MicroSense (LOT-QuantumDesign). Hysteresis loops were recorded both along the parallel and perpendicular-to-plane directions.

In order to probe the magnetic properties of some deposits at surface level, room temperature magnetic hysteresis loops were recorded using a MOKE setup (from Durham Magneto Optics) at a maximum field of 800 Oe, applied out-of-plane (polar configuration).

Compositional analyses with X-ray absorption spectroscopy (XAS) and magnetic contrast imaging through XMCD using element-specific polarized X-ray PEEM experiments were carried out at the beamline BL24 – CIRCE at the ALBA Synchrotron (Cerdanyola del Vallès).

2.2.5. Mechanical properties

The mechanical properties of the samples were evaluated by nanoindentation operating in the load control mode using the Ultra-Micro-Indentation System (UMIS) device from Fisher-Cripps laboratories,

equipped with a Berkovich pyramid-shaped diamond tip (Figure 2.5). The load-unload curves were taken using a maximum applied force of 5 mN.
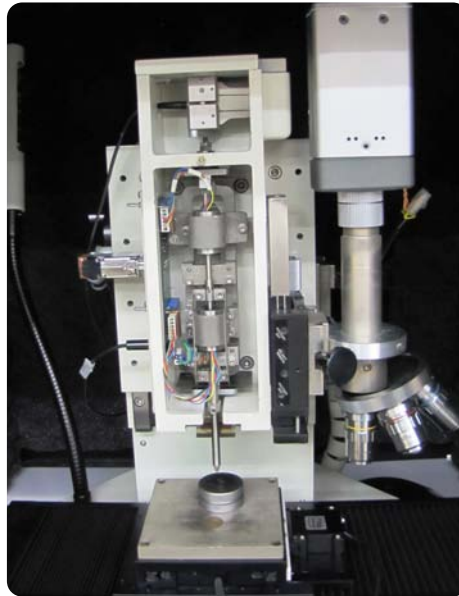

Figure 2.5: Picture of the Ultra-Micro-Indentation System (UMIS) device from Fisher-Cripps laboratories available at Gnm³ group.

2.2.6. Chemical analyses

To determine the metal content in the deposits more precisely, quantification was done using either an inductively coupled plasma mass spectroscopy (ICP-MS) with a 7500ce apparatus from Agilent Technologies or an inductively coupled plasma optical emission spectroscopy (ICP-OES) with an Optima 4300DV spectrometer from Perkin-Elmer. Aqua regia or nitric acid was used to fully dissolve the samples.

The oxidation state of the elements present in some deposits was assessed by X-ray photoelectron spectroscopy (XPS). XPS analyses were carried out at room temperature on a PHI 5500 Multitechnique System (from Physical Electronics) spectrometer, equipped with a monochromatic X-ray source ($K\alpha_{Al}$ line with energy of 1486.6 eV and 350 W), placed perpendicular to the analyser axis and calibrated using $3d^{5/2}$ line of Ag with a full width at half maximum (FWHM) of 0.8 eV. Charging effects were corrected by referencing the binding energies to that of the adventitious C1s line at 284.5 eV.

2.2.7. Contact angle measurements

Surface wettability measurements of the deposits were carried out on a DSA100 Contact Angle Measuring System (Krüss) using the sessile drop method. Contact angles (CA) were recorded after dropping 1.5 μm of MQ-water directly onto the sample's surface.

3

Results: compilation of articles

3.1. Cobalt-Indium system

In this set of articles we report on the spontaneous formation of spatio-temporal patterns during the electrodeposition of Co-In, both in film and microdisks array configurations. So far, Co-In remains as the only binary system able to form spatio-temporal patterns during electrodeposition and to simultaneously exhibit ferromagnetic properties. Our results demonstrate that the spatio-temporal patterns can develop spontaneously either over large areas or in confined cylindrical cavities without the assistance of any hard or soft template.

Firstly, Co-In films with tunable composition were electrodeposited galvanostatically from a chloride-citrate bath on Si substrate with e-beam evaporated Ti/Au adhesion/seed layers. A new bath containing 0.05 M InCl$_3$, 0.25 M CoCl$_3$, 0.05 M sodium citrate dihydrate and 0.1 M KCl (supporting electrolyte) was designed, which was left at its preparation pH (3.1). Prior to deposition, CV curves were recorded on both vitreous carbon and Si/Ti/Au substrates in order to find a range of current densities suitable for deposition. The detection of two different stripping peaks in the anodic branch of the CV indicated the formation of non-single phase deposits. A systematic study on the correlations existing between the morphology and composition, the crystallographic structure, and the resulting mechanical and magnetic properties of the deposits was carried out. The deposition charge was kept constant in order to obtain similar deposit thicknesses (10 μm). EDX analysis revealed that Co-In films with Co contents ranging from 25 at.% to 90 at.% could be straightforwardly electrodeposited on the Au surface. Bath speciation analyses were carried out to understand why deposits become enriched in Co as the absolute value of the current density was increased. EDX in both punctual and mapping modalities showed that the dark belts defined by the patterns were typically richer in Co compared to the bright belts. This effect was exacerbated as the deposition time was increased; namely the dark and bright belts became progressively more enriched in Co and In, respectively. XRD analyses indicated the coexistence of various phases in the films, which were assigned to tetragonal In, fcc-Co, hcp-Co and CoIn$_3$. In turn, the films exhibited tunable magnetic and mechanical properties mostly dependent on the Co content. The film with 90 at.% Co showed a square hysteresis loop in the in-plane direction with the largest H$_C$ (275 Oe). A magnetic micropatterning linked to the spatio-temporal patterning present on the surface of the films was suggested by MFM, thus opening

the possibility to use these films in applications like magnetic sensors, encoding magnetic stripes or even magnetic recording media.

Afterwards, Co-In microdisks were grown onto Si/Ti/Au substrates patterned by photolithography with arrays of cylindrical holes of 50 μm in diameter and 1 μm in height. The deposition was performed from the same electrolytic solution as for continuous films but potentiostatically at a selected potential of -0.98 V. The confined growth of Co-In into cylindrical microcavities enabled the control of the spatio-temporal pattern geometries to some extent. While a mixture of types of patterns was observed in the continuous films, the microdisks only showed one pattern type: spirals. These spirals were linked to a variation of the Co content as determined using the In-Lens detector of the SEM and EDX mapping analysis. In other words, the spiral-like pattern was not visible if the SE detector was used instead, as opposed to the case of continuous films. A set of surface sensitive characterization techniques was employed to investigate the properties of the spiral-like patterns formed in each microdisk. Due to the dissimilar magnetic character of Co and In elements, and their related phases, these spirals rendered a magnetic pattern measurable by polar MOKE, MFM and PEEM. In polar MOKE, hysteresis loops were acquired every 5 μm across the surface of an individual microdisk. A higher Kerr effect amplitude, which is proportional to M_S, was measured when the laser scanned a Co-rich region. Similar results were obtained by PEEM, which was carried out at the beamline BL24 – CIRCE of ALBA Synchrotron. C-AFM measurements also disclosed the occurrence of an electrical pattern, in agreement with the local modulation of the composition. The current ratio between the bright (Co-rich) and dark (In-rich) regions was about 100–10. Besides, using AFM in different working modes, namely KPFM and AM-FM, a periodic variation of both the work-function and the Young's modulus across the microdisks' surface was observed as well.

Finally, the cross-section of continuous Co-In deposits were investigated using advanced electron microscopy tools, as it was observed that they exhibited a layer-by-layer growth mode. Cross-sections for either SEM or (S)TEM imaging were prepared conveniently. Notably, such growth type developed under direct current electrodeposition conditions. Typically, multilayered structures are obtained by applying a pulsating scheme. In our case, 10 μm thick nanolayered films with an amazing periodicity of 175 ± 25 nm were obtained under nominally constant conditions. Closer analysis of each nanolayer demonstrated that they were not compositionally homogeneous (several regions parallel to the substrate plane were identified) and simultaneously exhibited a columnar microstructure. The nanolayers remained stacked together through In-rich anchor points. MFM measurements revealed the occurrence of a magnetic patterning at the cross-section of the Co-In coatings as well. The measurements were done in remanent state after applying a strong magnetic field perpendicular to the film cross-section.
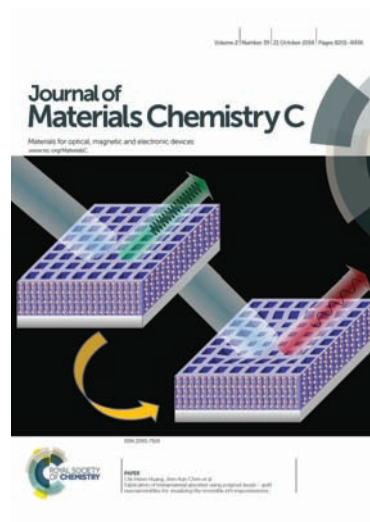
3.1.1. Self-organized spatio-temporal micropatterning in ferromagnetic Co-In films

Irati Golvano-Escobal [a], Berna Özkale [b], Santiago Suriñach [a], Maria Dolors Baró [a], Tsvetina Dobrovolska [c], Ivan Krastev [c], Salvador Pané [b,], Jordi Sort [d,*] and Eva Pellicer [a,*]*

[a] Departament de Física, Universitat Autònoma de Barcelona, E-08193 Bellaterra, Spain.

[b] Institute of Robotics and Intelligent Systems (IRIS), ETH Zürich, CH-8092 Zürich, Switzerland.

[c] R. Kaischew Institute of Physical Chemistry, Bulgarian Academy of Sciences, Sofía, Bulgaria

[d] Institució Catalana de Recerca i Estudis Avançats (ICREA), Departament de Física, Universitat Autònoma de Barcelona, E-08193 Bellaterra, Spain.

*To whom correspondence should be addressed:
Dr. Salvador Pané, Prof. Jordi Sort, Dr. Eva Pellicer
E-mail: vidalp@ethz.ch, Jordi.Sort@uab.cat, Eva.Pellicer@uab.cat

Self-organized spatio-temporal micropatterning in ferromagnetic Co–In films†

Irati Golvano-Escobal,[a] Berna Özkale,[b] Santiago Suriñach,[a] Maria Dolors Baró,[a] Tsvetina Dobrovolska,[c] Ivan Krastev,[c] Salvador Pané,*[b] Jordi Sort*[d] and Eva Pellicer*[a]

Cobalt–indium (Co–In) heterogeneous films, featuring spatio-temporal patterns, have been electrodeposited in a chloride–citrate electrolyte. The Co content can be tuned from 25 at% to 90 at% by varying the applied current density between −10 and −30 mA cm^{-2}. The spatio-temporal patterns consist of alternated dark and bright belts, which define micron-sized waves, targets and spirals. Cross-sectional images indicate layer-by-layer growth. Several crystallographic phases (hexagonal close-packed Co, face-centered cubic Co, tetragonal In and tetragonal CoIn$_3$) are identified in the corresponding X-ray diffractograms. The films exhibit a combination of large hardness with relatively large Young's modulus and a soft-magnetic behaviour with tunable saturation magnetisation and coercivity (H_C) values, mostly depending on the Co content and the effective magnetic anisotropy. The film with 90 at% Co shows the highest in-plane H_C (275 Oe) and a squareness ratio close to 1. Magnetic force microscopy observations reveal that the self-patterning is not only topographic but also magnetic. These results demonstrate that the electrodeposition of spatio-temporal structures is a simple method to grow magnetically patterned films, over large areas, in a rapid and inexpensive way. This procedure is highly attractive for the implementation of new types of magnetic sensors, encoding magnetic stripes or even magnetic recording media.

1. Introduction

The spontaneous formation of self-organized spatio-temporal patterns is a phenomenon related to chaos (*i.e.*, fluid instabilities or chemical instabilities) that occurs in dynamic non-linear open systems that are far from equilibrium.[1] Examples of such patterns can be either found in nature (*e.g.*, in the atmosphere and the oceans, in the skin of some animals like the zebra or some fish, in atrial fibrillation, *etc.*) or they can be experimentally generated in the laboratory, such as in nanomechanical oscillators or in reaction–diffusion chemical reactions that occur in some immiscible systems (*e.g.*, phase separation, eutectic solidification, *etc.*). Although linear stability analysis can give some basic understanding of the origin of the pattern formation and the basic length scales, non-linearity remains a

fundamental ingredient in order to adequately describe the experimental observations, thus making the problem much more complex and not fully resolved yet.[2,3] Nonetheless, studies aimed at unravelling the mechanisms governing spatio-temporal chaos in dynamic systems remain of utmost importance since more knowledge in the field could allow a better prediction of the nucleation and propagation paths for tornadoes and hurricanes, tectonic motion, the overall evolution of Earth's climate or the transition from normal to arrhythmic heartbeat, amongst others. Directional growth or solidification, in some materials, is also important in terms of the resulting physico-chemical properties. Some eutectic alloys exhibit, for example, outstanding mechanical hardness and have been proposed as ideal heat-transfer materials or as die molds for patterning applications.

The emergence of spatio-temporal patterns can be due to a flux of energy or a flux of matter, *e.g.* originated from the existence of externally imposed temperature variations (*e.g.*, convection), or by the flow of fluids or chemicals in a reactor. The formation of spatio-temporal structures during electrode-position was first observed in some Ag alloys (*e.g.* Ag–Bi, Ag–Cd, Ag–In, and Ag–Sb) and attracted the interest of researchers from both experimental and theoretical viewpoints.[4–8] Recently, pattern formation during the electrodeposition of non-Ag based alloys, like Co–In and Ni–P–W–Bi has been demonstrated, hence opening the possibility for additional functionalities (*e.g.*,

[a] *Departament de Física, Universitat Autònoma de Barcelona, E-08193 Bellaterra, Spain. E-mail: Eva.Pellicer@uab.cat*

[b] *Institute of Robotics and Intelligent Systems (IRIS), ETH Zürich, CH-8092 Zürich, Switzerland. E-mail: vidalp@ethz.ch*

[c] *R. Kaischew Institute of Physical Chemistry, Bulgarian Academy of Sciences, Sofia, Bulgaria*

[d] *Institució Catalana de Recerca i Estudis Avançats (ICREA), Departament de Física, Universitat Autònoma de Barcelona, E-08193 Bellaterra, Spain. E-mail: Jordi.Sort@uab.cat*

This journal is © The Royal Society of Chemistry 2014

J. Mater. Chem. C, 2014, **2**, 8259–8269 | 8259

magnetic) to the previous Ag-based alloys.[9,10] The underlying mechanism for the formation of the spatio-temporal structures is not yet clear and several factors are thought to contribute to the phenomenon, with small differences depending on the system under consideration:[10]

(i) the electrolyte hydrodynamic conditions, meaning that the flow along the electrode surface seems to be a necessary condition for pattern formation;

(ii) the overpotential, since a threshold value is required for pattern formation. In addition, the overpotential has been correlated with the switching among different types of patterns (labyrinths, waves, targets, spirals, broken spirals and mixed patterns);

(iii) the ability to self-organize during the growth of multi-phase alloys where spatial separation of the phases takes place. This has been reported to be one of the key reasons for pattern formation in Co–In electrodeposition;

(iv) the kinetic variables, the bath composition (e.g. the counter ion) and the appearance of Turing instabilities in reaction–diffusion systems when the diffusion constants of the different components are quite different from each other.[11]

Bozzini et al. have recently reviewed the literature dealing with pattern formation in alloy electrodeposition and proposed a very innovative and flexible mathematical model to explain the formation of the different types of spatio-temporal structures.[10] Compared to classical models based on systems of reaction–diffusion equations for chemical species, Bozzini's model goes one step further and includes an electrochemical source term to account for adsorbate-induced effects on the kinetic parameters of the electrodeposition process. In such a way, the coupling between the surface morphology and the surface composition is considered.

Compared to the Ag alloys series, the electrodeposition of Co–In alloys has been much less explored and most of the work has been conducted by Krastev's group. Pattern formation under both stagnant and high speed electrodeposition from electrolytes containing sulphate metal salts and di-ammonium hydrogen citrate at pH around 3 has been established.[9,12] Typically, the ordered spatio-temporal structures form at sufficiently negative current densities (large Co contents).

It cannot be denied that the formation of spatio-temporal structures in alloy electrodeposition is a fascinating phenomenon that deserves investigation. However, the usefulness of growing coatings featuring such patterning inevitably relies on the ability to find out chemical or physical properties that can certainly benefit from the self-organized structures. In this sense, the study of the physical properties of these self-patterned coatings should turn the corner towards a potential technological application. To the best of our knowledge, the physical properties of Co–In coatings featuring spatio-temporal structures have not been explored. Indium is a very ductile element and has a very low melting point (156.60 °C). For this reason, it has been extensively used in lead-free solders.[13] Indium metal is also employed as a thermal interface material in the electronic industry[14] and in CIS/GICS solar cells. For the latter application, the fabrication of CuInS₂ and Cu(InGa)Se₂ semiconductor compounds by electrodeposition of In metal on

Cu followed by sulfurization or selenization has already been reported.[15] From the magnetic point of view, it has been described that the addition of indium in arc-melted and post-annealed PrCo₅ magnets causes an increase of coercivity, H_C, likely due to the formation of the $Pr_3Co_9In_2$ phase.[16] Likewise, the addition of Co into InAs, InSb or In_2O_3 has been shown to be a very suitable strategy towards the development of diluted magnetic semiconductors with potential applications in spintronics.[17]

In this work, Co–In films have been electrodeposited from a simple aqueous electrolyte containing chloride metal salts and sodium citrate under stagnant conditions at different current densities. The morphology, composition and crystallographic structure of the galvanostatic deposits obtained on Au/Ti/Si substrates have been systematically studied. According to its phase diagram, In and Co are immiscible in both solid and liquid states.[18] Hence, the formation of multi-phase coatings is anticipated. Energy dispersive X-ray (EDX) mapping analyses of the Co–In films have been conducted in order to explore the chemical composition of the spatio-temporal patterns. Finally, the mechanical and magnetic properties of the Co–In films have been studied in detail and the data obtained have been correlated with the composition and microstructure of the deposits. The Co–In system is unique in the sense that it is the only binary alloy to simultaneously exhibit ferromagnetic properties with the ability to form spatio-temporal patterns during electrodeposition. This appealing combination of properties is confirmed by magnetic force microscopy observations, which reveal that the films do exhibit 'magnetic micropatterning' linked to the topographical self-organization.

2. Experimental section

2.1. Synthesis

Electrochemical experiments were conducted in a three-electrode cell connected to a PGSTAT302N Autolab potentiostat/galvanostat (Ecochemie). A double junction Ag|AgCl ($E = +0.210$ V/SHE) reference electrode (Metrohm AG) was used with 3 M KCl as the inner solution and 1 M NaCl as the outer solution. A platinum sheet served as the counter electrode. A vitreous carbon cylindrical rod with $\pi \times 10^{-2}$ cm² surface area was used as the working electrode (WE) for cyclic voltammetry (CV) studies, whereas silicon (111) substrates with e-beam evaporated Ti (100 nm)/Au (125 nm) adhesion/seed layers were used as WEs for both CV studies and deposit growth. The working area of Au/Ti/Si substrates was 5 × 5 mm².

In CV studies, three different electrolytes were used: the In bath containing 0.30 M $InCl_3$ + 0.05 M $C_6H_5Na_3O_7 \cdot 2H_2O$ + 0.1 M KCl, Co bath containing 0.30 M $CoCl_2$ + 0.05 M $C_6H_5Na_3O_7 \cdot 2H_2O$ + 0.1 M KCl and Co–In bath containing 0.05 M $InCl_3$ + 0.25 M $CoCl_2$ + 0.05 M $C_6H_5Na_3O_7 \cdot 2H_2O$ + 0.1 M KCl. The pH of the Co–In electrolyte was left at its unadjusted value (3.1) and the pH of the In and Co baths was adjusted to pH 3.1 by adding NaOH and HCl, respectively. The potential was scanned from 0 V toward different cathodic limits at a scan rate of 50 mV s^{-1}.

Analytical grade reagents and Millipore MilliQ water (MQ-water) were used to prepare the electrolytes. The electrolytic

8260 | J. Mater. Chem. C, 2014, **2**, 8259–8269

This journal is © The Royal Society of Chemistry 2014

35

volume was 100 ml. Before each experiment, the electrolyte was de-aerated with a nitrogen gas for 10 minutes through a glass purge pipe that provided a vigorous stream of nitrogen. Prior to deposition, the Au seed-layer was first degreased with acetone followed by isopropyl alcohol and MQ-water. Deposition was conducted galvanostatically at 25 °C. The electrical charge was adjusted across all depositions to 20 C cm^{-2} except for the study of the time-dependent spatio-temporal evolution. After deposition, the films were thoroughly rinsed in water and stored in air.

2.2. Characterization

The morphology and the composition of the films were characterized with a Zeiss Merlin field emission scanning electron microscope (FE-SEM) equipped with an energy dispersive X-ray (EDX) detector. Two replicas per condition were analysed. The structure of the films was determined by X-ray diffraction (XRD) using a Philips X'Pert Diffractometer in Bragg–Brentano geometry using Cu Kα radiation (note that both wavelengths $\lambda(K_{\alpha 1}) = 1.5406$ Å and $\lambda(K_{\alpha 2}) = 1.5443$ Å were used in intensity proportion of $I(K_{\alpha 2}) = I(K_{\alpha 1}) = 0.5$) in the 25–125° 2θ range (0.03° step size and 10 s holding time).

The mechanical properties of the Co–In films were evaluated by nanoindentation operating in the load control mode using the Ultra-Micro-Indentation System (UMIS) device from Fisher-Cripps laboratories equipped with a Berkovich pyramid-shaped diamond tip. The load–unload curves were taken on the films applying a maximum force of 5 mN. The value of the maximum applied force was chosen to ensure that the maximum penetration depth during the tests was kept below one tenth of the overall thin film thickness. This is considered a necessary condition to avoid any influence from the substrate on the measured mechanical properties.[19] The hardness (H) and reduced elastic modulus (E_r) values were obtained applying the method of Oliver and Pharr.[20] Finally, the elastic recovery was evaluated as the ratio between the elastic and the total (plastic + elastic) energies during nanoindentation, W_e/W_t. These energies were calculated from the nanoindentation experiments as the areas between the unloading curve and the displacement axis (W_e) and between the loading curve and the displacement axis (W_t).[19]

The room temperature magnetic properties were measured using a vibrating sample magnetometer (VSM) from Oxford Instruments. Hysteresis loops were recorded under a maximum applied field of 700 Oe applied along the parallel and perpendicular-to-plane directions. Atomic and magnetic force microscopy (AFM/MFM) images were acquired using a Dual Scope C-26 system from Danish Micro Engineering. The MFM maps were taken at a tip lift height of 50 nm.

3. Results

3.1. Cyclic voltammetry study

Cyclic voltammetries (CV) recorded from In, Co and Co–In electrolytes on a vitreous carbon electrode are shown in Fig. 1a. A moderate increase of the reduction current is observed in the In bath (curve 1) from −0.80 V. In the anodic scan, a double-
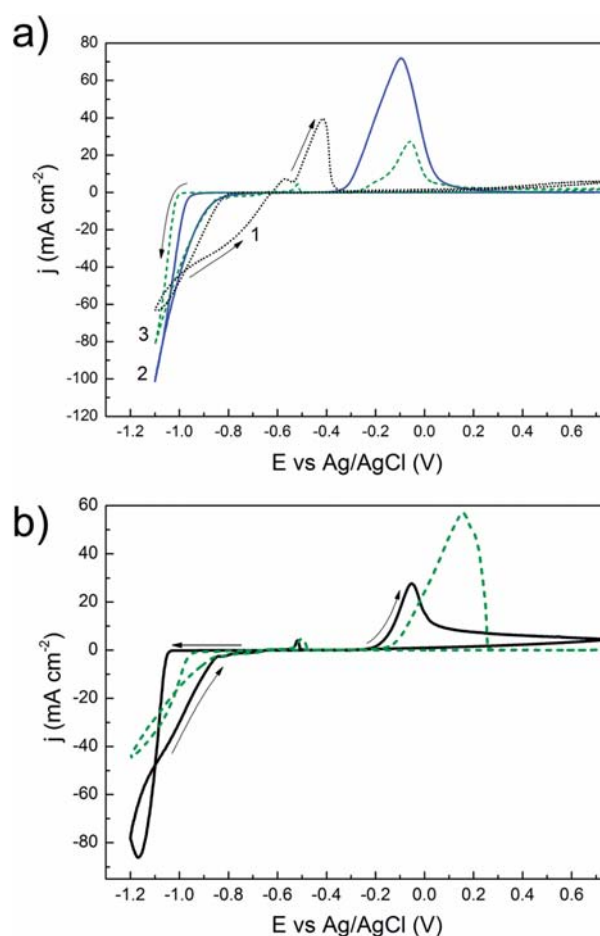

Fig. 1 Cyclic voltammetries obtained by polarizing (a) a vitreous carbon electrode at a cathodic limit of −1.1 V in the (1) In bath, (2) Co bath and (3) Co−In bath and (b) a vitreous carbon (continuous line) and a Au/Ti/Si substrate (dashed line) at a cathodic limit of −1.2 V in the Co−In bath. In all cases, a scan rate of 50 mV s^{-1} and quiescent conditions were used.

peak is recorded between −0.4 and −0.6 V. This double-peak corresponds to the oxidation of In-containing species formed on the substrate during the cathodic sweep rather than the oxidation of adsorbed H_2 bubbles arising from the reduction of H^+ ions. When a vigorous stream of Ar gas is provided to the electrolyte during the cathodic scan, the oxidation peak current does not decrease, which otherwise would be observed if most of the reduction current passing through the working electrode (WE) is used to reduce H^+ ions. In such a case, vigorous agitation removes the freshly adsorbed H_2 bubbles on the WE and the corresponding oxidation current recorded during the anodic scan diminishes. For the Co bath, a sharper increase of the reduction current is observed at around −0.95 V, which corresponds to the onset of Co deposition (curve 2). A single oxidation peak centered at −0.1 V is observed in the anodic scan. The CV curve recorded from the Co–In electrolyte (curve 3) shows similar behaviour to that from the Co bath in the cathodic scan, although the onset for deposition is slightly

This journal is © The Royal Society of Chemistry 2014

J. Mater. Chem. C, 2014, **2**, 8259–8269 | **8261**

36

delayed. In the anodic scan, a small oxidation peak centered at -0.5 V is recorded, followed by a higher oxidation peak at more positive potentials (-0.06 V). Since the first peak appears in the same position as for the In electrolyte, it is conjectured that it can be connected with the oxidation of In-rich species. Likewise, the second anodic peak could be assigned to the oxidation of Co-based species. This suggests that a heterogeneous deposit is being formed on the electrode. Finally, it was observed that the onset of deposition on a Au/Ti/Si substrate is shifted toward more positive potentials as compared to the vitreous carbon electrode although the main features of the CV are maintained (Fig. 1b).

According to the CV data, deposits could be in principle formed on the Au/Ti/Si electrode at current densities ranging from -10 mA cm^{-2} to -30 mA cm^{-2} (and higher). It was expected that deposits grown at low current densities would contain higher In percentages according to the onset of deposition (-0.95 V for the Co electrolyte *versus* -0.80 V for the In electrolyte).

3.2. Morphology and composition of the films

Fig. 2 shows the $E–t$ transients for Co–In plated onto Au/Ti/Si substrates at current densities ranging from -10 to -30 mA cm^{-2} and at a fixed deposition charge ($Q = 20$ C cm^{-2}). The curves are characterized by a minimum in the $E–t$ transients that turn into a clear spike with an increase of the absolute value of current density during the first seconds of deposition. This is followed in all cases by relaxation of the potential towards a rather stationary value. The value of the stabilized potential decreases as the applied current density is made more negative. The cobalt percentage obtained from EDX analyses drastically increases with a slight increase of the current density from almost pure In films at -10 mA cm^{-2} to 58 at% Co at -12 mA cm^{-2} (Table 1). It is not possible to obtain Co percentages in-between because deposits become rapidly enriched in Co soon after cobalt discharge is allowed. The Co
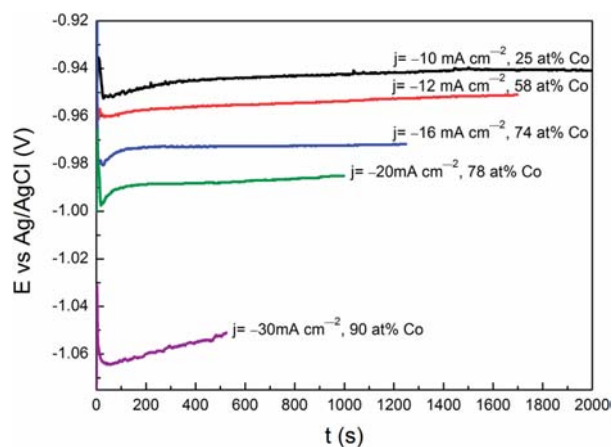
Table 1 Values of the applied current density ($-j$), stabilized potential ($-E_S$) of the $E–t$ curve and the corresponding Co percentage in the films (mean value ± standard deviation)

$-j$ (mA cm^{-2})	$-E_S$ (V)	at% Co
10	0.94	25[a]
12	0.95	58 ± 3
16	0.97	74 ± 1
20	0.99	78 ± 1
30	1.05	90 ± 2

[a] Non-homogeneous film composed of large areas with a In content approaching 100% and smaller areas showing spatio-temporal organization with *ca.* 50 at% Co.

percentage rises up to 90 at% with a further increase of the current density to -30 mA cm^{-2}.

With the naked eye, all Co–In deposits show slightly metallic luster appearance and are grey in colour except the coating at -10 mA cm^{-2} that is whitish. Good adhesion to the substrate is observed for nearly all current densities. Incipient peel-off is seen at the edges in films produced at a current density of -30 mA cm^{-2}. Hence, more negative current densities were not considered since film detachment extended across the entire sample–substrate interface. Thick films (10 ± 2 μm) are obtained under all conditions (*i.e.* for deposition times ranging from 9 min to 33 min).

The occurrence of spatio-temporal structures was already noticed using the optical microscope (not shown). FE-SEM images of the morphology of Co–In films are shown in Fig. 3. The spatio-temporal structures are already observed at the
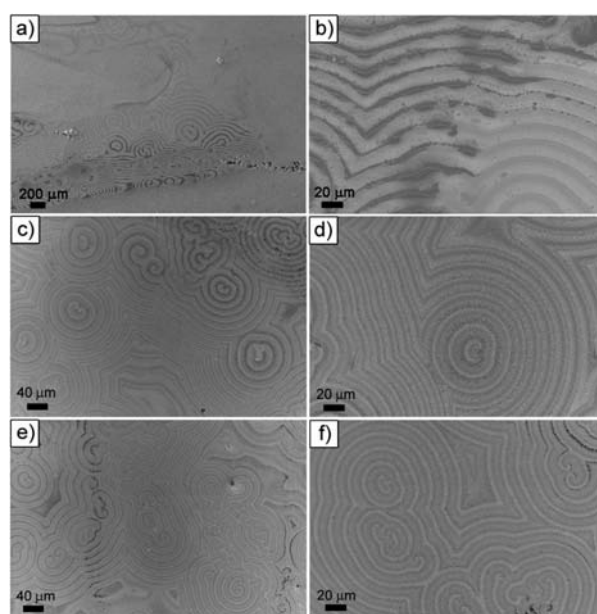

Fig. 2 Representative $E–t$ transients for Co–In deposition onto Au/Ti/Si substrates at the indicated current densities. The corresponding average cobalt content in the films is also specified.

Fig. 3 FE-SEM images of Co–In thin films obtained at: (a and b) $j = -10$ mA cm^{-2} (25 at% Co), (c and d) $j = -12$ mA cm^{-2} (58 at% Co) and (e–f) $j = -20$ mA cm^{-2} (78 at% Co).

8262 | *J. Mater. Chem. C*, 2014, **2**, 8259–8269

This journal is © The Royal Society of Chemistry 2014

37

lowest current density applied (Fig. 3a and b). However, in this case, the patterns do not spread all over the substrate but are visible only in some areas of the coating. At current densities of -12 mA cm^{-2} and higher, the spatio-temporal patterns are observed all over the film (Fig. 3c–f), and the corresponding deposits feature a mixture of waves, concentric rings (also termed "target patterns") and spirals of variable sizes. No apparent trend between the size of these patterns and the applied current density was seen. EDX analysis revealed that the brighter and darker belts defined by such patterns contained different amounts of Co and In, hence confirming the heterogeneity in composition of the films. EDX-point analyses showed that the dark belts are typically richer in Co compared to the bright belts by about 30 at% in the case of the film deposited at -10 mA cm^{-2} and about 10 at% for the rest of the films. Since the spatial resolution of the EDX is limited by the interaction volume (X-rays are able to escape not only close to the surface but basically from the whole interaction volume), it is reasonable to assume that the difference in the Co amount at the utmost part of the coating is underestimated.

At higher magnifications, a sand-like grain morphology is seen all over the film (Fig. 4a) except for the sample deposited at -10 mA cm^{-2}. For this sample, the sand-like morphology is also observed in the areas where the spatio-temporal patterns are formed but the rest of the coating features an island-like morphology (Fig. 4b) that resembles a Stranski–Krastanov growth mode.[14] In fact, while the Co content is 25 at% on average, the film is non-homogeneous in composition. The

regions showing spatio-temporal patterns have large Co contents (~50 at%) whereas the regions without spatio-temporal patterns are made of almost pure In.

Fig. 5 shows the molar fraction x_i of Co^{2+} and In^{3+} species as a function of pH in the electrolyte. The mole fractions were calculated using MEDUSA® software[21] for all of the bath compounds. The ionic strength was set iteratively by the program. Around pH = 3.0, the most predominant species of Co^{2+} are in the form of aquacomplexes (Fig. 5a). The molar fraction of cobalt(II) chloride and citrate complexes only represent together $x = 0.2$ of all the cobalt species. Hydroxocomplexes of Co^{2+} are almost negligible within the pH window hereby considered. On the other hand, In^{3+} is mostly complexed by chlorides (Fig. 5b). The formation of In^{3+} citrate complexes is not considered since there are no available data.[12] Hence, the formation of these species are not considered in this discussion.

The standard electrochemical potentials $E^0_{M^{z+}/M}$ for Co^{2+} and In^{3+} are, respectively, -0.28 V and -0.34 V. At very low current

Fig. 4 High magnification FE-SEM images of Co–In thin films obtained at: (a) $j = -30$ mA cm^{-2} and (b) $j = -10$ mA cm^{-2} (taken at the region without spatio-temporal patterns).
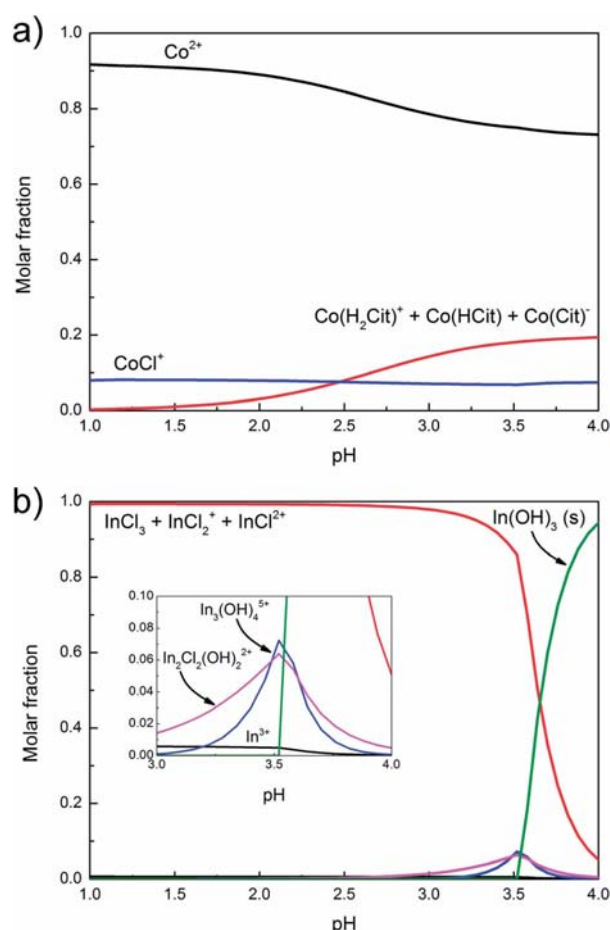

Fig. 5 Mole fraction diagrams of (a) Co^{2+} and (b) In^{3+} species as a function of pH in the electrolyte. The mole fractions were calculated using MEDUSA®. In order to simplify the diagrams, the sum of the mole fractions of the Co^{2+} citrates and the sum of the rest of In^{3+} compounds are represented instead of showing each separately.

38

densities, indium plates out preferentially respect to cobalt.[22] This fact seems counterintuitive if one considers the electrochemical potential and the fact that In is mostly complexed by chlorides, while water molecules mostly coordinate with Co. However, a study by Bessone and co-workers shows that chlorides facilitate the reduction of In^{3+}.[23] At acidic pHs, the presence of a high positive electrostatic barrier of H^+ near the cathode obstructs the access of positively charged species to the electrode. The high positive charge of In^{3+} is compensated by chloride anions, while Co^{2+} keeps its charge because it mainly exists as an aquacomplex. Therefore, it seems reasonable to suppose that deposits are richer in indium at low current densities. When increasing the current density, the deposition process changes drastically leading to films with high cobalt contents (Fig. 2 and Table 1). This effect could be related to the formation of hydroxocomplexes at the cathode neighbourhood due to hydrogen evolution. Cobalt(II) hydroxocomplexes are readily adsorbed on the cathode and, hence, its reduction is enhanced.

3.3. Structural characterization

The structural characteristics of the films obtained through the $E–t$ curves shown in Fig. 2 were studied by XRD (Fig. 6). Apart from some narrow reflections coming from the substrate (Si and Au seed-layer), all the patterns feature a collection of peaks arising from the electrodeposited films themselves. The diffractograms show reflections that can be assigned to tetragonal In (PCPDF 05-0642), tetragonal $CoIn_3$ (PCPDF 41-0880), face-centered cubic (fcc) Co and hexagonal-close packed (hcp) Co. As expected, the relative intensity of the In phase peaks decreases as the amount of Co in the films increases. Moreover, no shift of fcc- and hcp-Co peaks toward lower 2θ angles is noticed, indicating that eventual dissolution of In in the Co lattice does not take place (which is in agreement with the very limited solubility of In in Co), and the existence of a miscibility gap in this system as reported long ago by Koster and Horn.[24] The coexistence of tetragonal In, fcc-Co and hcp-Co phases clearly demonstrates that a solid solution is not formed but rather separate deposition of Co and In elements (together with intermetallic $CoIn_3$) takes place, instead, during electrodeposition. Nevertheless, the calculated equilibrium phase diagram of the Co + In system establishes the coexistence of hcp-Co and $CoIn_2$ phases at room temperature for Co percentages ≥ 33.3 at%.[18] Interestingly, the monoclinic $CoIn_2$ phase is not detected in our diffractograms, but only the ordered tetragonal $CoGa_3$-type $CoIn_3$ forms, in concordance with a previous study on the electrodeposition of Co–In.[12] It has been claimed that $CoIn_3$ is one of the phases forming the spatio-temporal patterns.[25] A hump at 2θ angles between 40° and 55° overlapped with the reflections is distinguished. This indicates the existence of an additional fraction of amorphous-like contribution, whose relative volume increases with the Co content. Moreover, the full with at half maximum (FWHM) of the fcc-Co, hcp-Co and $CoIn_3$ peaks is larger than for pure In peaks, which suggests that the crystal size of the latter phase is larger. To further confirm this observation, the Scherrer's formula has been applied to (101) In, (111) fcc-Co and (112) $CoIn_3$ reflections, to obtain a rough estimation of their crystallite sizes (Tables 2 and S1†). These reflections were selected so that they are univocally assigned to only one phase (i.e., no overlapping between phases). While crystallite sizes below 25 nm are generally obtained for fcc-Co or $CoIn_3$, much larger values (around 60 nm) are observed for pure In. It should be pointed out that Co–In coatings electrodeposited from a bath containing $InCl_3$, $CoSO_4$, $(NH_4)_2H$ citrate and KNa tartrate were also composed of tetragonal In and $CoIn_3$ phases together with hcp-Co.[12] In our work, Co is found as a mixture of fcc, hcp and possibly amorphous phases.

An explanation based on crystallographic considerations has been proposed to account for the spatio-temporal organization in some binary systems like Ag–In, Ag–Sb and Ag–Cd.[25] For example, the XRD patterns of spatio-temporal Ag–In coatings show the existence of fcc Ag and hexagonal $InAg_3$ phases. The similarity between the densely packed (111) plane of the fcc phase and the (0001) plane of the hexagonal $InAg_3$ is thought to contribute to the easy local transition from phase to phase during electrodeposition.[25,26] Likewise, the diffractograms of
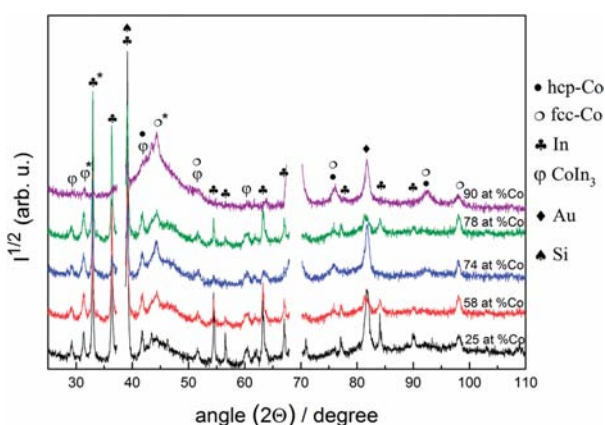

Fig. 6 X-ray diffractograms in the 25–110° 2θ region of Co–In films with different cobalt contents deposited on Au/Ti/Si (111) substrates. Breaks in data around 37° and 69° were applied to avoid the most intense reflections from Au and Si, respectively, of the substrate. * Peaks used in Table 2 for FWHM and $\langle D \rangle$ analysis.

Table 2 FWHM and the corresponding crystallite size (D) calculated using Scherrer's formula for In (101), fcc-Co (111) and $CoIn_3$ (112) peaks for the diffractograms shown in Fig. 6

at% Co	In (101)		fcc-Co (111)		$CoIn_3$ (112)	
	FWHM (°)	$\langle D \rangle$ (nm)	FWHM (°)	$\langle D \rangle$ (nm)	FWHM (°)	$\langle D \rangle$ (nm)
25	0.123	67	—	—	0.325	25
58	0.134	62	0.788	11	0.444	19
74	0.143	58	0.669	13	0.615	13
78	0.132	58	0.891	10	0.634	13
90	—	—	—[a]	—	0.614	13

[a] Cannot be precisely determined because it is overlapped with the amorphous background.

Ag–Cd films with 80 wt% Cd featuring spatio-temporal patterns evidence that the films are highly textured. The coatings are made of highly oriented hexagonal Cd-rich ($Ag_{1.05}Cd_{3.95}$) and hexagonal pure Cd phases. The coincidence in the (101) reflection for both phases is believed to contribute to the spatio-temporal organization to some extent.[5,25] However, this explanation does not hold for the Co–In system since such similarities cannot be drawn between the fcc or hcp phases of Co and tetragonal $CoIn_3$.

3.4. Magnetic behaviour

The magnetic properties of the films were measured by vibrating sample magnetometry (VSM) at room temperature by applying the magnetic field parallel and perpendicular to the film plane (Fig. 7). While the films show a ferromagnetic response, the saturation magnetization (M_S) does not linearly scale with the Co percentage. This result corroborates that a Co–In solid solution is not formed; otherwise the sample with 25 at% Co should exhibit a very weak ferromagnetic signal. The non-linear increase of M_S values is due in part to the presence of
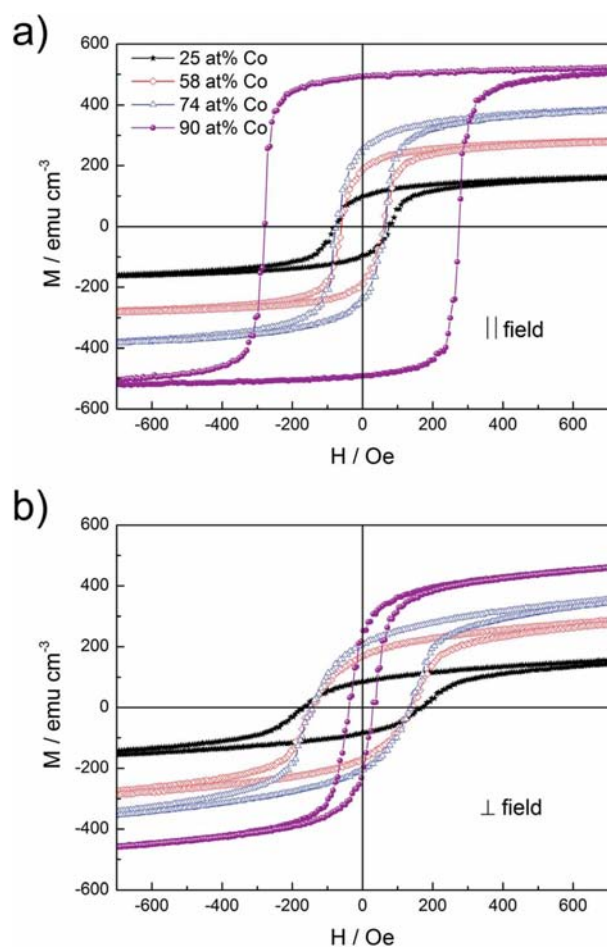

Fig. 7 Room-temperature hysteresis loops measured by VSM applying the magnetic field along (a) the in-plane direction and (b) the perpendicular-to-plane direction.

several phases (In, fcc-Co, hcp-Co and $CoIn_3$) whose relative amounts vary with the applied current density. Magnetic susceptibility measurements of polycrystalline $CoIn_3$ synthesized by reaction at high temperature in tantalum tubes indicate that this compound is weakly paramagnetic at room temperature,[27] while In is diamagnetic. Hence, the observed ferromagnetic response should mainly arise from the pure Co phases.

The films are rather soft-magnetic with in-plane and perpendicular-to-plane coercivities (H_C) and squareness ratios (M_R/M_S) that have different values depending on both the direction of the applied field and the chemical composition (Fig. 7 and Table 3). The film with 90 at% Co shows the largest in-plane H_C (275 Oe) and largest in-plane M_R/M_S (virtually 1, i.e. a square hysteresis loop), much larger than M_R/M_S along the perpendicular-to-plane direction ($M_R/M_S = 0.45$). Hence, this film exhibits a clear in-plane effective magnetic anisotropy, probably dominated by the shape anisotropy (i.e., planar contribution). This shape anisotropy could be due, at least in part, to the formation of the planar spatio-temporal patterns. Interestingly, the values of M_R/M_S along the in-plane direction are reduced in films with lower Co contents, although they remain larger than for measurements along the perpendicular-to-film direction (see Table 3). The in-plane effective magnetic anisotropy is reduced in these films, probably because the ferromagnetic regions (e.g., hcp-Co or fcc-Co) become less interconnected between them and the shape anisotropy arising from the planar geometry of the films is reduced to some extent.

The coercivity along the in-plane direction is also reduced when the cobalt content is decreased from 90 at% to 74 at% ($H_C = 65$ Oe) and 58 at% ($H_C = 60$ Oe). This is mainly due to the loss of magnetic shape anisotropy in the film plane, which in turn is related to an increase of the coercivity with the decrease of the Co content along the perpendicular to the film direction. For the sample with 90 at% Co the hysteresis loop along the out-of-plane direction is more difficult to saturate than along the in-plane direction, thus confirming that the easy magnetization axis lies in plane. For the other films, there is no such a clear easy axis, meaning that there is a competition between shape and magnetocrystalline anisotropies. The out-of-plane H_C of the film with 90 at% Co is 30 Oe, whilst higher values (140–170 Oe) apply for the other Co–In films.

Atomic force microscopy (AFM) coupled to magnetic force microscopy (MFM) analysis of the samples was performed to

Table 3 Saturation magnetization (M_S), squareness ratio (M_R/M_S) and coercivity (H_C) of Co–In films as a function of their average Co percentage. The symbols ∥ and ⊥ mean that the field was applied parallel and perpendicular to the film plane, respectively

at% Co	M_S [emu cm^{-3}]	M_R/M_S∥	H_C∥ [Oe]	M_R/M_S ⊥	H_C ⊥ [Oe]
25	163	0.59	75	0.52	170
58	275	0.68	60	0.61	138
74	387	0.65	65	0.54	136
90	525	0.93	275	0.45	30

40

reveal whether the spatio-temporal organization gave rise to any magnetic contrast besides the topological self-patterning. Fig. 8 shows the AFM and MFM images for the film deposited at −10 mA cm^{-2}, taken at a region where the spatio-temporal organization occurred. The AFM image displays the typical belts observed by SEM, being the peak-to-valley distance equal to 225 nm. Interestingly, the corresponding MFM image shows a clear magnetic contrast that follows the topographical pattern. This proves that the spatio-temporal patterns do exhibit some kind of inherent 'magnetic micropatterning'. A similar response was observed in corrugated cobalt filaments also made by electro-deposition.[28] The MFM analysis was also performed on other films produced at higher current densities. MFM images also reveal some magnetic contrast, but less pronounced because the films are probably entirely magnetic.

3.5. Mechanical behaviour

The mechanical properties of the Co–In films were studied by nanoindentation. Fig. 9a shows representative loading–unloading curves performed on-top of the films. The curve for the sample with 25 at% Co on average was obtained from an
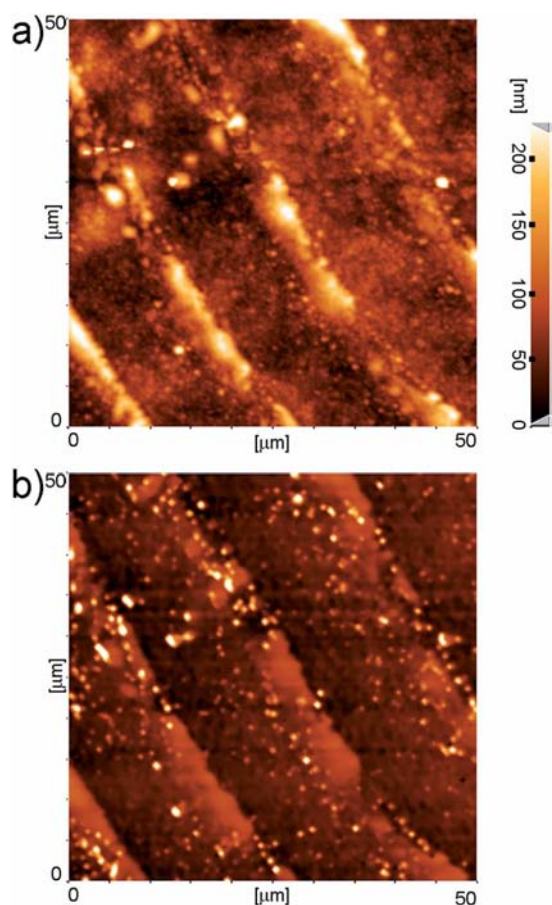
Fig. 8 (a) AFM and (b) MFM images taken on a scanned 50 × 50 μm^2 area containing spatio-temporal patterns for the sample deposited at −10 mA cm^{-2}.
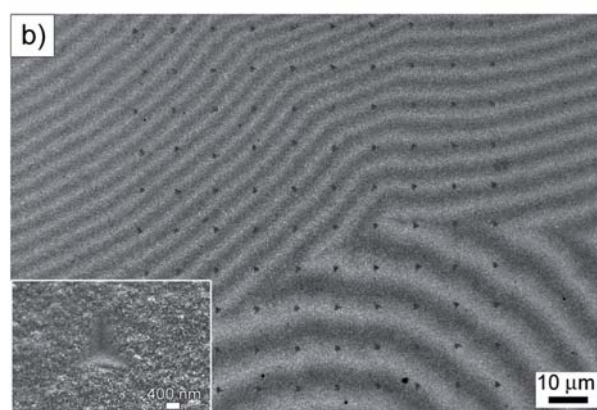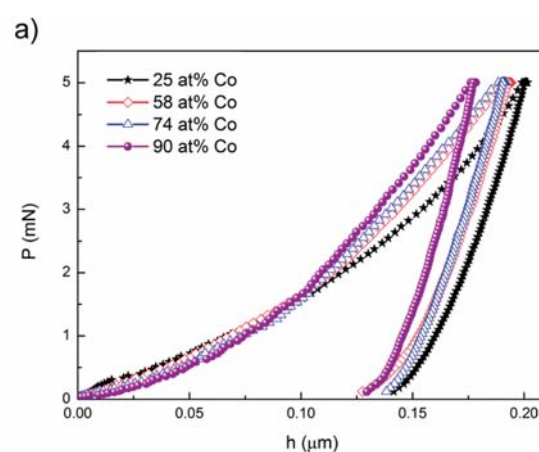
Fig. 9 (a) Load−unload nanoindentation curves performed on the surface of Co−In films with variable Co contents. (b) The SEM image showing an array of indentations performed on the surface of the Co−In film with 58 at% Co. The inset shows a magnified detail of an indent imprint.

area featuring spatio-temporal patterns (*i.e.*, not on the pattern-free areas which consists of almost pure In). The penetration depth at the end of the loading segment for this film is larger compared to the film with the highest Co content (90 at%). The values of hardness (H), reduced Young's modulus (E_r) and the H/E_r ratio are listed in Table 4. As expected, both H and E_r are slightly lower for the In-rich sample. Even if the indentation for this sample has been performed on the spatio-temporal patterns where $CoIn_3$ is thought to be the main component, the amount of pure In phase accompanying $CoIn_3$ is higher.

Table 4 Hardness (H), reduced Young's modulus (E_r) and H/E_r, W_e/W_t and W_p/W_t ratios for the Co−In films with the indicated Co contents

at% Co	H (GPa)	E_r (GPa)	H/E_r	W_e/W_t	W_p/W_t
25	6.2 ± 1.2	120.6 ± 13.8	0.05 ± 0.01	0.34 ± 0.03	0.66 ± 0.09
58	6.6 ± 1.1	128.4 ± 15.4	0.05 ± 0.01	0.33 ± 0.03	0.66 ± 0.09
74	6.9 ± 1.3	130.8 ± 16.3	0.05 ± 0.01	0.34 ± 0.03	0.66 ± 0.09
90	7.0 ± 1.6	151.3 ± 19.9	0.04 ± 0.01	0.30 ± 0.04	0.69 ± 0.14

41

Therefore, the obtained results make sense considering that In metal is recognized as a very ductile element due to its low Young's modulus.[29] In fact, a value of $E_r = 3.3$ GPa is obtained when the indentation is performed on the free-patterned area made of almost pure In. The film with 90 at% Co shows the largest H (7.00 GPa) and E_r (151.3 Ga). The H/E_r ratio, which provides an indirect estimation of the wear resistance of a coating,[30,31] is kept rather constant among all films. Similarly, the elastic recovery (W_e/W_t) and the ratio between the plastic and the total energy (W_p/W_t) are also similar for all coatings. Fig. 9b shows an array of indentations performed on the surface of the Co–In film with 58 at% Co. As can be seen in the figure, the lateral size of the indents is rather small (smaller than 0.5 μm, see the magnified detail of one indentation in the inset). No significant differences are observed in the size of the imprints as most of them do not indent only the dark or bright belts but lay in between.

3.6. Spatio-temporal pattern evolution with time

To gain a better understanding of the evolution of the spatio-temporal structures as a function of the deposition time (*i.e.*, the thickness), a new series of Co–In films was fabricated at a constant current density of −16 mA cm^{-2} for different deposition times (250–3000 s). Fig. 10A shows the E–t curve with dots labelled as (a–d) corresponding to each deposition time together with the average Co percentage. Fig. 10B shows secondary electron SEM images (left column) of a spiral together with the corresponding Co, In (and O) element distribution determined by EDX mapping analysis. The analysis reveals that the local distribution of Co (in red) and In (in green) elements within the spatio-temporal patterns is non-homogeneous and that such an effect is intensified with the deposition time. On comparing the SEM images of the coatings obtained through points (a–c) as indicated in the E–t curve, with the corresponding element mappings, one can observe that the Co signal is higher in the dark belt of the spiral whereas that of In is higher in the brighter belt. Furthermore, significant amounts of oxygen are detected in the films obtained for the longest deposition time (3000 s, point d of the E–t curve). The O signal is preferably detected in the In-rich belts, shown as black spots on the SEM image and in violet colour in the corresponding mapping, suggesting the incipient formation of oxide/hydroxide species in the In-rich belts of spatio-temporal patterns. Fig. 11 shows the XRD patterns of these films obtained at different deposition times. The relative intensity of both In and CoIn$_3$ reflections progressively increases with the deposition time. Concomitantly, the hcp- and fcc-Co reflections diminish in intensity. This result suggests that the volume fraction of In and CoIn$_3$ phases increases with the deposit thickness. The time-dependent magnetic and mechanical behaviours of these films are shown in Fig. S1 and Table S2,† respectively. Fig. 12 shows a cross-sectional image of the thickest film within this series, where a layer-by-layer growth type is evident. Due to the polishing procedure, the layers became separated from each other in some regions of the coating (Fig. 12a). The thickness of each layer is roughly around
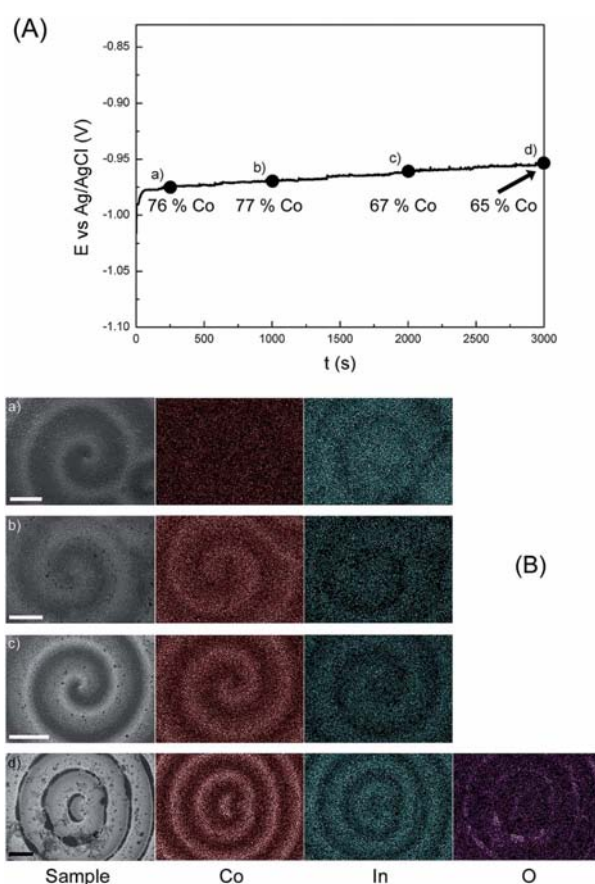

Fig. 10 (A) E–t transient for Co–In deposition onto the Au/Ti/Si substrate at a constant current density of −16 mA cm^{-2} and different deposition times: (a) 250 s, (b) 1000 s, (c) 2000 s and (d) 3000 s. (B) EDX mapping analysis of a region of the coating corresponding to the time-points (a–d) indicated in (A). Scale bars in (a and b) is 10 μm, 20 μm in (c) and 30 μm in (d).
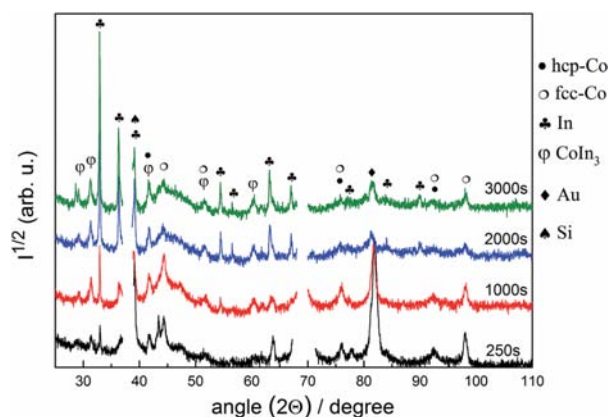

Fig. 11 XRD patterns of Co–In films obtained at −16 mA cm^{-2} for deposition times corresponding to the time-points (a–d) indicated in Fig. 10(A). Breaks in data around 37° and 69° were applied to avoid the most intense reflections from Au and Si, respectively, of the substrate.
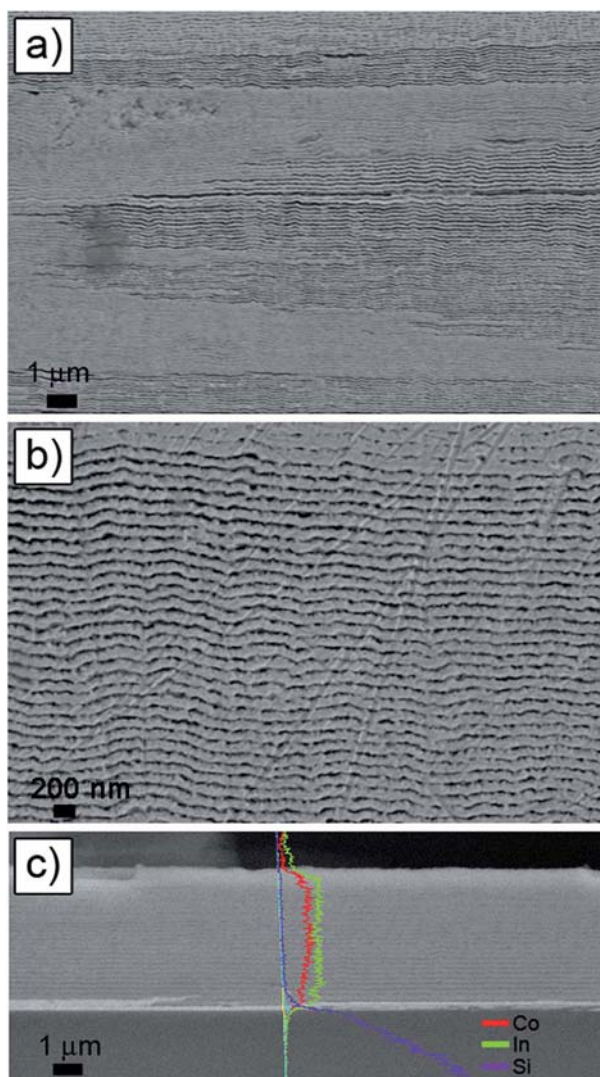
42

Fig. 12 Cross section of the Co–In film obtained at −16 mA cm^{-2} for 3000 s deposition time (a and b) SEM image, and (c) EDX line scan analysis.

properties as a function of the relative phase percentages and compositions. The films show soft ferromagnetic behaviour with in-plane coercivities between 75 and 275 Oe. Nano-indentation tests reveal that all samples exhibit a combination of large hardness with relatively high Young's modulus. It has been demonstrated by EDX mapping analyses that the dark and bright belts defined by the spatio-temporal structures are progressively enriched with Co and In, respectively, as the deposition time is increased. The occurrence of self-organization during electrodeposition renders a material featuring both topographical and magnetic micropatterning, which opens up new opportunities for Co–In films in magnetic applications such as sensors or encoders.

Acknowledgements

References

1 D. A. Egolf, I. V. Melnikov, W. Pesch and R. E. Ecke, *Nature*, 2000, **404**, 733–736.

2 M. Bestehorn and R. Friedrich, *Phys. Rev. E: Stat. Phys., Plasmas, Fluids, Relat. Interdiscip. Top.*, 1999, **59**, 2642–2652.

3 H. Kitahata and K. Yoshikawa, *J. Phys.: Condens. Matter*, 2005, **17**, S4239–S4248.

4 I. Krastev, T. Valkova and A. Zielonka, *J. Appl. Electrochem.*, 2004, **34**, 79–85.

5 T. Dobrovolska, D. A. López-Sauri, L. Veleva and I. Krastev, *Electrochim. Acta*, 2012, **79**, 162–169.

6 T. Dobrovolska, L. Veleva, I. Krastev and A. Zielonka, *J. Electrochem. Soc.*, 2005, **152**, C137–C142.

7 Y. Nagamine, O. Haruta and M. Hara, *Surf. Sci.*, 2005, **575**, 17–28.

8 I. Kristev and M. Nikolova, *J. Appl. Electrochem.*, 1986, **16**, 875–878.

9 M. A. Estrella Gutiérrez, T. Dobrovolska, D. A. López Sauri, L. Veleva and I. Krastev, *ECS Trans.*, 2011, **36**, 275–281.

10 B. Bozzini, D. Lacitignola and I. Sgura, *J. Solid State Electrochem.*, 2013, **17**, 467–479.

11 A. M. Turing, *Philos. Trans. R. Soc., B*, 1952, **237**, 37–72.

12 I. Krastev, T. Dobrovolska, U. Lačnjevac and S. Nineva, *J. Solid State Electrochem.*, 2012, **16**, 3449–3456.

13 L. J. Turbini and D. Bernier, *Handbook of lead-free solder technology for microelectronic assemblies*, ed. K. J. Puttlitz and K. A. Stalte, Marcel Dekker Inc., USA, 2004, p. 98.

14 X. C. Tong, *Advanced Materials for Thermal Management of Electronic Packaging*, Springer, New York, 2011, pp. 305–371.

15 Q. Huang, K. Reuter, S. Amhed, L. Deligianni, L. T. Romankiw, S. Jaime, P.-P. Grand and V. Charrier, *J. Electrochem. Soc.*, 2011, **158**, D57–D61.

16 A. M. Gabay and G. C. Hadjipanayis, *J. Alloys Compd.*, 2010, **500**, 161–166.

60 nm (Fig. 12b). The distribution of Co and In elements is kept rather constant throughout the deposit thickness (Fig. 12c) and within each nanolayer (Fig. S2†) in spite of using quiescent conditions during electrodeposition.

4. Conclusions

Heterogeneous Co–In films featuring spatio-temporal patterns have been electrodeposited by direct current on Au/Ti/Si substrates from a citrate–chloride bath. The applied current densities allow producing either In-rich films (25 at% Co) showing the incipient spatio-temporal organization on small areas of the coating or Co-rich films (58–90 at% Co) featuring spatio-temporal patterns on the entire surface. The films are composed of several phases (tetragonal In and CoIn$_3$, fcc-Co and hcp-Co) and exhibit tuneable magnetic and mechanical

43

17 T. Dietl, *Nat. Mater.*, 2010, **9**, 965–974.

18 J. P. Bros, M. Gaune-Escard, D. El Allam, R. Haddad and E. Hayer, *J. Alloys Compd.*, 1996, **233**, 264–271.

19 A. C. Fisher-Cripps, *Nanoindentation*, ed. F. F. Ling, Springer, New York, 2004.

20 W. C. Oliver and G. M. Pharr, *J. Mater. Res.*, 1992, **7**, 1564–1583.

21 I. Puigdomènech, *Medusa software*, http://www.kth.se/che/medusa.

22 Y. N. Sadana, A. E. Keskinen and M. Guindon, *Electrodeposition Surf. Treat.*, 1975, **3**, 149–157.

23 A. G. Muñoz, S. B. Saidman and J. B. Bessone, *J. Electrochem. Soc.*, 1999, **146**, 2123–2130.

24 W. Koster and E. Horn, *Z. Metallkd.*, 1952, **43**, 333–334.

25 I. Krastev and T. Dobrovolska, *J. Solid State Electrochem.*, 2013, **17**, 481–488.

26 T. Dobrovolska, G. Beck, I. Krastev and A. Zielonka, *J. Solid State Electrochem.*, 2008, **12**, 1461–1467.

27 R. Pöttgen, R.-D. Hoffmann and G. Kotzyba, *Z. Anorg. Allg. Chem.*, 1998, **624**, 244–250.

28 X.-P. Huang, Z.-L. Shi, M. Wang, M. Konoto, H.-S. Zhou, G.-B. Ma, D. Wu, R. Peng and N.-B. Ming, *Adv. Mater.*, 2010, **22**, 2711–2716.

29 H. Ledbetter, N. Sizova, S. Kim, H. Kobayashi, S. Sgobba and L. Parrini, *J. Phys. IV*, 1996, **C8**, 317–318.

30 A. Leyland and A. Matthews, *Wear*, 2000, **246**, 1–11.

31 E. Pellicer, A. Varea, S. Pané, B. J. Nelson, E. Menéndez, M. Estrader, S. Suriñach, M. D. Baró, J. Nogués and J. Sort, *Adv. Funct. Mater.*, 2010, **20**, 983–991.

This journal is © The Royal Society of Chemistry 2014

J. Mater. Chem. C, 2014, **2**, 8259–8269 | **8269**

44

Supporting Information

Self-organized spatio-temporal micropatterning in ferromagnetic Co-In films

Irati Golvano-Escobal, Berna Özkale, Santiago Suriñach, Maria Dolors Baró, Tsvetina Dobrovolska, Ivan Krastev, Salvador Pané[ξ], Jordi Sort[*] and Eva Pellicer[¥]

Table S1. List of peak positions, their assignation, and crystallite size calculated from the FWHM for each peak corresponding to the films with 25 and 78 at% Co.

	Peak position (°)	Assignation	FWHM (°)	$\langle D \rangle$ (nm)
25 at% Co	29.22	$CoIn_3$ (120)	0.326	25
	31.33	$CoIn_3$ (112)	0.325	25
	32.97	In (101)	0.123	67
	36.34	In (002)	0.146	57
	39.14	In (110) + Si	0.149	57
	41.78	$CoIn_3$ (130) + hcp-Co (100)	0.422	20
	51.59	$CoIn_3$ (004) + fcc-Co (200)	0.556	16
	54.47	In (112)	0.191	47
	56.55	In (200)	0.162	56
	60.37	$CoIn_3$ (124)+(240)	--	--
	63.24	In (103)	0.279	33
	67.05	In (211)	0.254	38
78 at% Co	29.22	$CoIn_3$ (120)	0.553	15
	31.34	$CoIn_3$ (112)	0.634	13
	32.95	In (101)	0.132	58
	36.30	In (002)	0.170	44
	39.12	In (110) + Si	n/f	n/f
	41.80	$CoIn_3$ (130) + hcp-Co (100)	0.658	13
	44.24	fcc-Co (111)	0.891	10
	51.50	$CoIn_3$ (004) + fcc-Co (200)	--	4
	54.48	In (112)	--	--
	60.40	$CoIn_3$ (124)+(240)	1.364	5
	75.97	hcp-Co (110) + fcc-Co(220)	1.412	4
	92.37	hcp-Co (112) + fcc-Co (311)	2.074	3
	98.02	fcc-Co (222)	0.658	8

Table S2. Hardness (H), reduced Young's modulus (E_r) and H/E_r, W_e/W_t and W_p/W_t ratios for the Co-In films electrodeposited with different depositions time at a constant value of current density of -16 mA cm^{-2}.

Deposition time	H (GPa)	E_r (GPa)	H/ E_r	W_e/W_t	W_p/W_t
250 s	4.6 ± 1.0	115.6 ± 14.4	0.04 ± 0.01	0.27 ± 0.03	0.72 ± 0.16
1000 s	5.8 ± 1.4	108.2 ± 26.1	0.05 ± 0.01	0.43 ± 0.3	0.56 ± 0.32
2000 s	5.9 ± 1.0	119.9 ± 13.0	0.07 ± 0.01	0.30 ± 0.04	0.69 ± 0.21
3000 s	6.1 ± 1.3	116.4 ± 16.9	0.05 ± 0.01	0.32 ± 0.07	0.67 ±0.33

2
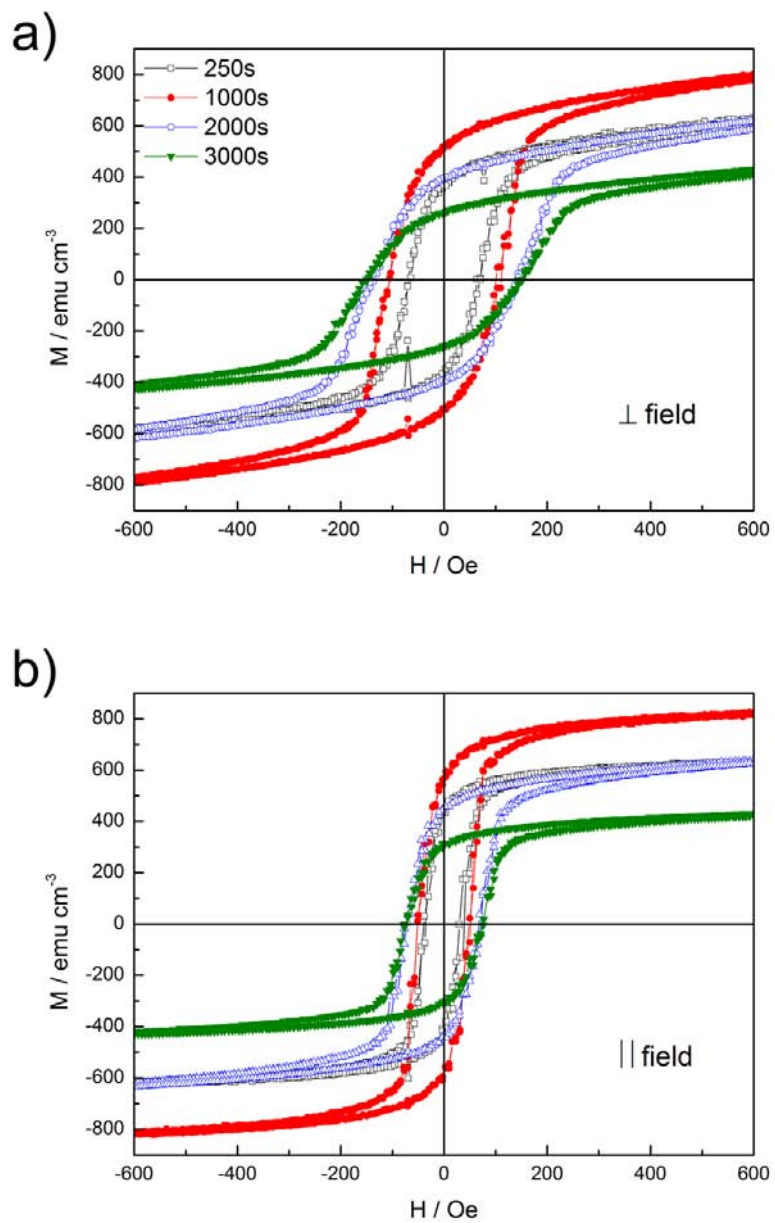
Figure S1. Room-temperature hysteresis loops of Co-In films obtained at −16 mA cm^{-2} for different deposition times measured in a) parallel and b) perpendicular configuration by VSM.

3
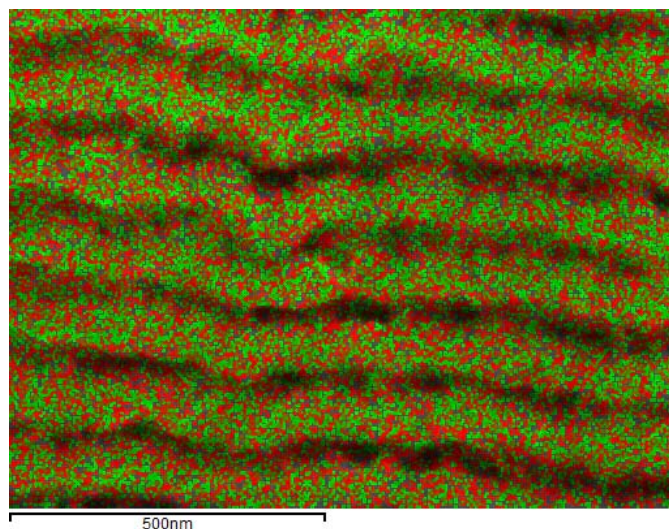
Figure S2. Mapping of the cross-section of Co-In film obtained at −16 mA cm^{-2} for 3000 s deposition time. Green spots: cobalt, red spots: indium.

4

3.1.2. Spontaneous formation of spiral-like patterns with distinct periodic physical properties by confined electrodeposition of Co-In disks

Irati Golvano-Escobal [1], Juan Carlos Gonzalez-Rosillo [2], Neus Domingo [3], Xavi Illa [4,5], José Francisco López-Barberá [1,3], Jordina Fornell [1], Pau Solsona [1], Lucia Aballe [6], Michael Foester [6], Santiago Suriñach [1], Maria Dolors Baró [1], Teresa Puig [2], Salvador Pané [7], Josep Nogués [3,8], Eva Pellicer [1,] and Jordi Sort [1,8,*]*

[1] Departament de Física, Universitat Autònoma de Barcelona, E-08193 Bellaterra, Spain.

[2] Institut de Ciència de Materials de Barcelona (ICMAB-CSIC), Campus UAB, E-08193 Bellaterra, Spain.

[3] Catalan Institute of Nanoscience and Nanotechnology (ICN2), CSIC and The Barcelona Institute of Science and Technology, Campus UAB, Bellaterra, E-08193 Barcelona, Spain.

[4] Institute of Microelectronics of Barcelona (IMB-CNM), Campus UAB, E-08193 Bellaterra, Spain.

[5] Biomedical Research Networking Center in Bioengineering, Biomaterials and Nanomedicine (CIBER-BBN), E-08193, Bellaterra, Spain.

[6] Alba Synchrotron Light Facility, CELLS, E-08280 Bellaterra, Spain.

[7] Institute of Robotics and Intelligent Systems (IRIS), ETH Zürich, CH-8092 Zürich, Switzerland.

[8] ICREA, Pg. Lluís Companys 23, 08010 Barcelona, Spain.

*To whom correspondence should be addressed:
Dr. Eva Pellicer, Prof. Jordi Sort
E-mail: Eva.Pellicer@uab.cat, Jordi.Sort@uab.cat

SCIENTIFIC REPORTS

Spontaneous formation of spiral-like patterns with distinct periodic physical properties by confined electrodeposition of Co-In disks

Irati Golvano-Escobal[1], Juan Carlos Gonzalez-Rosillo[2], Neus Domingo[3], Xavi Illa[4,5], José Francisco López-Barberá[1,3], Jordina Fornell[1], Pau Solsona[1], Lucia Aballe[6], Michael Foerster[6], Santiago Suriñach[1], Maria Dolors Baró[1], Teresa Puig[2], Salvador Pané[7], Josep Nogués[3,8], Eva Pellicer[1] & Jordi Sort[1,8]

Spatio-temporal patterns are ubiquitous in different areas of materials science and biological systems. However, typically the motifs in these types of systems present a random distribution with many possible different structures. Herein, we demonstrate that controlled spatio-temporal patterns, with reproducible spiral-like shapes, can be obtained by electrodeposition of Co-In alloys inside a confined circular geometry (i.e., in disks that are commensurate with the typical size of the spatio-temporal features). These patterns are mainly of compositional nature, i.e., with virtually no topographic features. Interestingly, the local changes in composition lead to a periodic modulation of the physical (electric, magnetic and mechanical) properties. Namely, the Co-rich areas show higher saturation magnetization and electrical conductivity and are mechanically harder than the In-rich ones. Thus, this work reveals that confined electrodeposition of this binary system constitutes an effective procedure to attain template-free magnetic, electric and mechanical surface patterning with specific and reproducible shapes.

The continuous progress in diverse areas of micro/nanotechnology relies on the ability to implement novel methods to create pre-defined patterned geometries at the surface of materials, with an ever-increasing resolution, using cost-effective, industrially-scalable methods. For this reason, lithographic techniques remain as core tools in the fields of electronics, photonics, microfluidics, or magnetic recording, among others[1–7].

Surface patterning processes can be divided into two main categories[7]: (1) template/mask-assisted patterning and (2) mask-less pattern formation. Template-assisted patterning usually requires multiple processing steps: (i) creation of the templates or masks using, for example, electron beam or photolithography, (ii) thin film deposition through sputtering, electrodeposition or other methods, and (iii) physical or chemical etching of the mask to release or reveal the synthesized micro- or nanostructures. This multi-step procedure is often costly and complex as it requires the use of clean room facilities and sophisticated experimental equipments. Moreover, different masks need to be designed each time one needs to prepare a different patterned arrangement.

Concerning mask-less patterning techniques, one can distinguish between methods in which each patterned structure is generated individually in an in-series sequence (e.g., nanoindentation[8], dip-pen nanolithography[9], laser patterning[10], focused ion beam irradiation[11], etc.) and methods in which periodic patterns are generated spontaneously at once (e.g., spatio-temporal pattern formation in some electrodeposited binary systems[12],

[1]Departament de Física, Universitat Autònoma de Barcelona, E-08193 Bellaterra, Spain. [2]Institut de Ciència de Materials de Barcelona (ICMAB-CSIC), Campus UAB, E-08193 Bellaterra, Spain. [3]Catalan Institute of Nanoscience and Nanotechnology (ICN2), CSIC and The Barcelona Institute of Science and Technology, Campus UAB, Bellaterra, E-08193 Barcelona, Spain. [4]Institute of Microelectronics of Barcelona (IMB-CNM), Campus UAB, E-08193 Bellaterra, Spain. [5]Biomedical Research Networking Center in Bioengineering, Biomaterials and Nanomedicine (CIBER-BBN), E-08193, Bellaterra, Spain. [6]Alba Synchrotron Light Facility, CELLS, E-08280 Bellaterra, Spain. [7]Institute of Robotics and Intelligent Systems (IRIS), ETH Zürich, CH-8092 Zürich, Switzerland. [8]ICREA, Pg. Lluís Companys 23, 08010 Barcelona, Spain. Correspondence and requests for materials should be addressed to E.P. (email: eva.pellicer@uab.cat) or J.S. (email: jordi.sort@uab.cat)

self-assembly of block-copolymers[13], anodization[14], maze-like magnetic domains in films with perpendicular magnetic anisotropy[15], self-assembled strain driven chemical solution derived nanostructures[16], etc.). Compared to the in-series generation of individual patterned elements, the spontaneous formation of self-organized arrangements is much faster and offers the possibility of easily patterning large surface areas. Yet, precise control of self-organized patterning to obtain reproducible specific shapes or periodic arrays of structures with long-range order remains a challenging issue.

Spatio-temporal pattern formation is a topic not restricted to materials science. Actually, this phenomenon occurs frequently in nature, in open systems far from equilibrium, for example in the environment (atmosphere and oceans), in the skin of some animals (like in zebras or giraffes), in atrial fibrillation, in geophysical systems, etc. Spatio-temporal patterns are related to chaos and their study is applicable to a wide range of disciplines, such as crime analysis[17], demography and epidemiology[18], cell proliferation and tissue engineering[19] and, of course, statistics and mathematics[20].

Formation of spatio-temporal patterns in nature can stem from either a flux of energy or a flux of matter, e.g. originated from the flow of fluids or chemicals in a reactor. The latter is responsible for the emergence of spatio-temporal patterns during the electrodeposition of some binary systems, like Ag-Bi, Ag-Cd, Ag-In, Ag-Sb or Co-In[12,21–27], leading to different areas having dissimilar local composition. Although the mechanism for spatio-temporal patterning during electrodeposition has not been fully elucidated yet, a variety of factors, such as the electrolyte hydrodynamic conditions, the overpotential, the enthalpy of mixing, kinetic variables and the appearance of Turing instabilities in reaction-diffusion systems seem to play a synergetic role on this phenomenon[12,28]. Archetypical morphologies observed in these electroplated materials include 'labyrinths', 'waves', 'targets', spirals, broken spirals and mixed patterns[12]. Unfortunately, since non-linearity and chaos are at the heart of spatio-temporal pattern formation, it is often difficult to control the shapes of the generated structures in electrodeposited continuous films, although some studies have reported certain variations of the pattern geometry depending on the film's composition, thickness and electrodeposition conditions[12].

Compared to the Ag-based alloys series, the electrodeposition of Co-In alloys has been far less explored. Pattern formation under both stagnant and high-speed electrodeposition from electrolytes containing sulphate metal salts and di-ammonium hydrogen citrate at pH around 3 has been well-established by Krastev *et al.*[27]. Typically, spatio-temporal structures form at sufficiently negative applied current densities (large Co contents). Since In and Co are immiscible in both solid and liquid states[29], the formation of multi-phase coatings is indeed anticipated. Remarkably, we have recently demonstrated that topographic and compositional spatio-temporal patterning in electrodeposited Co-In films induces a concomitant periodic change of the surface physical properties[26]. That is, compositional patterning in this system is accompanied by magnetic and mechanical micropatterning over large surface areas. This is of significant practical importance since it can be used as a mask-less or template-free inexpensive technique to achieve magnetic/mechanical surface patterning.

In the particular case of magnetic properties, adjustable lateral compositional modulation can lead not only to a range of interesting fundamental magnetic properties (e.g., domain wall manipulation[30–33]), but also to appealing potential applications such as lateral giant magnetoresistance sensors[34], magnetic remote motion control of nanoscale magnetic nanoparticles through microfluidic structures along specific stray field tracks[35,36], magnetic biosensors[37], magnetic encoders (e.g., for biomedical applications)[38,39] or possible 3D-magnetic states when combined with multilayers[40]. However, any exploitation of spatio-temporal patterning for devices necessarily relies on the ability to control the shapes of the generated motifs.

In this work, we demonstrate that the generation of patterns by spatio-temporal self-organization can be controlled by electrodeposition in confined areas, i.e., disks commensurate with the typical size of the spatio-temporal features. The idea is to use the edges of these disks as a guide for the formation of spiral-like spatio-temporal patterns. The procedure is to some extent analogous to "directed self-assembly" in block copolymers in which aligned lamellas form inside pre-defined stripes[41–43]. When grown as micrometer-sized circular disks, Co-In alloys develop clear spiral patterns with Co-rich and In-rich areas. This compositional patterning leads to patterning of the physical (magnetic, electrical and mechanical) properties, which locally vary also following the spiral-like geometries.

Results

Morphological and compositional analysis. Figure 1a shows a field emission scanning electron microscopy (FE-SEM) image of an array of electrodeposited Co-In microdisks using an In-Lens detector, which is sensitive to differences in the work function (i.e., electronic variations). A spiral-like pattern at the surface of each disk can be observed, although the exact shape of the spirals varies somewhat from one disk to the other. Figure 1b,c show the details of a single microdisk imaged using the secondary electrons (SE) and the In-Lens detectors, respectively. Remarkably, the spiral-like pattern is only revealed when using the In-Lens detector, not with the SE detector. Besides gathering information on morphology and surface topography of specimens, the In-Lens detector reveals differences in composition. On the contrary, topographic information predominates in any image recorded using the conventional SE detector. This indicates that the contrast in (a) and (c) is mainly due to the local changes in composition (i.e., Co/In stoichiometry) and distantly related to topographic variations (e.g., surface corrugation). This is in contrast to Co-In films, for which the surface spatio-temporal patterns were found to be linked to both topographical and compositional variations[26]. Since the films were several microns thick, probably the spatio-temporal topographic features had sufficient space to build up. Conversely, since microdisks are only 1 μm thick (the maximum thickness of the disks cannot be larger than the thickness of the resist used in the optical lithography), the deposition time is likely not sufficiently long for the spirals to fully develop. As a result, the typical periodic topographical features observed in continuous thick Co-In films are not visible in the disks. Nonetheless, the SE and atomic force microscopy (AFM) images indicate that the microdisks are not completely flat. Actually, they are slightly thicker toward the edges (see Fig. 1b). This can be explained by a non-uniform
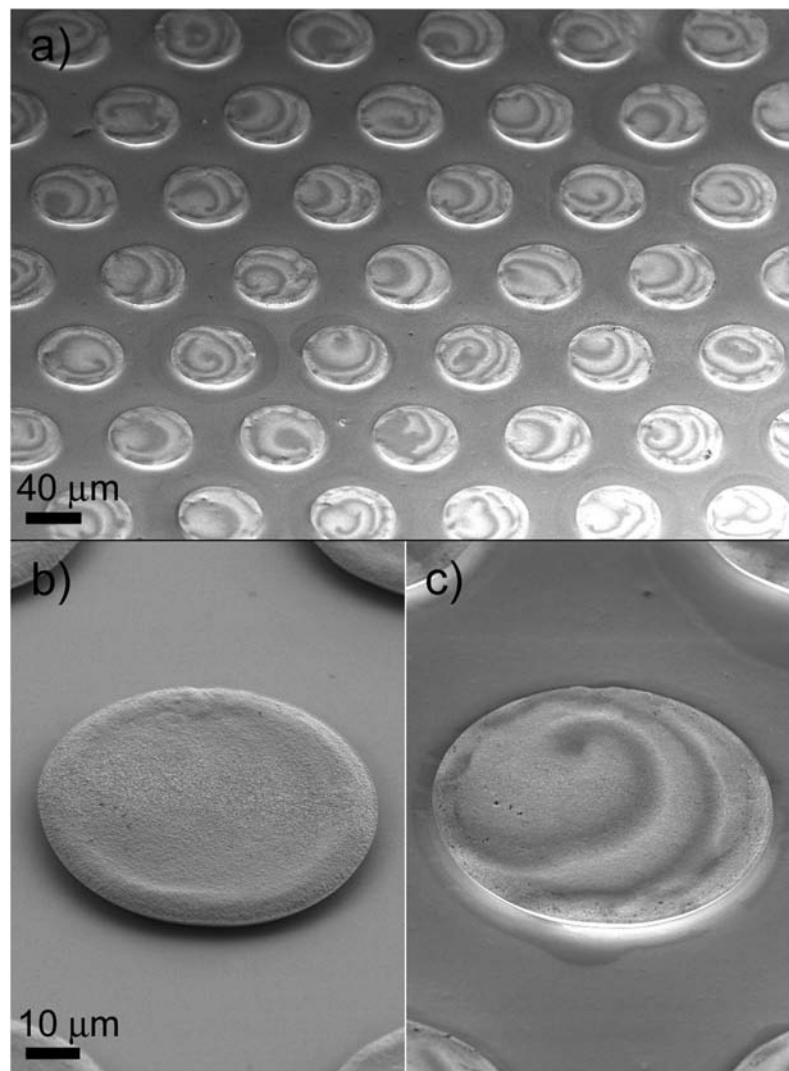
Figure 1. FE-SEM images of (**a**) an array of Co–In microdisks (taken with In-Lens detector), (**b**) detail of one microdisk taken with SE detector and (**c**) corresponding image obtained using the In-Lens detector.

distribution of the current density at the cylindrical cavities. Current density is typically higher at the edges, hence resulting in faster deposition rates[44]. However, it is clear that the strong contrast observed in Fig. 1a mainly stems from the differences in composition between the light and dark grey regions and it is not dominated by the surface topography.

The exact elemental composition of the Co-In microstructures was determined by energy dispersive X-ray spectroscopy (EDX) in the SEM. The overall composition of the disks is 78 ± 1 at% Co and 22 ± 1 at% In, which is in accordance with previous works on Co-In films electrodeposited at $j = -20\,\text{mA}\,\text{cm}^{-2}$ for $1000\,\text{s}^{26}$. The EDX mapping of the microdisks reveals that Co is not homogeneously distributed, but it follows the spiral-like pattern as previously observed by the SEM In-Lens detector imaging (Fig. 1). In particular, the darker areas in the In-Lens image are enriched in Co (Fig. 2b). On the other hand, the In distribution does not follow any obvious 'complementary' pattern to the Co one, but it rather seems that the In content increases toward the periphery of the disk (Fig. 2c). Thus, the compositional spiral pattern indicates a modulation of the Co content.

Remarkably, unlike the spatio-temporal patterns spontaneously formed over large areas, which typically show a mixture of spirals, targets and waves[12,26], electrodeposition of Co-In in confined areas lead to a preferential pattern shape, i.e., spirals in the case of disks. This spontaneous self-assembled chemical patterning should be related to the lateral constraint imposed by the cylindrical micron sized cavities. However, to optimize the pattern control the size of the confined electrodeposition space needs to be commensurate with the size of typical features of the spatio-temporal patterning (which depend on the type of alloy and its composition). For example, in $Co_{78}In_{22}$ films the size of the typical topographic-compositional motifs is of a few microns[26]. Thus, the size of the constraint growth area should tentatively be of tens of microns. The guided process for pattern formation with
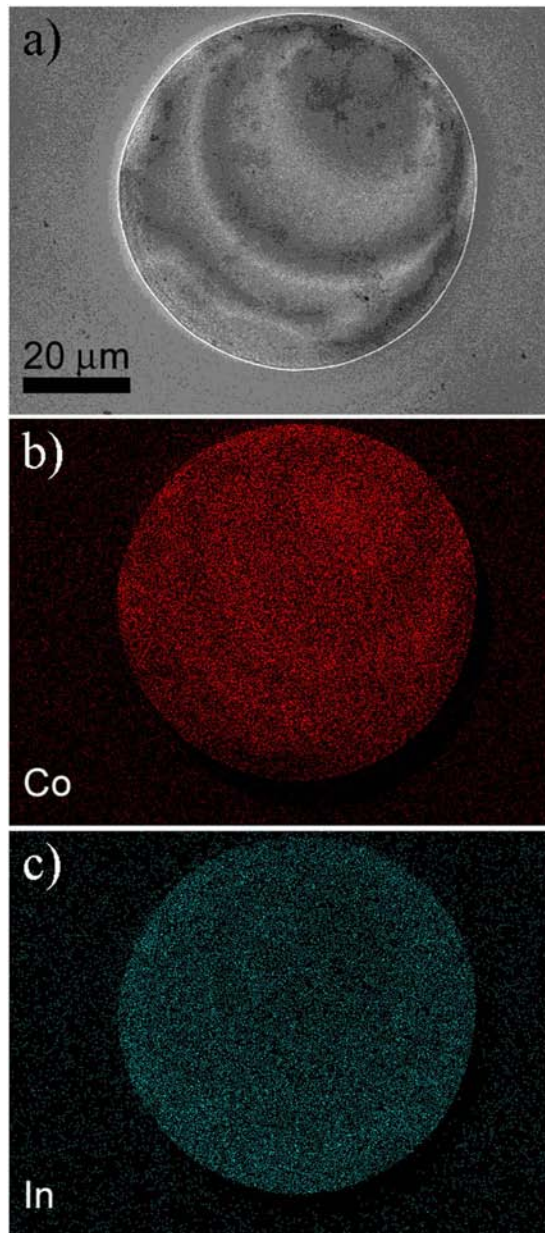
Figure 2. EDX mapping of a Co–In microdisk.

controlled geometry could be thought to be conceptually analogous to the so-called "directed self-assembly" in block copolymers to form aligned lamellas inside pre-defined stripes[41–43].

The modulated Co/In composition should result in distinct local physico-chemical properties. Thus, the electrical, magnetic and nanomechanical behavior, as well as the surface potential of the microdisks, were further explored.

Electrical characterization. Conductive atomic force microscopy (C-AFM) measurements using a bias voltage of 500 mN confirmed the presence of two different conductive domains, as shown in Fig. 3, being the current ratio between the bright (Co-rich) and dark (In-rich) regions about 100–10. These domains are not directly correlated to the surface topology (compare Fig. 3a,b) but to the aforementioned compositional variations. The occurrence of these domains with such large variation in conductivity cannot be simply explained based on the dissimilar electrical resistivity values for bulk Co ($6.2 \mu\Omega$ cm at $20\,°C$)[45] and bulk In ($8.8 \mu\Omega$ cm at $20\,°C$)[46]. In fact, X-ray diffraction analyses of continuous films indicated the co-existence of several phases: tetragonal In, face-centered cubic Co, hexagonal close-packed Co, tetragonal $CoIn_3$ and even an amorphous fraction in the deposits[26]. It has been argued that the formation of the intermetallic $CoIn_3$ phase is the key toward the

53
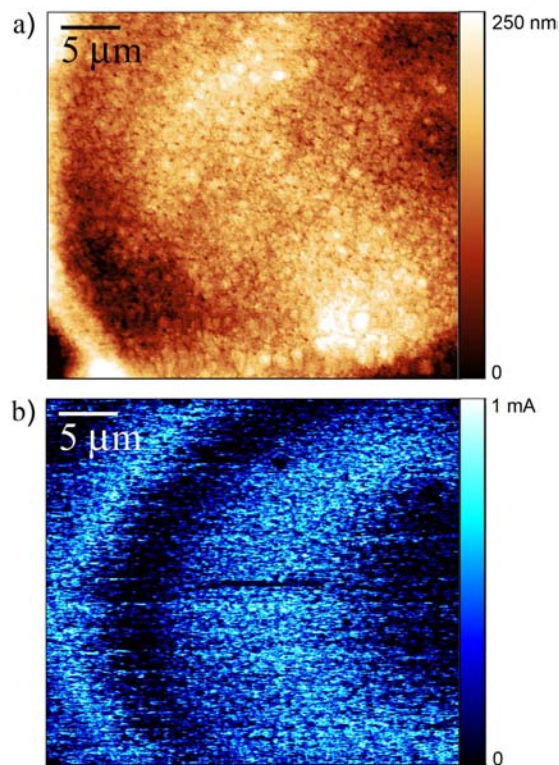
Figure 3. (**a**) AFM topographical and (**b**) current map image taken with the C-AFM under a constant applied load of 50 nN on 35×31 μm^2 scanned area of a Co-In microdisk.

formation of spatio-temporal features in this type of deposits[47]. Although no data on the electrical conductivity/resistance is available for $CoIn_3$ phase, it is known that intermetallic phases possess much higher electrical resistance than their pure constituents[48]. Therefore, it can be argued that the accumulation of $CoIn_3$ at certain areas could contribute to the presence of the markedly low current domains (i.e., dark blue regions in Fig. 2b). Note that while Fig. 3a shows the topography of the disk at the surface, the current map image (Fig. 3b) is obtained from the contribution of the overall thickness of the disk to the electrical resistivity. Hence, a one-to-one coincidence between the two images should not necessarily be anticipated.

Magnetic behavior. The local magnetic properties of individual Co-In microdisks were measured by magneto-optic Kerr effect (MOKE) in polar (out-of-plane) configuration at room temperature. The surface of the disk was probed every 5 μm along its diameter with a laser spot of 3 μm. Hysteresis loops were recorded at each location in order to reveal possible variations in the saturation magnetization (M_S) and/or the coercivity (H_C) (Fig. 4). Results show that the Co-rich regions exhibit a higher Kerr effect amplitude, which can be considered proportional to M_S. Actually, M_S periodically varies as the Co-rich and the Co-depleted regions are being scanned by the laser, hence indicating an obvious 'magnetic micro-patterning'. In addition, H_C shows values ranging between 200 to 400 Oe. The correlation between H_C and the composition is less obvious than that of M_S, probably because H_C depends not only on the Co content but also on other microstructural parameters (crystallographic phases, grain sizes, microstrains, etc.) which play a role on the propagation of domain walls and on the overall magnetization reversal process. Nonetheless, the H_C values of the microdisks are considerably higher than those of films featuring analogous composition ($H_{C\perp} = 136$ Oe)[26]. This increase in H_C compared to the unpatterned film is possibly due to domain wall hindrances caused by the constrained lateral size of the dots and their reduced thickness[7,49,50].

The occurrence of a 'magnetic micro-patterning' was further studied by magnetic force microscopy (MFM) at remanence after having saturated the sample in the in-plane direction applying a magnetic field of 10 kOe. Figure 5 shows a comparison of the topography, SEM compositional contrast and different AFM modes corresponding to the same Co-In disk. The MFM image in Fig. 5c shows a clear magnetic contrast, stemming from the strength of the stray fields over the different scanned areas, which should be proportional to the magnetization. The results are in accordance with MOKE measurements. Namely, the spiral-like pattern is clearly disclosed, in which regions of higher M_S are alternated with regions of lower M_S in a helicoidal fashion.

Additional evidence for the magnetic micro-patterning can be obtained from X-ray photoemission electron microscopy (PEEM), which is both element-specific and sensitive to the magnetization direction[51]. The X-ray absorption spectroscopy (XAS)-PEEM image at the Co L_3 edge (Fig. 6a) shows the expected compositional pattern, in agreement with the SEM In-Lens and EDX characterization.
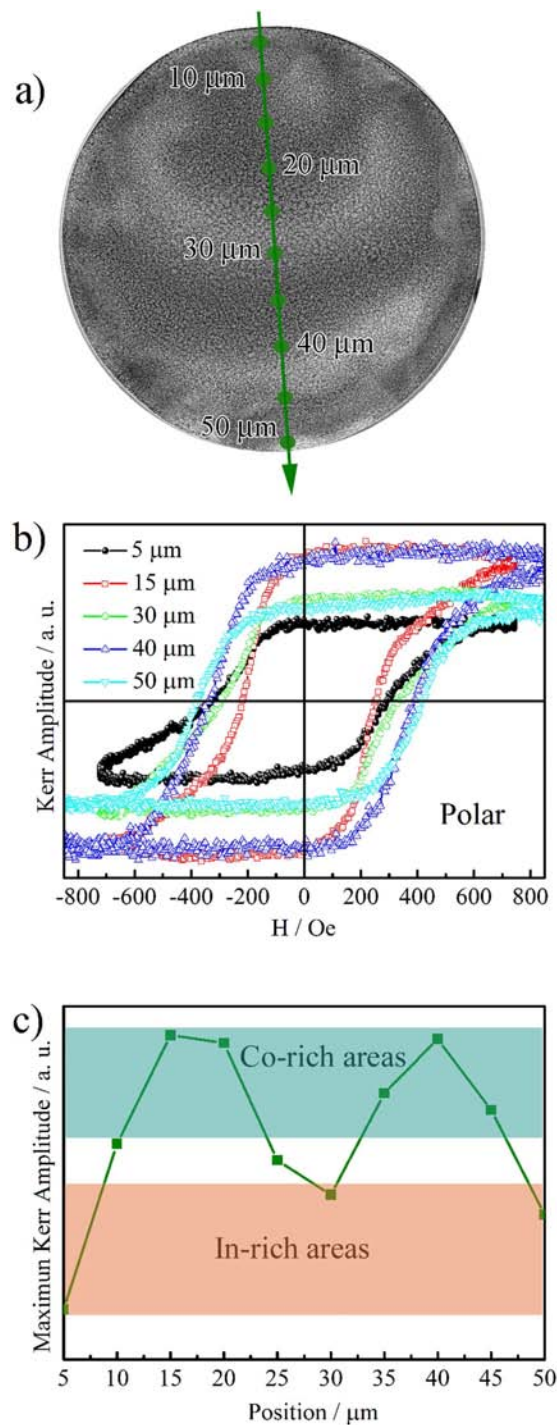
Figure 4. (**a**) In-Lens SEM image of a Co-In microdisk showing the positions onto which the MOKE laser was focused. (**b**) Polar (out-of-plane) room-temperature MOKE magnetic hysteresis loops for different positions across the diameter of the disk. (**c**) Dependence of the maximum Kerr amplitude as a function of position.

The X-ray magnetic circular dichroism (XMCD)-PEEM image at the same edge, also displays a spiral-like pattern. At remanence (after having applied a in-plane magnetic field of 650 Oe), the Co-rich areas show a majority of domains (either black or white) pointing along the previous saturation field, which has opposite sign for Fig. 6b,c. In both images there are small reverse domains (small dots or stripes) within the majority, which are most likely formed during the relaxation from saturation to remanence. Some of these reverse domains are exactly at the same position in both images indicating that they are most likely pinned to structurally or compositionally different seed areas. Furthermore, a few domains are not reversed between the two images, suggesting
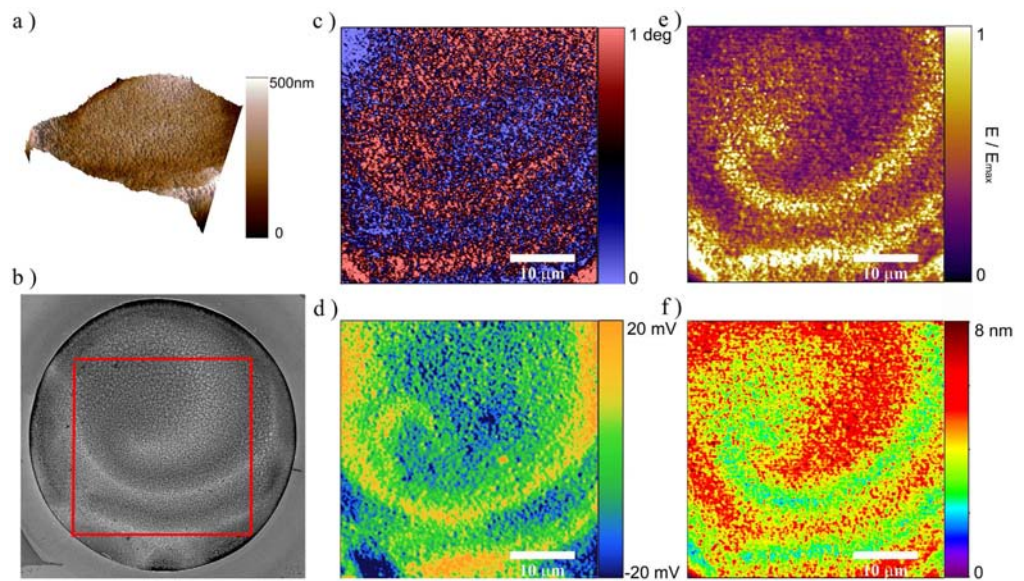
Figure 5. (**a**) AFM topography and (**b**) In-Lens SEM image of the Co-In microdisk. (**c**) MFM image at remanence after saturation at 1 T in plane. The image was taken in double pass mode, by scanning at a lift height of 30 nm with the same amplitude of oscillation as that used as setpoint for topography. Mapping of (**d**) work function acquired by KPFM using a tip voltage of 1 V, (**e**) normalized Young's modulus and, (**f**) penetration depth (in nm) measured in AM-FM viscoelastic mapping mode.
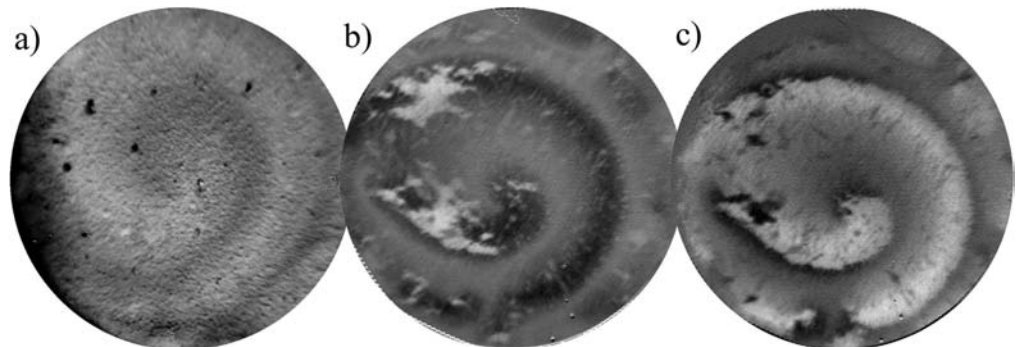
Figure 6. (**a**) XAS-PEEM (elemental map) and (**b,c**) XMCD-PEEM images at the Co L-edge. (**b,c**) are measured in remanence after applying a saturating field (650 Oe) in the (**b**) positive ($+M_R$) and (**c**) negative ($-M_R$) in-plane direction.

that there are some magnetically hard regions, which cannot be switched by the applied in-plane field (± 650 Oe). The PEEM observations corroborate the magnetic micro-patterning observed by MOKE and MFM. In addition, the correlation between the composition and magnetic properties becomes also evident when comparing the XAS with the XMCD PEEM images. Remarkably, the various magnetic techniques used in this study have different probing depths and lateral resolutions: PEEM (5 nm/100 nm), MOKE (20–30 nm/3 μm) and MFM (stray fields/50–100 nm). Hence, they provide complementary information and evidence that a net magnetic patterning probably extends from the surface down to several hundred nm.

Local compositional analysis by work-function and nanomechanical characterization. The work-function of a Co-In microdisk was mapped by Kelvin probe force microscopy (KPFM) and the images are shown in Fig. 5, together with AFM and MFM images recorded on exactly the same area (and the same dot). Since, Co and In have different work-functions (W(Co) = 5 eV and W(In) = 4.09 eV), changes in the KPFM images can be anticipated. Thus, the image in Fig. 5d corroborates the already assessed local modulation of the composition (Figs 1c and 2). Indeed, as for the other properties, the work function mapping is able to perfectly reconstruct the spiral-like pattern (Fig. 5d), confirming the EDX and In-Lens imaging results.

Finally, the mapping of the Young's modulus, E, obtained from amplitude modulation - frequency modulation (AM-FM) viscoelastic mapping in the same area (Fig. 5e) shows a clear contrast with spiral-like symmetry,

where the Co-rich areas correspond to the lighter color (yellowish), which indicate higher Young's modulus. Similar trends were observed for the penetration depth AFM map (Fig. 5f). The results indicate that the Co-rich areas are mechanically harder (larger E and smaller penetration) than the In-rich ones, in agreement to what has been found in thin films by nanoindentation[26]. Owing to the different mechanical properties of hcp/fcc-Co (with average Young's modulus around 210 GPa in non-porous bulk form ref. 52), and In (Young's modulus around 12.5 GPa[53]), the chemical patterning on the surface of the microdisks can explain the variations in the elastic modulus (Fig. 5e) and indentation depth (Fig. 5f), even if the exact distribution of the crystallographic phases within the patterns is not clear at present. Namely, even if the nanomechanical properties in In-rich regions could be influenced by the presence of intermetallic $CoIn_3$ (presumably with a relatively high Young's modulus), the amount of pure In phase accompanying $CoIn_3$ is likely higher in these regions[26]. Moreover, similar to the magnetic properties, there is an evident one-to-one correlation between the composition (work function) and mechanical properties.

Discussion

In conclusion, we have demonstrated that the morphology of spatio-temporal patterns in electrodeposited Co-In alloys can be adjusted by confining their growth. When electrodepositing in arrays of circular cavities of $50\,\mu$m in diameter, Co-In microdisks with spiral-like compositional variations are obtained. The local changes in composition lead to a periodic modulation of the physical (electric, magnetic and mechanical) properties, with a univocal correlation between composition and the resulting properties. The Co-rich areas are mechanically harder, more electrically conducting and exhibit higher saturation magnetization than the In-rich ones. The ability to control the pattern formation in spatio-temporal systems by confined growth may not only pave the way to possible new applications of electrodeposited alloys (e.g., encoders or magnonic crystals), but it may also open new research avenues in the many disciplines in which spatio-temporal patterns play an important role (e.g., biology, medicine or even social behavior).

Methods

Electrodeposition of Co-In was performed onto pre-lithographed Si (111) substrates with evaporated Ti (100 nm)/ Au (400 nm) adhesion/seed layers. Arrays of cylindrical holes of $50\,\mu$m in diameter and $1\,\mu$m in height were first patterned by photolithography using AZ-9260 photoresist and AZ-400K developer. The patterned area was used as a mask for the subsequent electrodeposition of the Co-In microdisks. A one-compartment thermostatized three-electrode cell connected to a PGSTAT302N Autolab potentiostat/galvanostat (Ecochemie) was employed. Deposition was conducted potentiostatically at -0.98 V in an electrolyte containing 0.05 M $InCl_3 + 0.25$ M $CoCl_2 + 0.05$ M $C_6H_5Na_3O_7 \cdot 2H_2O + 0.1$ M KCl. Bath temperature was kept at 25 °C. The electrolyte was prepared from analytical grade reagents and Milipore Milli-Q water (18 MΩcm). A representative current-time curve is shown in the S.I. The morphology and the composition of the Co-In microdisks were studied on a Zeiss Merlin FE-SEM equipped with an EDX detector. Room-temperature magnetic hysteresis loops were recorded using a MOKE setup (Durham Magneto Optics) with a maximum field of 800 Oe, applied out-of-plane (polar configuration). Note that to measure the local magnetic properties, the MOKE laser spot was focused down to $3\,\mu$m onto different regions of the Co-In microdisks. C-AFM measurements were performed with a commercial AFM (Agilent 5500LS) operating in contact mode with a commercial tip from AppNano (DD-SICONA) and with k = 0.2 N/m. A bias voltage of $V_{bias} = 500$ mV was applied to the sample while the tip was grounded. An Asylum AFM (MFP3D) operated in two different modes was used for the nanomechanical and magnetic characterization and surface potential function mapping. AM-FM viscoelastic mapping was used for the nanomechanical characterization. In this mode the cantilever is driven simultaneously at two excitation signals that are combined to excite the fundamental and second cantilever resonances. While the topography is recorded in normal AM mode at the fundamental resonance, the second resonance frequency is driven in FM, and the measured changes in frequency and dissipation of this resonance are correlated to loss tangent, sample stiffness and elasticity, and viscous behavior or dissipation. To map the different surface potential function, KPFM mode was used. Finally, to visualize the magnetic domains, a MFM study was performed in a dual-scan mode using a magnetized tip (Nanosensors MFMR tip with k = 2 N/m and a CoCr coating of 35 nm). Finally, compositional (XAS) and magnetic contrast imaging (XMCD) using element-specific polarized XPEEM experiments were carried out in beamline BL24 – CIRCE at the ALBA Synchrotron[54]. To construct the chemical or magnetic element-specific figures two images taken with opposite photon helicity are either added or subtracted pixel-by-pixel, respectively.

References

1. Kempa, T. J., Bediako, D. K., Kim, S.-K., Park, H.-G. & Nocera, D. G. High-throughput patterning of photonic structures with tunable periodicity. *Proc. Natl. Acad. Sci. USA* **112,** 5309–5313 (2015).
2. Cui, S. *et al.* Hybrid plasmonic photonic crystal cavity for enhancing emission from near-surface nitrogen vacancy centers in diamond. *ACS Photonics* **2,** 465–469 (2015).
3. Zhou, X., Boey, F., Huo, F., Huang, L. & Zhang, H. Chemically functionalized surface patterning. *Small* **7,** 2273–2289 (2011).
4. Chen, Y. Nanofabrication by electron beam lithography and its applications: A review. *Microelectron. Eng.* **135,** 57–72 (2015).
5. Vazquez-Mena, O. *et al.* Resistless nanofabrication by stencil lithography: A review. *Microelectron. Eng.* **132,** 236–254 (2015).
6. Betancourt, T. & Brannon-Peppas, L. Micro- and nanofabrication methods in nanotechnological medical and pharmaceutical devices. *Int. J. Nanomed.* **1,** 483–495 (2006).
7. Martin, J. I. *et al.* Ordered magnetic nanostructures: fabrication and properties. *J. Magn. Magn. Mater.* **256,** 449–501 (2003).
8. Sort, J. *et al.* Out-of-plane magnetic patterning based on indentation-induced nanocrystallization of a metallic glass. *Small* **6,** 1543–1549 (2010).
9. Salaita, K., Wang, Y. & Mirkin, C. A. Applications of dip-pen nanolithography. *Nat. Nanotechnol.* **2,** 145–155 (2007).
10. Sato, R., Benino, Y., Fujiwara, T. & Komatsu, T. Yag laser-induced crystalline dot patterning in samarium tellurite glasses. *J. Non-cryst. Solids* **289,** 228–232 (2001).
11. Menéndez, E. *et al.* Direct magnetic patterning due to the generation of ferromagnetism by selective ion irradiation of paramagnetic feal alloys. *Small* **5,** 229–234 (2009).

12. Bozzini, B., Lacitignola, D. & Sgura, I. Spatio-temporal organization in alloy electrodeposition: a morphochemical mathematical model and its experimental validation. *J. Sol. State Electrochem.* **17,** 467–479 (2013).
13. Park, C., Yoon, J. & Thomas, E. L. Enabling nanotechnology with self assembled block copolymer patterns. *Polymer* **44,** 6725–6760 (2003).
14. Fornell, J. *et al.* Anodic formation of self-organized Ti(Nb,Sn) oxide nanotube arrays with tuneable aspect ratio and size distribution. *J. Electrochem. Comm.* **33,** 84–87 (2013).
15. Brück, S. *et al.* Exploiting length scales of exchange-bias systems to fully tailor double-shifted hysteresis loops. *Adv. Mater.* **17,** 2978–2983 (2005).
16. Obradors, X. *et al.* Chemical solution route to self-assembled epitaxial oxide nanostructures. *Chem. Soc. Rev.* **43,** 2200–2225 (2014).
17. Ratcliffe, J. H. Aoristic signatures and the temporal analysis of high volume crime patterns. *J. Quant. Criminol.* **18,** 23–43 (2002).
18. Liu, C. *et al.* Sequential establishment of stripe patterns in an expanding cell population. *Science* **334,** 238–241 (2011).
19. Puliafito, A. *et al.* Collective and single cell behavior in epithelial contact inhibition. *Proc. Natl. Acad. Sci. USA* **109,** 739–744 (2012).
20. Cressie, N. & Wikle, C. K. In *Statistics for Spatio-Temporal Data* (Wiley, 2011).
21. Krastev, I., Valkova, T. & Zielonka, A. Structure and properties of electrodeposited silver–bismuth alloys. *J. Appl. Electrochem.* **34,** 79–85 (2004).
22. Dobrovolska, T., Veleva, L., Krastev, I. & Zielonka, A. Composition and structure of silver-indium alloy coatings electrodeposited from cyanide electrolytes. *J. Electrochem. Soc.* **152,** C137–C142 (2005).
23. S. Nagamine, Y., Haruta, O. & Hara, M. Morphology of spatiotemporal stripe patterns formed by Ag/Sb co electrodeposition. *Surf. Sci.* **575,** 17–28 (2005).
24. Estrella Gutiérrez, M. A., Dobrovolska, T., López Sauri, D. A., Veleva, L. & Krastev, I. Self-organization phenomena during electrodeposition of Co-In alloys. *ECS Trans.* **36,** 275–281 (2011).
25. Dobrovolska, T., López-Sauri, D. A., Veleva, L. & Krastev, I. Oscillations and spatio-temporal structures during electrodeposition of agcd alloys. *Electrochim. Acta* **79,** 162–169 (2012).
26. Golvano-Escobal, I. *et al.* Self-organized spatio-temporal micropatterning in ferromagnetic Co-In films. *J. Mater. Chem. C* **2,** 8259–8269 (2014).
27. Krastev, I., Dobrovolska, T., Lačnjevac, U. & Nineva, S. Pattern formation during electrodeposition of indium–cobalt alloys. *J. Sol. State Electrochem.* **16,** 3449–3456 (2012).
28. Turing, A. M. The chemical basis of morphogenesis. *Philos. Trans. R. Soc. B* **237,** 37–72 (1952).
29. Bros, J. P., Gaune-Escard, M., Allam, D. E., Haddad, R. & Hayer, E. The cobalt-indium system: enthalpy of formation and phase diagram. *J. Alloy Comp.* **233,** 264–271 (1996).
30. Li, S. P. *et al.* Magnetic domain confinement by anisotropy modulation. *Phys. Rev. Lett.* **88,** 087202 (2002).
31. Martin, N. *et al.* Influence of dipolar energy on the magnetization reversal in magnetization-modulated thin film systems: Model and experiment. *Phys. Rev. B* **83,** 174423 (2011).
32. Hierro-Rodriguez, A. *et al.* Fabrication and magnetic properties of nanostructured amorphous Nd–Co films with lateral modulation of magnetic stripe period. *J. Phys. D: Appl. Phys.* **46,** 345001 (2013).
33. Huang, K. *et al.* Magnetic patterning: local manipulation of the intergranular exchange coupling via grain boundary engineering. *Sci. Rep.* **5,** 11904 (2015).
34. Tober, E. D. *et al.* Magnetoresistance of self-assembled lateral multilayers. *Appl. Phys. Lett.* **77,** 2728–2730 (2000).
35. Ehresmann, A. *et al.* Asymmetric magnetization reversal of stripe-patterned exchange bias layer systems for controlled magnetic particle transport. *Adv. Mater.* **23,** 5568–5573 (2011).
36. Van Reenen, A., de Jong, A., den Toonder, J. & Prins, M. Integrated lab-on-chip biosensing systems based on magnetic particle actuation – a comprehensive review. *Lab Chip* **14,** 1966–1986 (2014).
37. Graham, D. L., Ferreira, H. A. & Freitas, P. P. Magnetoresistive-based biosensors and biochips. *Trends Biotechnol.* **22,** 455–462 (2004).
38. Vyas, K. N., Hong, B., Cooper, J. F. K., Palfreyman, J. J. & Barnes, C. H. W. Detection of magnetically labelled microcarriers for suspension based bioassay technologies. *IEEE Trans. Magn.* **47,** 1571–1574 (2011).
39. Love, D. M. *et al.* A composite element bit design for magnetically encoded microcarriers for future combinatorial chemistry applications. *RSC Adv.* **5,** 10211–10218 (2015).
40. McCord, J., Schultz, L. & Fassbender, J. Hybrid soft-magnetic lateral exchange spring films prepared by ion irradiation. *Adv. Mater.* **20,** 2090–2093 (2008).
41. Kim, S. O. *et al.* Epitaxial self-assembly of block copolymers on lithographically defined nanopatterned substrates. *Nature* **424,** 411–414 (2003).
42. Fernández-Regúlez, M., Evangelio, L., Lorenzoni, M., Fraxedas, J. & Pérez-Murano, F. Sub-10 nm resistless nanolithography for directed self-assembly of block copolymers. *ACS Appl. Mater. Interf.* **6,** 21596–21602 (2014).
43. Salaun, M. *et al.* Fabrication of highly ordered sub-20 nm silicon nanopillars by block copolymer lithography combined with resist design. *J. Mater. Chem. C* **1,** 3544–3550 (2013).
44. Luo, J. K. *et al.* Uniformity control of Ni thin-film microstructures deposited by through-mask plating. *Electrochem. Soc.* **152,** C36–C41 (2005).
45. Utke, I. *et al.* Focused electron beam induced deposition of high resolution magnetic scanning probe tips. *MRS Proc.* **706,** Z9.24.1 (2001).
46. Fogclholm, R., Rapp, O. & Grimvall, G. Electrical resistivity of indium: Deviation from linearity at high temperatures. *Phys. Rev. B* **23,** 3845–3851 (1981).
47. Bozzini, B. *et al.* Intermetallics as key to spiral formation in In–Co electrodeposition. a study based on photoelectron microspectroscopy, mathematical modelling and numerical approximations. *J. Phys. D: Appl. Phys.* **48,** 395502 (2015).
48. Slade, P. G. In *Electrical Contacts*: *Principles and Applications*, 2nd Edition (CRC Press, 2013).
49. Haast, M. A. M., Schuurhuis, J. R., Abelmann, L., Lodder, J. C. & Popma, T. J. Reversal mechanism of submicron patterned CoNi/Pt multilayers. *IEEE Trans. Magn.* **34,** 1006–1008 (1998).
50. Kläui, M. & Fernandes Vaz, C. A. Magnetization configurations and reversal in small magnetic elements. In *Handbook of Magnetism and Advanced Magnetic Materials* (Wiley, 2007).
51. Zabaleta, J. *et al.* Photoemission electron microscopy study of sub-200 nm self-assembled $La_{0.7}Sr_{0.3}MnO_3$ epitaxial islands. *Nanoscale* **5,** 2990–2998 (2013).
52. Fellah, F. *et al.* Microstructure and mechanical properties of ultrafine-grained fcc/hcp cobalt processed by a bottom-up approach. *J. Alloys Compd.* **489,** 424–428 (2010).
53. Ledbetter, H. *et al.* Internal friction and creep-recovery in indium. *J. Phys. IV* **C8,** 317–319 (1996).
54. Aballe, L., Foerster, M., Pellegrin, E., Nicolas, J. & Ferrer, S. The alba spectroscopic LEEM/PEEM experimental station: layout and performance. *J. Synchrotron Radiat.* **22,** 745–752 (2015).

Acknowledgements

58

Author Contributions

E.P. and J.S. designed research; I.G.-E. performed research; J.C.G.-R., N.D., X.I., J.F.L.-B., J.F., P.S., L.A., M.F., S.S., M.D.B., T.P. and S.P. contributed new analytic tools/discussion; I.G., E.P., J.S., N.D. and J.N. analyzed data; and I.G.-E., N.D., E.P., J.S. and J.N. wrote the paper. All authors reviewed the manuscript.

Additional Information

Supplementary information accompanies this paper at http://www.nature.com/srep

Competing financial interests: The authors declare no competing financial interests.

How to cite this article: Golvano-Escobal, I. *et al.* Spontaneous formation of spiral-like patterns with distinct periodic physical properties by confined electrodeposition of Co-In disks. *Sci. Rep.* **6**, 30398; doi: 10.1038/srep30398 (2016).

Electrical, magnetic and mechanical spiral-like spatio-temporal patterns in Co-In microdisks grown by confined electrodeposition

Irati Golvano-Escobal[1], Juan Carlos Gonzalez-Rosillo[2], Neus Domingo[3], Xavi Illa[4,5], José Francisco López-Barbera[1,3], Jordina Fornell[1], Pau Solsona[1], Lucia Aballe[6], Michael Foerster[6], Santiago Suriñach[1], Maria Dolors Baró[1], Teresa Puig[2], Salvador Pané[7], Josep Nogués[3, 8], Eva Pellicer[1,], Jordi Sort[1, 8,*]*

[1]Departament de Física, Universitat Autònoma de Barcelona, E-08193 Bellaterra, Spain

[2]Institut de Ciència de Materials de Barcelona (ICMAB-CSIC), Campus UAB, E-08193 Bellaterra, Spain

[3]Catalan Institute of Nanoscience and Nanotechnology (ICN2), CSIC and The Barcelona Institute of Science and Technology, Campus UAB, Bellaterra, E-08193 Barcelona, Spain

[4]Institute of Microelectronics of Barcelona (IMB-CNM), Campus UAB, E-08193 Bellaterra, Spain

[5]Biomedical Research Networking Center in Bioengineering, Biomaterials and Nanomedicine (CIBER-BBN), E-08193, Bellaterra, Spain

[6]Alba Synchrotron Light Facility, CELLS, E-08280 Bellaterra, Spain

[7]Institute of Robotics and Intelligent Systems (IRIS), ETH Zürich, CH-8092 Zürich, Switzerland

[8]Institució Catalana de Recerca i Estudis Avançats (ICREA), E-08010 Barcelona, Spain
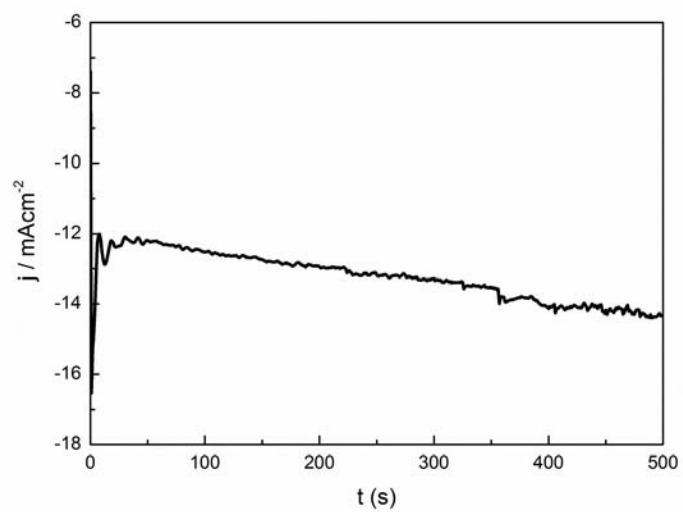
Figure S1. Potentiostatic curve for Co-In alloy micro-disks deposition onto pre-lithographed Au/Ti/Si substrates at –0.98 V .
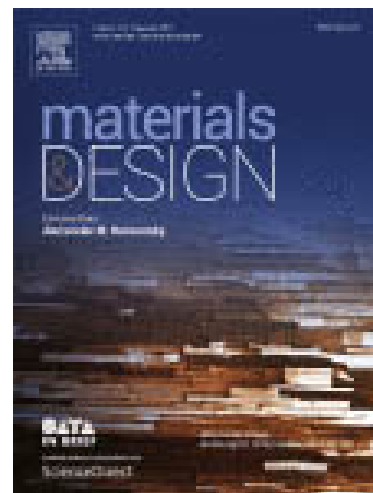
3.1.3.   Cross-sectioning spatio-temporal Co-In electrodeposits: Disclosing a magnetically-patterned nanolaminated structure

*Irati Golvano-Escobal [a], Juan de Dios Sirvent [a], Marta Ferran-Marqués [a], Santiago Suriñach [a], Maria Dolors Baró [a], Salvador Pané [*b], Jordi Sort [a,c,*] and Eva Pellicer [a,*]*

[a] Departament de Física, Universitat Autònoma de Barcelona, E-08193 Bellaterra, Spain.

[b] Institute of Robotics and Intelligent Systems (IRIS), ETH Zürich, CH-8092 Zürich, Switzerland.

[c] Institució Catalana de Recerca i Estudis Avançats (ICREA), Pg. Lluís Companys 23, E-08010 Barcelona, Spain.

*To whom correspondence should be addressed:
Prof. Jordi Sort, Dr. Eva Pellicer
E-mail: Jordi.Sort@uab.cat, Eva.Pellicer@uab.cat

Cross-sectioning spatio-temporal Co-In electrodeposits: Disclosing a magnetically-patterned nanolaminated structure

Irati Golvano-Escobal [a], Juan de Dios Sirvent [a], Marta Ferran-Marqués [a], Santiago Suriñach [a], Maria Dolors Baró [a], Salvador Pané [b], Jordi Sort [a,c], Eva Pellicer [a,*]

[a] Departament de Física, Universitat Autònoma de Barcelona, E-08193 Bellaterra, Spain
[b] Institute of Robotics and Intelligent Systems (IRIS), ETH Zürich, CH-8092 Zürich, Switzerland
[c] Institució Catalana de Recerca i Estudis Avançats (ICREA), Pg. Lluís Companys 23, E-08010 Barcelona, Spain

HIGHLIGHTS

- Cobalt-indium (Co-In) multilayered films are produced by direct current electrodeposition from a single electrolyte.
- A periodicity of 175 ± 25 nm has been observed from the cross-section of the films.
- Each layer exhibits a columnar microstructure and well-defined compositionally different (In-rich and Co-rich) regions.
- Magnetic force microscopy measurements reveal the occurrence of a cross-sectional stripe-like magnetic patterning.

GRAPHICAL ABSTRACT
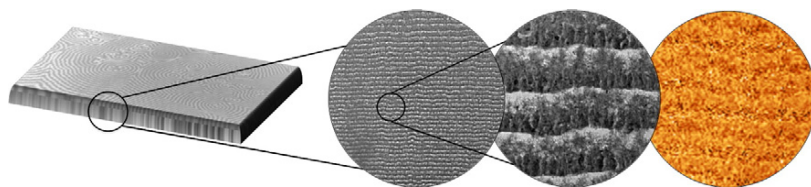
ARTICLE INFO

ABSTRACT

Micrometer-thick cobalt-indium (Co-In) films consisting of self-assembled layers parallel to the cathode plane, and with a periodicity of 175 ± 25 nm, were fabricated by electrodeposition at a constant current density. These films, which exhibit spatio-temporal patterns on the surface, grow following a layer-by-layer mode. Films cross-sections were characterized by electron microscopies and electron energy loss spectroscopy. Results indicate the spontaneous formation of nanolayers that span the whole deposit thickness. A columnar structure was revealed inside each individual nanolayer which, in turn, was composed of well-distinguished In- and Co-rich regions. Due to the dissimilar magnetic character of these regions, a periodic magnetic nanopatterning was observed in the cross-sectioned films, as shown by magnetic force microscopy studies.

© 2016 Elsevier Ltd. All rights reserved.

1. Introduction

Nanolaminates, defined as stacks of alternating ultra-thin layers of different materials, hold great promise for several applications requiring outstanding mechanical properties [1,2], optical [3] and magnetic features [4]. Moreover, since nanolaminates are frequently made of metal oxides, they find uses in biomedical devices requiring biocompatible materials [5]. Several approaches including sputtering [6,7], atomic layer deposition (ALD) [8,9], pulsed-laser deposition (PLD) [10], physical vapor deposition [11], ball-milling [12] and electrodeposition [4, 13–15] have been adopted to produce composite films made of alternated layers. Sputtering, ALD and PLD processes are relatively common deposition techniques but they have a few disadvantages. Namely,

residual stress during films' growth yield coatings with poor mechanical properties. This often leads to cracking, buckling, or delamination of the nanolaminates [16,17]. Besides, the deposition rates are rather slow. Electrodeposition has been widely utilized to produce micrometer-thick structures composed of alternated layers (metals, alloys and even polymers) in different configurations (films, rods and wires). Because electrodeposition from aqueous solutions works at room pressure and temperature, it possesses many attractive features like low cost and industrial scalability [18]. Layered coatings are typically fabricated from a single electrolyte by conveniently switching the deposition potential or current density [19] or by using different electrolytes [20]. The former approach is preferred when smaller layer thicknesses and a high number or repetitions are desired.

The in-situ formation of spatio-temporal patterns during the electrodeposition of some binary systems such as Ag-Bi, Ag-Cd, Ag-In, Ag-Sb or Co-In was previously demonstrated [21–27]. The spatio-temporal patterns typically consist of a mixture of waves, targets and spirals whose relative proportion was shown to depend on a number of factors, such as the nature of the system and the applied current density. Interestingly, it was recently found that the Co-In system not only exhibits the spatio-temporal self-pattern on the surface, but also a fancy layer-by-layer growth type [28]. Although the spontaneous formation of layered deposits with a repeat length of tens or hundreds of nanometers was observed in a quite few instances [29–31], this growth mode in immiscible systems exhibiting spatio-temporal patterns has not been studied in detail.

The aim of this work is to characterize the layer-by-layer growth in electrodeposited spatio-temporal Co-In films using electron microscopy techniques. The goal is to explore the cross-section of the electrodeposits in order to determine whether composition is homogeneous across the nanolayers or, instead, it varies within each layer or from one layer to another. This could eventually lead to dissimilar magnetic properties and hence, confer these materials new technological functionalities. In such a case, Co-In nanolaminates would be spontaneously produced from a single electrolyte under nominally constant conditions, which represents a step forward within the field of electrodeposited multilayered materials.

2. Experimental

Deposition of Co-In coatings was conducted in a three-electrode cell connected to a PGSTAT302N Autolab potentiostat/galvanostat (Ecochemie). A double junction Ag|AgCl (E = +0.210 V/SHE) reference electrode (Metrohm AG) was used with 3 M KCl inner solution and 1 M NaCl outer solution. A platinum spiral served as a counter electrode. Silicon (111) substrates with e-beam evaporated Ti (100 nm)/Au (125 nm) adhesion/seed layers were used as cathodes for Co-In growth. The working area of the Au/Ti/Si substrates was 5×5 mm^2. Co-In layers 10 μm thick were obtained at constant current densities from -10 mA cm^{-2} to -20 mA cm^{-2}.

The on-top morphology of the films was characterized with a Zeiss Merlin field emission scanning electron microscope (FE-SEM). The average Co content in the coatings was determined by energy dispersive X-ray spectroscopy (EDX) at 20 kV and probe current of 500 pA. The structure of the films was determined by X-ray diffraction (XRD) using a Philips X'Pert diffractometer in Bragg–Brentano geometry using Cu Kα radiation (note that both wavelengths $\lambda(K_{\alpha 1}) = 1.5406$ Å and $\lambda(K_{\alpha 2}) = 1.5443$ Å were used in intensity proportion of $I(K_{\alpha 2})/I(K_{\alpha 1}) = 0.5$) in the 25–110° 2θ range (0.03° step size and 10 s holding time). Films' cross-section was prepared differently depending on whether transmission electron microscopy (TEM) or FE-SEM was targeted. For TEM purposes, cross-sections were prepared by embedding the film in epoxy resist followed by cutting thin slices with an ultramicrotome (Leica EM UC6, Leica Microsystems Ltd., Milton Keynes, UK) using a 35° diamond knife at room temperature. Analyses were performed on a FEI Tecnai20 high-resolution (S)TEM operated at 200 kV,

equipped with EDX detector. For SEM analyses (Zeiss Merlin), the films were embedded in a conductive epoxy resin, grinded to remove the resin, and polished using Struers MD-Largo composite disc onto which 9 μm water based diamond suspension was applied. The room temperature magnetic properties were measured using a vibrating sample magnetometer (VSM) from Oxford Instruments. Hysteresis loops were recorded under a maximum applied field of 700 Oe applied along the parallel and perpendicular-to-plane directions. Atomic and magnetic force microscopy (AFM/MFM) images were acquired using Dual Scope C-26 system from Danish Micro Engineering. The MFM maps were taken at a tip lift height of 100 nm.

3. Results and discussion

FE-SEM images of the on-top and cross-section morphologies of the Co-In films are shown in Fig. 1. While the top view of the films (Fig. 1a) show spatio-temporal patterns with micrometer lateral sizes consisting of a mixture of spirals, waves and targets spread all over the surface, the film's cross-section (Fig. 1b) displays a layer-by-layer nanoarchitecture. Such a multilayered structured was seen in all coatings deposited at current densities between -10 and -20 mA cm^{-2}, corresponding to average Co contents ranging from 25 to 90 at.%. Remarkably, this layered arrangement was also observed in cross-sectioned Ag-Sb electrodeposited coatings exhibiting surface spatio-temporal patterns [32]. According to the authors, current oscillations recorded during stationary potentiostatic deposition corresponded to the formation of coarse travelling waves consisting of phases with different Sb content and their propagation in front of the Haber-Luggin capillary. This led to the formation of layered structures visible in the cross-sections of the deposits. Although some of the investigated systems with self-organization phenomena show either current or potential oscillations in the j-t or E-t curves [26], the E-t transients recorded during Co-In deposition did not show such oscillations. Instead, they showed some random
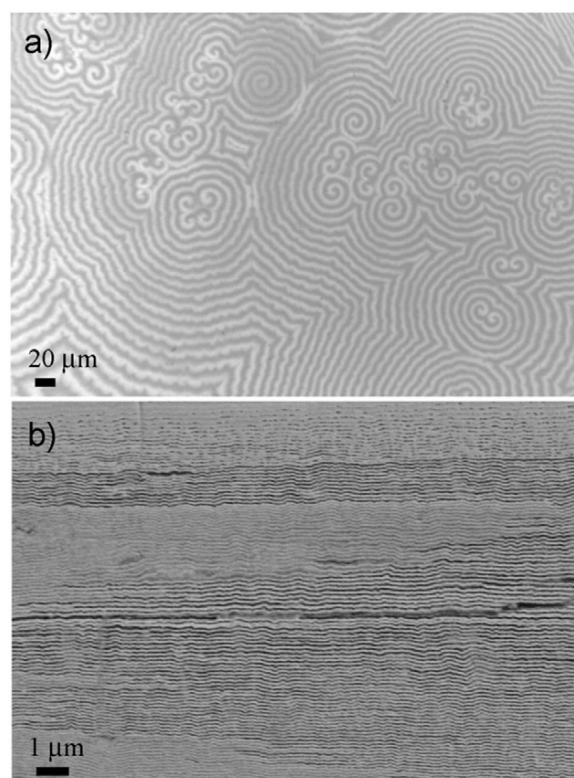

Fig. 1. SEM images of a Co-In coating obtained at j = -12 mA cm^{-2} (58 at.% Co) a) top view and b) cross section.
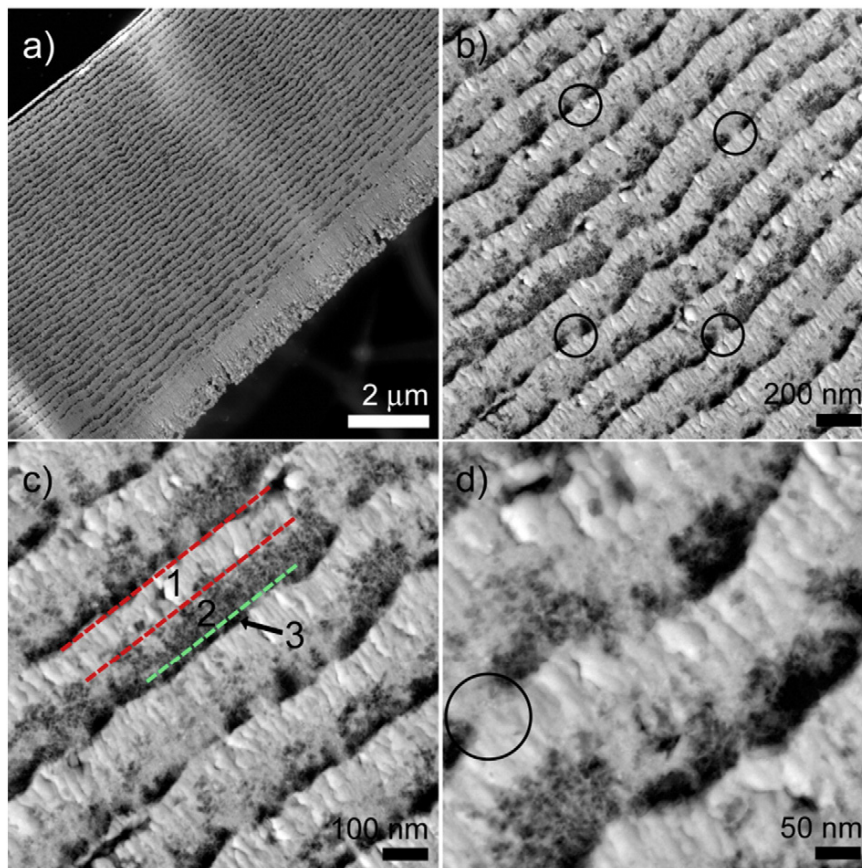
Fig. 2. a–d) STEM micrographs of the cross-section of Co-In coating obtained at j = − 20 mA cm^{-2} (78 at.% Co) at different magnifications. In b) and d) some In-rich anchor points are encircled. In c) the three distinct regions within each layer are indicated.

fluctuations around a stationary potential value (Fig. S1, Supporting information).

A closer look to the cross-section of the Co-In films was taken by TEM working on STEM mode (Fig. 2). The formation of partially stacked individual layers, undulated and rather uniform in thickness was observed (Fig. 2a and b), in agreement with previous SEM analyses. Interestingly, a kind of columnar structure is observed in each nanolayer (Fig. 2c). Such a columnar grain structure is often observed in electrodeposited metals and alloys [33]. The repetition length as measured by TEM was 175 nm ± 25 nm across the entire deposit thickness, thus furnishing a highly, almost perfect, repeatable 2D pattern expanding several micrometers. Three regions were distinguished within each layer. Namely, a wider, dense, bright region followed by a more irregular, fluffy, grey region, and finally a dark area (Fig. 2c). EDX line scan analyses across two adjacent nanolayers were conducted in order to shed light on the chemical composition profile (Fig. 3a). The
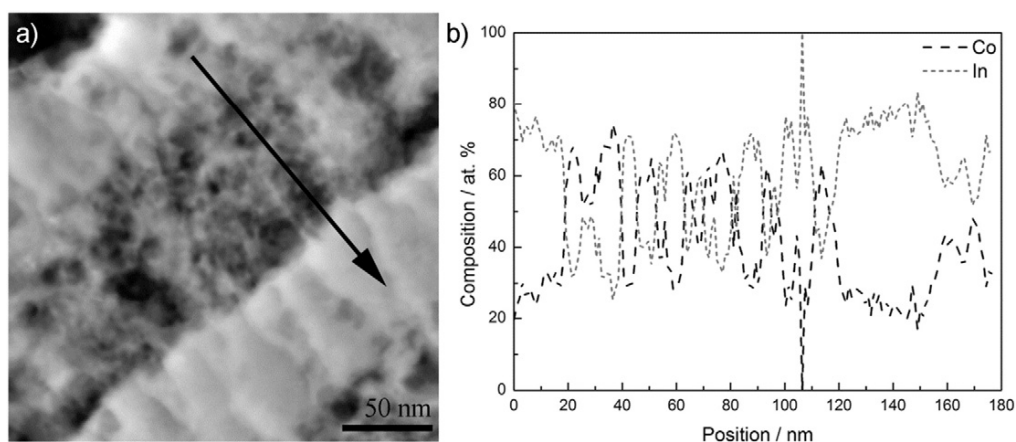
Fig. 3. a) STEM micrograph and b) EDX line scan acquired across the black line indicated in a) on the cross-section of a Co-In coating obtained at j = − 12 mA cm^{-2} (58 at.% Co). Notice that the In content in some regions is higher than the average value estimated from global EDX analyses. The local character of the measurement and the fact that the Co/In ratio is not constant throughout deposit thickness (deposition was performed under stagnant conditions) should be taken into account.

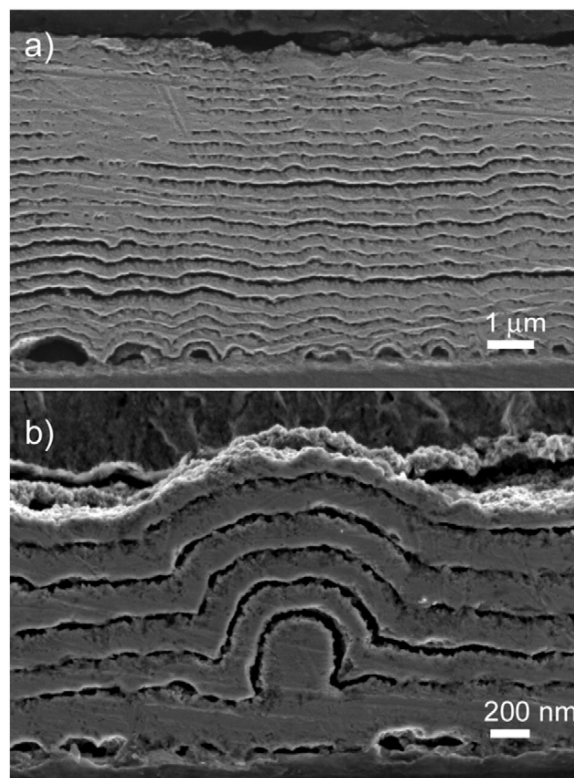**Fig. 5.** SEM images of a) the cross-section of a Co-In coating obtained at $j = -12$ mA cm^{-2} (58 at.% Co) showing undulations at the substrate interface and b) detail of one undulation.

Fig. 4. a,b) TEM and c) HRTEM images of the cross-section of a Co-In coating obtained at $j = -20$ mA cm^{-2} (78 at.% Co). In b) the three distinct regions within each layer are indicated.

above-mentioned heterogeneity was evident as the beam was scanning from the center of one nanolayer toward the center of the adjacent nanolayer (Fig. 3b) for all samples. The relatively dense bright area was enriched in In whereas the spongy-like grey area contained a larger amount of Co on average, although the In and Co signals strongly fluctuate. Remarkably, the dark regions correspond to areas mainly free from material. STEM-EDX line scan analyses across these dark regions confirmed the occurrence of holes in the material (Fig. S2 and S3, Supporting information). Eventual delamination during sample preparation (cutting by ultramicrotome) for STEM analyses that could explain the existence of these gaps is unlikely. Therefore, such apparently 'empty' regions already develop during film deposition, likely because of hydrogen co-evolution. Interestingly, lateral growth is favored over vertical growth in spite of these discontinuities. The occurrence of In- and Co-rich regions was observed in different areas of the cross-sectioned films and therefore was proven neither to be an artifact of the measurement nor an anomaly of the deposit in the region of interest. It was also observed that the nanolayers were joined together mostly through In-rich anchor points (see Fig. 2b and d). The compositional heterogeneity observed on the cross-section of the deposits translated into complex XRD patterns (Fig. S4, supporting information). These showed the existence of several phases (namely, tetragonal In, tetragonal CoIn$_3$, face-centered cubic Co, and hexagonal-close packed Co).

Previous EDX mappings conducted on the cross-section of a Co-In deposit seemingly indicated that the distribution of Co and In elements was homogeneous [28]. Current STEM-EDX analyses do demonstrate that this is not the case and that composition heterogeneities exist at the nanoscale. Notice that STEM-EDX analyses were performed on a thin slice (less than 100 nm thick) taken from the deposit's cross-section, hence they are much less affected from the sublayers' background. TEM images of the same region imaged by STEM are displayed in Fig. 4a and b. Notice that the contrast is opposed to that observed in STEM mode. Bright regions correspond to hollow spaces in the deposit. The HRTEM image (Fig. 4c) demonstrates that the material is polycrystalline, in agreement with previous works [28]. It was claimed that the spatio-temporal structures do move in the vertical direction. This is
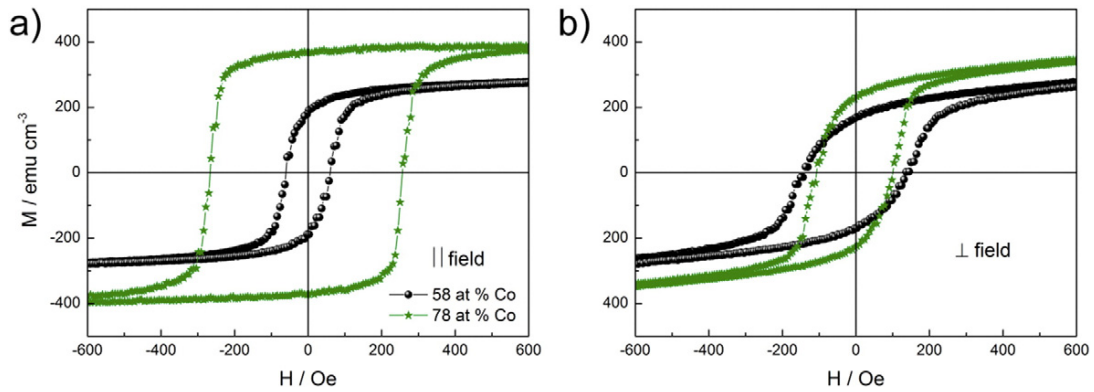
Fig. 6. Room-temperature hysteresis loops measured by VSM applying the magnetic field along the a) film plane and b) perpendicular to the film plane.

possibly connected with the effect of natural convection during electro-deposition and results in the formation of layered coatings [32]. Indeed, a zoomed detail of the very first layers deposited on the substrate reveals that when an undulation or a "defect" appears, this is conformally wrapped by the subsequent layers until the growing front becomes flattened (Fig. 5).

The room-temperature magnetic properties of Co-In deposits were first assessed by VSM before any cross-sectioning. A ferromagnetic response was observed as shown in Fig. 6, in agreement with previous results [28]. Interestingly, the loops for these two samples exhibit an opposite trend in terms of coercivity (H_C). While a higher H_C is observed along the film plane for the sample with 78 at.% Co, the sample with 58 at.% Co shows higher H_C in the perpendicular to film plane direction. It can be conjectured that an interplay exists between the "thin film or lamellae" shape anisotropy (which promotes in-plane easy axis) and the shape anisotropy induced by the growth of a columnar microstructure within the magnetic layers.

MFM characterization of the cross-section of the deposits was carried in order to assess any kind of magnetic patterning arising from the layer-by-layer architecture of the Co-In films. Fig. 7a shows the AFM image obtained upon scanning an area of $1 \times 1 \ \mu m^2$ of a deposit with 58 at.% Co, in which the periodical layered structure, already observed by SEM and (S)TEM, was captured. In this topological image, alternating dark and bright fringes are observed, corresponding to the In-rich and Co-In lamellae. The corresponding MFM image (Fig. 7b) was acquired in remanent state after applying a strong magnetic field perpendicular to the film cross-section. In the MFM image, a magnetic nanopatterning is observed, which correlates well with the layered structured seen in Fig. 2a. Remarkably, the bright fringes in the AFM image do match the brighter regions in the MFM image, hence evidencing that the MFM contrast is magnetic, rather than topological. Indeed, topological features (e.g. scratches) seen in the AFM mode are not 'visible' in the MFM image. Narrower stripes with magnetic contrast likely matching the Co-rich regions (dark bands in STEM) are separated by wider featureless In-rich regions (bright bands in STEM). The local heterogeneity of the cottony-like Co region is though not captured by MFM due to the small size of the compositionally varying regions. Fig. 7c and d show the AFM and MFM images, respectively, of the cross-section of a
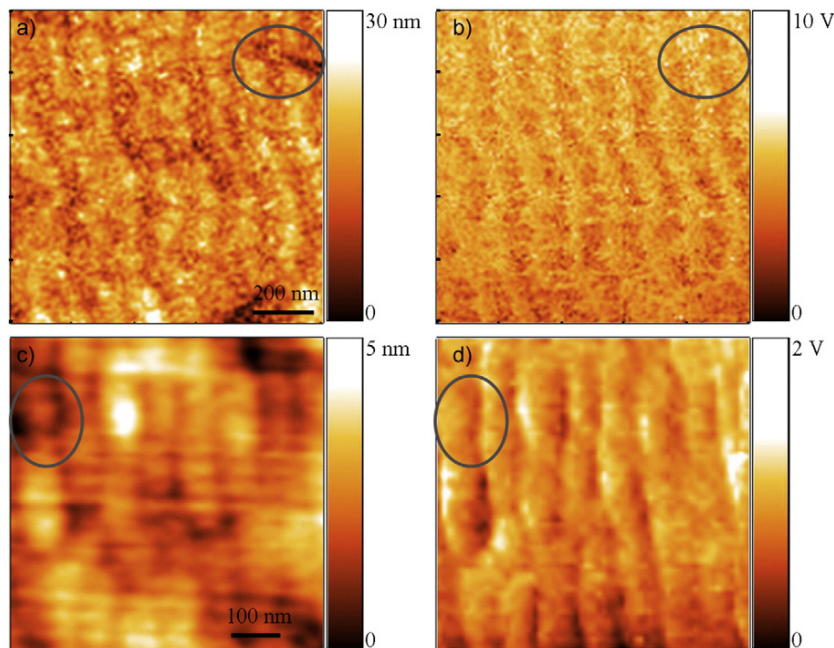

Fig. 7. a), c) AFM and b), d) MFM images taken at the cross-section of Co-In films obtained at j = − 12 mA cm^{-2} (58 at.% Co) and j = − 20 mA cm^{-2} (78 at.% Co). Notice that MFM images are not affected by topographical features like scratches or gaps (see encircled regions).

deposit with a higher Co content (78 at.%). The scale bar in the AFM image reveals that the lamellae are probably more densely packed than for the deposit with 58 at.% Co.

4. Conclusions

Co-In nanolayered films were obtained by direct current electrodeposition on Au surfaces. (S)TEM investigations of the films' cross-section showed the occurrence of self-assembled nanolayers along the entire deposit thickness. The layers were not compositionally homogeneous but Co- and In-rich regions coexisted in them. Moreover, each layer showed a columnar structure. A stripe-like magnetic patterning developed as a consequence of the nanolaminated structure. The possibility to electrodeposit, under direct current conditions, a system that spontaneously features a spatio-temporal pattern with micrometer lateral sizes over its surface coupled to a magnetically-patterned nanolayered vertical structure, represents a breakthrough in the field of nanocomposites science.

Acknowledgements

Appendix A. Supplementary data

Supplementary data to this article can be found online at http://dx.doi.org/10.1016/j.matdes.2016.11.088.

References

[1] B.M. Clemens, H. Kung, S.A. Barnett, Structure and strength of multilayers, MRS Bull. 24 (1999) 20–26.
[2] J.J. Zhang, M.X. Wang, J. Yang, Q.X. Liu, D.J. Li, Enhancing mechanical and tribological performance of multilayered CrN/ZrN coatings, Surf. Coat. Technol. 201 (2007) 5186–5189.
[3] G.S. Hickey, S.-S. Lih, T.W. Barbee Jr., Development of nanolaminate thin-shell mirrors, Proc. SPIE 4849 (2002) 63–76.
[4] J. Kim, J.-K. Kim, M. Kim, F. Herrault, M.G. Allen, Microfabrication of toroidal inductors integrated with nanolaminated ferromagnetic metallic cores, J. Micromech. Microeng. 23 (2013) 114006.
[5] W. Li, B. Kabius, O. Auciello, Science and technology of biocompatible thin films for implantable biomedical devicesProceedings of the IEEE 2010 Annual International Conference of the Engineering in Medicine and Biology Society (EMBC) 2010, pp. 6237–6242.
[6] Y.Y. Tse, D. Babonneau, A. Michel, G. Abadias, Nanometer-scale multilayer coatings combining a soft metallic phase and a hard nitride phase: study of the interface structure and morphology, Surf. Coat. Technol. 180–181 (2004) 470–477.
[7] K. Ikeda, K. Kobayashi, M. Fujimoto, Multilayer nanogranular magnetic thin films for GHz applications, J. Appl. Phys. 92 (2002) 5395–5400.
[8] J.W. Elam, Z.A. Sechrist, S.M. George, ZnO/Al$_2$O$_3$ nanolaminates fabricated by atomic layer deposition: growth and surface roughness measurements, Thin Solid Films 616 (2002) 43–55.
[9] I. Iatsunskyi, E. Coy, R. Viter, G. Nowaczyk, M. Jancelewicz, I. Baleviciute, K. Załęski, S. Jurga, Study on structural, mechanical, and optical properties of Al$_2$O$_3$–TiO$_2$ nanolaminates prepared by atomic layer deposition, J. Phys. Chem. C 119 (2015) 20591–20599.
[10] G. Balakrishnan, P. Kuppusami, D. Sastikumar, Growth of nanolaminate structure of tetragonal zirconia by pulsed laser deposition, Nanoscale Res. Lett. 8 (2013) 82.
[11] A. Misra, R.G. Hoagland, Plastic flow stability of metallic nanolaminate composites, J. Mater. Sci. 42 (2007) 1765–1771.
[12] K.V. Manukyan, B.A. Mason, L.J. Groven, Y.-C. Lin, M. Cherukara, S.F. Son, A. Strachan, A.S. Mukasyan, Tailored reactivity of Ni + Al nanocomposites: microstructural correlations, J. Phys. Chem. C 116 (2012) 21027–21038.
[13] F. Ebrahimi, A.J. Liscano, Microstructure/mechanical properties relationship in electrodeposited Ni/Cu nanolaminates, Mater. Sci. Eng. A301 (2001) 23–34.
[14] L. Péter, G.L. Katona, Z. Berényi, K. Vad, G.A. Langer, E. Toth-Kadar, J. Padar, L. Pogany, I. Bakonyi, Electrodeposition of Ni–Co–Cu/Cu multilayers: 2. Calculations of the element distribution and experimental depth profile analysis, Electrochim. Acta 53 (2007) 837–845.
[15] H. Zhang, L. Liu, J. Bai, X. Liu, Corrosion behavior and microstructure of electrodeposited nano-layered Ni–Cr coatings, Thin Solid Films 595 (2015) 36–40.
[16] L.B. Freund, S. Suresh, Thin Film Materials: Stress, Defect Formation and Surface Evolution, Cambridge University Press, 2004.
[17] D.C. Meyer, A. Klingner, T. Holz, P. Paufler, Self-organized structuring of W/C multilayers on Si substrate, Appl. Phys. A Mater. Sci. Process. 69 (1999) 657–659.
[18] M. Schlesinger, M. Paunovic (Eds.), Modern Electroplating, fifth ed. John Wiley & Sons Inc., New Jersey, 2010.
[19] D. Rafaja, C. Schimpf, T. Schucknecht, V. Klemm, L. Péter, I. Bakonyi, Microstructure formation in electrodeposited Co–Cu/Cu multilayers with GMR effect: influence of current density during magnetic layer deposition, Acta Mater. 59 (2011) 2992–3001.
[20] J. Zhang, S. Agramunt-Puig, N. Del-Valle, C. Navau, M.D. Baró, S. Estradé, F. Peiró, S. Pané, B.J. Nelson, A. Sánchez, J. Nogués, E. Pellicer, J. Sort, Tailoring staircase-like hysteresis loops in electrodeposited tri-segmented magnetic nanowires: a strategy towards minimization of interwire interactions, ACS Appl. Mater. Interfaces 8 (2016) 4109–4117.
[21] B. Bozzini, D. Lacitignola, I. Sgura, Spatio-temporal organization in alloy electrodeposition: a morphochemical mathematical model and its experimental validation, J. Solid State Electrochem. 17 (2013) 467–479.
[22] I. Krastev, T. Valkova, A. Zielonka, Structure and properties of electrodeposited silver–bismuth alloys, J. Appl. Electrochem. 34 (2004) 79–85.
[23] T. Dobrovolska, L. Veleva, I. Krastev, A. Zielonka, Composition and structure of silver-indium alloy coatings electrodeposited from cyanide electrolytes, J. Electrochem. Soc. 152 (2005) C137–C142.
[24] Y. Nagamine, O. Haruta, M. Hara, Surface morphology of spatiotemporal stripe patterns formed by Ag/Sb co-electrodeposition, Surf. Sci. 575 (2005) 17–28.
[25] M.A. Estrella Gutiérrez, T. Dobrovolska, D.A. López Sauri, I. Krastev, Self-organization phenomena during electrodeposition of Co-In alloys, ECS Trans. 36 (2011) 275–281.
[26] T. Dobrovolska, D.A. López-Sauri, L. Veleva, I. Krastev, Oscillations and spatio-temporal structures during electrodeposition of AgCd alloys, Electrochim. Acta 79 (2012) 162–169.
[27] I. Krastev, T. Dobrovolska, U. Lačnjevac, S. Nineva, Pattern formation during electrodeposition of indium–cobalt alloys, J. Solid State Electrochem. 16 (2012) 3449–3456.
[28] I. Golvano-Escobal, B. Özkale, S. Suriñach, M.D. Baró, T. Dobrovolska, I. Krastev, S. Pané, J. Sort, E. Pellicer, Self-organized spatio-temporal micropatterning in ferromagnetic Co–In films, J. Mater. Chem. C 2 (2014) 8259–8269.
[29] P.L. Cavallotti, B. Bozzini, L. Nobili, G. Zangari, Alloy electrodeposition for electronic applications, Electrochim. Acta 39 (1994) 1123–1131.
[30] Y. Wang, Y. Cao, M. Wang, S. Zhong, M.-Z. Zhang, Y. Feng, R.-W. Peng, X.-P. Hao, N.-B. Ming, Spontaneous formation of periodic nanostructured film by electrodeposition: experimental observations and modeling, Phys. Rev. E 69 (2004) 021607.
[31] S.-I. Baik, A. Duhin, P.J. Phillips, R.F. Klie, E. Gileadi, D.N. Seidman, N. Eliaz, Atomic-scale structural and chemical study of columnar and multilayer Re–Ni electrodeposited thermal barrier coating, Adv. Eng. Mater. 18 (2016) 1133–1144.
[32] I. Krastev, T. Dobrovolska, Pattern formation during electrodeposition of alloys, J. Solid State Electrochem. 17 (2013) 481–488.
[33] L. Peraldo Bicelli, B. Bozzini, C. Mele, L. D'Urzo, A review of nanostructured aspects of metal electrodeposition, Int. J. Electrochem. Sci. 3 (2008) 356–408.

Supporting Information

Cross-sectioning spatio-temporal Co-In electrodeposits: disclosing a magnetically-patterned nanolaminated structure

Irati Golvano-Escobal[1], Juan de Dios Sirvent[1], Marta Ferran-Marqués[1], Santiago Suriñach[1], Maria Dolors Baró[1], Salvador Pané[2], Jordi Sort[1,3,] Eva Pellicer[1,*]*
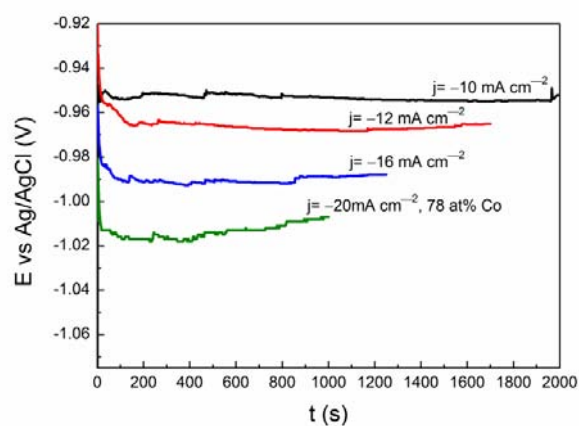
Figure S1. Representative E–t transients for Co–In deposition onto Au/Ti/Si substrates at the indicated current densities.
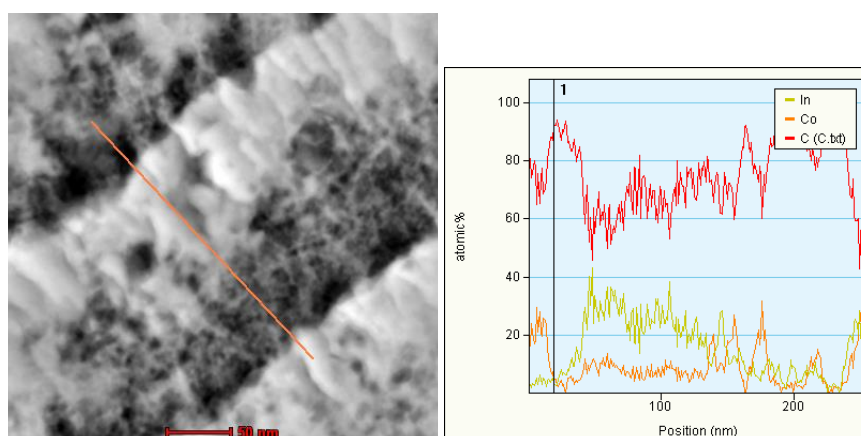

Figure S2. STEM micrograph (left) and EDX line scan (right) acquired across the orange line indicated in a) on the cross-section of a Co-In coating obtained at j =−12 mA cm^{-2} (58 at% Co).
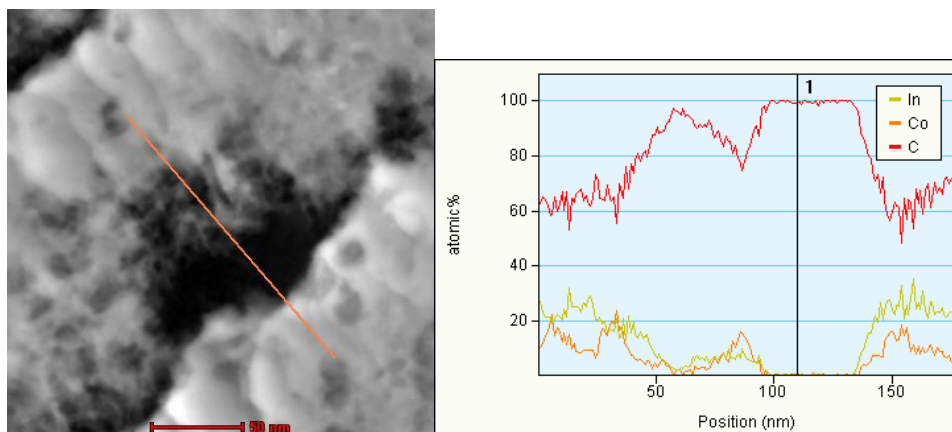
Figure S3. STEM micrograph (left) and EDX line scan (right) acquired across the orange line indicated in a) on the cross-section of a Co-In coating obtained at j =−12 mA cm^{-2} (58 at% Co).
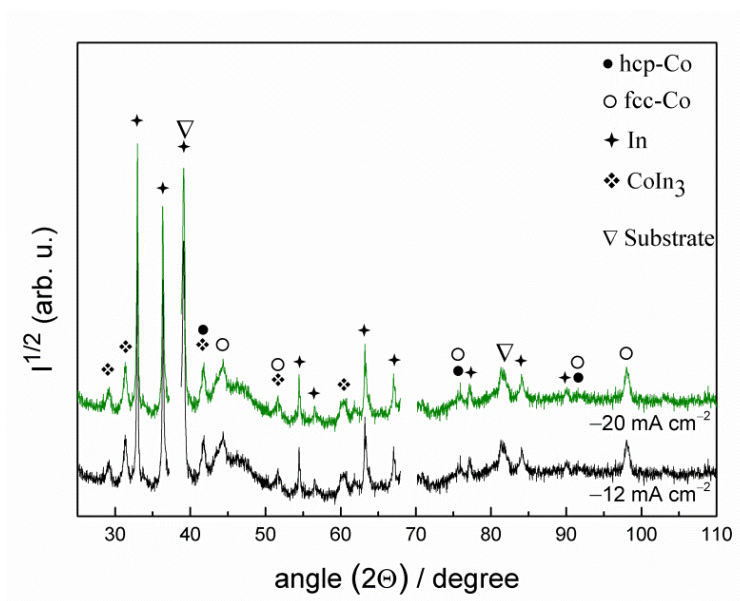
Figure S4. X-ray diffractograms in the 25–110º 2θ region of Co–In films electrodeposited on Au/Ti/Si (111) substrates at different current densities. Breaks in data around 37º and 69º were applied to avoid the most intense reflections from Au and Si, respectively, of the substrate.

3.2. Iron-Rhodium system

In the following article we report for the first time on the direct current electrodeposition of bimetallic rhodium-iron (Rh-Fe) NPs for its subsequent use in electrocatalytic hydrogen production (Figure 3.1). An electrolyte containing 0.5 mM Cl_6Na_3Rh, 0.01 M $FeCl_3$, 0.05 M glycine and 0.05 M NaCl (pH = 2.4) was formulated. Importantly, Fe(III) was used instead of Fe(II) to preclude the formation of a continuous coating, so that finely distributed NPs were obtained on Si/Ti/Au substrates. The composition, the size and the coverage degree of the NPs were tuned on-demand by adjusting the applied current density and deposition time.

EDX analyses revealed that NPs featuring Fe contents ranging from 15 at.% to 36 at.% could be readily obtained at current densities between –0.5 and –4 mA cm^{-2} since Fe discharge is favored at higher overpotentials (or current densities). Simultaneously, their size (20 nm - 80 nm) could be varied by both changing the current density and the deposition time. In any case, relatively narrow size distributions were achieved at each growth condition, which is probably the most challenging issue when NPs are produced by electrodeposition. XPS analyses indicated that the NPs were mostly metallic and that a very thin passivation shell (ca. 1 nm thick) coated the metallic cores. HR-TEM observations indicated that they were mostly crystalline. Each NP was made of tiny crystallites smaller than 5 nm. STEM-EDX line scan analyses aimed at determining the Fe distribution within the NPs indicated that it was homogeneously distributed.

To study the electrocatalytic activity of the deposited Rh-Fe NPs towards HER, LSV curves were recorded in Ar-purged 0.1 M NaOH at a sweeping rate of 50 mV s^{-1}. The samples showed excellent electrocatalytic activity towards HER with a complex dependence on both NP composition and coverage degree. The trends indicated that costly Rh can be safely replaced by cheaper Fe without compromising its electrocatalytic activity. Pure Rh NPs electrodeposited under similar conditions indeed showed a reduced HER activity compared to some Rh-Fe NPs. The NPs also showed acceptable stability as determined by CV (50 cycles were run) and chronoamperometry at −1.1 V for 2 h. The HER activity of Rh–Fe nanoparticulated denser films showed a declined electrocatalytic activity, highlighting the importance of large S/V ratios for HER output.
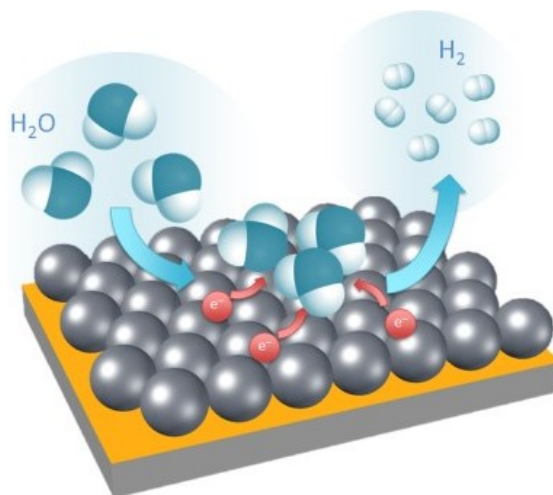

Figure 3.1: Schematic drawing showing the electrochemical reduction of water molecules into hydrogen catalyzed by Rh-Fe NPs deposited on a Au surface.

3.2.1. Electrodeposition of sizeable and compositionally tunable rhodium-iron nanoparticles and their activity toward hydrogen evolution reaction

*Irati Golvano-Escobal [a], Santiago Suriñach [a], Maria Dolors Baró [a], Salvador Pané [*b], Jordi Sort [*c] and Eva Pellicer [*a]*

[a] Departament de Física, Universitat Autònoma de Barcelona, E-08193 Bellaterra, Spain.

[b] Institute of Robotics and Intelligent Systems (IRIS), ETH Zürich, CH-8092 Zürich, Switzerland.

[c] Institució Catalana de Recerca i Estudis Avançats (ICREA), Departament de Física, Universitat Autònoma de Barcelona, E-08193 Bellaterra, Spain.

*To whom correspondence should be addressed:

Dr. Salvador Pané, Prof. Jordi Sort, Dr. Eva Pellicer

E-mail: vidalp@ethz.ch, Jordi.Sort@uab.cat, Eva.Pellicer@uab.cat

CrossMark

Electrodeposition of sizeable and compositionally tunable rhodium-iron nanoparticles and their activity toward hydrogen evolution reaction

Irati Golvano-Escobal[a], Santiago Suriñach[a], Maria Dolors Baró[a], Salvador Pané[b,*], Jordi Sort[c,*], Eva Pellicer[a,*]

[a] Departament de Física, Facultat de Ciències, Universitat Autònoma de Barcelona, E-08193 Bellaterra, Spain
[b] Multi-Scale Robotics Lab (MSRL), Institute of Robotics & Intelligent Systems (IRIS), ETH Zürich, Zürich 8092, Switzerland
[c] Institució Catalana de Recerca i Estudis Avançats (ICREA) and Departament de Física, Universitat Autònoma de Barcelona, E-08193 Bellaterra, Spain

A B S T R A C T

Rh-Fe nanoparticles (NPs) with variable Rh/Fe ratios have been obtained by direct current electrodeposition onto Au-metalized Si/Ti substrates from an electrolyte containing Rh(III) and Fe(III) chloride salts. NP mean diameter could be varied in the range of 20–80 nm by playing with the applied current density ($-j = 0.5$–2 mA cm^{-2}) and deposition times (t = 200–3200 s). NPs were very well adhered to the substrate and became progressively enriched in Fe as the absolute value of the current density increased. X-ray photoelectron spectroscopy analyses revealed that the NPs are mostly metallic. The oxygen signal detected at surface level is relatively high but reduces down to less than 1 at% after 1 min Ar ions sputtering. The as-deposited Rh-Fe NPs are active toward hydrogen evolution reaction in alkaline medium. Different values of the onset potential for water reduction have been observed depending on the j and t values applied for NPs growth. Cycling stability tests reveal that NPs do not suffer from excessive deterioration of their electrocatalytic activity with time.

© 2016 Elsevier Ltd. All rights reserved.

1. Introduction

Nanoparticles (NPs) exhibit a wealth of physical and chemical properties associated with their crystal structure, chemical and electrochemical reactivity or electrical and magnetic properties at the nanoscale [1]. For this reason, NPs have become the cornerstone for the development of next generation of sensing, energy conversion, electronic, optoelectronic, and magnetic devices [2–4]. Among the synthesis methods to produce substrate-supported NPs, electrochemical deposition is one of the least expensive, highly productive and readily available methods [5–7]. Electrodeposition enables not only directly growing the NPs onto the substrate, but also to tune on-demand the NPs composition, the crystallographic structure, the size, and the shape by playing with the electrodeposition parameters [8–10].

Rhodium (Rh) is a precious transition metal with intriguing properties including chemical inertness towards mineral acids, outstanding catalytic properties for a variety of organic transformations [11–14] and electrocatalytic properties [15]. For those reasons, Rh has been broadly employed in fuel cells, solar energy conversion devices and for environmental remediation [16].

However, one of the main drawbacks associated with Rh is its high price, which makes it necessary to partially replace Rh by more abundant and less expensive elements. Iron (Fe), as one of the most earth-abundant elements, is a suitable candidate. For example, Haider and co-workers synthesized Fe-promoted Rh catalysts by incipient wetness impregnation. They showed that the addition of Fe to the catalyst significantly improved the catalytic activity and the selectivity of the material toward ethanol and other oxygen-containing compounds [17]. Likewise, Nakamula et al. synthesized bimetallic Rh/Fe NPs by stepwise complexation for the hydrogenation of olefins and nitroarenes. They showed improved catalytic performance toward these hydrogenation reactions, under relatively mild conditions, in comparison with previously reported hydrogenation reactions using pure Rh NPs [18].
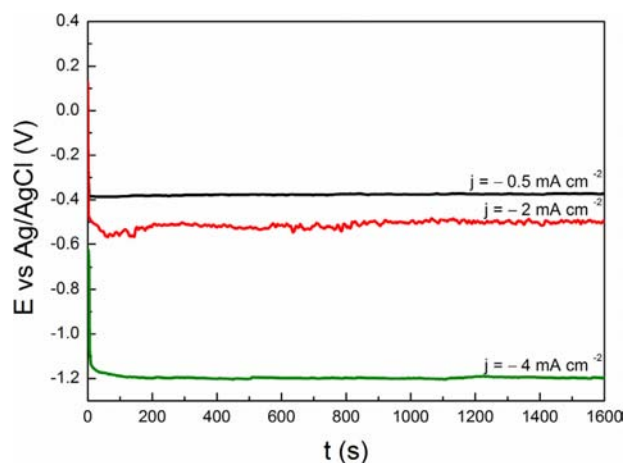
Fig. 1. Representative E–t transients for NPs deposition onto Au/Ti/Si substrates at the indicated current densities.

and solar hydrogen devices [20]. Although Rh cannot compete with Pt in terms of HER in alkaline medium, Rh still shows a reasonable activity [21,22]. For example, Smiljanic et al. found that bimetallic catalysts composed of Rh nanoislands on Pt exhibited enhanced HER performance with respect to bare Pt [23]. Meanwhile, Fe and its compounds (e.g. hydro(oxy) oxides) have been developed as highly efficient HER electrocatalysts under acidic or alkaline conditions [24,25]. Due to their large surface area, NPs are expected to outperform thin films in HER.

The present work aims to demonstrate that Rh- and Fe-containing NPs can be successfully prepared by electrodeposition. Although there are studies on either the electrodeposition of Rh [26,27] or Fe [28], little attention has been paid to the codeposition of these two elements [29,30], and certainly not in the form of NPs. It will be shown that the here-presented deposition scheme renders Rh-Fe NPs whose chemical composition and size can be adjusted by simply changing the current density and deposition time. The HER characteristics of the deposited NPs have been investigated in alkaline media and the trends observed have been outlined.

2. Experimental

2.1. Electrochemical synthesis of Rh-Fe NPs

Hydrogen evolution reaction (HER) is a cathodic reaction in the electrolysis of water that allows producing hydrogen as a key energy carrier [19]. HER is of uttermost importance in electrochemical energy conversion devices such as electrolysers, fuel cells

NPs were synthesized by direct current electrodeposition in a thermostatized three-electrode cell using a PGSTAT 302 N Autolab

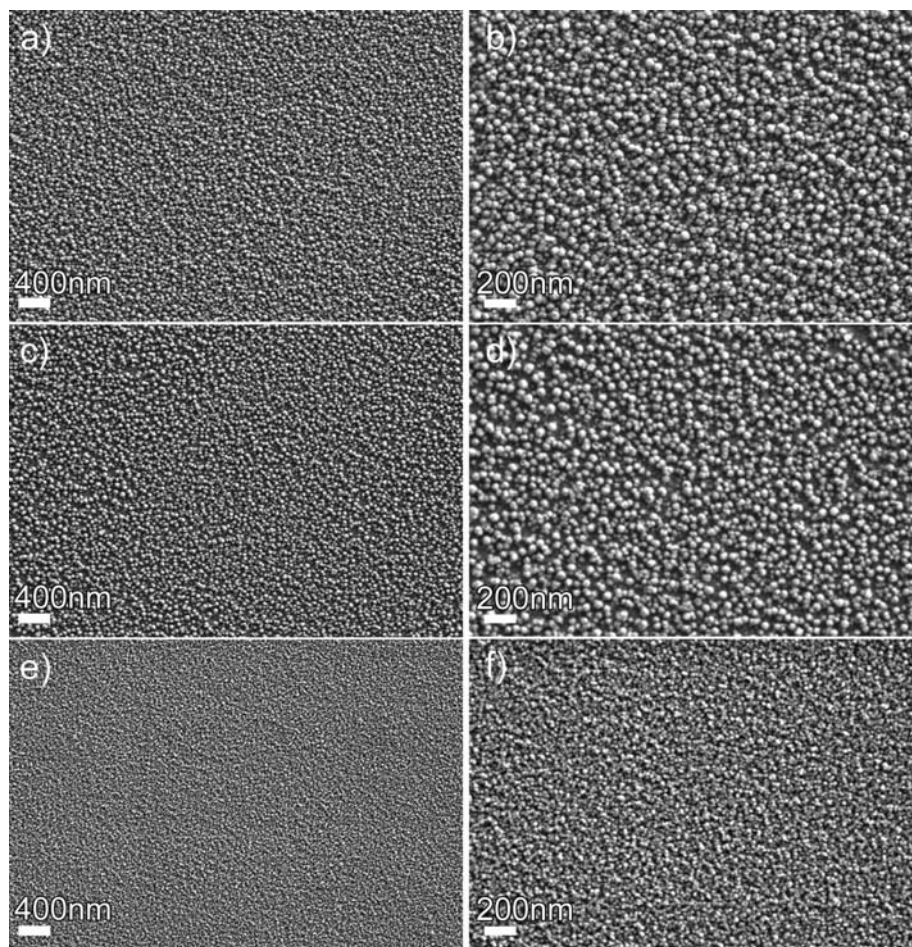**Fig. 2.** FE-SEM images of NPs obtained at fixed deposition charge: (a, b) $j = -0.5\,\mathrm{mA\,cm^{-2}}$, 1600 s, (c, d) $j = -2\,\mathrm{mA\,cm^{-2}}$, 400 s and (e, f) $j = -4\,\mathrm{mA\,cm^{-2}}$, 200 s.

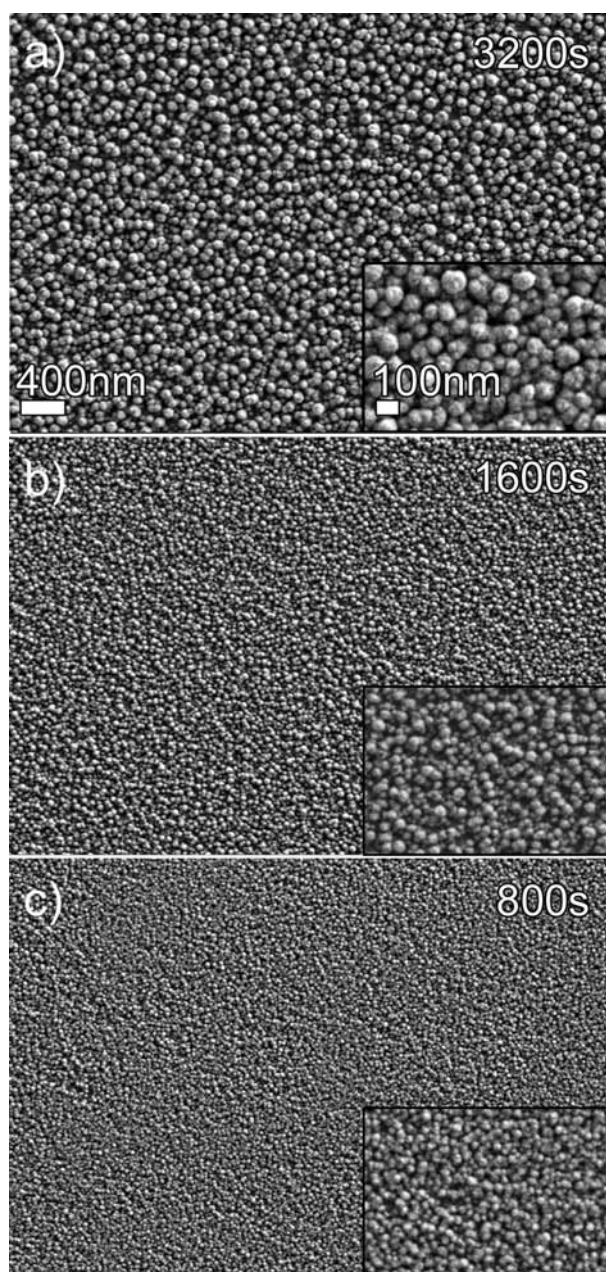**Fig. 3.** FE-SEM images of NPs obtained at j = −0.5 mA cm^{-2} for different deposition times (3200, 1600 and 800 s). Magnification is the same for both the large SEM images and the insets. Scale bar is the same for all images (and insets).

potentiostat/galvanostat (Ecochemie). Au (125 nm)/Ti (25 nm) coated Si/SiO$_2$ chips were used as cathodes (working area 0.25 cm^2). A double junction Ag|AgCl (E = +0.210 V/SHE) reference

Table 1
Mean size (±standard deviation) of the NPs as a function of the applied current density and deposition time.

		Mean size (± nm)		
	−j (mA cm^{-2})	0.5	2	4
time (s)	200	31.4 ± 7.1	24.5 ± 4.3	22.5 ± 3.4
	400	41.1 ± 9.3	48.2 ± 8.5	29.8 ± 5.5
	800	37.8 ± 5.6	41.5 ± 7.8	49.2 ± 8.3
	1600	42.7 ± 11.1	52.3 ± 8.9	49.0 ± 6.6
	3200	58.3 ± 13.4	76.6 ± 12.8	81.2 ± 18.8

electrode (Metrohm AG) was used with 3 M KCl inner solution and interchangeable outer solution made of 1 M NaCl. A platinum spiral served as counter electrode. The electrolyte consisted of 0.5 mM Cl$_6$Na$_3$Rh, 0.01 M FeCl$_3$, 0.05 M glycine and 0.05 M NaCl. The pH of the as-prepared electrolyte was 2.4 and it was kept for the electrodeposition experiments. Solutions were prepared from analytical grade reagents and Milipore MilliQ water. Prior to deposition, the Au surface was first degreased with acetone followed by washing in isopropyl alcohol and water. Before each deposition, the electrolyte was de-aerated with nitrogen gas. Deposition was conducted galvanostatically, by applying a constant current density in the range from −0.5 to −4 mA cm^{-2}, under mild stirring (200 rpm) using a magnetic stirrer bar. After deposition, the samples where thoroughly rinsed in water
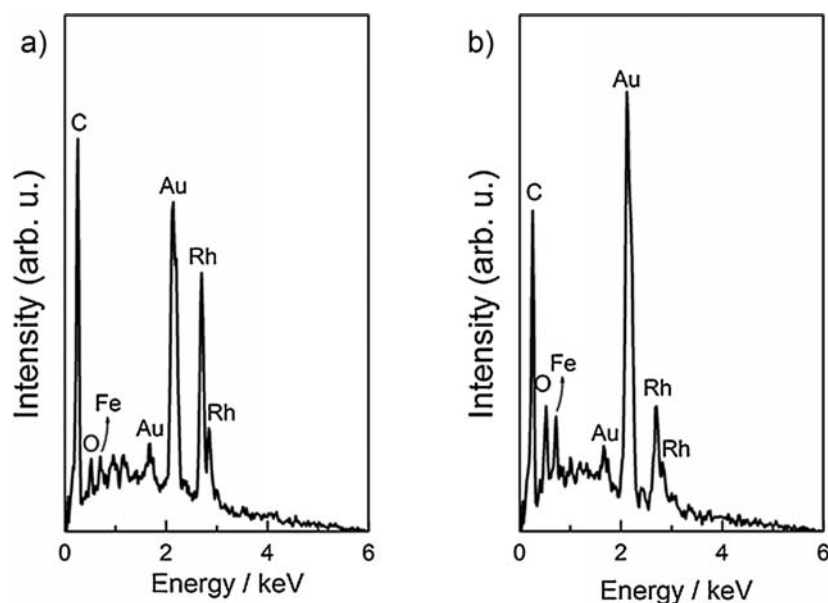
Fig. 4. Representative EDX patterns corresponding to NPs obtained at (a) $j = -0.5\,\text{mA cm}^{-2}$ for 1600 s and (b) $j = -4\,\text{mA cm}^{-2}$ for 200 s.

followed by 1 min sonication in methanol and stored in a low pressure container to minimize oxidation of the NPs.

2.2. Characterization

The morphology, size and composition of the Rh-Fe NPs were characterized with a Zeiss Merlin field emission scanning electron microscope (FE-SEM) equipped with an energy dispersive X-ray (EDX) detector. At least two replicas per condition were analysed. In order to determine the mean NP size, 100 NPs were counted per condition using the ImageJ software. The crystallographic structure of the electrodeposited NPs was studied by transmission electron microscopy (TEM) in a JEOL JEM-2011 microscope operated at 200 kV. Scanning transmission electron microscopy (STEM)-EDX line profile analyses were performed on a Tecnai F20 microscope. The NPs were scratched from the Au/Ti/Si substrate with an agate mortar. Complementary inductively coupled plasma mass spectroscopy (ICP-MS) analyses were conducted to determine the metal content. To ensure Rh dissolution, aqua regia was used. Measurements were done on a 7500ce spectrometer from agilent technologies. The oxidation state of the NPs was assessed by X-ray photoelectron spectroscopy (XPS). XPS analyses were carried out at room temperature on a PHI 5500 Multitechnique System (from Physical Electronics) spectrometer, equipped with a monochromatic X-ray source ($\text{K}\alpha_{\text{Al}}$ line with energy of 1486.6 eV and 350 W), placed perpendicular to the

analyser axis and calibrated using $3d^{5/2}$ line of Ag with a full width at half maximum (FWHM) of 0.8 eV. The analysed area was a 0.8 mm diameter disk surface for each sample. Charging effects were corrected by referencing the binding energies to that of the adventitious C1s line at 284.5 eV.

2.3. Electrocatalytic activity towards HER

The electrocatalytic activity of the NPs towards HER in alkaline medium was also explored in a conventional three-electrode cell, using a Ag|AgCl (3 M KCl) and a Pt spiral as reference and counter electrodes, respectively. The NPs previously deposited on Si/Ti/Au substrate served as the working electrode. Linear sweep voltammetry (LSV) and cyclic voltammetry (CV) measurements were conducted under stagnant conditions in de-aerated 0.1 M NaOH solution at 25 °C. The potential was scanned between −0.5 V and −1.5 V at a scan rate of 50 mV s^{-1}. The potential was held at −0.4 V during 5 min in LSV and in the first CV scan before sweeping the potential toward cathodic values. The stability of the catalysts was assessed by both cycling tests and chronoamperometry.

3. Results and discussion

3.1. Morphology and structure of the Rh-Fe NPs

A series of NPs with varying size and composition were prepared on Au/Ti/Si substrates by applying the following current densities: −0.5, −2, and −4 mA cm^{-2}. These values were chosen from cyclic voltammetry (CV) experiments (not shown).

In order to prevent the formation of continuous films, an Fe(III) salt was selected. It is known that the current efficiency of Fe(III) electrolytes is typically very low so that long deposition times are needed to obtain films [31]. Moreover the standard reduction potential of Fe (III) is −0.04 V whereas that of Fe (II) is −0.41 V. Taking into account that the standard reduction potential for Rh (III) is +0.44 V, the co-deposition of Fe and Rh from Fe (III) salts should be in principle more favourable. The E-t curves recorded during deposition are shown in Fig. 1. The potential remained fairly
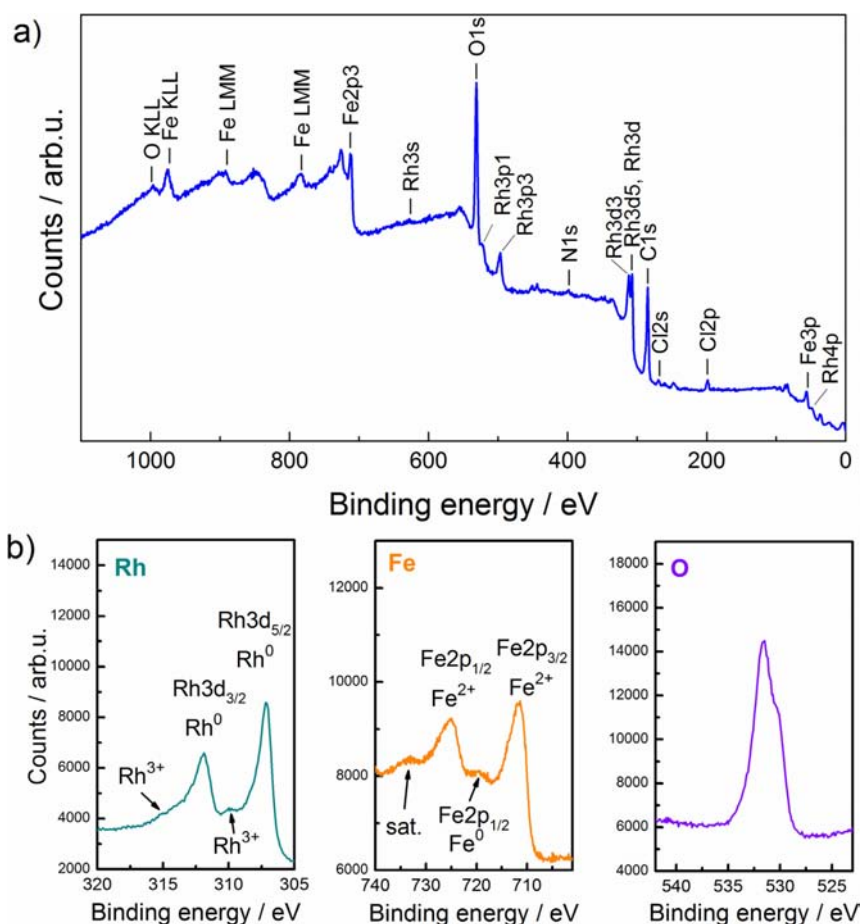
Table 2
Fe content (at%) determined by EDX in NPs grown at different current densities and deposition times. Oxygen was excluded before normalization. The standard deviation is ± 2-5 at%.

−j (mA cm^{-2})	at% Fe				
	t = 200 s	t = 400	t = 800	t = 1600	t = 3200
0.5	N/A	N/A	15	19	21
2	N/A	28	14	16	17
4	N/A	32	36	31	25

*N/A: Conditions leading to the smallest nanoparticles and/or the lowest coverage. The associated Fe amounts are not reported because they have high associated error.

Fig. 5. (a) XPS survey spectrum and detail of (b) Rh3d, Fe2p and O1s regions (before 1 min Ar sputtering) for NPs fabricated at $-0.5\,mA\,cm^{-2}$ for 1600s.

constant soon after deposition started. Rounded NPs at relatively moderate or high coverage were achieved in all conditions. Fig. 2 shows SEM images of the NPs grown at current densities of -0.5, -2, and $-4\,mA\,cm^{-2}$. At fixed deposition charge ($Q = 800\,mC$ cm^{-2}), the mean NP size decreased with the current density (cf. Fig. 2b and f). There are two factors that could explain the reduction in size with the current density at fixed deposition charge. Secondary reactions such as hydrogen co-evolution or electrogeneration of oxohydroxides are likely taking place coupled to the discharge of Rh and Fe ions, and they are enhanced at higher current densities. Additionally, as the current density is made more negative, the density of nucleation sites increases as well. Both factors would lead to smaller NPs.

For a fixed current density, finer NPs were obtained for shorter deposition times. Fig. 3a shows that NPs of ∼60 nm in diameter are obtained at $-0.5\,mA\,cm^{-2}$ for 3200 s of deposition time. At half deposition time, the mean NP diameter decreases to ∼40 nm (Fig. 3b). With further decrease of the deposition time (800 s) the NPs get apparently even smaller (Fig. 3c). Fig. S1 and S2 show FE-SEM images of NPs grown at $-2\,mA\,cm^{-2}$ and different deposition times as well. The trend is clear when comparing extreme deposition times (see Table 1), but fluctuations were noticed for intermediate deposition times due to the uncertainty of the image analysis for particle sizing and the inherent complexity of the deposition process. The histograms for all deposition conditions are shown in the Supporting Information (Fig. S3). Even though

monosized NPs are not achieved, which is probably the most challenging and not yet solved issue related to NPs growth by electrodeposition, relatively narrow particle size distributions are obtained up to 1600 s irrespective of the current density. At long deposition times (3200 s) the size distributions become broader as NPs tend to coalesce.

EDX analyses revealed the presence of Rh and Fe elements, together with Au (coming from the substrate), C and O (Fig. 4). Table 2 lists the amount of Fe (in at%) detected in NPs deposited within the selected experimental conditions. Although these values should be taken with care due to the small volume of deposited material, trends show that the Rh content decreases with an increase in the absolute value of current density. At a fixed current density, variations in the chemical composition with the deposition time were also noticed in spite of stirring the solution. At current densities of -0.5 and $-2\,mA\,cm^{-2}$ and at a fixed time, the composition of the NPs remained the same. Upon increasing of current density, the Fe content increases. Complementary ICP-MS analyses were in concordance with the observed trends. This is in agreement with some observations made by Tabakovic et al. in their studies of electrodeposited CoFeRh alloy films [32]. In their work, similar trends were observed regarding the Fe and Rh content with the applied current density. Since Rh is nobler than Fe, the growth of Rh-rich deposits is in principle expected at low overpotentials (or current densities). Likewise, Fe discharge is to be favoured at higher overpotentials (or current densities). It is
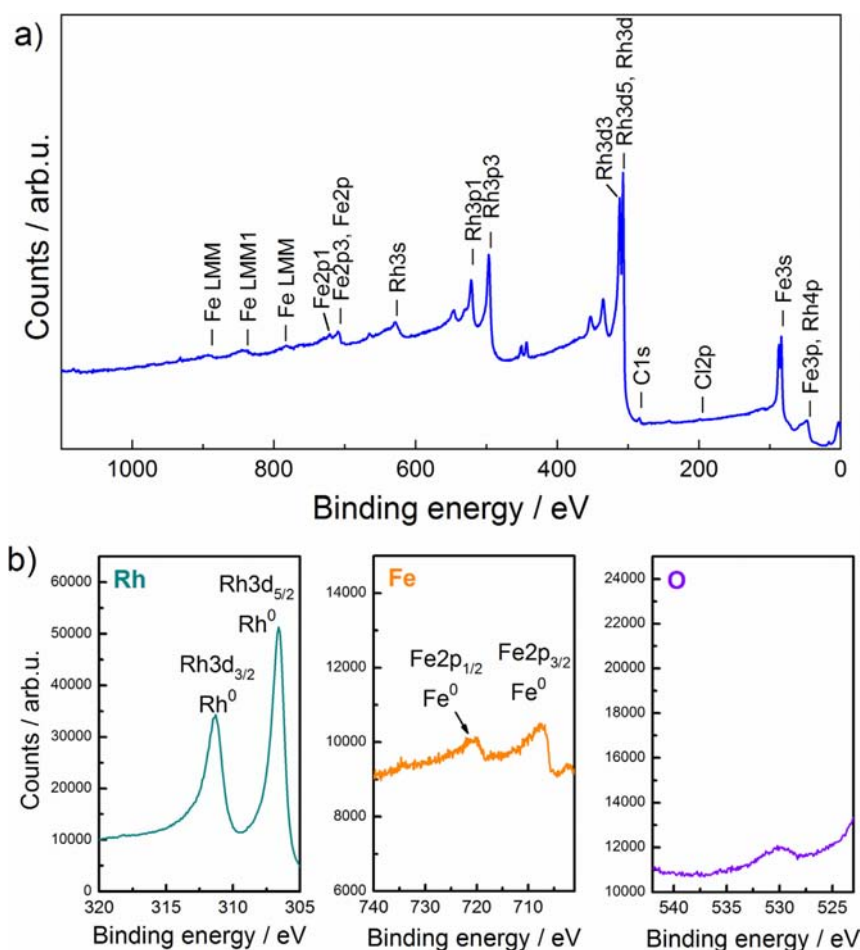
Fig. 6. (a) XPS survey spectrum and detail of (b) Rh3d, Fe2p and O1s regions (after 1 min Ar sputtering) for NPs fabricated at $-0.5\,\mathrm{mA\,cm^{-2}}$ for 1600s.

conjectured that Rh(III) discharge is mainly controlled by diffusion [33]. Other studies suggest that Rh growth proceeds via mixed kinetics, charge transfer and diffusion [34]. Fe is likely activation-controlled within the deposition potentials range used in this study. As a result the NPs become gradually enriched in Fe upon making the overpotential more negative.

XPS measurements were performed in order to gain further insight on the chemical composition of the NPs. Measurements were carried out both before and after Ar ions sputtering for 1 min. Fig. 5a displays the survey spectrum (taken before Ar sputtering) of NPs electrodeposited at $-0.5\,\mathrm{mA\,cm^{-2}}$ for 1600s. The spectrum shows the presence of Rh, Fe, O, C, N and Cl elements. The latter (C, N and Cl) are appended to surface contamination. Nevertheless, C is also a typical impurity in electrodeposited metals and alloys [35]. In our case, glycine decomposition could well be a source of C. The small peak of chlorine can be well attributed to the electrolyte

residue remaining after samples' washing. The corresponding Rh3d, Fe2p and O1s core-level electronic transitions are given in Fig. 5b. Regarding Rh3d signal, the $3d_{5/2}$ and $3d_{3/2}$ doublet peaks located at 307.1 and 311.9 eV, respectively, correspond to the zero oxidation state of Rh ($\Delta_{\mathrm{metal}} = 4.8\,\mathrm{eV}$). Besides, they show the typical asymmetric peak shape for Rh metal [36]. The higher binding energy shoulders located at 309.7 and 314.2 eV can be attributed to Rh(III). The presence of Rh_2O_3 in the NPs is not unexpected. Actually, Rh_2O_3 was detected by XPS in electrodeposited Rh films from $RhCl_3$-NH_4Cl solution at pH = 4 [37]. Concerning the Fe2p core level XPS spectrum, the position of $Fe2p_{3/2}$ peak (711.7 eV) and $Fe2p_{1/2}$ peak (725.3 eV) are characteristics of Fe^{2+} [38]. The shoulder in between could be assigned to metallic Fe. The O1s spectrum shows a relatively intense double peak with two maxima at 532 eV, typical for metal hydroxides (M_xOH_y) and at 530 eV, distinctive for metal oxides (M_xO_y). Tabakovic et al. also noticed relatively high contents of oxygen (32 at%) in electrodeposited Rh films [37].

After 1 min Ar ions sputtering, the O signal in the corresponding XPS survey pattern and core-level transition detail is clearly reduced (Fig. 6a and b). Interestingly, the Rh3d signal only shows the doublet assigned to Rh metal (Fig. 6b). Likewise, the peaks assigned to zero-valent Fe (707.6 eV for $2p_{3/2}$ and 720.4 eV for $2p_{1/2}$) [37] clearly emerge. Nevertheless, care should be taken

Table 3
Rh, Fe and O content in the NPs as determined by XPS both before and after Ar ions sputtering for NPs fabricated at $-0.5\,\mathrm{mA\,cm^{-2}}$ at 1600s.

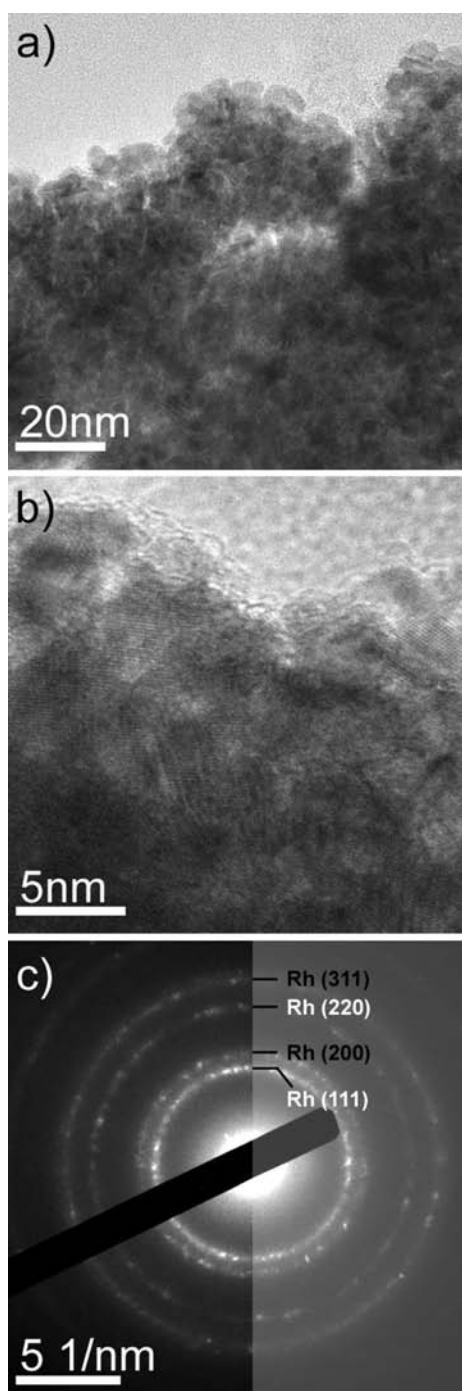|	at% Rh	at% Fe	at% O
before Ar ions sputtering	11	19	70
after Ar ions sputtering	86	14	< 1

Fig. 7. (a) TEM and (b) HRTEM images and (c) SAED pattern of NPs obtained at −0.5 mA cm^{-2} for 1600 s.

when analysing the oxidation state of iron oxides since reduction of iron oxidation state by Ar-ions bombardment has been observed, in particular from Fe^{3+} to Fe^{2+} [39]. Full reduction of Fe^{2+} toward $Fe°$ upon Ar-ions irradiation is less probable and indeed STEM-EDX analyses indicate that the oxygen signal is rather low.
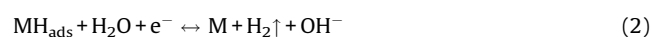
Table 3 shows the Rh, Fe and O amounts (in at%) for NPs electrodeposited at −0.5 mA cm^{-2} for 1600s determined by XPS before and after Ar ions sputtering. It is clear that the oxygen signal

greatly diminishes down to less than 1 at% after Ar ions sputtering. Similar results were obtained for other Rh-Fe NPs. This result suggests that the NPs have oxidized surfaces. Nevertheless, assuming a sputter rate of about 7–10 nm min^{-1}, the results indicate that the oxidized shell is indeed very thin and hence, the NPs are mostly metallic. Bearing in mind the nobility of Rh, the detection of Rh(III) by XPS before sputtering suggests that Rh oxides already form during deposition, in agreement with Tabakovic et al. [37] Concerning Fe, oxides could also form during electrodeposition as for Rh or show afterwards. Fe is prone to oxidation on standing in air, a phenomenon that is exacerbated in nanoscale materials [40]. Notice that the samples were not stored in high vacuum. Yet, the NPs displayed similar levels of oxygen both in the as-deposited state and after storage for a few days. Therefore eventual passivation likely takes place immediately after electrodeposition.

HRTEM was used to retrieve structural information of the NPs. It is worth mentioning that the NPs were very well adhered to the substrate since ultrasonication did not cause detachment of the NPs even for long sonication times. Fig. 7a shows most probably part of an aggregate of a few NPs. A close-up image reveals that the NP is composed of small crystallites of less than 5 nm (Fig. 7b). An extremely thin (ca. 1 nm-thick) layer is seen at the uttermost surface. The lattice fringes are evident, which demonstrates that the NPs are highly crystalline. Additional HRTEM images are shown in the Supporting Information (Fig. S4). The selected area electron diffraction (SAED) pattern, taken on an aggregate of NPs (Fig. 7c), shows spotty rings. The corresponding interplanar distances match those of (111), (200), (220) and (311) planes of cubic metallic Rh (PCPDF 05-0685). Some distances are also consistent with iron and rhodium oxides (Rh_2O_3), in agreement with XPS results. In order to determine the Fe distribution within the NPs, STEM-EDX line scan analyses were performed. Representative results are provided in Fig. 8. Fe was found to be homogeneously distributed within the NPs. Moreover, a uniform distribution was also disclosed when analysing the single crystallites (about 3–4 nm in size) which compose the bimetallic NPs.

3.2. Electrocatalytic activity

The deposited NPs were expected to be suitable candidates for HER not only because of their chemical composition but also because of the high surface area. Fig. 9 shows the LSV curves recorded in Ar-purged NaOH 0.1 M at a sweeping rate of 50 mV s^{-1} for different Rh-Fe NPs. NPs featuring different Fe contents (between 16 and 36 at% Fe) obtained at deposition times up to 1600 s were selected. For comparison, the LSV curve of the bare Si/Ti/Au substrate is shown. While the Au surface shows almost negligible catalytic activity, the NPs are active toward HER. A large density of hydrogen bubbles emerging from the Rh-Fe NPs was visible at naked eye when the potential passed by −1.2 V toward the negative direction. There is an agreement that HER mechanism in alkaline media consists of three steps [19]:

$$M + H_2O + e^- \leftrightarrow MH_{ads} + OH^- \tag{1}$$

$$MH_{ads} + H_2O + e^- \leftrightarrow M + H_2\uparrow + OH^- \tag{2}$$

$$2MH_{ads} \leftrightarrow 2M + H_2\uparrow \tag{3}$$

The first reaction (Eq. 1), which involves the electroreduction of water into adsorbed hydrogen, is termed Volmer reaction. This is followed by the electrochemical hydrogen desorption (Eq. 2) known as Heyrovsky reaction, or the chemical hydrogen
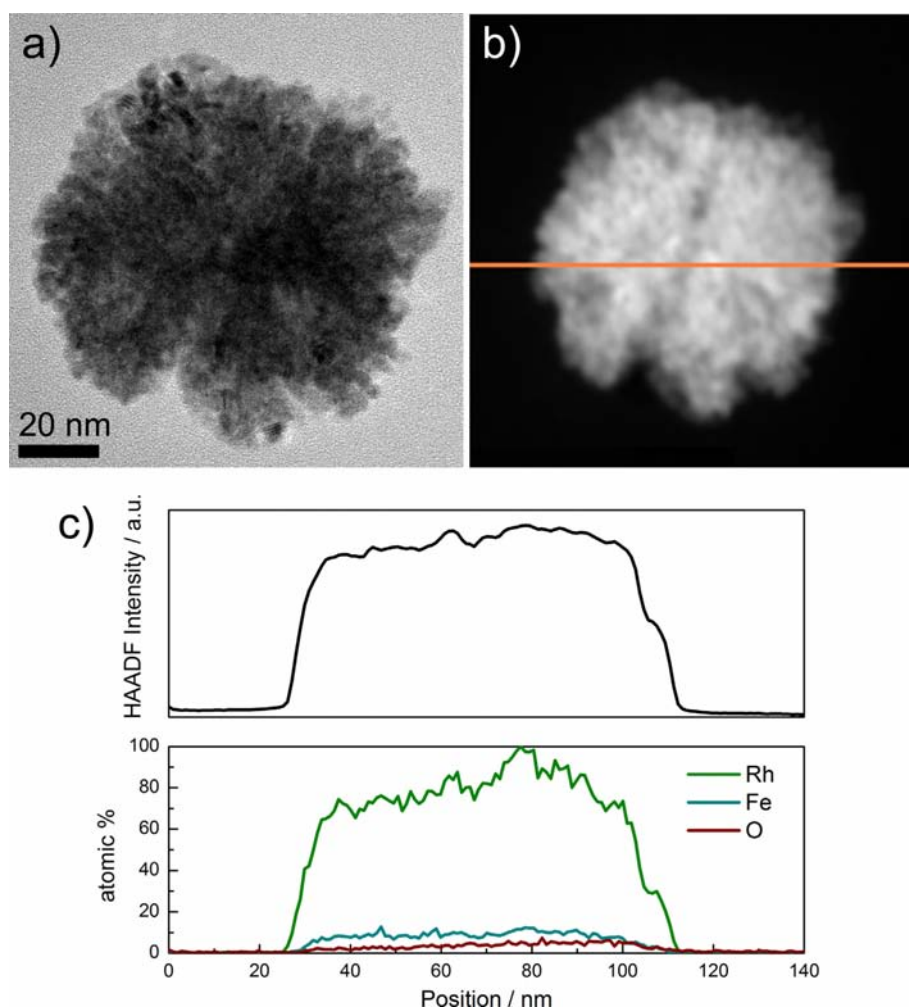
Fig. 8. (a) TEM, (b) STEM images and (c) EDX line scan of a Rh-Fe NP obtained at $-0.5\,\mathrm{mA\,cm^{-2}}$ for 1600 s. Mean Fe content is 15 at%, in agreement with Table 1.

desorption (Eq. 3) known as Tafel reaction. The Heyrovsky and Tafel reactions proceed either alternatively or simultaneously. Note that 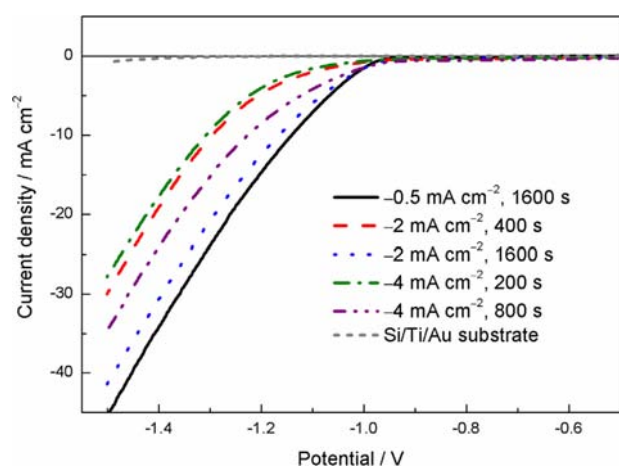although M designates the metal, both metallic and oxidized forms of Fe and Rh would contribute. Since HER takes place at the surface of the NPs, the role of a partially oxidized shell coating the NPs cannot be neglected.

Slightly different onset potentials for H_2O reduction toward H_2 were observed depending on the electrodeposition conditions used to grow the NPs. The sample obtained at $-0.5\,\mathrm{mA\,cm^{-2}}$ for 1600 s exhibits the best performance. The corresponding onset potential for HER is $-0.93\,\mathrm{V}$, whereas the rest of the samples show more negative values (Table 4). Interestingly, at a potential of $-1.2\,\mathrm{V}$ the corresponding current density is not far away to the value reported for polycrystalline Pt ($j \sim 13\,\mathrm{mA\,cm^{-2}}$) tested in 0.1 M NaOH, although at a lower scan rate of $10\,\mathrm{mV\,s^{-1}}$ [23]. The

Fig. 9. LSV curves in 0.1 M NaOH ($50\,\mathrm{mV\,s^{-1}}$) of Rh-Fe NPs obtained at different current densities and deposition times.

Table 4
Onset potential for HER and current density at $-1.2\,\mathrm{V}$ for NPs deposited at different electrodeposition conditions. Values are extracted from the LSV curves shown in Fig. 8.

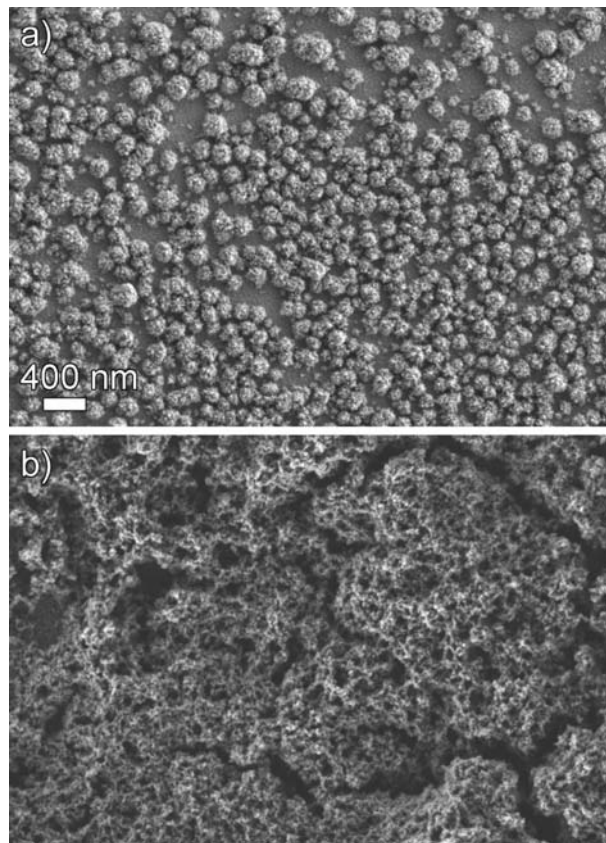| Electrodeposition conditions	Onset potential for HER/V	$-j/\mathrm{mA\,cm^{-2}}$ at $E = -1.2\,\mathrm{V}$
$-0.5\,\mathrm{mA\,cm^{-2}}$, 1600 s	-0.93	15.0
$-2\,\mathrm{mA\,cm^{-2}}$, 400 s	-0.95	4.7
$-2\,\mathrm{mA\,cm^{-2}}$, 1600 s	-0.95	12.2
$-4\,\mathrm{mA\,cm^{-2}}$, 200 s	-0.96	4.1
$-4\,\mathrm{mA\,cm^{-2}}$, 800 s	-0.94	8.4

Fig. 10. SEM image of (a) pure Rh NPs electrodeposited at $-0.5\,\text{mA}\,\text{cm}^{-2}$ for 1600 s from an Fe-free bath containing 0.5 mM Cl_6Na_3Rh + 0.05 M glycine + 0.05 M NaCl (pH = 2.4) and b) pure Fe electrodeposited at $-4\,\text{mA}\,\text{cm}^{-2}$ for 1600 s from a Rh-free bath containing 0.01 M $FeCl_3$ + 0.05 M glycine + 0.05 M NaCl (pH = 2.4). Scale bar is the same for both images.

outperforming NPs are Rh-rich (19 at% Fe as listed in Table 2) and show moderate substrate coverage. However, since changes in composition, nanoparticle size and coverage degree occur simultaneously with varying the current density during the electrodeposition step, it is difficult to draw straightforward conclusions. Nevertheless, upon carefully examining the LSV curves, some other interesting features emerge. For example, although the electrocatalytic activity of the NPs deposited at

$-4\,\text{mA}\,\text{cm}^{-2}$ for 800 s diminishes compared to that of NPs deposited at $-0.5\,\text{mA}\,\text{cm}^{-2}$ for 1600 s, its Fe content is much higher (36 at%). Therefore, there is a trade-off between the slight loss in electrocatalytic activity and the partial replacement of pricy Rh by cheaper and more abundant Fe.

For the aim of comparison pure Rh and Fe materials were electrodeposited from Fe-free and Rh-free electrolytes,
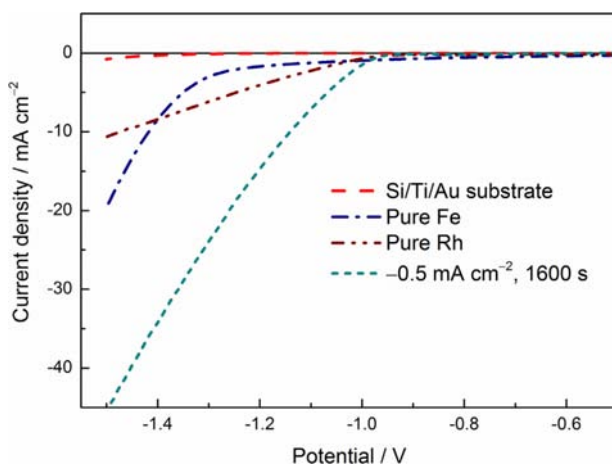

Fig. 11. LSV curves in 0.1 M NaOH ($50\,\text{mV}\,\text{s}^{-1}$) of bare Au surface (Si/Ti/Au substrate), pure Rh and pure Fe materials, and the outperforming Rh-Fe NPs (at the indicated current density and deposition time).
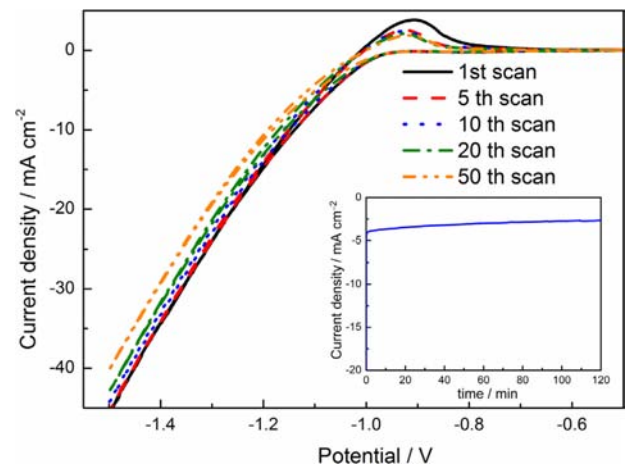

Fig. 12. CV curves in 0.1 M NaOH ($50\,\text{mV}\,\text{s}^{-1}$) of Rh-Fe NPs obtained at j = -0.5 $\text{mA}\,\text{cm}^{-2}$ and 1600 s. The inset shows the j vs. t curve for an applied potential of -1.1 V.
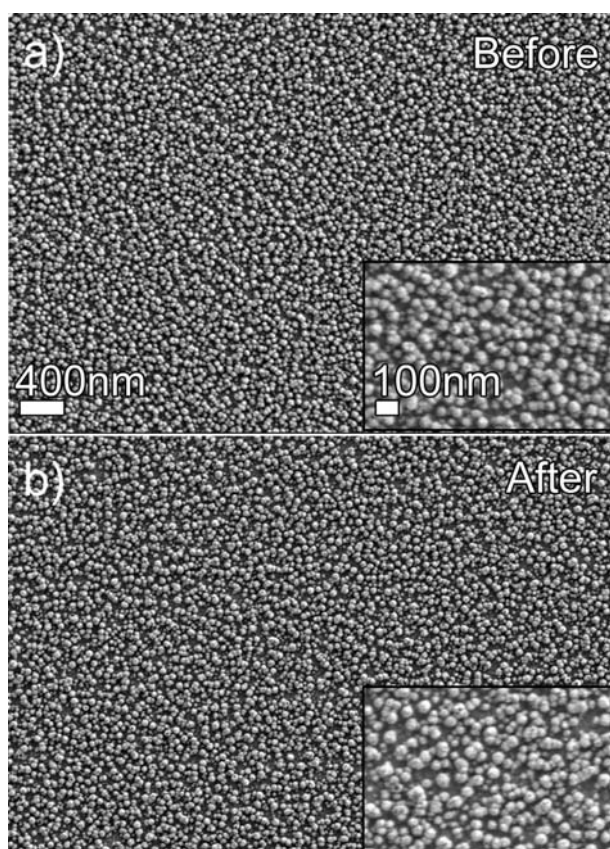
Fig. 13. FE-SEM images taken (a) before and (b) after 50CV cycles of Rh-Fe NPs obtained at j = −0.5 mA cm^{-2} for 1600s.

respectively. Although baths were similar to that of Rh-Fe, both the coverage degree and the morphology were distinct (Fig. 10), which indicates that there is a synergistic effect when Rh and Fe are electrodeposited together. Pure Rh can be deposited as NPs but their surface looks much rougher as reported by Kibler et al. [41] These authors showed that electrodeposition of Rh at low overpotentials start with the formation of a bilayer and that further deposition proceeds via a Stranski-Krastanov growth
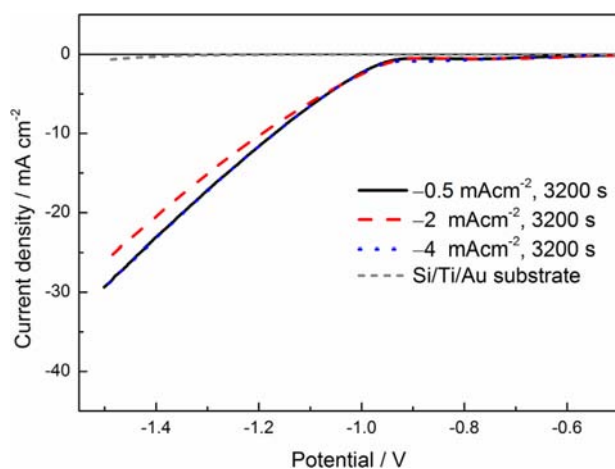
mode, accompanied by a strong roughening of the surface. Moreover, at a current density of −0.5 mA cm^{-2} and 1600 s of deposition time the mean size is larger than that of Rh-Fe NPs grown under the same conditions (Fig. 3(b)). Pure Fe did not form NPs but, instead, a highly porous film developed onto the electrode. In this case it was necessary to apply a current density of −4 mA cm^{-2} in order to get some deposition. Interestingly, both pure Rh and Fe are less active than most of the Rh-Fe NPs. The corresponding LSV curves are compared with that of the out-performing Rh-Fe NPs in Fig. 11.

Bimetallic systems often show improved electrocatalytic activity compared to their pure counterparts. Synergisms, modification of electronic/chemical properties or geometric considerations have been advocated as responsible for the improvement. Introducing another element into the lattice of a given metal is an effective way to modify its electronic/chemical properties by creating a bimetallic surface through: i) formation of heteroatom bonds leading to a ligand effect, and ii) alteration of the average metal–metal bond length, resulting in a strain (e.g. compressive or tensile) effect [20]. Besides the aforementioned changes in morphology (i.e., geometric features), the formation of a bimetallic surface likely gives rise to modifications of the electronic properties of both Rh and Fe metals and alters the average Rh-Rh metal bond. This might partially explain the observed enhancement of the HER activity.

In order to examine the stability of the catalysts, the Rh-Fe NPs were subjected to 50CV cycles in 0.1 M NaOH electrolyte within the potential range from −0.5 V to −1.5 V (Fig. 12 and Fig. S5-S9). Fig. 12 shows the 1st, 5th, 10th, 20th and 50th CV corresponding to the

Fig. 14. LSV curves 0.1 M NaOH (50 mV s^{-1}) of Rh–Fe NPs obtained at different current densities and fixed long deposition time (3200 s).
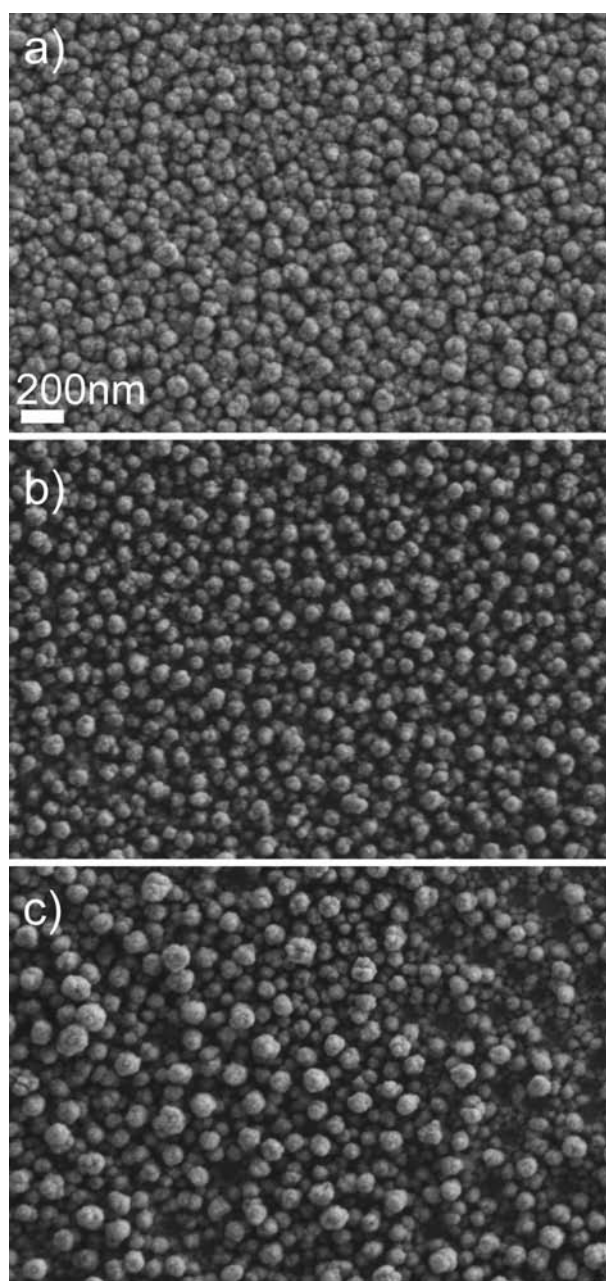
Fig. 15. FE-SEM images of NPs obtained at (a) j = −0.5 mA cm^{-2}, (b) −2 mA cm^{-2} and (c) −4 mA cm^{-2} for 3200 s of deposition time. Scale bar is the same for all images.

sample obtained at −0.5 mA cm^{-2} for 1600 s (i.e., the best performing HER catalyst). It can be seen that the electrocatalytic activity starts to slightly fade from the 10th cycle, although the loss is not pronounced. The broad oxidation band recorded ca. −0.95 V corresponds to the oxidation of H$_2$ adsorbed onto the catalyst. In order to reveal possible changes on NP morphology and composition, FE-SEM images were taken after the HER tests (Fig. 13). No big changes in NP morphology were noticed when comparing the images before and after the HER experiments. The chemical composition remained the same although the density of NPs seemingly diminished a little bit. Stability was also assessed by means of chronoamperometry at −1.1 V (inset of Fig. 12). A reduction of 35% of the current density was observed after holding the potential for 2 h. The previously observed decrease of NP

density can partly explain such apparent decrease in the catalytic activity. Nevertheless, the loss in not pronounced and an increase in the electrocatalytic activity was indeed observed in some cases (Fig. S9). Therefore, the here-developed substrate-supported Rh-Fe NPs hold promise in hydrogen production.

Finally, the HER activity of Rh–Fe NPs obtained at −0.5, −2 and −4 mA cm^{-2} but longer deposition times (3200 s) show a declined electrocatalytic activity (Fig. 14) probably due to an exceedingly large coverage and concomitant decrease of the surface area. In fact, the samples obtained under these conditions show bigger particles (Fig. 15). Deposits feature more than one layer of NPs (see for instance Fig. 15c) so that one can refer to them as 'nanoparticulate films'. This result puts forward the importance of high surface area for enhancing HER activity.

4. Conclusions

Rh and Fe can be successfully co-deposited in the form of NPs by means of a low-cost method directly on a substrate. NPs showing tunable composition and size have been obtained by galvanostatic electrodeposition from the same electrolyte formulation. Relatively narrow particle size distributions were obtained within the studied range of current densities and up to 1600 s of deposition time. Larger deposition times render nanoparticulate-like films. The Fe content could be increased from 15 at% to 36 at% by increasing the applied current density. In this way, Rh can be partially replaced by a more abundant and less expensive element like Fe. XPS measurements are consistent with the presence of mainly metallic NPs. The electrocatalytic activity toward HER has been assessed in alkaline media with good results. Tunable HER performance has been observed depending on the electrodeposition conditions utilized to grow the NPs. The present work indicates that electrodeposition is a convenient method to prepare substrate-supported Rh-Fe based NPs for hydrogen production.

Acknowledgements

Appendix A. Supplementary data

Supplementary data associated with this article can be found, in the online version, at http://dx.doi.org/10.1016/j.electacta.2016.02.112.

References

[1] Nanoscale Materials (eds L. M. Liz-Marzán, P. V. Kamat), Kluwer Academic Publishers, Springer, 2003.

[2] J.M. Pingarrón, P. Yáñez-Sedeño, A. González-Cortés, Gold nanoparticle-based electrochemical biosensors, Electrochim. Acta 53 (2008) 5848–5866.

[3] H. Wei, Plasmonic silver nanoparticles for energy and optoelectronic applications, in: K. Lu, N. Manjooran, M. Radovic, E. Medvedovski, E.A. Olevsky, C. Li, G. Singh, N. Chopra, G. Pickrell (Eds.), Advances in Nanomaterials and Nanostructures, vol. 229, John Wiley & Sons, Inc., Hoboken, NJ, USA, 2011.

[4] M. Estrader, A. López-Ortega, S. Estradé, I.V. Golosovsky, G. Salazar-Alvarez, M. Vasilakaki, K.N. Trohidou, M. Varela, D.C. Stanley, M. Sinko, M.J. Pechan, D.J. Keavney, F. Peiró, S. Suriñach, M.D. Baró, J. Nogués, Robust antiferromagnetic coupling in hard-soft bi-magnetic core/shell nanoparticles, Nature Commun. 4 (2013) 2960.

[5] P. He, H. Liu, Z. Li, Y. Liu, X. Xu, J. Li, Electrochemical deposition of silver in room-temperature ionic liquids and its surface-enhanced raman scattering effect, Langmuir 20 (2004) 10260–10267.

[6] D. Zhang, W.C. Chang, T. Okajima, T. Ohsaka, Electrodeposition of platinum nanoparticles in a room-temperature ionic liquid, Langmuir 27 (2011) 14662–14668.

[7] B. Özkale, E. Pellicer, M.A. Zeeshan, J.F. López-Barberá, J. Nogués, J. Sort, B.J. Nelson, S. Pané, One-pot electrosynthesis of multi-layered magnetic metallopolymer nanocomposites, Nanoscale 6 (2014) 4683–4690.

[8] M.S. El-Deab, On the preferential crystallographic orientation of Au nanoparticles: effect of electrodeposition time, Electrochim. Acta 54 (2009) 3720–3725.

[9] Y.-X. Chen, S.-P. Chen, Z.-Y. Zhou, N. Tian, Y.-X. Jiang, S.-G. Sun, Y. Ding, Z.L. Wang, Tuning the shape and catalytic activity of Fe nanocrystals from rhombic dodecahedra and tetragonal bipyramids to cubes by electrochemistry, J. Am. Chem. Soc. 131 (2009) 10860–10862.

[10] Y. Li, P. Diao, T. Jin, J. Sun, D. Xu, Shape-controlled electrodeposition of standing Rh nanoplates on indium tin oxide substrates and their electrocatalytic activity toward formic acid oxidation, Electrochim. Acta 83 (2012) 146–154.

[11] J. Schulz, A. Roucoux, H. Patin, Unprecedented efficient hydrogenation of arenes in biphasic liquid–liquid catalysis by re-usable aqueous colloidal suspensions of rhodium, Chem. Commun. (1999) 535.

[12] Y. Motoyama, M. Takasaki, S.H. Yoon, I. Mochida, H. Nagashima, Rhodium nanoparticles supported on carbon nanofibers as an arene hydrogenation catalyst highly tolerant to a coexisting epoxido group, Org. Lett. 11 (2009) 5042–5045.

[13] J.M. Ziegelbauer, D. Gatewood, F. Gullá, J.F. Andrea, M. Guinel, F. Ernst, D.E. Ramaker, S. Mukerjee, Fundamental investigation of oxygen reduction reaction on rhodium sulfide-based chalcogenides, J. Phys. Chem. C 113 (2009) 6955–6968.

[14] H. Lam-Wing, M.J. Weaver, Adsorption and electrooxidation of some simple organic molecules on rhodium(111) as probed by real-time FTIR spectroscopy: Comparisons with platinum (111), J. Phys. Chem. 93 (1989) 7218–7226.

[15] B.R. Sathe, High aspect ratio rhodium nanostructures for tunable electrocatalytic performance, Phys. Chem. Chem. Phys. 15 (2013) 7866–7872.

[16] M. Doyle, G. Rajendran, Handbook of Fuel Cells Fundamentals, Technology and Applications, John Wiley & Sons, Chichester, U.K, 2003.

[17] M.A. Haider, M.R. Gogate, R.J. Davis, Fe-promotion of supported Rh catalysts for direct conversion of syngas to ethanol, J. Catal. 261 (2009) 9–16.

[18] I. Nakamula, Y. Yamanoi, T. Imaoka, K. Yamamoto, H. Nishihara, A uniform bimetallic rhodium/iron nanoparticle catalyst for the hydrogenation of olefins and nitroarenes, Angew. Chem. 123 (2011) 5952–5955.

[19] F. Safizadeh, E. Ghali, G. Houlachi, Electrocatalysis developments for hydrogen evolution reaction in alkaline solutions −A review, Int. Hydrog. Energy 40 (2015) 256–274.

[20] Y. Zheng, Y. Jiao, M. Jaroniec, S.Z. Qiao, Advancing the electrochemistry of the hydrogen-evolution reaction through combining experiment and theory, Angew. Chem. Int. Ed. 54 (2015) 52–65.

[21] P.K. Wrona, A. Lasia, M. Lessard, H. Ménard, Kinetics of the hydrogen evolution reaction on a rhodium electrode, Electrochim. Acta 37 (1992) 1283–1294.

[22] R. Palaniappan, D.C. Ingram, G.G. Botte, Hydrogen evolution reaction kinetics on electrodeposited Pt-M (M = Ir, Ru Rh, and Ni) cathodes for ammonia electrolysis electrochemical engineering, J. Electrochem. Soc. 161 (2004) E12–E22.

[23] M. Smiljanic, Z. Rakocevic, A. Maksic, S. Strbac, Hydrogen evolution reaction on platinum catalyzed by palladium and rhodium nanoislands, Electrochim. Acta 117 (2014) 336–343.

[24] J.-R. McKone, S.-C. Marinescu, B.S. Brunschwig, J.R. Winkler, H.B. Gray, Earth-abundant hydrogen evolution electrocatalysts, Chem. Sci. 5 (2014) 865–878.

[25] R. Subbaraman, D. Tripkovic, K.-C. Chang, D. Strmcnik, A.P. Paulikas, P. Hirunsit, M. Chan, J. Greely, V. Stamenkovic, N.M. Markovic, Trends in activity for the water electrolyser reactions on 3d M(Ni, Co, Fe, Mn) hydr(oxy) oxide catalysts, Nature Mater. 11 (2012) 550–557.

[26] A.T. Miller, B.L. Hassler, G.G. Botte, Rhodium electrodeposition on nickel electrodes used for urea electrolysis, J. Appl. Electrochem. 42 (2012) 925–934.

[27] S.-H. Son, H.-K. Lee, S.-C. Park, Kinetics of rhodium electrodeposition for semiconductor interconnect applications, Surf. Interface Anal. 42 (2012) 1244–1246.

[28] M. Izaki, Electrodeposition of Iron and Iron alloys, in: M. Schlesinger, M. Paunovic (Eds.), Modern electroplating, Fifth edition, John Wiley & Sons, Inc., Hoboken, NJ, USA, 2010.

[29] R.D. Noce, A.V. Benedetti, E.C. Passamani, H. Kumar, D.R. Cornejo, M. Magnani, Use of conventional electrochemical techniques to produce crystalline FeRh alloys induced by Ag seed layer, J. Alloys Compd. 573 (2013) 37–42.

[30] S. Salem-Sugui Jr., A.D. Alvarenga, R.D. Noce, R.B. Guimarães, C. Salazar Mejia, H. Salim, F.G. Gandra, Anomalous metamagnetic-like transition in a FeRh/Fe₃Pt interface occurring at T ≈ 120 K in the field-cooled-cooling curves for low magnetic fields, AIP Adv. 2 (2012) 032168.

[31] Electrochemical Production of Metal Powders (ed S. S. Djokić), Springer, 2012, p. 281.

[32] I. Tabakovic, S. Riemer, V. Vas'ko, M. Kief, CoFeRh alloys: Part 2. Electrodeposition of CoFeRh alloys with high saturation magnetic flux density and high corrosion resistance, Electrochim. Acta 53 (2008) 8008–8014.

[33] K. Mech, P. Żabiński, R. Kowalik, Analysis of rhodium electrodeposition from chloride solutions electrochemical/electroless deposition, J. Electrochem. Soc. 161 (2014) D458–D461.

[34] S. Langerock, L. Heerman, Study of the electrodeposition of rhodium on polycrystalline gold electrodes by quartz microbalance and voltammetric techniques, J. Electrochem. Soc. 151 (2004) C155–C160.

[35] Y.M. Wang, S. Cheng, Q.M. Wei, E. Ma, T.G. Nieh, A. Hamza, Effects of annealing and impurities on tensile properties of electrodeposited nanocrystalline Ni, Scripta Mater. 51 (2004) 1023–1028.

[36] http://xpssimplified.com/elements/rhodium.php.

[37] I. Tabakovic, J.-M. Qiu, S. Riemer, M. Sun, V. Vas'ko, M. Kief, CoFeRh alloys: Part 1. Electrodeposition of Rh and nonmagnetic CoFeRh alloy, Electrochim. Acta 53 (2008) 2483–2493.

[38] Handbook of Surfaces and Interfaces of Materials, Five-Volume Set (eds Hari Singh Nalwa), Academic Press, 2001, pp. 566–567.

[39] S. Suzuki, K. Sugiyama, Y. Waseda, Changes in the chemical state and composition of the surface of iron oxides due to argon ion sputtering, J. Surf. Anal. 9 (2002) 455–458.

[40] C.S. Tiwary, S. Kashyap, K. Biswas, K. Chattopadhyay, Synthesis of pure iron magnetic nanoparticles in large quantity, J. Phys. D: Appl. Phys. 46 (2013) 385001.

[41] L.A. Kibler, M. Kleinert, D.M. Kolb, The initial stages of rhodium deposition on Au(111), J. Electroanal. Chem. 467 (1999) 249–257.

Supplementary data

Electrodeposition of sizeable and compositionally tunable rhodium-iron nanoparticles and their activity toward hydrogen evolution reaction

Irati Golvano-Escobal, Santiago Suriñach, Maria Dolors Baró, Salvador Pané[*], Jordi Sort[ξ] and Eva Pellicer[¥]
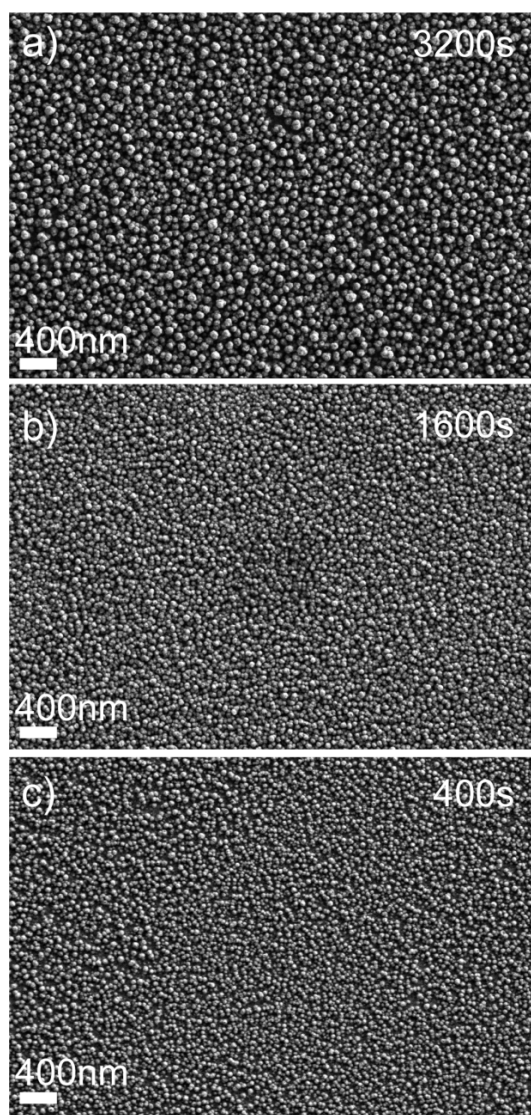
Figure S1. FE-SEM images of NPs obtained at j= –2 mA cm^{-2} for different deposition times (3200, 1600 and 400 s).

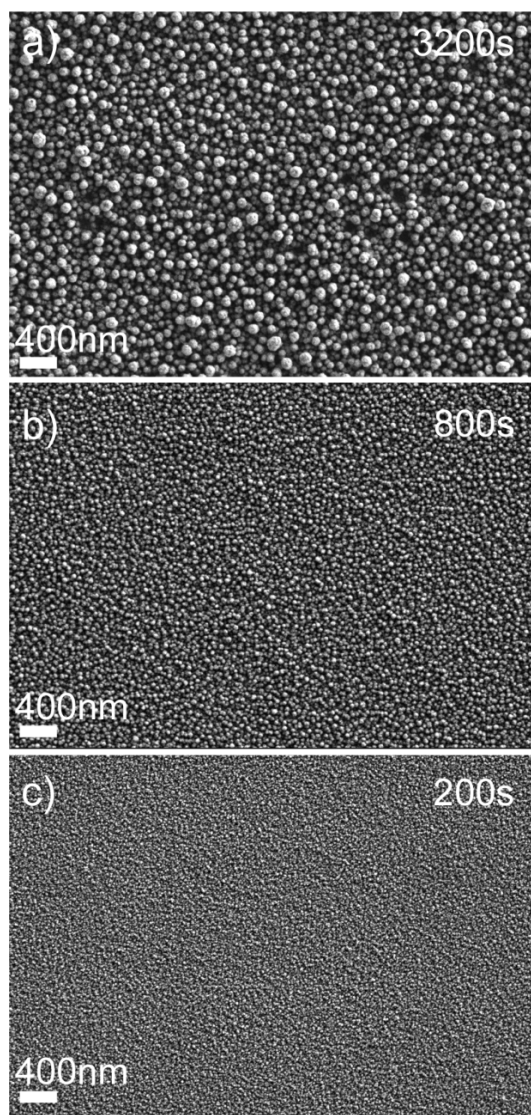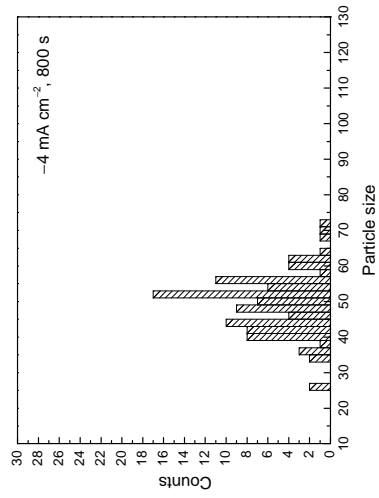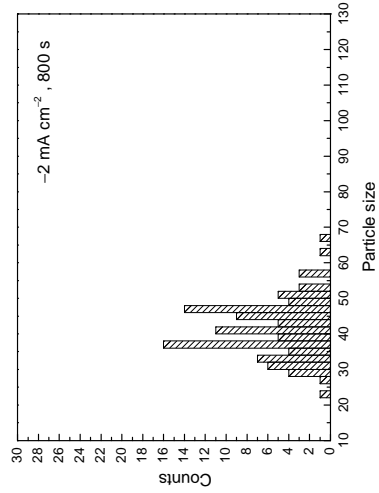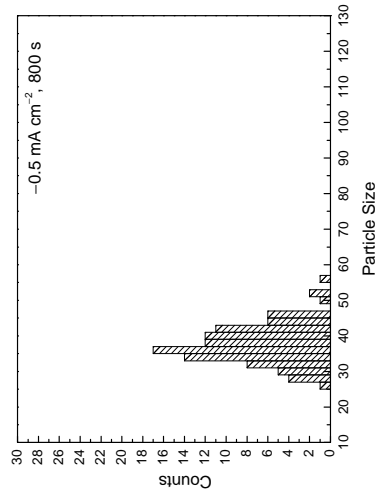Figure S2. FE-SEM images of NPs obtained at j= –4 mA cm^{-2} for different deposition times (3200, 800 and 200 s).

Figure S3. Particle size distribution at the indicated current densities and deposition times.

In the following sheets the size distribution histograms for NPs electrodeposited under the studied electrodeposition conditions are shown.
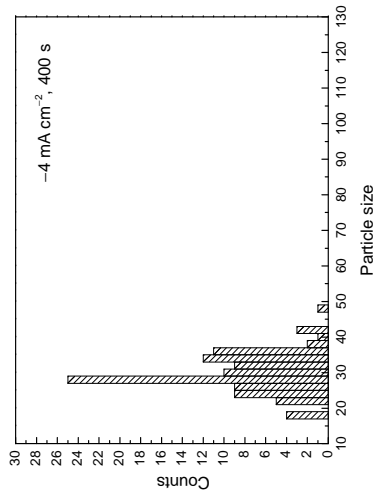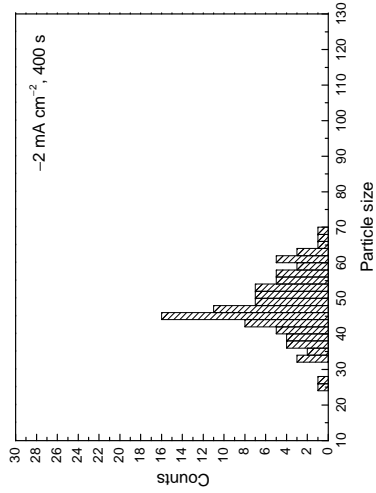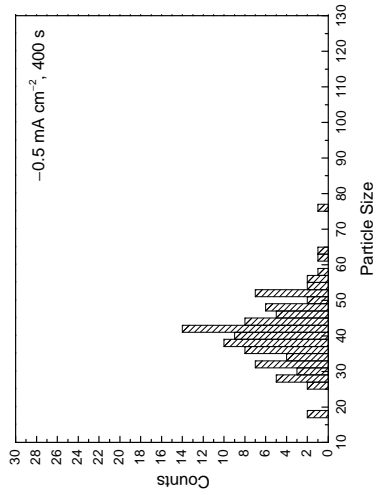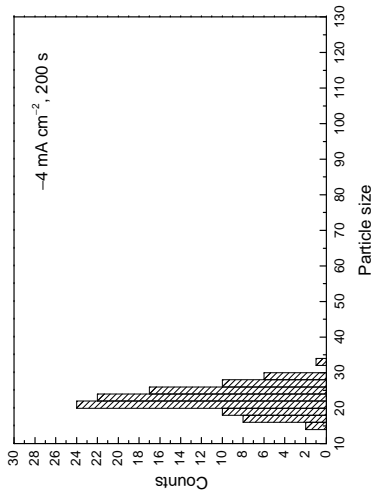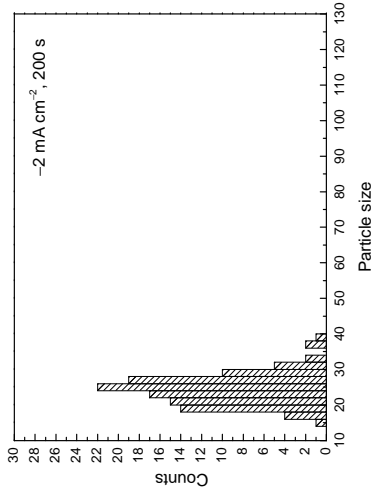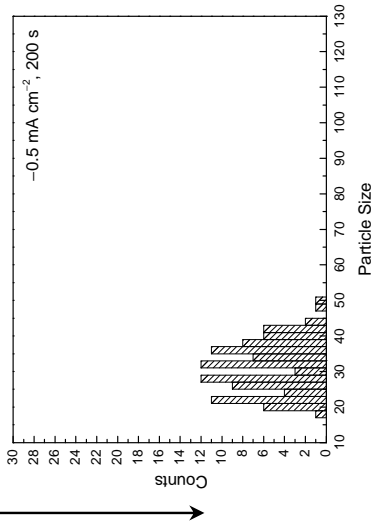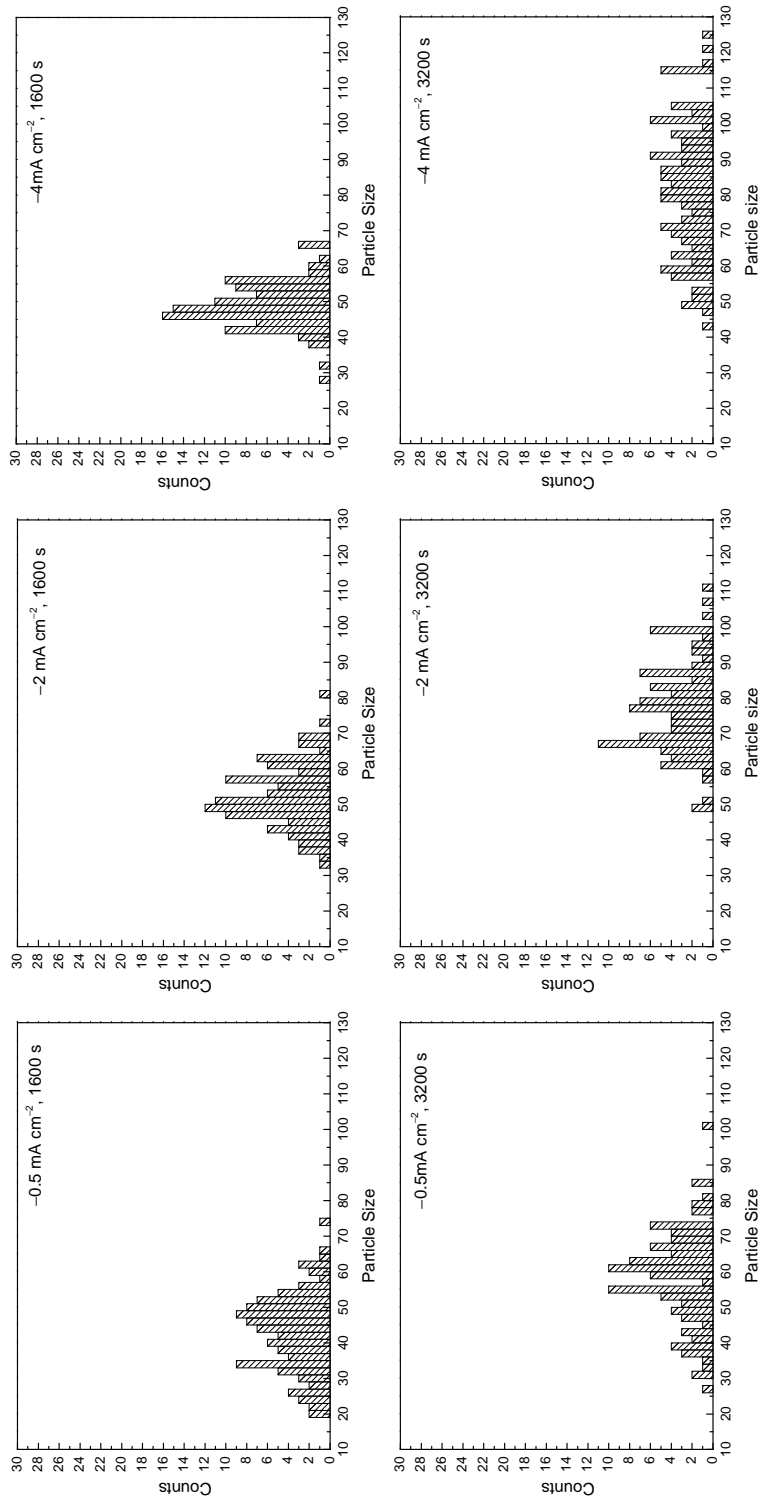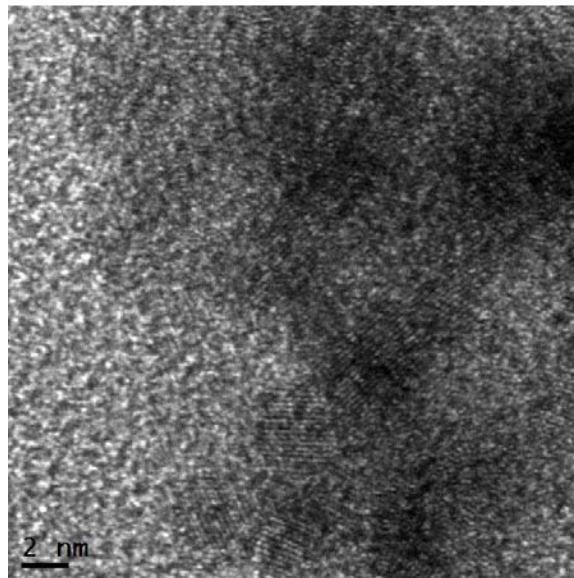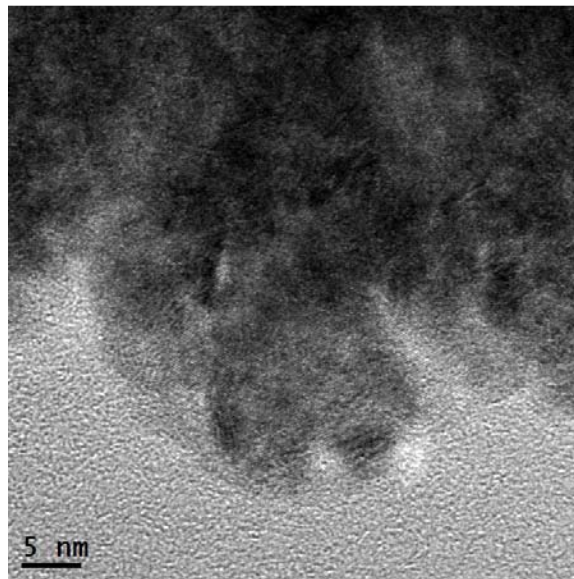
Figure S4. HRTEM images of Rh–Fe NPs obtained at j = –4 mA cm^{-2}, t = 400 s.
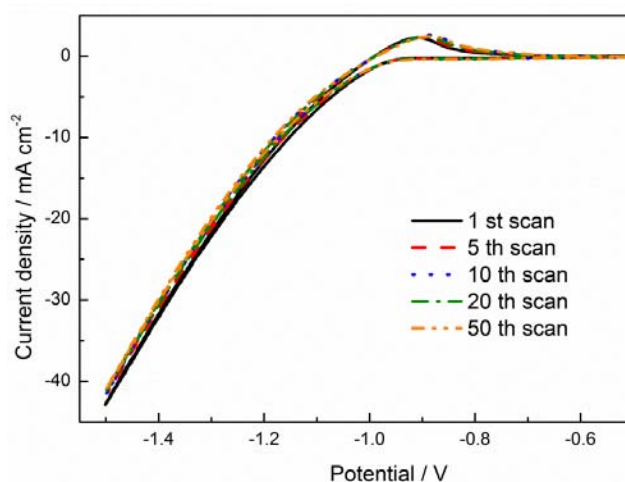
Figure S5. CV curves of Rh–Fe NPs obtained at j = –2 mA cm^{-2}, t = 1600 s.
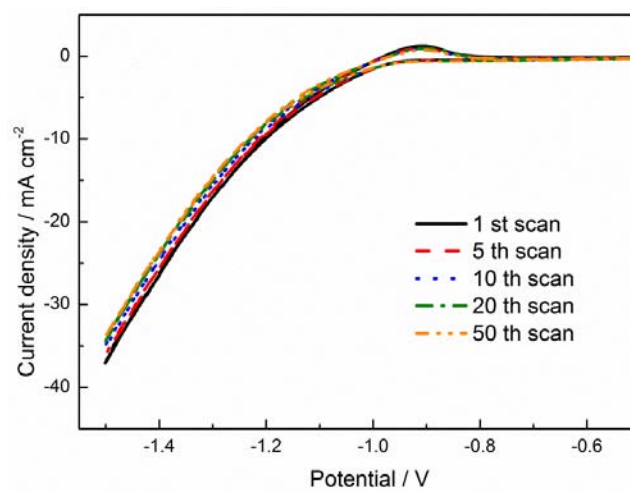
Figure S6. CV curves of Rh–Fe NPs obtained at j = –4 mA cm^{-2}, t = 800 s.
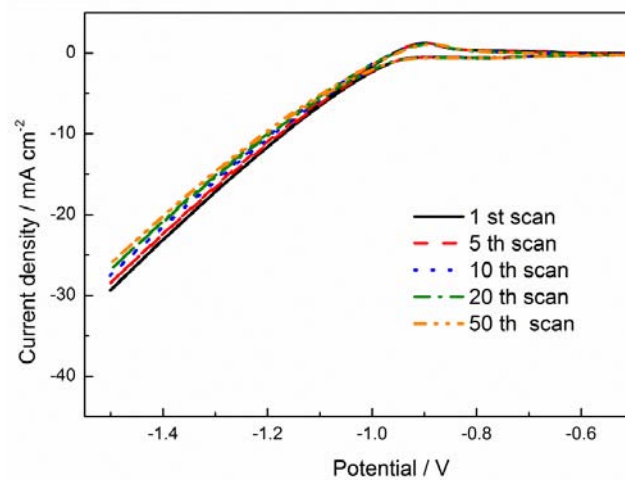
Figure S7. CV curves of Rh–Fe NPs obtained at j = –0.5 mA cm^{-2}, t = 3200 s.
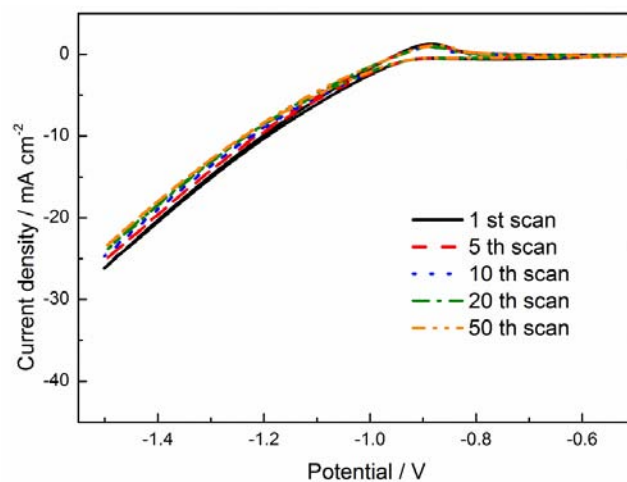
Figure S8. CV curves of Rh–Fe NPs obtained at j= –2 mA cm^{-2}, t = 3200s.
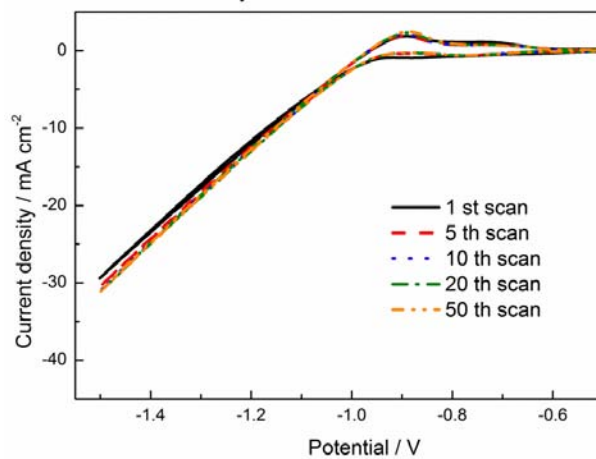
Figure S9. CV curves of Rh–Fe NPs obtained at j = –4 mA cm^{-2}, t = 3200s.

4

Highly-ordered macroporous Fe-P films with magnetic and electrocatalytic properties

For consistency's sake, this chapter is structured like a research article:

Abstract

Highly-ordered macroporous iron-phosphorous (Fe-P) films have been electrodeposited potentiostatically from a citrate-sulfate bath onto Au surfaces pre-patterned with a colloidal crystal mask of polystyrene spheres of 350 nm in diameter. The electrolyte contained sodium hypophosphite as the P source, enabling the incorporation of up to 14 at.% P in the porous samples. For comparative purposes, continuous films have been obtained galvanostatically on unpatterned Au surfaces. In both cases, the P content could be varied by adjusting the deposition potential or current density. Remarkably, oxygen incorporation in the films declined with an increase in the P content. Tunable magnetic response was observed due to the dissimilar chemical composition, with coercivity values being larger in the macroporous films. Additionally, wettability analyses showed that these were more hydrophobic, reaching contact angle values of about 130°. Both hydrogen and oxygen evolution reactions (HER and OER, respectively) have been studied in alkaline media. The macroporous Fe-P films showed faster kinetics for OER.

4.1. Introduction

Hydrogen is a key energy carrier that can be obtained from water splitting or, more precisely, electrolysis, which means that an electric current is being passed through the water [1, 2, 3]. The electrolysis of water provides a sustainable and environmentally-friendly way to contribute towards the constantly growing demand for energy supply and storage. However, the production of H_2 is constrained by the sluggish kinetics of the oxygen evolution reaction (OER) at the anode side of a water electrolyzer [4, 5]. For this reason, huge efforts are devoted to develop low cost bifunctional electrocatalysts with high activity towards both OER and hydrogen evolution reaction (HER) in the same electrolyte. RuO_2 and IrO_2 are the benchmark catalysts for OER [6] whereas Pt is the jewel in the crown of HER. However, Ru, Ir and Pt are

all costly and their supply is not sustainable [7, 8, 9]. Therefore, the production of more efficient and cheap HER/OER catalysts remains an ongoing challenge. During the last years, transition metal phosphides (TMPs) have attracted the interest of the scientific community for their outstanding catalytic activity towards HER [10, 11, 12, 13]. Their OER performance has been comparatively less investigated [14, 15]. Very recently, Hu et al. demonstrated that Ni_2P is an efficient bifunctional catalyst for water splitting [15]. Paik and co-workers also demonstrated that porous carbon coated nickel phosphides nanoplates (Ni_5P_4 and Ni_2P) outperformed NiO and $Ni(OH)_2$ in OER experiments [16].

Downscaling, and/or the introduction of porosity into the catalyst structure are already some of the effective strategies that have been reported to further enhance the OER and HER activity of the transition metal-based catalysts [17, 18, 19, 20]. Materials with spatially ordered porous features at the nanometer scale have been explored over the last years. Owing to the synergies arising from their constituent elements, fancy shape, and large surface-to-volume ratio (S/V), these materials are advantageous for a wide variety of applications. Photonic devices, catalysis, separation technology, nano-electronics, sensors, batteries, supercapacitors, fuel cells, sorption, thermal insulation, surfaces with special wetting properties, are just some of the myriad applications of porous materials. Although several methods toward periodic porous structures are available, deposition of the material over a colloidal crystal template followed by the selective removal of the latter is attractive for several reasons [21]. The approach encompasses the following steps: (1) the preparation of a colloidal dispersion, (2) the anchorage of the fine particles (typically uniformly sized spheres) onto a substrate by dip-coating, spin-coating, or electrophoretic deposition, (3) the filling of the empty space between the close-packed spheres with the target material, and (4) the selective removal of the colloidal particles, which can be accomplished by their dissolution in an organic solvent or calcination. As a result, the inverse replica of the parent colloidal crystal template is obtained. Several routes have been employed to date to fill the voids between the beads, namely, sol-gel, emulsion-gel, or liquid phase reaction [22, 23, 24]. Electrodeposition has also been employed to fill the interstitial space between the particles with great success [25]. Compared to other methods, it offers a good control on the degree of filling and wall thickness. Most importantly, many elements can be deposited and co-deposited from the same electrolyte with the possibility of fine-tuning their atomic ratio by simply adjusting the electrochemical parameters [26, 27]. For bead sizes (and, in turn, pore sizes) greater than 50 nm, the resulting films are commonly termed *macroporous*.

Motivated by the encouraging performance of TMPs as OER/HER electrocatalysts, we report here on the synthesis of ordered Fe-P macroporous thin films by electrodeposition through colloidal crystal templates. Special emphasis is laid on ensuring the growth of high-quality porous films with tunable phosphorous content and magnetic properties. Alongside, continuous (also named *fully dense* for the sake of clarity) Fe-P films directly electrodeposited on an unpatterned electrode were produced for comparative purposes. The electrocatalytic properties of the films toward both OER and HER are assessed in alkaline media, indicating its bifunctional character.

4.2. Results and discussion

4.2.1. Morphology and structure of fully dense and macroporous Fe-P films

Fully dense and macroporous Fe-P films were deposited on Si/Ti/Au substrates by electrodeposition from the same electrolyte. For the latter, polystyrene (PS) spheres were previously self-assembled on the Au

surface by electrophoresis. Fully dense P-free Fe deposits could be prepared as well using this electrolyte after proper adjustment of the electrodeposition conditions (see below). For the sake of comparison, macroporous films made of pure Fe were also synthesized. In this case, however, a different electrolyte (see Experimental section for details) was employed since the inclusion of P in the deposits could not be avoided when plating from the P-containing electrolyte. Figure 4.1 shows the E-t and j-t transients, respectively, recorded during the growth of the fully dense and porous Fe-P films. The former were plated at current densities ranging from -10 to -50 mA cm^{-2} (Figure 4.1a), whereas the latter were deposited at constant potential values ranging from -0.96 to -1.1 V (Figure 4.1b). Notice that potentiostatic deposition onto the patterned Au surfaces was selected since the real working area (unshielded areas of the substrate) could not be precisely determined. Values close to the stabilized potential (E$_s$) previously recorded during the growth of fully dense films were applied for the deposition of the macroporous films. Nevertheless, the lowest applied potential was -0.96 V since no significant deposition was observed at less negative potentials even for long deposition times.

Figure 4.1a shows that the value of E$_s$ decreases as the applied current density is made more negative. A similar trend is observed in Figure 4.1b. Namely, the current density shifts toward more negative values as the applied potential is decreased. The j-t curve corresponding to the deposition of pure Fe onto the
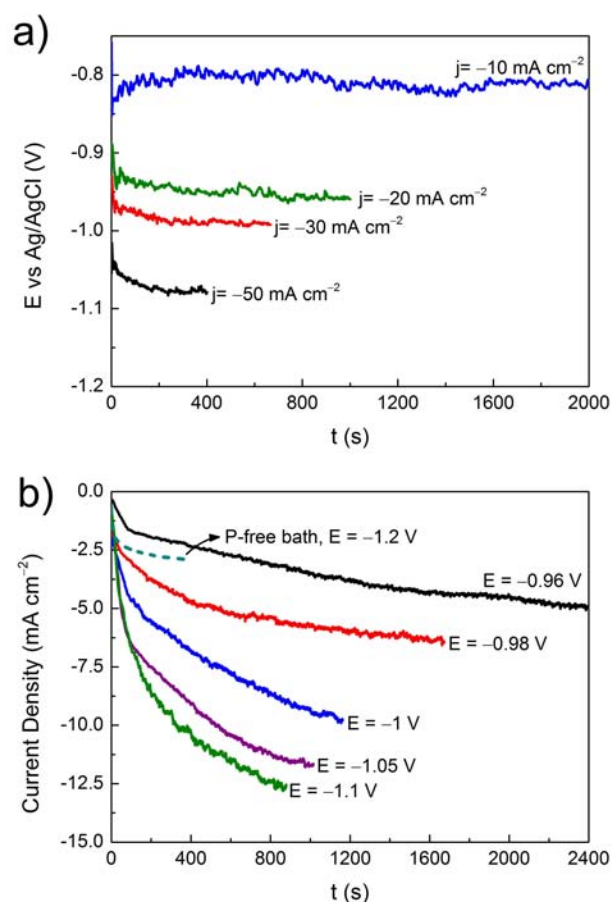

FIGURE 4.1: Representative a) E-t transients recorded during the deposition of fully dense Fe-P films on the Au surface at the indicated current densities and b) j-t transients recorded during the deposition of Fe-P on colloidal template arrays patterned on Au at the indicated potentials.

patterned Au surface is included in Figure 4.1b. In this case, the applied potential was -1.2 V since Fe(II) was not efficiently discharged at less negative potentials and, therefore, complete coverage of the voids was not attained even for long deposition times.

Figure 4.2 shows the field emission scanning electron microscope (FE-SEM) images of the fully dense films grown at current densities of -10, -20, -30 and -50 mA cm^{-2} and fixed deposition charge. The films show a very smooth, featureless surface at the lowest current density. The grain morphology becomes gradually visible and cracks appear upon increasing the current density. These changes in morphology are accompanied by variations in the chemical composition. The deposit produced at -10 cm^{-2} is virtually free from phosphorous (<4 at.% P as determined by ICP-OES) whereas the rest contains a significant amount of P between 15 and 22 at.% (see Table 4.1) Notice that the inclusion of P in the films brings about a reduction in the oxygen content. In Ni-P electroless coatings, the presence of P is known to trigger the formation of a protective layer consisting of metallic Ni and nickel phosphide that acts as a barrier for oxygen diffusion on the metal surface [28]. Nevertheless, the presence of oxygen could not be completely avoided, in agreement with previous reports on electroplated Fe-P coatings [29]. Figure 4.3 shows the FE-SEM images of the Fe-P macroporous films obtained through the E-t curves shown in Figure 4.1b after PS spheres removal. The films display an ordered pore arrangement, the pore size being determined by the diameter of the spheres (350 nm). Slight differences in both pore wall morphology and pore size were noticed as a function of the applied potential. The samples deposited at potentials ranging from -0.96 to -1.0 V showed an almost identical architecture consisting of nearly a monolayer of hemispherical orderly arranged pores. The occurrence of domain sizes as large as 250 μm^2 was observed. Meanwhile, the films obtained at more negative potentials (Figure 4.3d, e) showed an ill-defined pore structure, featuring discontinuities between neighboring pores and rougher pore walls. Nevertheless, high porosity remained. Typically, the removal of the PS beads is accomplished by immersing the samples in an organic solvent like chloroform or toluene. However, it did not work out in our case. Instead, a multi-step cleaning process was devised to successfully etch away the beads. The as-deposited samples were first ultrasonicated in dimethyl sulfoxide (DMSO) and dimethylformamide (DMF) (4 min each), followed by CHCl$_3$ for 15 min. Finally, the PS-free porous deposits were thoroughly rinsed in water.

Table 4.1: Fe, P and O content (in at.%) determined by EDX in the fully dense Fe-P films as a function of the applied current density.

j [mA cm^{-2}]	at. % Fe	at. % P	at. % O
-10	61	0	39
-20	64	20	16
-30	61	22	17
-50	63	15	22

Table 4.2 lists the amount of Fe, P and O detected in the porous films deposited within the selected experimental conditions. The phosphorous content generally increased as the applied potential was made more negative from 6-8 at.% to 14 at.%. Notice that the P contents were lower than in the fully dense counterparts, which can be understood considering that the diffusion and nucleation events in confined cavities are different from those on planar substrates. Besides, the codeposition of higher amount of phosphorus was accompanied by a reduction in the oxygen content, as it was observed for the fully dense films. However, the variation did not follow a monotonic trend. The porous pure Fe film obtained from
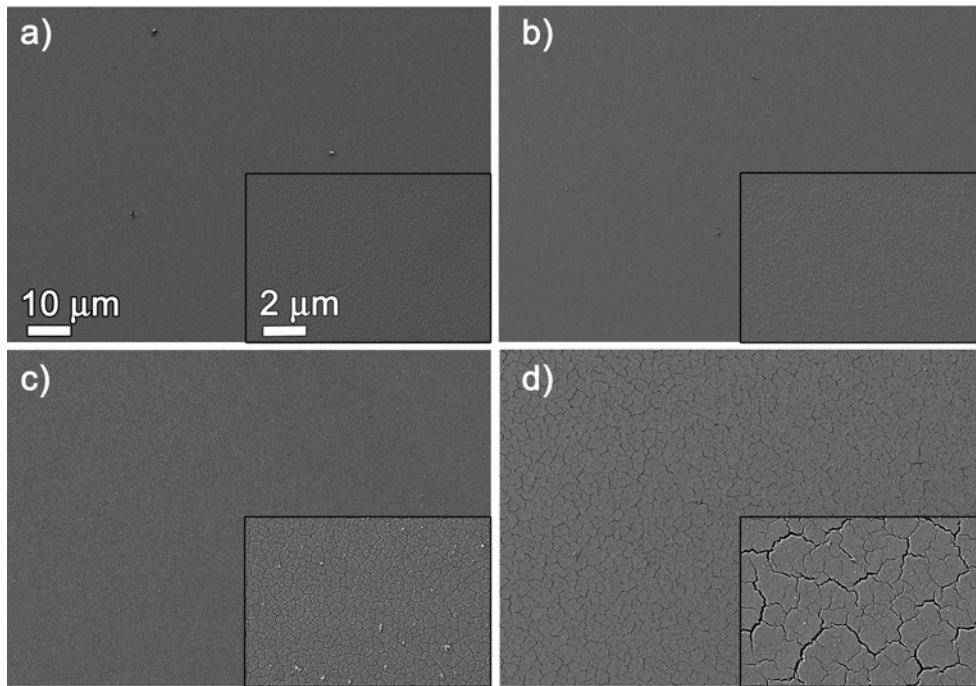
FIGURE 4.2: Low and high (inserts) magnification FE-SEM images of the fully dense Fe-P films obtained at different current densities: a) j = -10 mA cm^{-2}, b) j = -20 mA cm^{-2} and c) j = -30 mA cm^{-2}, and d) j = -50 mA cm^{-2}. The scale bars indicated in a) apply to b)-d).

a different bath showed an oxygen percentage similar to the macroporous Fe-P films with 10-14 at.% P. However, in this case the applied potential is not strictly comparable and, therefore, the bath formulation itself also plays a role in determining the Fe/O ratio.

TABLE 4.2: Fe, P and O content (in at.%) determined by EDX in the macroporous Fe-P films as a function of the deposition potential.

E [V]	at. % Fe	at. % P	at. % O
-0.96	60	8	32
-0.98	57	6	37
-1.0	69	10	21
-1.05	62	12	26
-1.1	65	14	21
-1.2[1]	74	0	26

[1]Note that this sample was electrodeposited from a P-free electrolyte as detailed in the Experimental section.

Figure 4.4 shows a detail of the X-ray diffraction (XRD) patterns in the 43-46° 2θ range of some selected fully dense and porous Fe-P films. The main peak of the body-centered cubic (bcc) phase of Fe, if so, appears in this angular range. The weak diffraction peak located at $2\theta = 43.6°$ is due to the holder. It is known that Fe-P produced by electrodeposition gradually changes from micro/nanocrystalline to amorphous-like by increasing the phosphorus content [30]. The boundary between a microcrystalline and a fully homogeneous amorphous structure is difficult to determine and depends on the bath formulation and electrodeposition conditions. Typically, it stands for 20 at.% P. The fully dense films did not show

97
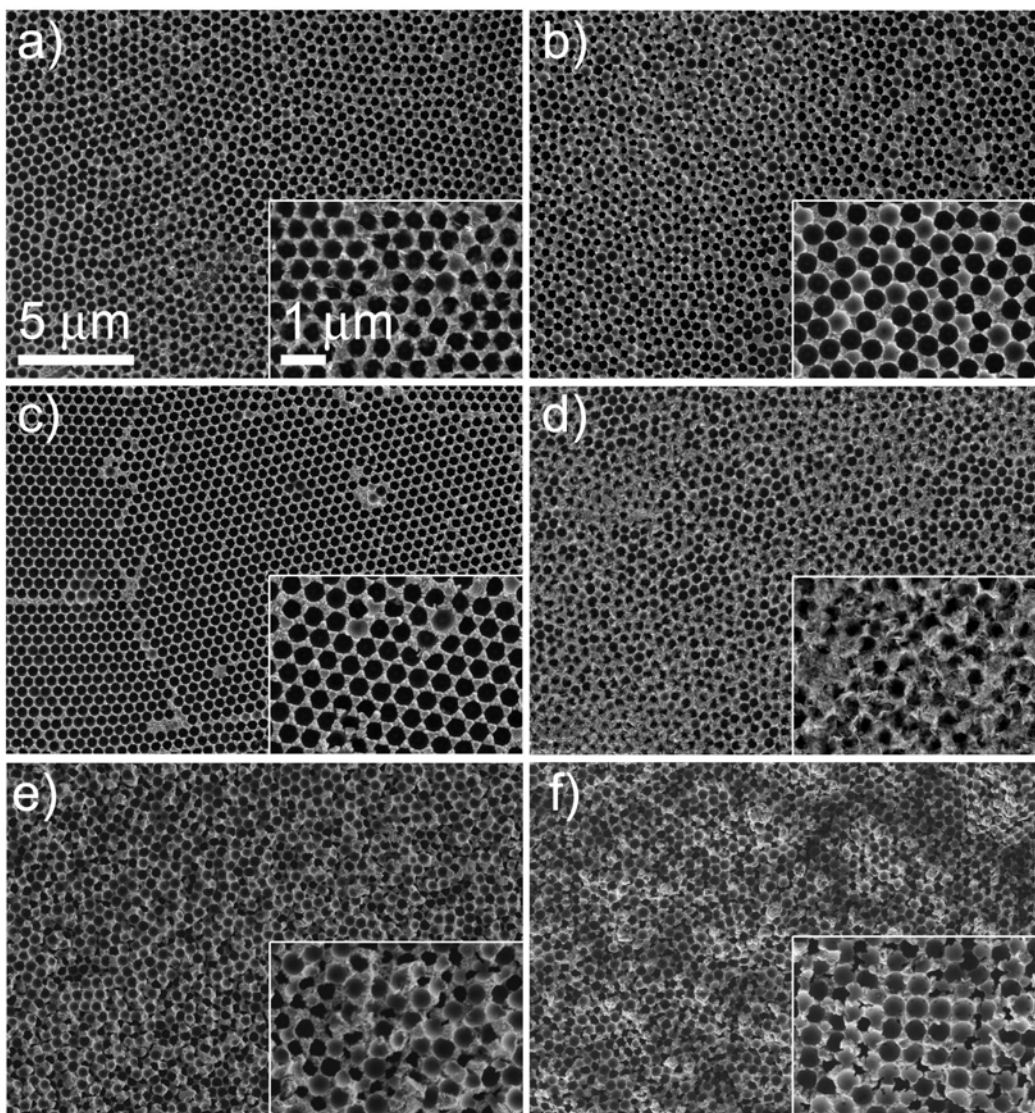
FIGURE 4.3: Low and high (inserts) magnification FE-SEM images of the macroporous Fe-P films obtained at different deposition potentials: a) E = -0.96 V, b) E = -0.98 V, c) E = -1.0 V, d) E = -1.05 V and e) E = -1.1 V. f) FE-SEM image of a P-free Fe macroporous film deposited at E = -1.2 V. The PS spheres were removed prior to the imaging. The scale bars indicated in a) apply to b)-f).

any reflection independently of the P content. Meanwhile, the porous samples did show a relatively wide (110) bcc-Fe peak always. No other peaks ascribed to intermetallic phases such as FeP, Fe_2P or Fe_3P phases were detected in the full XRD patterns. Therefore, the continuous films were ultra-nanocrystalline or amorphous-like, whereas the walls of the porous films were nanocrystalline. For the macroporous films, the position of the α-Fe reflection shifted toward higher angles as P was incorporated into the deposits. For example, a shift ca. 0.2° was observed when 12 at.% P was alloyed with Fe (compare green and blue profiles in Figure 4.4). This shift can be explained considering that the atomic radius of P is smaller than that of Fe, which causes a shrinkage of the unit cell.
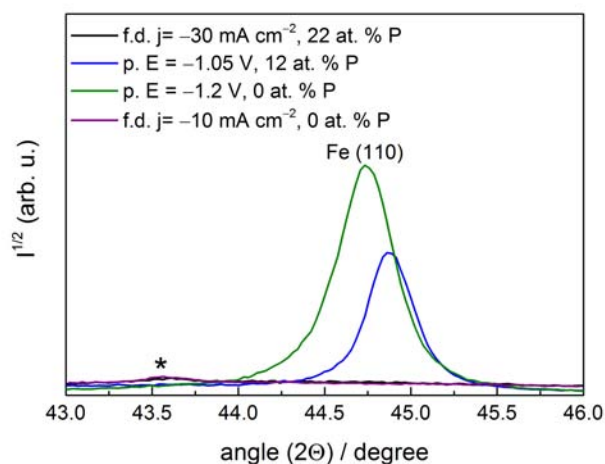
FIGURE 4.4: Zoomed detail of the XRD patterns in the 43-46 2° range of selected samples. The peak marked with an asterisk belongs to the holder. 'f.d.' and 'p.' stand for fully dense and porous films, respectively.

4.2.2. SURFACE WETTABILITY

The wettability of the fully dense and macroporous Fe-P films was characterized by the sessile drop technique, using 1.5 μL of Milli-Q (MQ) quality water droplets. Figure 4.5 and 4.6 show photographs of the drop profile immediately after the drop was placed onto the films' surface. The corresponding contact angle values are depicted in each case. The macroporous Fe-P films exhibit higher contact angles than the fully dense counterparts. For the latter, the values range from 80° to 100°. For the former, the values vary between 107° and 135°. Therefore, it is clear that the porous surfaces are more hydrophobic, which is likely because the air trapped within the pores precludes their wetting. This indicates that the Cassie and Baxter model predominates in the macroporous films [31]. Fluctuation of the contact angle values within the same series of samples (fully dense vs. macroporous) can be understood on the basis of their dissimilar chemical composition (P, O contents) and slightly different morphology (see for example Figure 4.3). In any case, the effect of porosity dominates over the chemical composition.

4.2.3. MAGNETIC PROPERTIES

The room temperature hysteresis loops of the fully dense and macroporous Fe-P films deposited at varying current densities and potentials, respectively, are shown in Figure 4.7. Well-defined hysteresis loops were recorded in all cases irrespective of the P content. For the fully dense films, a soft-ferromagnetic behavior with H_C values ranging between 2 Oe and 11 Oe was observed. The saturation magnetization (M_S) decreased as the P content increased. However, the film obtained at the lowest current density, with virtually no P, showed an M_S lower than expected. Indeed, the value was smaller than either the film with 15 at.% P or the M_S of bulk Fe (217.6 emu/g). This result can be understood considering that this sample contains twice the amount of oxygen than the others, as determined by EDX. The hysteresis loops were normalized after dissolving the films for ICP-OES analyses, which enabled to determine the deposited mass of iron but not that of oxygen. Although Fe is mostly oxidized at the outermost surface, the occurrence of either antiferromagnetic (hematite) or ferrimagnetic iron oxides with lower M_S (maghemite,
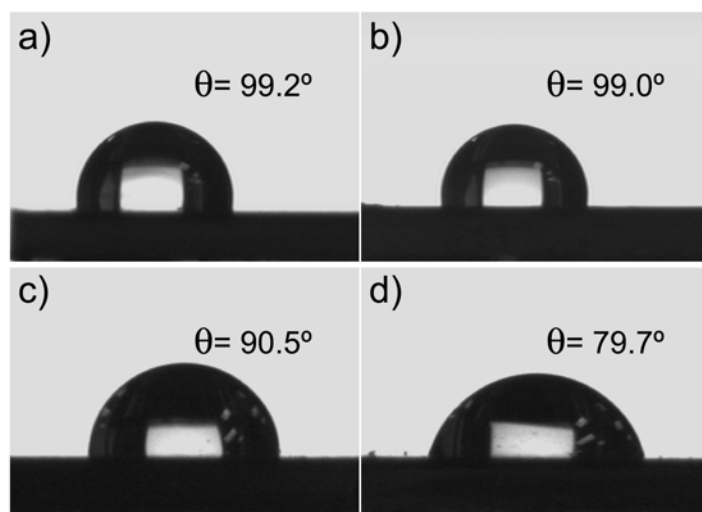
FIGURE 4.5: Photographs of the MQ-water droplets on the surface of fully dense Fe-P films obtained at: a) j = -10 mA cm^{-2}, b) j = -20 mA cm^{-2} and c) j = -30 mA cm^{-2}, and d) j = -50 mA cm^{-2}.
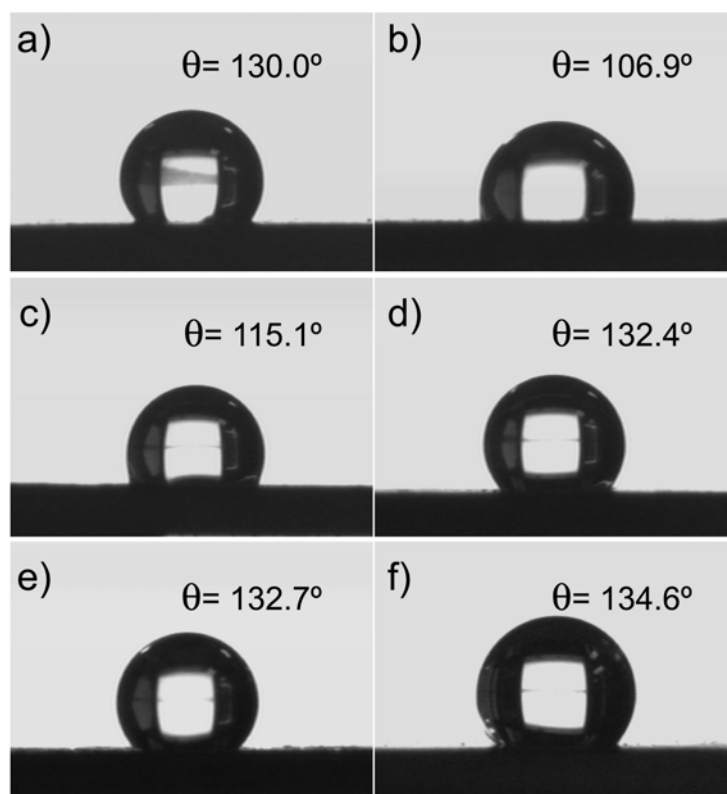
FIGURE 4.6: Photographs of the MQ-water droplets on the surface of Fe-P macroporous films obtained at: a) E = -0.96 V, b) E = -0.98 V, c) E = -1.0 V, d) E = -1.05 V and e) E = -1.1 V. f) P-free Fe macroporous film deposited at E = -1.2 V.

magnetite) would cause a decrease of the M$_S$.

Compared to the fully dense films, saturation was reached at much higher applied fields in the macroporous analogues. This is probably due to the hindrances imposed by the reduced lateral size of
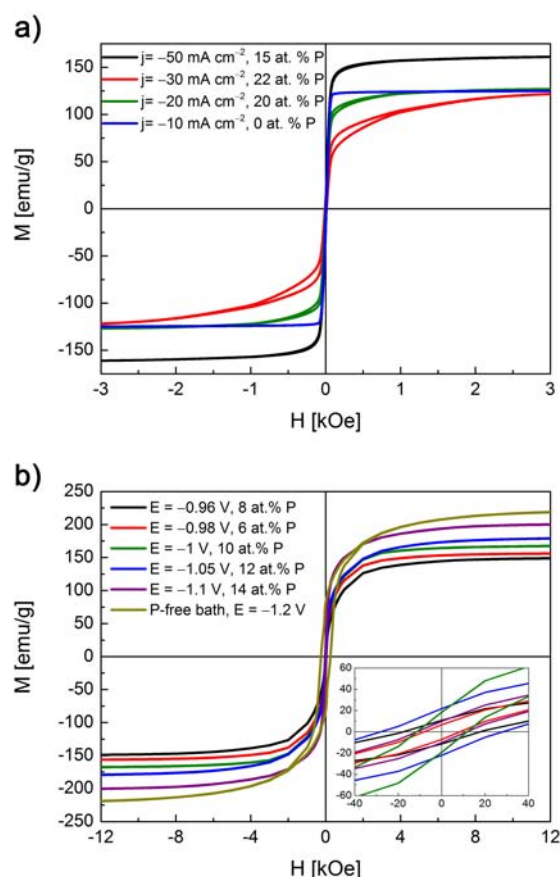
Figure 4.7: Room temperature hysteresis loops of a) fully dense Fe-P films prepared at the indicated current densities and b) macroporous Fe-P films prepared at the indicated potentials. The inset in b) shows a magnified detail at low fields.

the pore walls on domain wall propagation as well as the loss of the in-plane shape anisotropy. Pure Fe sample does show the highest M_S. A gradual decrease of the M_S with an increase of the P content has been reported in the literature for most of the metal-metalloid systems before any heat-treatment is applied [32]. However, the macroporous films show the opposite trend, which again can be correlated with the simultaneous change in the oxygen content. As the P content increases, that of O decreases and, therefore, the relative amount of the ferromagnetic α-Fe phase raises. In addition, the H_C values are larger than in the fully dense films (9-253 Oe), again as a result of the hindrances imposed by the pore walls to domain wall propagation [25].

4.2.4. Electrocatalytic activity towards OER and HER

The macroporous Fe-P films are expected to be suitable candidates for OER, not only because of their chemical composition but also large surface area. Figure 4.8 shows the steady-state polarization curves of the fully dense and porous Fe-P catalysts in 1 M Ar-purged KOH solution at a sweeping rate of 50 mV s^{-1}. Although 6 M KOH solution would be more realistic considering the current water electrolysis in industrial conditions, the selected electrolyte allows a relatively good comparative analysis. While the onset for OER is similar in both sets of samples, the kinetics is faster in the macroporous films. At potentials

more positive than the onset potential, the corresponding current density is higher. Since the reported current density values are referred to the geometrical area, the current densities calculated considering the real surface area are expected to be even higher. The onset potentials for OER are similar to those reported in the literature for nanostructured Fe-P based catalysts [33]. Another important observation is that the addition of P to the fully dense films enhances the OER performance (see Figure 4.8a). This effect is lost in the macroporous films. Except for the two samples fabricated at -0.96 V (8 at.% P) and -0.98 V (6 at.% P) that nearly overlap with the response of pure Fe, the others show lower OER activity. This results is not surprising since electrocatalyts based on transition metal oxides/hydroxides of Co, Ni and Fe have been demonstrated as the most active OER catalysts [34]. The surface of the macroporous pure Fe film likely contains a significant amount of oxides/hydroxides.

FIGURE 4.8: Steady-state polarization curves recorded in Ar-saturated 1 M KOH electrolyte for a) fully dense and b) macroporous Fe-P films. The response of a macroporous pure Fe film is shown for comparison in b). Scan rate: 50 mV s^{-1}.

In electrocatalytic processes, catalysts may suffer from deformation of the structure, poisoning and thus loss of the catalytic activity. In order to examine their catalytic durability, the fully dense and macroporous films were subjected to 25 cycles in 1 M KOH within the potential range from +1.0 to +2.2 V. As shown in Figure 4.9, the current density severely declines after the 5th cycle for the fully dense film prepared at -10 mA cm^{-2} (0 at.% P) because it fully dissolved in the dissolution. Meanwhile, for the P-containing fully dense films, the catalytic activity either decreases a bit or even increases after 25 cycles. Similar results

were observed for the macroporous Fe-P films (Figure 4.10). Therefore, the macroporous films show faster kinetics than their fully dense counterparts and similar durability.
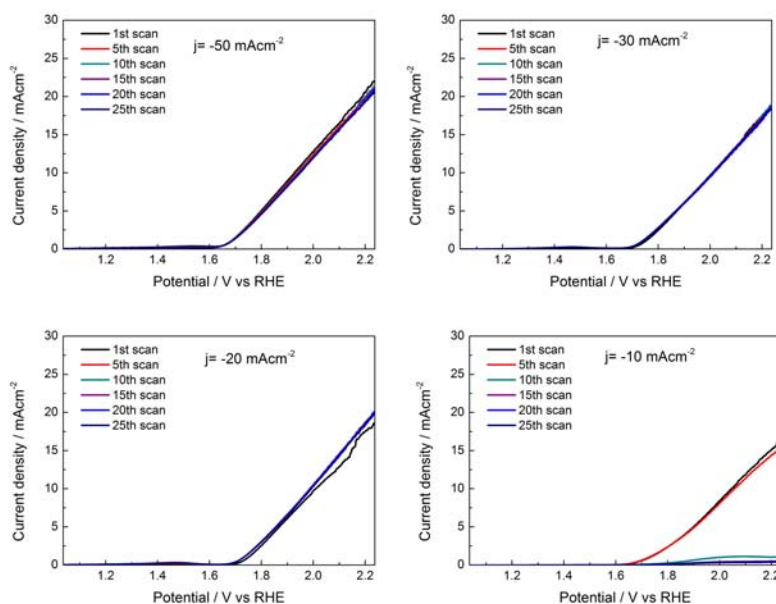
FIGURE 4.9: LSV cycling in 1M KOH (50 mV s^{-1}) of the fully dense Fe-P films obtained at different current densities: j = -10 mA cm^{-2}, j = -20 mA cm^{-2} and j = -30 mA cm^{-2}, and j = -50 mA cm^{-2}.
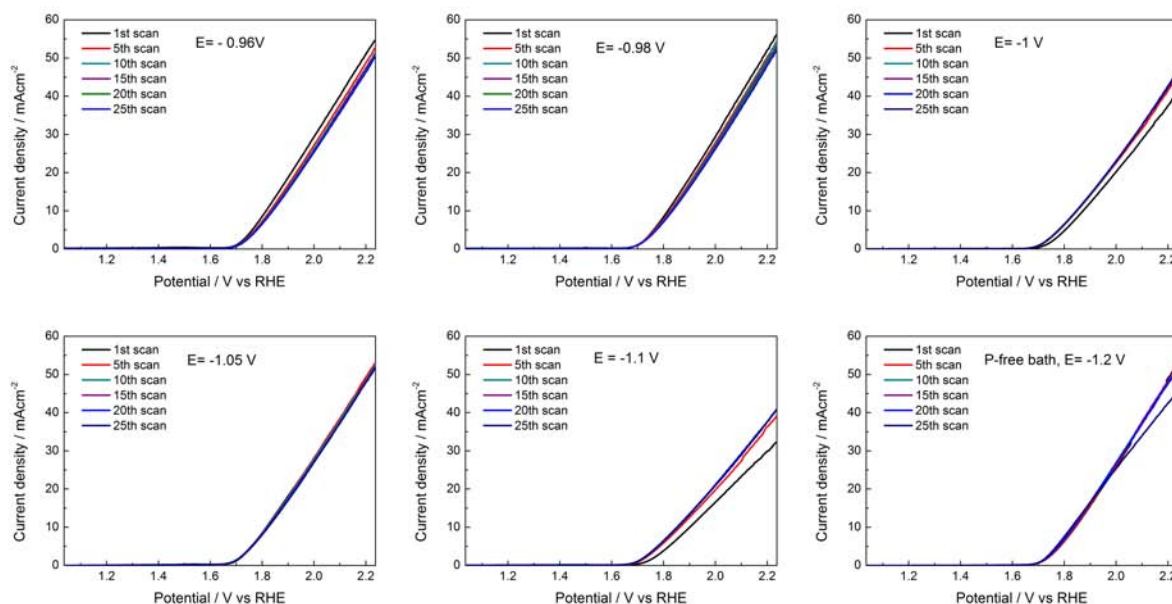
FIGURE 4.10: LSV cycling in 1M KOH (50 mV s^{-1}) of the macroporous Fe-P films obtained at different deposition potentials: E = -0.96 V, E = -0.98 V, E = -1 V, E = -1.05 V, E = -1.1 V and pure Fe at E = -1.2 V.

Regarding their HER behavior, similar trends were observed (Figure 4.11). Namely, the addition of P to the fully dense films gradually shifted the onset for HER toward more positive potentials. On the contrary, the P-free macroporous Fe film showed the best HER activity compared to the Fe-P macroporous films.

Actually, none of them outperformed pure Fe. Therefore, further improvements in either film composition or pore architecture are needed to enhance the HER behavior of the macroporous Fe-P samples.
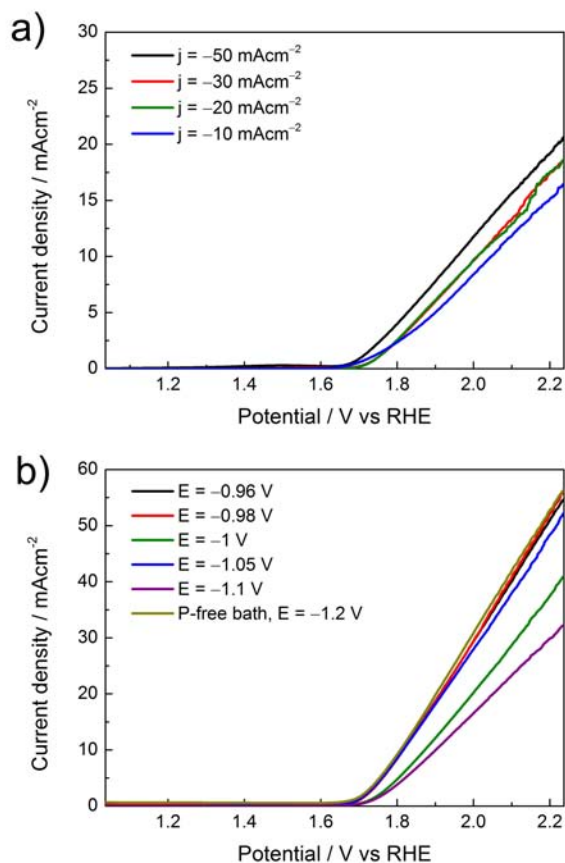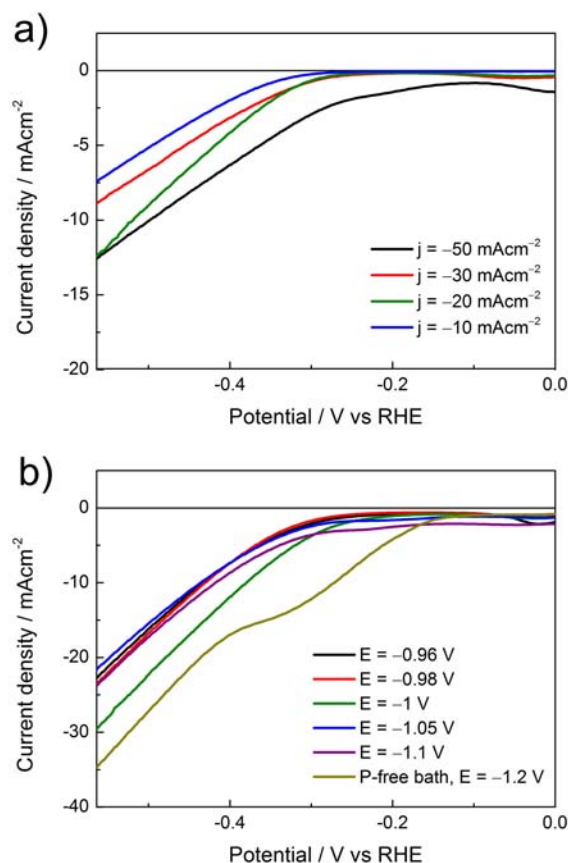

FIGURE 4.11: Steady-state polarization curves recorded in Ar-saturated 1 M KOH electrolyte for a) fully dense and b) macroporous Fe-P films. The response of a macroporous pure Fe film is shown for comparison. Scan rate: 50 mV s^{-1}.

Conclusions

Macroporous Fe-P films with varying P content were obtained by direct current electrodeposition on PS colloidal crystal templates. The inclusion of phosphorous in the films reduced the oxygen amount, as detected by EDX. The pore walls were nanocrystalline and showed the bcc-Fe structure. Higher hydrophobic character was observed compared to the fully dense counterparts. Besides, the macroporous films were more difficult to saturate and exhibited higher coercivity values. The saturation magnetization varied with the Fe:P:O ratio. Both the macroporous and fully dense Fe-P films displayed reasonably good OER and HER activity in alkaline media. The OER performance of the macroporous films was better than the fully dense samples.

4.3. Experimental section

4.3.1. Electrochemical synthesis

Electrodeposition was conducted in a double-jacketed three-electrode cell connected to a PGSTAT302N Autolab potentiostat/galvanostat (Ecochemie). A double junction Ag|AgCl (E=+0.210 V/SHE) reference electrode (Metrohm AG) was used with 3M KCl inner solution and 1M Na_2SO_4 outer solution. A platinum spiral served as a counter electrode. To prepare the continuous films, silicon (111) substrates with e-beam evaporated Ti (100 nm)/Au (125 nm) adhesion/seed layers were used as cathodes. In the case of macroporous films, Si/Ti/Au substrates patterned by colloidal lithography with carboxylated PS spheres of 350 nm in diameter (purchased from Polysciences) were used. The spheres were electrophoretically deposited on the substrate in a custom-made cell consisting of a chamber (1 cm x 1 cm x 0.6 cm) of poly(methyl methacrylate) (PMMA) glued to a counter electrode of platinized titanium. The Au-coated substrate (anode) was fixed at a distance of 0.5 cm from the counter electrode (cathode). A constant potential was then applied between the anode and the cathode using an Agilent B2902A power source. An electric field of of 120 V cm^{-1} was applied during 5 min. Immediately after the electrophoretic deposition, the samples were dried on a hot plate at 50 °C for 10 min.

The electrolyte consisted of 1 M $FeSO_4 \cdot 7H_2O$, 0.1 M citric acid, 0.5 M $NaH_2PO_2 \cdot H_2O$, 0.1 M $(NH_4)_2SO_4$ and 0.005 M ascorbic acid. The pH of the as-prepared electrolyte was 2.0 and it was kept unadjusted for the electrodeposition experiments. Solutions were prepared from analytical grade reagents and MQ-water. Before each deposition, the electrolyte was de-aerated with nitrogen gas. Deposition was conducted galvanostatically in the case of the fully dense films and potentiostatically in the case of the porous films. A constant current density between -10 and -50 mA cm^{-2} or a constant potential in the range from -0.96 to -1.1 V were applied, respectively. All deposition processes were carried out at 32 °C under stagnant conditions. The temperature was maintained by circulating water through the external jacket of the electrochemical cell using refrigerated/heated circulator from Julabo (F12 model). After deposition, the samples were rinsed with MQ-water and dried in air. The PS spheres were selectively etched away by ultrasonication for 4 min in DMSO, followed by 4 min in DMF and finally 15 min in $CHCl_3$. The resulting porous films where thoroughly rinsed in MQ-water again. Pure macroporous Fe films were synthesized from a different electrolyte containing 0.2 M $FeSO_4 \cdot 7H_2O$, 0.1 M glycine and 0.0028 M ascorbic acid (left at its unadjusted pH).

4.3.2. Characterization

The morphology and composition of the fully dense and macroporous Fe-P films were characterized on a Zeiss Merlin field emission scanning electron microscope (FE-SEM) equipped with an energy dispersive X-ray (EDX) detector. Room temperature hysteresis loops were recorded using a vibrating sample magnetometer (VSM) from MicroSense (LOT-Quantum Design), with a maximum applied magnetic field of 2 T applied in-plane. Inductively coupled plasma optical emission spectrometry (ICP-OES) analyses were conducted on a Optima 4300DV spectrometer from Perkin-Elmer to determine the total metal content in the samples. For this purpose, the samples were dissolved in 6 wt.% HNO_3. Normalized hysteresis loops by the total Fe and P weights are reported. A surface analyzer (Smartdrop, Femtofab) was used to study the wetting properties of the films (sessile drop technique). The liquid utilized in the measurements was 1 μL droplets of 5 wt.% MQ-water at room temperature. The reported contact angle values

correspond to the average of two independent measurements. XRD patterns were recorded on a Philips X'Pert diffractometer in the 25-90° 2θ-range (step size = 0.03°, holding time = 10 s) using Cu K_α radiation (note that both wavelengths $\lambda(K_{\alpha1})$=1.5406 Å and $\lambda(K_{\alpha2})$=1.5443 Å were used in the intensity proportion of $I(K_{\alpha2})$=$I(K_{\alpha1})$ = 0.5).

4.3.3. Electrocatalytic activity towards OER and HER

The electrochemical activity of the fully dense and macroporous Fe-P films towards OER and HER was measured in the same three-electrode system used for electrodeposition. The outer solution of the Ag/AgCl (3M KCl) electrode was made of 0.5 M KOH. All potentials measured were calibrated to RHE using the following equation: E(RHE) = E(Ag|AgCl) + 0.210 + 0.059 pH. The as-prepared Fe-P samples served as the WE. Polarization curves were recorded in a de-aerated 1 M KOH solution by scanning the potential between 1.0 V and 2.2 V (vs. RHE), and between 0 V and -0.55 V (vs. RHE) during OER and HER experiments, respectively, at 50 mV s^{-1}. The temperature of the cell was set at 25 °C. 25 cycles were run in order to assess electrode stability.

Bibliography

[1] A. Kudo and Y. Miseki, "Heterogeneous photocatalyst materials for water splitting," *Chemical Society Reviews*, vol. 38, pp. 253 – 278, 2009.

[2] Y. Jiao, Y. Zheng, M. Jaroniec, and S. Z. Qiao, "Design of electrocatalysts for oxygen- and hydrogen-involving energy conversion reactions," *Chemical Society Reviews*, vol. 44, pp. 2060 – 2086, 2015.

[3] M. Ledendecker, S. Krick Calderón, C. Papp, H.-P. Steinrück, M. Antonietti, and M. Shalom, "The synthesis of nanostructured Ni$_5$P$_4$ films and their use as a non-noble bifunctional electrocatalyst for full water splitting," *Angewandte Chemie International Edition*, vol. 54, no. 42, pp. 12361 – 12365, 2015.

[4] R. D. L. Smith, M. S. Prévot, R. D. Fagan, Z. Zhang, P. A. Sedach, M. K. J. Siu, S. Trudel, and C. P. Berlinguette, "Photochemical route for accessing amorphous metal oxide materials for water oxidation catalysis," *Science*, vol. 340, no. 6128, pp. 60 – 63, 2013.

[5] T. R. Cook, D. K. Dogutan, S. Y. Reece, Y. Surendranath, T. S. Teets, and D. G. Nocera, "Solar energy supply and storage for the legacy and nonlegacy worlds," *Chemical Reviews*, vol. 110, no. 11, pp. 6474 – 6502, 2010.

[6] M. Carmo, D. L. Fritz, J. Mergel, and D. Stolten, "A comprehensive review on PEM water electrolysis," *International Journal of Hydrogen Energy*, vol. 38, no. 12, pp. 4901 – 4934, 2013.

[7] T. Reier, M. Oezaslan, and P. Strasser, "Electrocatalytic oxygen evolution reaction (OER) on Ru, Ir, and Pt catalysts: A comparative study of nanoparticles and bulk materials," *ACS Catalysis*, vol. 2, no. 8, pp. 1765 – 1772, 2012.

[8] M. G. Walter, E. L. Warren, J. R. McKone, S. W. Boettcher, Q. Mi, E. A. Santori, and N. S. Lewis, "Solar water splitting cells," *Chemical Reviews*, vol. 110, no. 11, pp. 6446 – 6473, 2010.

[9] A. Han, S. Jin, H. Chen, H. Ji, Z. Sun, and P. Du, "A robust hydrogen evolution catalyst based on crystalline nickel phosphide nanoflakes on three-dimensional graphene/nickel foam: high performance for electrocatalytic hydrogen production from pH 0-14," *Journal of Materials Chemistry A*, vol. 3, pp. 1941 – 1946, 2015.

[10] Y. Shi and B. Zhang, "Recent advances in transition metal phosphide nanomaterials: synthesis and applications in hydrogen evolution reaction," *Chemical Society Reviews*, vol. 45, pp. 1529 – 1541, 2016.

[11] J. Wang, W. Cui, Q. Liu, Z. Xing, A. M. Asiri, and X. Sun, "Recent progress in cobalt-based heterogeneous catalysts for electrochemical water splitting," *Advanced Materials*, vol. 28, no. 2, pp. 215 – 230, 2016.

[12] P. Xiao, W. Chen, and X. Wang, "A review of phosphide-based materials for electrocatalytic hydrogen evolution," *Advanced Energy Materials*, vol. 5, no. 24, p. 1500985, 2015.

[13] Z. Pu, Q. Liu, P. Jiang, A. M. Asiri, A. Y. Obaid, and X. Sun, "CoP nanosheet arrays supported on a Ti plate: An efficient cathode for electrochemical hydrogen evolution," *Chemistry of Materials*, vol. 26, no. 15, pp. 4326 – 4329, 2014.

[14] J. Ryu, N. Jung, J. H. Jang, H.-J. Kim, and S. J. Yoo, "In situ transformation of hydrogen-evolving CoP nanoparticles: Toward efficient oxygen evolution catalysts bearing dispersed morphologies with Co-oxo/hydroxo molecular units," *ACS Catalysis*, vol. 5, no. 7, pp. 4066 – 4074, 2015.

[15] L.-A. Stern, L. Feng, F. Song, and X. Hu, "Ni$_2$P as a Janus catalyst for water splitting: the oxygen evolution activity of Ni$_2$P nanoparticles," *Energy & Environmental Science*, vol. 8, pp. 2347 – 2351, 2015.

[16] X.-Y. Yu, Y. Feng, B. Guan, X. W. (David) Lou, and U. Paik, "Carbon coated porous nickel phosphides nanoplates for highly efficient oxygen evolution reaction," *Energy & Environmental Science*, vol. 9, pp. 1246 – 1250, 2016.

[17] H. Tüysüz, Y. J. Hwang, S. B. Khan, A. M. Asiri, and P. Yang, "Mesoporous Co$_3$O$_4$ as an electrocatalyst for water oxidation," *Nano Research*, vol. 6, no. 1, pp. 47 – 54, 2013.

[18] J. D. Blakemore, H. B. Gray, J. R. Winkler, and A. M. Müller, "Co$_3$O$_4$ nanoparticle water-oxidation catalysts made by pulsed-laser ablation in liquids," *ACS Catalysis*, vol. 3, no. 11, pp. 2497 – 2500, 2013.

[19] A. J. Esswein, M. J. McMurdo, P. N. Ross, A. T. Bell, and T. D. Tilley, "Size-dependent activity of Co$_3$O$_4$ nanoparticle anodes for alkaline water electrolysis," *The Journal of Physical Chemistry C*, vol. 113, no. 33, pp. 15068 – 15072, 2009.

[20] R. Wu, J. Zhang, Y. Shi, D. Liu, and B. Zhang, "Metallic WO$_2$–carbon mesoporous nanowires as highly efficient electrocatalysts for hydrogen evolution reaction," *Journal of the American Chemical Society*, vol. 137, no. 22, pp. 6983 – 6986, 2015.

[21] A. Stein and R. C. Schroden, "Colloidal crystal templating of three-dimensionally ordered macroporous solids: materials for photonics and beyond," *Current Opinion in Solid State and Materials Science*, vol. 5, no. 6, pp. 553 – 564, 2001.

[22] S. A. Davis, S. L. Burkett, N. H. Mendelson, and S. Mann, "Bacterial templating of ordered macrostructures in silica and silica-surfactant mesophases," *Nature*, vol. 385, no. 6615, pp. 420 – 423, 1997.

[23] A. Imhof and D. J. Pine, "Ordered macroporous materials by emulsion templating," *Nature*, vol. 389, no. 6654, pp. 948 – 951, 1997.

[24] J. E. G. J. Wijnhoven and W. L. Vos, "Preparation of photonic crystals made of air spheres in titania," *Science*, vol. 281, pp. 802 – 804, 1998.

[25] P. N. Bartlett, M. A. Ghanem, I. S. El Hallag, P. de Groot, and A. Zhukov, "Electrochemical deposition of macroporous magnetic networks using colloidal templates," *Journal of Materials Chemistry*, vol. 13, pp. 2596 – 2602, 2003.

[26] P. V. Braun and P. Wiltzius, "Microporous materials: Electrochemically grown photonic crystals," *Nature*, vol. 402, no. 6762, pp. 603 – 604, 1999.

[27] P. V. Braun and P. Wiltzius, "Electrochemical fabrication of 3D microperiodic porous materials," *Advanced Materials*, vol. 13, no. 7, pp. 482 – 485, 2001.

[28] S. Afroukhteh, C. Dehghanian, and M. Emamy, "Preparation of electroless Ni-P composite coatings containing nano-scattered alumina in presence of polymeric surfactant," *Progress in Natural Science: Materials International*, vol. 22, no. 4, pp. 318 – 325, 2012.

[29] C. Sequeira, D. Santos, and P. Brito, "Electrocatalytic activity of simple and modified Fe-P electrodeposits for hydrogen evolution from alkaline media," *Energy*, vol. 36, no. 2, pp. 847 – 853, 2011.

[30] F. Wang, K. Itoh, and T. Watanabe, "Relationship between the crystallographic structure of electrodeposited Fe-P alloy film and its thermal equilibrium phase diagram," *Materials Transactions*, vol. 44, no. 1, pp. 127 – 132, 2003.

[31] V. R. Gonçales, M. H. Gaitán, A. de O.P. Bragatto, G. J. Soler-Illia, L. M. Baraldo, and S. I. C. de Torresi, "Correlation between pore size and reactivity of macro/mesoporous iron and copper hexacyanoferrates for H_2O_2 electrocatalysis," *Journal of Electroanalytical Chemistry*, vol. 706, pp. 48 – 54, 2013.

[32] T. S. Narayanan, S. Selvakumar, and A. Stephen, "Electroless Ni-Co-P ternary alloy deposits: preparation and characteristics," *Surface and Coatings Technology*, vol. 172, no. 2-3, pp. 298 – 307, 2003.

[33] A. Mendoza-Garcia, D. Su, and S. Sun, "Sea urchin-like cobalt-iron phosphide as an active catalyst for oxygen evolution reaction," *Nanoscale*, vol. 8, pp. 3244 – 3247, 2016.

[34] Y. Cheng and S. P. Jiang, "Advances in electrocatalysts for oxygen evolution reaction of water electrolysis-from metal oxides to carbon nanotubes," *Progress in Natural Science: Materials International*, vol. 25, no. 6, pp. 545 – 553, 2015.

5

Discussion

Three different advanced, platable, binary systems, namely Co-In, Fe-Rh and Fe-P, have been investigated from an applied perspective. Although they are dissimilar in nature, they share some common features:

- An iron-group transition metal (Fe or Co) is combined with a post-transition metal (In), a noble metal (Rh) or a metalloid (P).

- In the electrodeposition field, cobalt is seldom alloyed with In whereas Fe alloys (with the exception of Fe-Ni) have been less investigated mostly due to the complex Fe electrochemistry. Therefore, these three systems have been scarcely tackled.

- Multiphase deposits are often obtained since the mutual solubility of the elements involved is limited.

- These systems can show highly tunable ferromagnetic response depending on the In content (for Co-In) and the Rh and P contents (for Fe-X where X = Rh, P).

The formation of spatio-temporal patterns is a phenomenon related to chaos that occurs in dynamic non-linear open systems driven far from equilibrium. Both fluid and chemical instabilities are thought to be behind this phenomenon. Electrodeposition does not escape from these instabilities and indeed spatio-temporal patterns can develop in certain binary and ternary systems. This is the case of Co-In deposits. We have observed that the spatio-temporal patterns visible at the surface of the electrodeposited Co-In films consist of a mixture of waves, concentric rings and spirals of variable sizes. Although the underlying mechanism is not yet clear, it seems that they originate as a result of the interplay of several factors, being the ability to form an intermetallic compound, in particular $CoIn_3$, one of key factors as recently pointed out. Interestingly, while hcp-Co and monoclininc $CoIn_2$ are the stable phases at room temperature for Co percentages equal or larger than 33.3 at.% according to the phase diagram, tetragonal $CoIn_3$ was detected by XRD instead of $CoIn_2$.

A threshold potential value was required as well for pattern formation all over the coating. This coincided with an abrupt change in composition from In-rich deposits (25 at% Co on average but with regions made of almost pure In) to deposits with Co contents beyond 50 at%. XRD analyses indicated the presence of In, Co and the intermetallic $CoIn_3$ compound in the deposits. A single-phase solid solution was

thus not formed but highly heterogeneous deposits, in agreement with the known immiscibility of In and Co in both solid and liquid states. Detailed EDX mappings were in concordance with this observation as the distribution of Co and In elements was not homogeneous across the surface but followed "separately" the bright and dark belts defined by the motifs. An important issue is that such spatio-temporal structures developed under stagnant conditions, which means that natural convection is enough to promote their formation. It was claimed in the past that intensive hydrodynamic flow and improved mass transport conditions were needed to trigger the formation of spatio-temporal patterns. Besides, we did not observe any switching among different types of patterns (labyrinths, waves, targets, spirals, broken spirals and mixed patterns) with the overpotential nor a trend between the size of these patterns and the overpotential. It might be that the potential window was not large enough so as to observe any switching, considering that it only varied from -0.94 V to -1.05 V (E = 0.11 V). Unfortunately, the current density and, hence the overpotential, could not be extended further since the deposits peeled off.

Due to the existence of fcc-Co and hcp-Co in the deposits, the films showed ferromagnetic response at room temperature. Indium is diamagnetic and $CoIn_3$ is weekly paramagnetic, therefore only the pure Co phases contributed to the ferromagnetic signal. Indeed, Co-In is a rather unique system in the sense that it is the only binary ferromagnetic alloy having the ability to form spatio-temporal patterns during electrodeposition. An issue which remains open is to understand to what extent these spatio-temporal patterns compete with the shape anisotropy. Regarding the nanomechanical properties, both hardness and Young's modulus increased with the Co content in the films. Although the mechanical response of pure $CoIn_3$ is unknown, the fact that In is a very ductile element and possesses much lower Young's modulus than either hcp- or fcc-Co serves to understand the observed trends.

Further miniaturization of Co-In deposits in confined micron-sized cavities led to a preferential pattern shape instead of the "chaotic" mixture of motifs observed for continuous films. We demonstrated the possibility to obtain reproducible spiral-like shapes inside a confined circular geometry that is commensurate with the micrometer size of the spatio-temporal features. Notably, when the continuous films were imaged by SEM using the SE detector, the spatio-temporal patterns were clearly revealed, indicating that the topographic features were strong. In contrast, SE images of the microdisks were featureless and the spirals emerged only when using the In-Lens detector, which is sensitive to variations in the chemical composition. It might be that differences in thickness (10 μm versus for continuous films vs. 1 μm for microdisks) can explain why the spirals did not show topographic features. We observed that the spatio-temporal patterns required some thickness to build up and it can be supposed that for larger thicknesses the spiral topography would gradually appear. As a result of the local changes in composition defined by the spiral, a periodic modulation of the physical (electric, magnetic and mechanical) properties was revealed. The use of a set of surface-sensitive techniques with slightly different probing depths and lateral resolutions suggested that a net magnetic patterning extends from the surface down to several hundreds of nanometers. The mapping of the Young's modulus and penetration depth in individual microdisks using the AM-FM tool of the AFM technique clearly showed that higher Young's modulus and larger hardness stand for Co-rich areas. Such a nanomechanical patterning was less evident in continuous films likely because nanoidentation was used instead. Although the maximum applied force was made small enough so that the indentation imprints were kept at the size of the bright and dark belts defining the motifs, a larger volume of material is probed, which means that the response is no longer kept at surface level.

Furthermore, an in-depth characterization of the layer-by-layer growth of the continuous Co-In films

was performed. It was observed that the formation of partially stacked individual layers, undulated and rather uniform in thickness spanned the whole film thickness. Unlike other systems (e.g. Ag-Sb), though, we did not observe any clear oscillatory pattern in either the j-t or E-t curves registered during Co-In deposition, which could be attributed to the formation of the nanolayers. In addition to the layered architecture, HR-TEM studies revealed the occurrence of a columnar structure inside each individual nanolayer. Most interestingly, MFM measurements showed that not only a magnetic patterning existed on-top but also at the level of the cross-section, making Co-In a complex, magnetically rich system.

According to the literature, the formation of spatio-temporal patterns also took place in other Co-In bath formulations containing di-ammonium hydrogen citrate as a pH buffer agent (replacing sodium citrate), cobalt sulfate instead of cobalt chloride, and at different concentrations of the reagents involved. However, we noted that the formation of spatio-temporal structures was immediately suppressed if zinc chloride was added to the electrolyte to partially replace cobalt chloride. Co-In-Zn tertiary system was synthesized by following the same strategy as in the case on Zn-free Co-In films, without any evidence of the formation of self-organized patterns. Therefore, the self-organization phenomena is very sensitive to changes in the chemical composition of the deposits.

Iron-containing materials for electrocatalytic applications were also considered in this Thesis. Electrodeposition was again the technique of choice to produce Fe-Rh and Fe-P. In order to increase the S/V ratio, the formation of NPs (Fe-Rh) and porous films (Fe-P) was targeted. In the first case, precious Rh was partially replaced by Fe with the aim to contribute toward cost-effective hydrogen production pathways. The concentration of sodium hexachlororhodate (III) in the electrolyte was very low (0.5 mM) to decrease costs since the average price of the salt is comparable to that of Pt precursors (e.g. hexachloroplatinate (IV)) used in electrodeposition. Despite the low concentration of Rh(III) in the bath, several samples could be produced until the NPs became significantly depleted in Rh. Typically, a low conductive substrate is employed to favor the formation of isolated NPs by electrodeposition. Here, a different strategy was pursued. Namely, deposition was performed from an Fe(III) salt. Although Fe(III) often gets bad press since it is related to low current efficiency depositions, its use precluded the formation of dense films. As a result, finely distributed rounded NPs were obtained over the substrate. Their size (20-80 nm) and Fe/Rh ratio could be varied by properly adjusting the applied current density and deposition time. From the structural viewpoint, the formation of fully alloyed Rh-Fe NPs could not be unambiguously ascertained and phase separation likely exists at the nanoscale. Nonetheless, the NPs were mostly metallic and the distribution of Fe across individual NPs was homogeneous. Although these NPs cannot compete with pure Pt and some of their alloys (e.g. Pt-Ni) in terms of HER, the results were interesting for several reasons. First of all, NPs with moderate Fe content (19 at.% Fe) outperformed pure Rh NPs obtained under similar electrodeposition conditions. Secondly, the large surface area displayed by the NPs directly benefited the HER response since denser coatings showed a decreased catalytic activity. This work also demonstrated that the electrodeposition from Fe(III) salts can be advantageous in many cases, in particular when nanosized Fe-containing materials are to be synthesized.

Fe-P films showing long range order of macropores (ca. 350 nm in diameter) were obtained by combining template-assisted colloidal method with electrodeposition. In this case, Fe(II)-containing bath was employed, to which sodium hypophosphite salt was added as the P precursor. The P content could be varied between 6 at.% P and 14 at.% P by adjusting the deposition potential. Fully dense films prepared at -50 mA cm^{-2} contained 15 at.% P, a percentage comparable to that of the macroporous Fe-P films prepared at -1.1 V (14 at.% P). Remarkably, the former were amorphous-like whereas the latter were

nanocrystalline. This indicates that not only the P content but also the substrate conditioning (planar vs. patterned) have an influence on the crystallographic structure of the deposits. Both fully dense and macroporous films showed tunable magnetic response, with saturation magnetization values that depended on the relative Fe:P:O ratio in the deposits. The macroporous films were magnetically harder in comparison to the plain films. Besides, wetting of the macroporous surfaces was hindered compared to the fully dense counterparts, giving rise to higher contact angle values. In spite of their higher hydrophicity, the macroporous films displayed faster kinetics toward OER. Notice that the reported contact angle values are static and not dynamic. Therefore, direct correlation between wettability and OER/HER performance might not be straightforward. Hydrophilic surfaces with large surface area are in principle desired for OER/HER applications. However, in many cases, higher surface areas are linked to a higher hydrophobic character, at it is the case here for the macroporous films.

6

Conclusions

The following bullet points summarize the conclusions that can be drawn:

1. Co-In films prepared by direct current electrodeposition from a chloride-citrate electrolyte show a magnetic patterning of micrometer size linked to the spatio-temporal patterns spontaneously formed during their growth. The occurrence of spatio-temporal patterns involves both compositional and topographical heterogeneities, whose spatial distribution defines the motifs observed.

2. The confined electrodeposition of Co-In in arrays of cylindrical cavities reveals that spiral-like patterns preferentially develop against the mixture of motifs observed for the unpatterned films. The spiral-like pattern formed in each Co-In microdisk has been studied with a set of surface sensitive characterization techniques that have disclosed well-defined magnetic, electrical and mechanical patterning.

3. Besides the self-organization phenomena observed at surface level, Co-In films exhibit an incredibly regular layer-by-layer growth mode which spans the whole deposit thickness. Detailed local analyses of each layer (ca. 175 nm thick) has proven the occurrence of compositional variations parallel to the substrate plane and a columnar microstructure. As a result of the layer-by-layer architecture, the films cross-section exhibit a stripe-like magnetic patterning.

4. Nanoparticles made of Fe and Rh can be obtained by electrodeposition from a Fe(III) containing electrolyte. The Fe/Rh ratio, size and electrode coverage can be conveniently adjusted by tuning the current density and deposition time. The obtained nanoparticles exhibit HER activity in alkaline media. For same particular Fe/Rh ratios, the nanoparticles outperform pure Rh synthesized under analogous conditions.

5. Highly-ordered macroporous Fe-P films with variable P contents can be obtained by potentiostatic electrodeposition in colloidal crystal templates. The resulting films are crystalline, show tunable magnetic properties, and are more hydrophobic than their fully dense analogues. The macroporous films show higher OER kinetics in alkaline media.

7

FUTURE PERSPECTIVES

Considering the results shown in the preceding sections, we briefly introduce several avenues for future work:

- In order to improve the adhesion of continuous Co-In deposits produced at current densities beyond -30 mA cm^{-2}, different substrates could be explored (e.g. copper, brass, stainless steel). This would allow to investigate whether the size of the spatio-temporal patterns and/or the motif type can be changed as the absolute value of the current density and hence, the overpotential, is made more negative.

- The confined electrodeposition of Co-In could be tested on lithographed substrates with arrays of triangles or squares in order to investigate whether the spatio-temporal patterns can form in non-circular geometries and if other motifs different from spirals are favored. In addition, the size of the cylindrical cavities could be progressively diminished in order to find the minimum diameter required for the spirals to develop.

- To optimize the synthesis of fully dense Fe-Rh films with near equiatomic stoichiometry so that the formation of the CsCl-type ordered Fe-Rh alloy is guaranteed and to study the antiferromagnetic (AFM)-ferromagnetic (FM) first-order phase transition by VSM. After electrodeposition, annealing treatments could be applied in order to increase the crystallinity of the as-deposited film and favor the formation of the target phase.

- The synthesis of Fe-Rh porous films could be explored and their HER performance compared to that of Fe-Rh NPs of similar chemical composition. Their electrochemical surface area (ECSA) could be determined by means of CV in order to have a quantitative comparison of the surface area.

- Regarding the HER performance of both Fe-Rh and Fe-P materials, although the LSV curves provide information on the onset of HER and the current density involved, the actual volume of hydrogen gas released remains unknown. The gas could be directly taken from the headspace of the electrochemical cell at different time intervals and injected into a gas chromatograph to determine the mmol h^{-1}cm^{-2} of H$_2$ generated.

- Either annealing of the macroporous Fe-P films or the synthesis from non-aqueous solvents could be implemented to trigger the formation of the hexagonal 1:1 FeP phase. This phase is claimed to be one of the most electroactive iron phosphides in OER.

Curriculum Vitae

Irati Golvano-Escobal

Address	Departament de Física, Sciences building, C3/210 Universitat Autònoma de Barcelona
City, State	08193 Bellaterra, Spain
e-mail	irati.golvano@uab.cat
Web address	http://jsort-icrea.uab.cat/htm/golvano.htm
LinkedIn	https://es.linkedin.com/in/iratigolvano-escobal

Education

2013–Currently **PhD in Materials Science**,
Universitat Autònoma de Barcelona, Barcelona, Spain.
Group: Smart Nanoengineered Materials, Nanomechanics and Nanomagnetism (Gnm^3)
Supervisor: Prof. Jordi Sort and Dr. Eva Pellicer
Place: Física de Materials II, Universitat Autònoma de Barcelona (Barcelona), Spain

2011–2012 **Master in Nanotechnology and Material Science**,
Universitat Autònoma de Barcelona, Barcelona, Spain.
Master Thesis: Structural Characterization of Polymers and Nanocomposites by Electron Microscopy.
Supervisor: Dr. Emma Rossinyol
Place: Servei de microscòpia, Universitat Autònoma de Barcelona (Barcelona), Spain

2010–2011 **Master in Photonics**,
Universitat Politècnica de Catalunya, Universitat Autònoma de Barcelona and Universitat de Barcelona, Barcelona, Spain.
Master Thesis: Optical Phase Control for Interferometric Near-Field Optics Applications.
Supervisor: Dr. Niek Van Hulst
Place: ICFO - Institut de Ciències Fotòniques, Mediterranean Technology Park, Castelldefels (Barcelona), Spain

2006–2010 **Electronic engineering (Bachelor's degree)**,
Mondragon Goi Eskola Politeknikoa, Arrasate - Mondragon, Spain.

Experience

2012–2015 **Electron microscopy technician**,
Universitat Autònoma de Barcelona, Barcelona, Spain.
Responsible for Electron Microscopy for Material Science

2009–2010 **Final degree project**,
Fagor Brandt SAS, Orleans, France.
Electronic Boards Designs and Development.

2008–2009 **Internship in the Department of Computing and Electronics**,
Mondragon Goi Eskola Politeknikoa, Arrasate - Mondragon, Spain.

Languages

Spanish	**Mother Tongue**	
Basque	**Independent User**	
English	**Proficient user**	*IELTS: Overall Band Score 6.5 (2010)*
		Listening 6.5 - Reading 8.5 - Writing 5.5 - Speaking 5.5

French	**Independent User**
Catalan	**Independent User**

Publications

I.Golvano-Escobal, B. Özkale, S. Suriñach, M. D. Baró, T. Dobrovolska, I. Krastev, S. Pané, J. Sort, E. Pellicer; *Self-organized spatio-temporal micropatterning in ferromagnetic Co-In films.* J. Mater. Chem. C, 2014, 2, 8259–8269. **I.F.=4.596** (2014)

I.Golvano-Escobal, S. Suriñach, M. D. Baró, J. Sort, E. Pellicer; *Electrodeposition of sizeable and compositionally tunable rhodium-iron nanoparticles and their activity toward hydrogen evolution reaction.* Electrochim. Acta, 2016, 194, 263–275. **I.F.=4.803** (2015)

I. Golvano-Escobal, J. C. Gonzalez-Rosillo, N. Domingo, X. Illa, J. F. López-Barbera, J. Fornell, P. Solsona, L. Aballe, M. Foerster, S. Suriñach, M. D. Baró, T. Puig, S. Pané, J. Nogués, E. Pellicer, J. Sort; *Spontaneous formation of spiral-like patterns with distinct periodic physical properties by confined electrodeposition of Co-In disks.* Sci. Rep., 2016, 6, 30398. **I.F.=5.228** (2015)

G. Piga, M. D. Baró, **I. Golvano-Escobal**, D. Gonçalves, C. Makhoul, A. Amarante, A. Malgosa, S. Enzo, S.; *A structural approach in the study of bones: fossil and burnt bones at nanosize scale.* Appl. Phys. A, 2016, 122, 1031. **I.F.=1.444** (2015)

I. Golvano-Escobal, J. de D. Sirvent, M. Ferran-Marqués, S. Suriñach, M. D. Baró, T. Puig, S. Pané, J. Sort, E. Pellicer; *Cross-sectioning spatio-temporal Co-In electrodeposits: disclosing a magnetically-patterned nanolaminated structure.* Mater. & Des., 114 (2017) 202-207. **I.F.=3.997** (2015)

I. Golvano-Escobal, et al.; *Highly-ordered macroporous Fe-P films with magnetic and electrocatalytic properties.* To be submitted.

Congresses

May 2013	**I. Golvano-Escobal**, E. Rossinyol, M. Roldán, A. Varea, M. D. Baró, J. Sort, E. Pellicer, *Characterization of electrodeposited Cu-Ni nanopillars by CSLM imaging.* ⊱ 13th International ELMI 2013 - Arcachon, France. Poster
June 2014	**I. Golvano-Escobal**, S. Pané, B. Özkale, B. J. Nelson, S. Suriñach, M. D. Baró, E. Pellicer, J. Sort, *Magnetic and mechanical behaviour of spatio-temporal patterned cobalt-indium films grown by electrodeposition.* ⊱ XIII Congreso Nacional de Materiales (CNM) - Barcelona, Spain. Oral contribution
June 2014	**I. Golvano-Escobal**, S. Pané, B. Özkale, B. J. Nelson, S. Suriñach, M. D. Baró, E. Pellicer, J. Sort, *Spontaneously formed spatio-temporal patterns in electrodeposited cobalt-indium films: structure, magnetism and mechanical properties.* ⊱ CCMR 2014 - Incheon, South Korea. Oral contribution
July 2014	**I. Golvano-Escobal**, B. Özkale, Ll. Abad, X. Borrissé, A. Varea, S. Suriñach, M. D. Baró, B.J. Nelson, S. Pané, J. Sort, E. Pellicer, *Electrochemical Deposition Strategies for the Growth of Films and Micro/nanostructures of Co-In and Co-Ni-W Functional Materials.* ⊱ ISMANAM 2014 - Cancún, Mexico. Oral contribution
May 2015	**I. Golvano-Escobal**, S. Suriñach, M. D. Baró, J. Sort, E. Pellicer, *Electrodeposited rhodium-iron nanoparticles: Control of size, composition and electrocatalytic activity for hydrogen evolution reaction.* ⊱ E-MRS 2015 - Lille, France. Oral contribution

June 2015	**I. Golvano-Escobal**, S. Suriñach, M. D. Baró, J. Sort, E. Pellicer, *Synthesis, electrocatalytic and other physico-chemical properties of electrodeposited rhodium-iron: nanoparticles and porous films.* ≻ CCMR 2015 - Busan, South Korea. **INVITED**
July 2015	**I. Golvano-Escobal**, N. Domingo, J. C. Gonzalez-Rosillo, T. Puig, S. Pané, S. Suriñach, M. D. Baró, J. F. López-Barbera,J. Nogués, E. Pellicer, J. Sort, *Self-Organised Spatio-Temporal Electric, Mechanical and Magnetic Micropatterning in Electrodeposited Cobalt-Indium Films and Microdisks.* ≻ ISMANAM 2015 - Paris, France. **INVITED**
September 2015	**I. Golvano-Escobal**, S. Suriñach, M. D. Baró, S. Pané, J. Sort, E. Pellicer, *Controlled electrodeposition of Rh-Fe nanoparticles for hydrogen evolution reaction applications.* ≻ EDNANO 2015 - Balatonfüred, Hungary. Oral contribution
September 2015	**I. Golvano-Escobal**, S. Suriñach, M. D. Baró, S. Pané, J. Sort, E. Pellicer, *Electrodeposited Rh-Fe films and nanoparticles for electrocatalytic hydrogen production.* ≻ EMN Spain Meeting 2015 - San Sebastian, Spain. Oral contribution
March 2016	G. Piga, M. D. Baró, **I. Golvano-Escobal**, A. Brunetti, S. Enzo, S. Garroni, *Nanoscale structures of fossil bones and growth processes for burned bones.* ≻ inArt 2016 - Ghent, Belgium. Poster
July 2016	**I. Golvano-Escobal**, S. Suriñach, M. D. Baró, S. Pané, J. Sort, E. Pellicer, *Fe–based electrodeposited nanomaterials for functional applications.* ≻ ISMANAM 2016 - Nara, Japan. Oral contribution
July 2017	**I. Golvano-Escobal**, J. C. Gonzalez-Rosillo, N. Domingo, X. Illa, J. F. López-Barbera, J. Fornell, P. Solsona, L. Aballe, M. Foerster, S. Suriñach, M. D. Baró, T. Puig, S. Pané, J. Nogués, E. Pellicer, J. Sort, *Spatio-temporal Patterns Formation In Co-In System: Films Vs. Microdisks.* ≻ FiMPART 2017 - Bordeaux, France. **INVITED**

Managerial activities

JPHD2015. 1st Scientific Meeting of BNC-b Students
Type of Activity: Co-organizer of the meeting
Place: Universitat Autònoma de Barcelona (UAB), Barcelona, Spain.
Date: 20-21 February 2015

Attendance to Courses

11-18 November 2011	**V Curs Intern Avançat de SEM**. ≻ Servei de Microscòpia - Universitat Autònoma de Barcelona (UAB) - Barcelona, Spain.
4–5 April 2013	**Jornada de Confocal Aplicada a Materiales**. ≻ Universitat Autònoma de Barcelona (UAB) - Barcelona, Spain.
15-19 April 2013	**V Curs Intern TEM**. ≻ Servei de Microscòpia - Universitat Autònoma de Barcelona (UAB) - Barcelona, Spain.
5-7 November 2013	**IV Curso de Microanálisis de Rayos-X en Microscopía Electrónica de Barrido**. ≻ Universidad Carlos III de Madrid (UC3M) - Madrid, Spain.
12-13 November 2013	**Análisis de Rugosidad y Textura Superficial con Microscopio 3D (Leica)**. ≻ Centres Científics i Tecnològics (CCiT), Universitat de Barcelona - Barcelona, Spain.
4-8 April 2016	**1st e-MINDS Training School: Electrochemical processing methods**, MPNS COST Action MP1407. ≻ Central European Institute of Technology (CEITEC) - Brno, Czech Republic.

User participation in synchrotron experiments

CELLS - **ALBA Synchrotron**
Experiment: 2015021227
Date: 27-29 November 2015
Place: Cerdanyola del Vallès, Spain.

Supervision of Final Degree Projects

Title: Spatio temporal patterns in electrodeposited alloys. **Pràctiques de Empresa i/o Institucions of Grau en Nanociències i Nanotecnologia**
Student: Juan de Dios Sirvent Verdú
Faculty: Facultat de Ciències
University: Universitat Autònoma de Barcelona (UAB)
Date: 01/10/2015

Title: Practicas Externas. Servei de Microscòpia UAB, **Pràctiques en Empresa i/o Institucions of Grau en Nanociències i Nanotecnologia**
Student: David Piña Muñoz
Faculty: Facultat de Ciències
University: Universitat Autònoma de Barcelona (UAB)
Date: 15/09/2014

Courses delivered (graduate level)

○ Laboratori de Microscòpies i Tècniques de Caracterització de Materials, **Grau de Nanociència y Nanotechnologia**
Courses: From 2011-2012 to 2015-2016
University: Universitat Autònoma de Barcelona (UAB)
144h

○ V Curs FESEM Avançat, **Servei de Microscòpia**
Courses: From 2011-2012 to 2015-2016
University: Universitat Autònoma de Barcelona (UAB)
16h

○ Practical Sessions: TEM, SEM and Confocal microscopy, **Master in Nanotechnology and Material Science**
Course: From 2012-2013 to 2015-2016
University: Universitat Autònoma de Barcelona (UAB)
28h

○ Practical Sessions: SEM, **Master in Chemistry**
Courses: 2012-2013 and 2014-2015
University: Universitat Autònoma de Barcelona (UAB)
20h

○ Material Characterization Techniques, **Master in Advanced Nanoscience and Nanotechnology**
Course: 2015-2016
University: Universitat Autònoma de Barcelona (UAB)
10h

Skills and Expertise

Electron Microscopy	TECHNICAL PROFILE: Field Emission Scanning Electron Microscopy (FESEM), Energy-dispersive X-ray spectroscopy (EDS), X-ray photoelectron spectroscopy (XPS), Electron Backscatter Diffraction (EBSD), Transmission Electron Microscopy (TEM), Sample preparation.	Microstructure studies of materials	Determination of particle size and shape, quality controls and production processes, surface microstructure characterization of different types of materials: weave, plastics, metals, etc.
Optical Microscopy	Confocal Microscopy and Interferometry 3D topography, Stereo-Fluorescence Microscope.	Other techniques	Autolab potentiostat/galvanostat, Vibrating sample magnetometer (VSM), Magnetic force microscope (MFM), Naoindentation, X-Ray Difraction (XRD).
Material characterization	SmartSEM, INCA, EDAX, HKL Channel 5.	Graph and Data Analysis	Origin Pro, X'Pert HighScore, MagicPlot-Student.
Image Processing	Image J, Digital Micrograph.	Programming languages	C/C++, Java J2SE, Step7 (Siemens), Python.
Development environments	MATLAB, Simulink, Scilab, NetBeans, Eclipse, Visual C++, LabVIEW.		